PSFC/RR-02-06

A Novel Quasioptical Gyrotron Traveling Wave Amplifier

Jagadishwar R. Sirigiri

October 2002

Plasma Science and Fusion Center
Massachusetts Institute of Technology
Cambridge, MA 02139, USA

This work was supported by the U.S. Department of Defence under the MURI for Innovative Microwave Vacuum Electronics.

A Novel Wideband Gyrotron Traveling Wave Amplifier

by

Jagadishwar R. Sirigiri

S.M.(EECS), Massachusetts Institute of Technology (2000)
B.Tech. (EcE), Banaras Hindu University, India (1996)

Submitted to the
Department of Electrical Engineering and Computer Science
in partial fulfillment of the requirements for the degree of

Doctor of Philosophy

at the

MASSACHUSETTS INSTITUTE OF TECHNOLOGY

February 2003

Signature of Author .....
Department of Electrical Engineering and Computer Science
7 October 2002

Certified by .....
Richard J. Temkin
Senior Scientist, Department of Physics
Thesis Supervisor

Accepted by .....
Arthur C. Smith
Chairman, Committee on Graduate Students
Department of Electrical Engineering and Computer Science

A Novel Wideband Gyrotron Traveling Wave Amplifier

by

Jagadishwar R. Sirigiri

Submitted to the Department of Electrical Engineering and Computer Science
on 7 October 2002, in partial fulfillment of the
requirements for the degree of
Doctor of Philosophy

Abstract

We present the design and the experimental results of a novel wideband quasioptical Gyrotron Traveling Wave Tube (gyro-TWT) amplifier and the first Vacuum Electron Device (VED) with a Photonic Band Gap (PBG) structure. The theory and experimental results from two other quasioptical gyrotron oscillator experiments are also presented.

The gyro-TWT amplifier at 140 GHz produced up to 30 kW of peak power in operation with 3 μs pulses at 6 Hz, 2.30 GHz unsaturated bandwidth, a peak linear gain of 29 dB and an efficiency of 12 %. This is the highest frequency gyro-TWT reported as yet. The use of a very high order operating mode in a novel mode selective interaction structure namely, a quasioptical open confocal waveguide makes the gyro-TWT potentially capable of up to 100 kW CW operation at 140 GHz and at 94 GHz in the W-band (75-110 GHz) if built to industrial standards.

The theory and experimental results from the first VED with a PBG resonator, in the form of a high power high frequency gyrotron oscillator at 25 kW power level at 140 GHz in a high order mode, TE_{041} are also presented. The absence of any spurious mode excitation over 30 % variation in the magnetic field corresponding to an equal variation in the cyclotron frequency indicates that the PBG resonator was highly mode selective while operating in a higher order mode. This opens up promising avenues for building highly oversized resonators for generating Terahertz radiation with low voltage electron beams. The successful operation of this high frequency gyrotron suggests that overmoded PBG resonators can also be used in conventional slow-wave devices to build moderate power (few hundreds of Watts) VEDs in the millimeter and sub-millimeter wave regime for a variety of applications.

A gyrotron oscillator experiment with an overmoded open confocal resonator was also run at a peak power of up to 83 kW at 136 GHz with an efficiency of 16 %. The gyrotron oscillator experiment had excellent mode stability which makes an oversized quasioptical open confocal resonator a candidate for use in high frequency millimeter and sub-millimeter wave gyrotrons. A second harmonic confocal gyrotron experiment was also tried at 280 GHz but the poor quality electron beam prevented the generation of the second harmonic, however, the stronger fundamental mode interaction

was suppressed thus validating the advantages of using confocal resonators in high harmonic gyrotrons to suppress the stronger fundamental interaction.

The experiments on three millimeter wave VEDs with two novel kinds of highly oversized interaction structures described in this work have demonstrated a novel technique for building high power (> 1 kW) high frequency (> 100 GHz) VEDs.

Thesis Supervisor: Richard J. Temkin
Title: Senior Scientist, Department of Physics

Acknowledgements

I have been privileged to work with so many wonderful people during the course of this research. My research supervisor, Dr. Richard Temkin guided me through this work with a lot of interest and patience and taught me the significance of starting from first principles. I am thankful to him for giving me an opportunity to work on this research. Dr. Michael Shapiro helped me with many aspects of the design of all the experiments and his insights and explanations about the theory of quasioptical structures was very useful. Mr. Ivan Mastovsky was very helpful in the design and fabrication of the experimental setup and his dedicated efforts led to the successful building of four different experiments during the course of this work. I am thankful to Mr. William Mulligan especially for his help in ensuring that the high voltage modulator performed very well during each experiment. Dr. Kenneth Kreischer gave valuable suggestions which proved to be very useful in running the experiments.

I wish to thank Dr. John Machuzak for his help in running the photonic band gap gyrotron experiment and Dr. Paul Woskow for his suggestions in conducting the microwave measurements and various diagnostics. I thank Steve Korbly for his encouragement and his help with the electron gun simulations. My fellow graduate students Mark Hess, Winthrop Brown and William Davis Lee were a great company and have always been a source of encouragement. I also thank Jim Anderson and Melissa Hornstein for their help in the laboratory. Dr. Chiping Chen and Evgenya Smirnova were very helpful with the theory of wave propagation in photonic band gap structures. Dick Koch of American Cryotech fabricated most of the parts for the various experiments very timely and with great care. Ron DeRocher of the MIT Magnet Lab Machine Shop was very generous in letting us use his facility for quick modifications to the various parts used in the experiments.

This research was carried under the auspices of the Innovative Microwave Vacuum Electronics (MVE) program of the Multi-Disciplinary University Research Initiative (MURI) funded by the U.S. Department of Defense. I wish to thank my Prof. Abraham Bers and Prof. David Staelin who served in my thesis committee. Prof. Bers

also served as my academic advisor and in my oral exam and area exam committees.

I am thankful to my parents and my sisters for their encouragement and patience during this work. Mr. P. Mishra, my teacher and mentor has always been a constant source of encouragement. Mr. K. G. Arora and Mrs. V. Arora have been very encouraging and supportive throughout my graduate studies. I thank Prof. B. N. Basu and Prof. P. K. Jain of the Banaras Hindu University who cultivated my interest in microwave tubes and supervised my research during my undergraduate studies. They have always encouraged me in my research.

So many of my friends have been a tremendous source of encouragement. Manish Arora, Kanishka Das, Shaily Srivastava, Sridhar Subramanian and Chandrika Tripathy have been very good friends since my undergraduate days and have always been interested in my work. I am very thankful to Rahul and Simran Advani, Deepti Arora, Prakash Chauhan and Debaleena Das, Narendra and Suchita Gathoo, Kriten Joshi, Nikhil and Ritu Joshi, Jenn and Steve Korbly, Sangeeta Singh, Satyen and Uma Vyas for being such good friends. They made my graduate school days very enjoyable and have always encouraged me in my studies and research.

Dedicated to the memory of Ginni Mishra (4/15/1956 – 3/17/2001)

Contents

List of Figures

List of Tables

Chapter 1

Introduction

1.1 The Empire of Tubes

Microwaves are the lifeline of this era of communications. Their use is ubiquitous, from ground based communications to the control of deep space probes far above in the heavens. The microwave regime of the electromagnetic spectrum is the most widely used since the discovery of radio communication in the early twentieth century. The Second World War was a major catalyst for the rapid development of microwave sources for radar applications [1]. In the early 1930's various researchers saw the feasibility of generating higher frequencies using resonant cavities connected to electrical circuits. The first such device, namely, the *klystron* was invented by the Varian brothers in 1937 [2]. This was followed by the rapid development of other devices such as the magnetron and the Traveling Wave Tube (TWT) [3],[4], the Backward Wave Oscillator (BWO) during World War II and later the cross-field amplifier in the 1960's. Traveling wave tubes continue to be the mainstay for satellite communication for both military and civilian applications. Recently, millimeter waves have made inroads into the traditional microwave domains such as communications and radar in the Ka-band (26.5–40 GHz) and the W-band (75-110 GHz). The success of Electron Cyclotron Resonance Heating (ECRH) in stabilization of thermonuclear fusion experiments has fueled the interest in high power gyrotrons, which to date remain the only high average power, high efficiency sources above 100 GHz [5]–[7].

The development of solid-state technology beginning in the 1970's saw the strong emergence of solid-state sources in the generation of microwaves. However, till date Vacuum Electron Devices (VED), also called microwave tubes have the unique capability to generate very high power in the microwave and millimeter wave regime – several orders of magnitude higher than solid-state sources [8]. The full promise of wide bandgap semiconductor transistors is yet to materialize for high average power applications. There is an inexorably growing gap between the requirements of modern high power communication and radar systems and the state-of-the-art in solid-state devices. Numerous examples can be cited of how VEDs eventually came to the rescue where solid-state power amplifiers could not meet the final specifications in some military systems or how VEDs such as the inductive output tube and the constant efficiency amplifier are preferred over their solid-state counterparts in television broadcasting [9]. The state-of-the-art AlGaN/GaN Heterostructure Field Effect Transistors (HFET) has demonstrated 4-5 Watts of power over 3–20 GHz [10], where as Microwave Power Modules (MPM), which use a solid state driver with a TWT power amplifier, also called a Vacuum Power Booster (VPB) can routinely produce hundreds of Watts of power at these frequencies and beyond [8]! A state-of-the-art Northrop Grumann MPM with 100 W CW power, 123 cm^3 in size and weighing only 363 gm achieves a power density of 0.81 W/cm^3 at 45 % efficiency [8].

The electron flow in VEDs is collisionless in contrast to the charge carrier flow in semiconductors which renders higher efficiency to the VED. Furthermore, VEDs can operate at much higher temperature than their solid-state counterparts and hence are better suited for dissipating waste heat that, unavoidably, goes along with the production of high power. A comparison of the capability of solid-state devices versus VEDs is shown in Fig. 1-1 on page 31.

Microwave tubes such as the klystron are the only option for driving linear collider experiments such as the Next Linear Collider (NLC). The 75XP klystron [11] developed at SLAC for use in the NLC can produce 75 MW of peak power at 11 GHz with 50% efficiency. Gyrotron amplifiers are in serious contention to serve as drivers for higher frequency linear colliders [12] especially if the collider RF frequency goes

in to the millimeter wave band [13], [14].

The requirements for a modern ECRH system, such as for the DIII-D tokamak at General Atomics, San Diego, is about 10-15 MW of CW power for tens of seconds at 110 GHz. Gyrotron oscillators (up to 1.5 MW per unit) are currently the only viable option for such a system and can operate at an electronic efficiency of about 35% [15]. The use of a depressed collector can further enhance the total efficiency to above 50 % [16]. The requirements of 10 kW of average power at 94 GHz for the W-band radar is possible only in the realm of VEDs – the option being, quasioptical power combining of solid-state sources, which is beset by problems of phase synchronization and low efficiency.

A compact 250 GHz gyrotron oscillator at MIT produces 100 W of CW power for applications in Electron Paramagnetic Resonance (EPR) experiments in Nuclear Magnetic Resonance (NMR) spectroscopy studies [17]. Gyrotrons capable of operating at frequencies up to 889 GHz have been built at Fukui University [18] in Japan for a variety of applications.

The recent experimental demonstration of the W-band gyroklystron [19], [20] has yielded a staggering 10 kW average power and 92 kW of peak power with a 420 MHz instantaneous bandwidth at 93 GHz. Traveling wave tubes also have a presence in the W-band around the 94 GHz window frequencies. The Millitron series [21] of tubes from Communication Power Industries (CPI) can produce up to 100 W of CW or 1 kW of peak power in the 80–100 GHz range. Recently, Thomson Tubes Electroniques reported a 94 GHz slow-wave TWT with an instantaneous bandwidth of 500 MHz, output power of 200 W and a maximum duty cycle of 10 % [22]. Extended Interaction Klystrons (EIK) from CPI can produce in excess of 1 kW of peak power at 94 GHz with a mechanically tunable bandwidth from 91-96 GHz [23].

In spite of the rich history, new VED concepts are still emerging with amazing regularity. The MPM or the VPB has already been mentioned earlier in this section. It has all the advantages of low weight, compactness, high gain and robustness which make it very attractive for airborne applications. Recently, interest has reemerged in an old concept, namely the Multiple Beam Klystron (MBK) [24]. MBKs have

several advantages over conventional klystrons in terms of higher power capability and wider bandwidth [25]–[28]. The use of multiple beams mitigates the space charge effects and thus allows larger amount of current relative to the cavity gap capacitance. Recent investigation of MBKs show that they can emerge as a low voltage compact klystron with significantly enhanced instantaneous bandwidth compared to that of the klystron [8]. The electron beam current increases with the number of beams, however, the capacitance of the fringing fields which limit the bandwidth scale only as the radius of each electron beam thus improving the bandwidth. Since each beam has its own drift tube the space charge effects are better neutralized than in a single beam device operating at the same current.

Sandwiched between the microwave and the optical spectrum, millimeter waves enjoy distinct advantages. The benefits of operating at higher frequencies is well understood for communication and radar applications. Optical frequencies seem to be a better choice than either microwaves or millimeter waves on this count but the detrimental effects of weather on free space optical communication has limited its role in long range wireless communication applications. Millimeter waves find extensive application in a wide range of communication and other applications. For example, a source in the range of 180-1000 GHz can be used as a local oscillator for astronomical telescopes, heating of confined plasmas in fusion experiments require high powers (tens of MW's) in frequencies ranging from 84-170 GHz [5] and a modern W-band radar requires 5 kW of average power in the 92-100 GHz band. Interesting applications for millimeter waves are also emerging in material processing [29] and Dynamic Nuclear Polarization (DNP) in Nuclear Magnetic Resonance (NMR) spectroscopy [30].

1.2 Physics of Microwave Sources

All VED's are based on the principle of converting the free kinetic energy of an electron beam to electromagnetic wave energy. A charged particle that encounters acceleration radiates electromagnetic energy. The following manifestations of this principle lead to different kinds of VED's.

- An electron moving in a circular path in a magnetic field experiences an accelerating or a braking force thus generating radiation by a process called magnetic *bremsstrahlung*. This is the basic principle behind cyclotron and synchrotron radiation. Gyrotrons fall under this category.

- Electrons traveling in a medium with a velocity greater than that of the propagating electromagnetic wave in the same medium radiate energy in the form of a shock wave. Such a scenario is realized in practice in a slow-wave-structure in TWTs and BWOs. This form of radiation is popularly known as *Cherenkov* radiation.

- The stimulated emission of photons by free electrons in a wiggler is the principle of a free electron laser (FEL). In contrast to traditional lasers where the fixed energy levels imply a fixed wavelength of radiation, in a FEL the radiation wavelength depends on the free energy of the electrons which results in a tunable source.

- Transition radiation is generated when electrons experience a change in the refractive index of the medium in their path. This is an effective way for generating Terahertz radiation by mega-electron-volt beams.

In every coherent radiation source a different scheme is used to bunch the radiating electrons to produce coherent radiation. The different mechanisms of bunching call for different shapes of the interaction structures, accelerating voltages and magnetic field configurations.

The beam-wave interaction in a microwave circuit such as a cavity or a waveguide can be designed to generate unstable solutions to the coupled beam-wave dispersion relation. This is similar to the electron beam-plasma interaction which has been well studied in the area of plasma physics [31]. The instability can be either an absolute instability or a convective instability or both [32]. The absolute instability can be usefully exploited to form an oscillator while, the convective instability can be harnessed for amplification.

1.3 Cyclotron Resonance Masers

Microwave vacuum electron devices based on Cherenkov radiation, such as the TWT have dominated other kinds of devices ever since World War II. The unique combination of gain and bandwidth in a TWT has earned it an enviable place in the era of satellite communication. *Cherenkov* devices employ a slow-wave-structure (SWS) to slow down the phase velocity of the electromagnetic wave to bring it into synchronism with a subluminous electron beam to allow beam-wave interaction. The SWS takes the form of either the most popular helix or various other forms such as a coupled-cavity structure, a dielectric-loaded waveguide etc. For optimum interaction, the transverse dimensions of the SWS need to be a fraction of the wavelength of the radiation. This leads to rapid miniaturization of the transverse dimensions with increasing frequency, which not only poses great difficulty in the fabrication of the fragile SWS but also a severe limitation on the thermal capability of the device. This ultimately limits the power that can be generated in such a device. On the other hand, conventional lasers and Free Electron Lasers (FEL), which dominate the far infrared and the optical regimes suffer from low efficiencies and bulkiness in the millimeter wave regime [33]–[35].

Instead of using a periodic slow-wave circuit for interaction with a pencil electron beam (as in a conventional TWT) one may use a periodic beam propagating in a smooth walled interaction structure supporting a fast waveguide mode. The possibility of generation of radiation by interaction between gyrating electrons and a fast wave was independently suggested in [36], [37] and [38]. This scheme is based on the Electron Cyclotron Resonance Maser (ECRM) instability, which involves the interaction between a mildly relativistic to a relativistic gyrating electron beam with a transverse waveguide or resonator mode. One of the earliest Cyclotron Resonance Maser (CRM) experiments was reported by Hirshfield [39]. In CRMs coherent radiation is produced by the phase bunching of the mildly relativistic electrons gyrating in their Larmor orbits around the guiding center. CRMs can be built as either coherent oscillators or amplifiers [40]. There are fundamental differences between conventional

slow-wave devices such as the klystron, TWT etc. and CRMs. It is worthwhile at this juncture to highlight some of the basic differences in the interaction physics of the conventional slow-wave and the CRM fast-wave devices.

In CRMs the transverse energy of the electrons contained in the gyrations is converted to RF radiation, while the axial energy is left undisturbed. However, the axial energy is very important for the interaction as it facilitates the Doppler shifted cyclotron resonance of the electron cyclotron wave with a waveguide mode. The physics of the interaction is discussed in detail in Chapter 2. In contrast, slow-wave devices rely on the extraction of the axial energy of the electron beam for the generation or amplification of the RF wave.

The radiation frequency in CRMs is at either the cyclotron frequency or at one or many of its harmonics. Thus the radiation frequency is not entirely controlled by the size and shape of the waveguide or the resonator, henceforth referred to as the interaction structure. This can be contrasted to the slow-wave devices where the radiation frequency is almost entirely dependent on the shape and size of the resonator. Thus slow-wave devices are more susceptible to parasitic oscillations than CRMs, which can employ a higher order mode of the interaction structure thus increasing its transverse size. Any increase in the size of the interaction structure is always an advantage for operation at high peak and average powers. This allows gyrotron oscillators to employ a very large resonator operating in a higher order mode, such as the $TE_{22,6}$ to generate 1 MW of CW power at 110 GHz!

Furthermore, slow wave devices rely on axial bunching of the electron beam which is born from the velocity modulation of the electrons as they pass through a very narrow gap in a resonator such as in a klystron. The gap needs to be much smaller than the operating wavelength to increase the depth of modulation [41] which becomes quite a problem at higher frequencies. Firstly, the small gap increases the electric field in high power devices and causes breakdown which, severely limits the peak power of the device. This is an important issue in high power klystrons such as the 75XP at SLAC [11]. At millimeter wave frequencies the rapidly decreasing wavelength miniaturizes the gap which dramatically complicates the fabrication of the resonator.

Since CRMs rely on the interaction of the electron over a Larmor orbit with a rotating electric field (such as a TE_{mn} mode) the interaction takes place over a large number of orbits and hence there is no need for a localized interaction as necessary in klystrons. Thus the gyroklystrons use resonators which are a few wavelengths long compared to a klystron which relies on the use of narrow gap reentrant resonators.

The gyromonotron more popularly known as the gyrotron employs an annular gyrating electron beam exciting oscillations in a large overmoded cavity. This device is presently the workhorse for heating fusion plasmas in magnetic confinement fusion experiments [5]. A review of high power gyrotrons is presented in [15] and [42]– [44]. Results from high power high frequency gyrotron research have improved steadily over the past two decades. Some notable high power gyrotron experiments are reported in [47]–[56] and high frequency high harmonic gyrotrons have also been well investigated [18], [57],[58]. Of the many configurations of gyrotrons, the Gyrotron Traveling Wave Tube (gyro-TWT), the gyroklystron and the gyrotwystron can be used as amplifiers [40]. The gyro-TWT harnesses the convective instability between a mildly relativistic gyrating electron beam and a co-propagating fast wave in a waveguide. The Cyclotron Auto-Resonance Maser (CARM) employs a highly relativistic beam in a configuration similar to that of a gyro-TWT, but operates far away from the waveguide cut-off resulting in a large Doppler upshift.

1.4 Gyrotron Amplifiers

While gyrotron oscillators have become the mainstay for ECRH of fusion plasmas, gyrotron amplifiers are only recently emerging as viable amplifiers in the millimeter wave band. The presence of low attenuation bands in the millimeter and sub-millimeter parts of the electromagnetic spectrum are very useful for long distance communication. The availability of sources and amplifiers in these *windows* will be useful for space communication and high resolution radar. One such window centered around 94 GHz is presently being pursued for millimeter wave radar applications [59].

Instead of a single large resonator to support oscillations excited by an electron

beam as in gyrotrons, a different manifestation of the CRM can amplify an input signal by using either two or more resonators separated by a drift tube (gyroklystron) or an input resonator followed by an output traveling wave section (gyrotwystron) or only a traveling wave section (gyro-TWT) or combinations thereof. All these devices are cousins of the counterpart slow wave devices such as the klystron, the twystron and the TWT.

Following the success of the development of W-band gyro-klystron in Russia [60], extensive research and development of the W-band (70-110 GHz) gyroklystron has proven to be a tremendous success in the United States [19]. The recent gyroklystron experiments at the Naval Research Laboratory (NRL) and Communication and Power Industries (CPI) have demonstrated for the first time average powers above 10 kW in the W-band [20]. A series of experiments have demonstrated 67 kW peak power, 460 MHz 3dB bandwidth at 28 % efficiency [19], 60 kW peak power, 640 MHz 3dB bandwidth at 25 % efficiency [61], 10 kW average power (92 kW peak at 11 % RF duty cycle), 420 MHz 3 dB bandwidth at 33.5 % efficiency or 115 kW peak power at 600 MHz bandwidth [20], 72 kW peak power, 410 MHz 3 dB bandwidth with 50 dB saturated gain and 27 % efficiency [62]. Recent experimental investigation of W-band gyrotwystrons has yielded 50 kW peak power at 93.9 GHz with 925 MHz 3 dB bandwidth at 17.5 % efficiency [64].

The gyro-TWT has the potential to generate high powers over a wide frequency band in the millimeter and sub-millimeter wave part of the spectrum. The inherent promise of wide bandwidth in a gyro-TWT comes from the use of a nonresonant interaction structure such as a smooth wall waveguide. This makes the gyro-TWT more attractive than the gyroklystron which uses resonant input and output cavities which are synonymous with small bandwidth unless the cavities are stagger tuned or clustered [65]. However, gyro-TWTs are significantly more difficult to build and operate due to the competition from the absolute instability of various modes and Backward Propagating Wave Oscillations (BPWO) arising from the long interaction structure and sensitivity to velocity spread in the electron beam.

Gyro-TWTs have received significant attention since the late 1970's. There has

been steady progress in the development of both theory and experiments in the past three decades [66]–[85]. Some of the noteworthy experiments include the demonstration of a 14 % bandwidth at 35 GHz [66], 20 % bandwidth with 25 dB gain from 32-39 GHz [74], 70 dB gain at 35 GHz [78], 1 MW peak power at 10 GHz [79], 137 kW peak power, 47 dB gain with 1.11 GHz bandwidth (3.3 %) at an efficiency of 17 % [83] and 180 kW peak power, 25-30 dB gain, 10 % bandwidth at an efficiency of 27 % in the second harmonic operation [85]. Most of these experiments have either used the fundamental mode in a circular waveguide or at most the TE_{01} mode to alleviate the problems of mode competition. The helical waveguide gyro-TWT experiment [79], however, uses a hybrid mode excited by the skew boundary conditions presented by the helical corrugation on the waveguide walls. These methods cannot be employed to generate high powers at the W-band due to the following problems. Choice of the fundamental waveguide mode leads to miniaturization of the circuit leading to the familiar problems of thermal limitation as observed in conventional slow-wave devices. The size and precision of the helical corrugations on the waveguide wall are likely to dramatically complicate the fabrication at 94 GHz operating frequency and above. Choice of an overmoded structure may allow larger transverse dimensions but brings forth a new problem – increased mode competition.

Another interesting alternative is a relativistic gyro-TWT amplifier. The first multimegawatt relativistic gyro-TWT amplifier experiment at MIT [86] produced 4 MW with 8 % efficiency at 17.1 GHz. Excellent phase stability of ± 10 % was measured over a 9 ns period in the TE_{31} mode of operation. The experiment however, used a Pierce wiggler beam formation system resulting in a poor beam quality, especially a very high energy spread.

A smooth walled interaction structure preferentially favoring the harmonics than the fundamental modes, with an additional parameter for suppressing the competing modes seems to be the likely candidate for generating higher powers. A quasioptical open waveguide formed by two confocal mirrors precisely satisfies these requirements and presents itself as a potential candidate for an interaction structure of a gyro-TWT in the millimeter and sub-millimeter wave band. The diffraction from the

open ends of such a waveguide can be used to preferentially attenuate the competing modes in favor of the operating mode. Wave propagation and confinement in open mirror systems has been well studied in the past [87]. Experiments based on such a confocal cavity based gyrotron oscillator were performed at MIT [88]. These initial experiments generated 66 kW of peak power at 136 GHz in the HE_{06} mode of the confocal waveguide.

The success with such a quasioptical interaction structure motivates one to investigate an amplifier configuration in the 94 GHz band. Such an amplifier operating in a higher order waveguide mode will have larger transverse dimensions of the interaction structure compared to the operating wavelength. Besides, one may use the diffraction from the open lateral ends of the waveguide to suppress the parasitic modes. In a confocal waveguide, the higher order modes suffer less diffraction than the fundamental mode – a property which may be successfully exploited in a high harmonic gyro-TWT.

In this work we report the design and experimental results the first quasioptical gyro-TWT capable of operating at W-band (94 GHz) and beyond. The gyro-TWT will use a quasioptical open confocal waveguide as the interaction structure. Operation in a higher order mode which resembles the TE_{03} mode of a cylindrical waveguide should allow up to 100 kW CW operation at 94 GHz. Mode competition will be suppressed in this highly overmoded interaction structure by diffraction of the most dangerous lower order parasitic modes from the open sidewalls. In a conventional design using a cylindrical waveguide the strong presence of the parasitic modes presents significant threat from Backward Propagating Wave Oscillations (BPWO) and gyrotron oscillations. The choice of larger transverse dimensions and a smooth walled waveguide without any dielectric loading will also simplify fabrication. The use of a higher order Gaussian like mode in the experiment should significantly simplify the design of the internal mode converter and allow an easy formation of a Gaussian beam at the window for an efficient coupling to the HE_{11} mode of a corrugated waveguide for an ultra low loss transmission to the antenna of a radar or a communication system.

Various important gyro-TWT experiments of the past and some ongoing experiments have been summarized in Table 1.1 on page 32. We propose to setup the first quasioptical gyro-TWT experiment at MIT at 140 GHz. The choice of the frequency was based on the availability of a driver and an electron gun at 140 GHz rather than the preference of 94 GHz for radar applications. The present design can easily be scaled down to 94 GHz without any degradation in performance.

A second harmonic gyrotron oscillator will also be conducted to test the feasibility of the confocal waveguide interaction structure for use in a high harmonic gyro-TWT. The primary advantage of a high harmonic gyro-TWT is the reduction in the necessary magnetic field by the cyclotron harmonic number. Higher harmonic gyro-TWTs are more stable than fundamental gyro-TWTs and allow the operation at higher beam currents and hence are capable of producing higher output power provided the fundamental mode interaction with gyro-BPWO and gyrotron modes is effectively suppressed. The confocal waveguide by its unique ability to impart higher diffraction losses to the lower order modes should be a suitable candidate for high harmonic operation.

Another novel concept that can revolutionize the way gyro-TWTs are built will be investigated in the form of a gyrotron oscillator experiment. We plan to use an interaction structure made of a Photonic Band Gap (PBG) structure to suppress mode competition in a highly overmoded waveguide. This presents a unique opportunity to take advantage of overmoded operation while avoiding mode competition without significantly perturbing the operating mode. In a confocal waveguide the open side walls of the waveguide deviate the symmetry of the operating mode from the cylindrical electron beam thus reducing the efficiency. However, a PBG waveguide can support a mode almost identical to a TE_{0n} mode which would improve coupling to the electron beam. We propose to demonstrate a gyrotron oscillator experiment in a higher order operating mode as a proof-of-principle experiment to validate the claimed advantages of a PBG interaction structure for all classes of microwave tubes including slow-wave devices.

The successful demonstration of a confocal guide as a suitable interaction struc-

ture at sub-millimeter wavelengths for gyro-TWTs will herald the next generation of harmonic gyro-TWT operating at frequencies as high as 250–500 GHz. Such devices may find attractive application in DNP experiments at 460 GHz for which currently a gyrotron oscillator is being built at MIT [89] or in high resolution radars and imaging applications.

1.5 Thesis Outline

This thesis is organized broadly in two parts. The first part which includes Chapters 1-3 contains the introduction and the theoretical part of the research. Chapters 4-8 present the design of the experiments, the experimental results and conclusions.

In Chapter 2, we present a summary of the theory of gyrotron amplifiers developed as part of this work and especially for application to gyrotrons with quasioptical interaction structures such as the one used in this work. A review of the gyrotron oscillator theory is also presented. Computer codes based on the above theories developed during the course of this work are also described. Chapter 3 contains a discussion of mode selective interaction structures and their applications in VEDs. In Secs. 3.1.1 and 3.1.2 the theory for wave propagation in Photonic Band Gap (PBG) structures is reviewed. This theory was developed by Smirnova et al. [90] in which this author developed the techniques of simulating PBG structures in the Ansoft High Frequency Structure Simulator (HFSS) [91]. In Chapter 3 we also discuss the limitations of conventional techniques for building millimeter wave devices and propose the idea of using overmoded yet mode selective interaction structures, which permit operation in a higher order mode without mode competition. Two specific kinds of mode selective structures investigated during this work, namely, quasioptical open confocal waveguides and PBG structures are described. The theory and techniques for designing mode selective resonators and waveguides using these structures is also presented.

Before we describe the various experiments the experimental techniques and diagnostics used in all the experiments are described in Chapter 4. The PBG resonator

gyrotron experiment is presented in Chapter 5. The 140 GHz confocal gyrotron oscillator and the 280 GHz second harmonic gyrotron oscillator experiment are discussed in Chapter 6. The design of the 140 GHz confocal gyro-TWT and the experimental results are described in Chapter 7. A discussion and the conclusions from this research are detailed in Chapter 8.

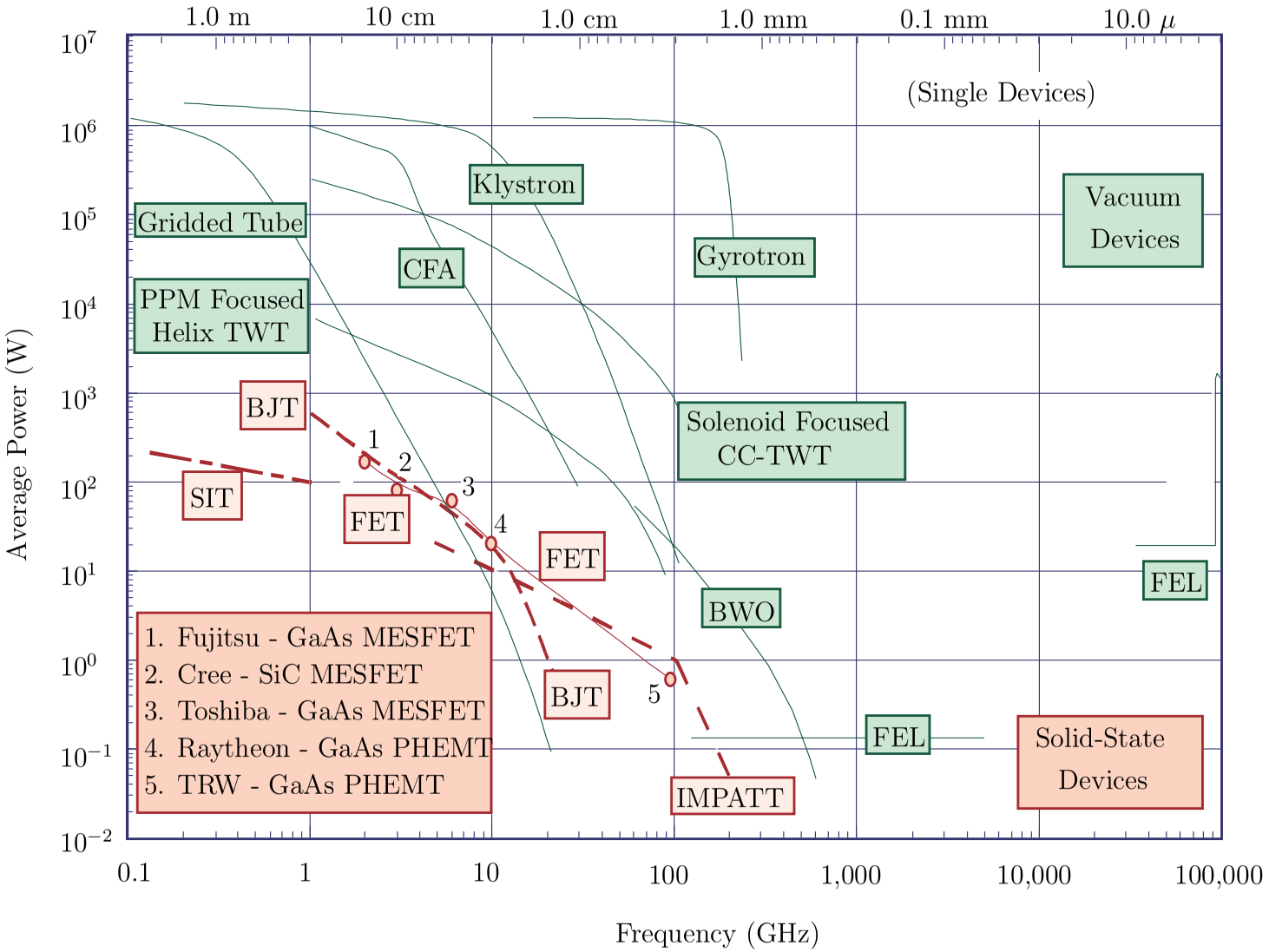

Figure 1-1: Comparision of the frequency and power capability of single solid-state and vacuum electron devices (Courtesy of Bruce Danly, NRL).

Year	Institution	Cyclotron Harmonic	Voltage (kV)	Frequency (GHz)	3dB(%) Bandwidth (%)	Peak Power (kW)	Saturated Gain (dB)	Efficiency (%)
1981	NRL [66]	1	70	35	13	–	18	–
1981	Varian [67]	1	65	5	7.25	128	20	24.0
1994	UCDAVIS [72]	2	80	16	2.1	207	16	13.0
1995	NRL [74]	1	33	32-39	20	10	25	16.0
1995	NTHU [76]	1	100	35	12	62	33	21.0
1996	MIT [86]	3	400	17.1	–	4000	50	8.0
1997	NTHU [77]	1	100	35	8.6	93	70	26.5
1998	IAP/UoS [79]	2	185	8.4-10.4	21	1100	37	29.0
2002	NRL [83]	1	72	34.1	3.3	137	47	17.0
2002	IAP [85]	2	80	35	10	180	30	27.0
Proposed Experiment at MIT		**1**	**65**	**140**	**4**	**100**	**40**	**27.5**

Table 1.1: Comparison of the proposed gyro-TWT experiment at MIT with other successful gyro-TWT experiments.

Chapter 2

Theory of Gyrotrons

2.1 Introduction

An electron beam traversing through a dispersive medium is known to be susceptible to numerous instabilities. The free energy in the electron beam emanating from its drift velocity can be exchanged with a forward wave (traveling wave amplifier), backward wave (backward wave oscillator or backward wave amplifier) or a stationary electromagnetic wave (oscillator) in the system. The earliest expositions of such beam-wave coupling were devoted to the interaction of the space charge waves on the electron beam with a *slow* electromagnetic wave propagating in the medium [92],[93]. The term *slow* is used to denote the magnitude of the phase velocity of the wave in the direction of the drifting electron beam as compared to the velocity of light in that medium. The TWT which constitutes such a system has been studied extensively [93].

Various kind of instabilities thrive in a beam-wave system. Almost all of them can be explained in terms of the interaction between either the slow and fast space charge waves, or the cyclotron waves on the electron beam and the electromagnetic waves in the circuit. The terms slow and fast space charge waves refer to the space charge waves that exist on the electron beam (a non-neutral plasma), with phase velocities slower and faster than the beam velocity, respectively. The slow and fast space charge waves are also classified as negative and positive energy waves. The

energy extraction process is unique to each instability but generally for any coherent radiation the electrons need to be bunched by the RF field before energy extraction by the deceleration of the bunch by the RF field at the exit of the interaction structure. The Cherenkov interaction [93] in a TWT between the slow space charge wave and the RF wave leads to energy extraction from the longitudinal component of the electron velocity. Hence, such devices employ a pencil electron beam which has only longitudinal kinetic energy and are known as slow-wave devices. The interaction between a beam of gyrating electrons, in the presence of a static axial magnetic field and a fast electromagnetic wave (phase velocity is superluminous) can lead to extraction of the transverse kinetic energy of the electrons. This interaction referred to as the Cyclotron Resonance Maser (CRM) instability was independently suggested in [36]–[38]. These devices are also called fast-wave devices. The gyrating electrons can also interact with a slow-wave and this mechanism is called the Weibel instability [94] and is the operating principle of a Slow-Wave Cyclotron Amplifier (SWCA). The linear and nonlinear theories of the CRM instability are well described in [95] and [96]. The CRM mechanism phase bunches electrons in their Larmor orbits due a change in their relativistic mass as they gain or lose energy from the transverse electric field in the waveguide, on the other hand the Weibel instability results from the axial bunching of the electrons perpendicular to the cyclotron orbit by the RF magnetic field [97]. The CRM mechanism dominates in the fast wave regime while the Weibel mechanism is dominant in the slow wave regime [98]. Another kind of cyclotron interaction called the peniotron interaction was first described in [99] at about the same time as the discovery of the CRM mechanism. The peniotron interaction differs significantly from that of the CRM and Weibel interactions because phase bunching does not constitute the energy extraction mechanism in the peniotron interaction. This interaction is characterized by a drift of the electron guiding centers in directions which cause each electron to lose energy to the transverse electric field. This guiding center drift and energy loss can only occur when the field contains a strong right hand circularly polarized harmonic with angular mode number n that is related to the beam cyclotron harmonic number s by $n = s + 1$. The guiding center drift which

results from the rotating RF electric field is produced by the radial variation of the field. The peniotron has also been described in [100] and [101]. The CRM, Weibel and the peniotron interactions do not have exclusive domains and hence they interact with each other under certain conditions.

In the following section we describe the mechanism of the CRM interaction. Comprehensive linear and nonlinear theories for gyrotrons [40], [102]–[105] and gyrotron amplifiers [106]–[133] are well developed. A review of the theory of gyrotron traveling wave amplifiers and gyrotron oscillators is presented in this chapter to serve as a basis for the design of the experiments, which will be described in later chapters. A detailed derivation of the kinetic theory and single particle theory for gyrotron traveling wave amplifiers is presented by the author elsewhere [134]. The nonlinear theory results for gyrotron oscillators is summarized from [104].

After a phenomenological description of the CRM interaction in Section 2.2 we present the linear dispersion relation for a gyro-TWT obtained using a kinetic theory approach by solving the relativistic Vlasov equation in Section 2.3. A single particle theory which is a nonlinear formulation of the CRM interaction in gyrotron amplifiers is presented in Section 2.4. The nonlinear equations describing the interaction can be linearized to obtain a cubic dispersion relation in the small signal limit, as described in Section 2.4.1 or solved in full rigor as outlined in Section 2.4.2. In Section 2.5 we summarize the nonlinear theory of gyrotron oscillators. Some results from computer codes developed for the design and analysis of gyrotron amplifiers and oscillators based on the above theories will be presented in Section 2.6.

2.2 Phenomenological Description of CRM Interaction

A typical setup for CRM interaction is a hollow annular gyrating electron beam drifting through a waveguide immersed in a background axial static magnetic field as shown in Fig. 2-1. The beam is usually formed in a Magnetron Injection Gun

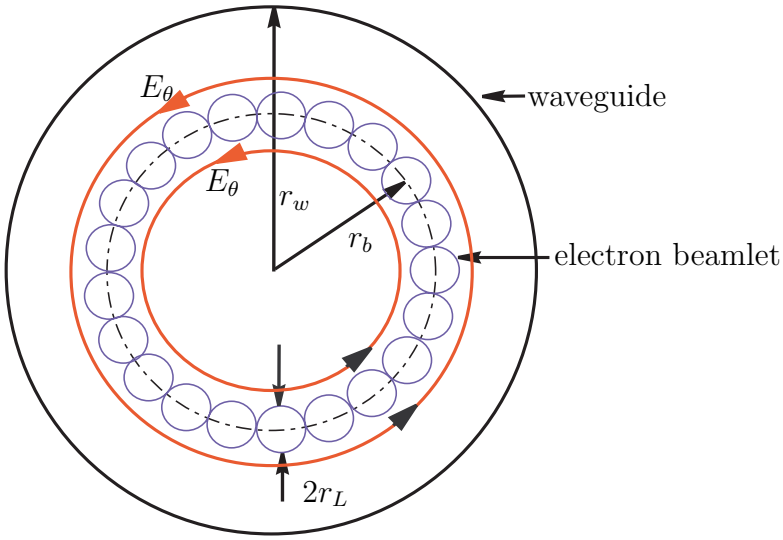

Figure 2-1: Schematic of the cross-section of interaction region in a typical cylindrical guide gyro-TWT operating in a TE_{0n} mode.

(MIG) [135] by launching a hollow annular electron beam at an angle to the static axial magnetic field to induce gyrations in the trajectory of each electron. Ideally, the thickness of the beam is equal to twice the Larmor radius defined in Eqn. (2.3). The direction of the field lines of a TE_{0n} mode is also shown in Fig. 2-1. The electron beam is characterized by a longitudinal velocity, v_z, a transverse velocity, v_t and the relativistic mass factor

$$\gamma = \frac{1}{\sqrt{1 - \left(\frac{v_t^2 + v_z^2}{c^2}\right)}}, \tag{2.1}$$

where c is the velocity of light in vacuum. The CRM instability is a relativistic instability based on the relativistic cyclotron frequency of the electrons

$$\Omega_{rel} = \frac{eB_0}{\gamma m_{e0}}, \tag{2.2}$$

where B_0 is the axial DC magnetic field, e and m_{e0} are the magnitude of the charge and the rest mass of an electron, respectively. The average beam radius is r_b, which is also the guiding center radius of the beamlets and the Larmor radius of the gyration

of the electrons is defined as

$$r_L = \frac{v_t}{\Omega_{rel}}. \tag{2.3}$$

For simplicity, we consider the electron beam drifting down a smooth walled cylindrical waveguide, which supports a transverse electric (TE) mode such as the TE_{01}. We consider the electrons in a particular beamlet (Fig. 2-1), rotating in a counter clockwise direction with a uniform initial distribution over a Larmor orbit as shown in Fig. 2-2(a). The electrons with a component of velocity in the direction of the RF field are decelerated while the electrons with a component of velocity opposite to the RF field gain energy. The cyclotron frequency of an electron is inversely proportional to its relativistic mass γm_{e0}, thus the electrons gaining energy from the RF field gyrate slower while the ones that lose energy gyrate faster causing the electrons to bunch in the Larmor orbit. Furthermore, the Larmor radii of the faster gyrating electrons decreases while those of the slower gyrating electrons increases resulting in a change in the shape of each beamlet as showing in Fig. 2-2. If the RF field oscillates at a frequency slightly higher than the electron's cyclotron frequency Ω_{rel}, i.e. $\omega \gtrapprox \Omega_{rel}$, then electrons first begin to move in phase so as to produce a higher density of electrons, popularly designated as an electron bunch on one side of the ring. The bunch first begins to form at the phase position of the electron field and then drifts behind in phase resulting in net energy extraction from the bunch. After the energy extraction the electrons lose synchronism with the wave and eventually enter the accelerating phase thus extracting energy from the RF wave typical of saturation due to nonlinear effects.

The phase bunching of the electrons in CRM interaction is shown in Fig. 2-2 by plotting the Larmor radii of the electrons in the phase space as a function of time. The figures were created by tracking the trajectories of electrons in a gyro-TWT using the particle tracking code described later in this thesis. We use 128 representative electrons in the beamlet which are initially uniformly distributed around a Larmor orbit. The figures are normalized $x - y$ plots showing the transverse position of the electrons with respect to the direction of the local electric field. The electron

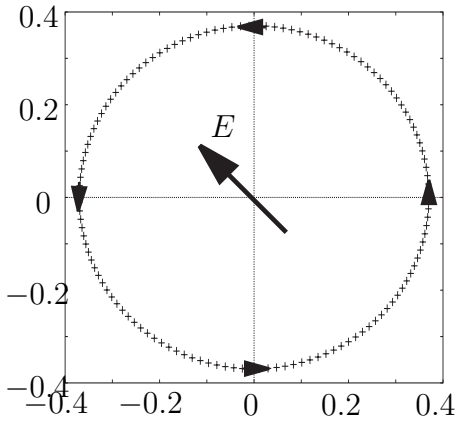

(a) $t = 0$ ps, $\eta = 0.0$ %.

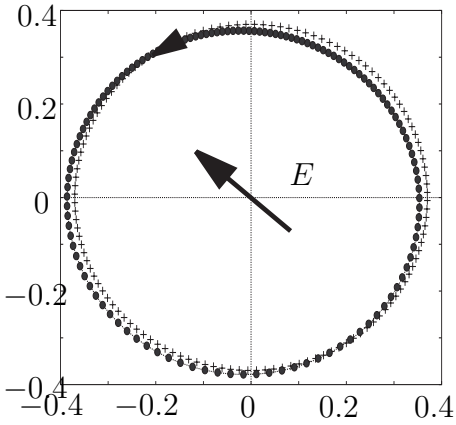

(b) $t = 100$ ps, $\eta = 0.52$ %.

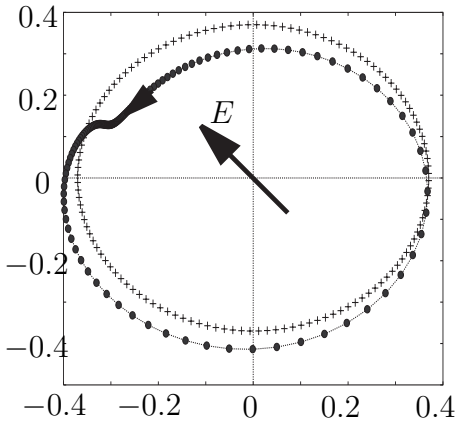

(c) $t = 133$ ps, $\eta = 4.12$ %.

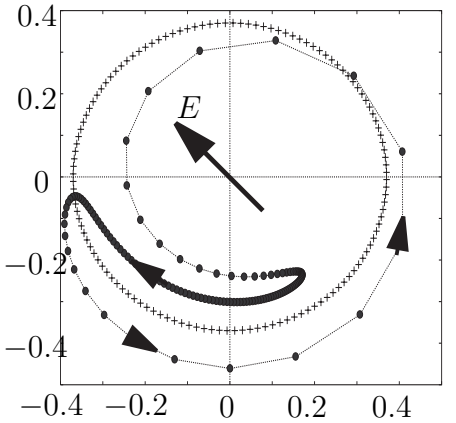

(d) $t = 167$ ps, $\eta = 12.50$ %.

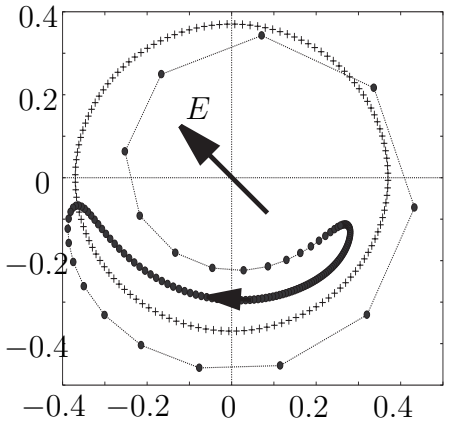

(e) $t = 173$ ps, $\eta = 12.10$ %.

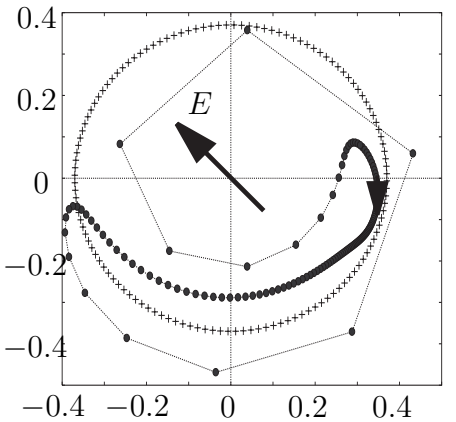

(f) $t = 183$ ps, $\eta = 9.60$ %.

Figure 2-2: Phase distribution of electrons (shown as •) in the Larmor orbit. The initial position of the electrons is shown as +.

bunch follows the rotating RF electric field. For ease of plotting, we always show the orientation of the electron bunch with respect to the electric field in a reference frame located on the rotating electric field. Another representation of phase bunching is shown in Chapter 3 by tracking the trajectories of the electrons as they traverse the length of the interaction structure.

The gyrotron interaction saturates due to two effects namely, the energy depletion from the electron beam and the phase trapping of the particles. These effects have been studied in detail in [96]. Saturation by energy depletion occurs when the average transverse velocity is reduced below a critical threshold value necessary to generate the instability in the small signal dispersion relation. The other mechanism of saturation called phase trapping is caused by the trapping of particles that lose sufficient energy in the electric field. An alternative explanation to this mechanism is the detuning of the interaction due to a change in the relativistic mass factor, γ as the electron lose energy resulting in a deviation from the cyclotron resonance condition Eqn. (2.5)which will be described later.

A gyrating electron beam which, may be either annular (small-orbit) or on-axis (large-orbit), drifting through an interaction structure capable of supporting a fast electromagnetic mode would constitute a CRM system. The first CRM experiment used a periodic electron beam produced by a Pierce gun and a wiggler [39]. Contemporary experiments in the erstwhile Soviet Union used hollow annular beams produced by a MIG and a rectangular waveguide as the interaction structure. Most of the later experiments for both the oscillator and amplifier configurations have used a cylindrical waveguide for enhancing the coupling to the electron beam by virtue of the symmetry of the fields.

2.3 Kinetic Theory

The linear dispersion relation for the CRM system can be derived by either a kinetic theory approach, by the way of solving the relativistic Vlasov's equation to obtain the perturbed electron distribution function, or by linearizing the single particle equations

of motion in the small signal limit to obtain a dispersion relation. It is easier to perform a kinetic treatment for a cylindrical guide configuration in the absence of any velocity spread in the beam, however, inclusion of velocity spread and consideration of an arbitrary shape of the waveguide dramatically increase the complexity. On the other hand, the derivation of the single particle equations of motion for an arbitrary shape of the waveguide is easier.

The beam-wave interaction in a gyrotron can be most simply understood as the coupling between the electromagnetic waveguide mode and the beam cyclotron harmonic modes. The combined dispersion relation, which is derived in this section can ultimately be presented as the product of the waveguide mode dispersion and the beam cyclotron mode dispersion relations coupled by the source term namely, the normalized electron beam current. The dispersion relation for TE waveguide modes in a cylindrical waveguide is

$$k^2 - k_t^2 - k_z^2 = 0, \tag{2.4}$$

where k is the free space propagation constant, k_z is the axial propagation constant, $k_t\,(=\nu_{mn}/r_w)$ is the transverse propagation constant of the TE_{mn} mode under consideration, ν_{mn} is nth root of $J_m^{'}(x)$ and r_w is the radius of the waveguide wall. The resonance condition for the Doppler shifted beam cyclotron modes can be derived as [136]

$$\omega - k_z v_z - s\Omega/\gamma \gtrsim 0, \tag{2.5}$$

where, $\Omega\ (=eB_0/m_{e0})$is the nonrelativistic cyclotron frequency. The beam mode dispersion relation and the waveguide mode dispersion relations have been plotted for different kinds of CRM devices in Figs. 2-3–2-6. The interaction in all these devices except the SWCA [137] is very similar, the difference being limited to the magnitude of the Doppler shift term $k_z v_z$ and the traveling or stationary nature of the electromagnetic mode. In the SWCA (Fig. 2-6) electron bunching occurs due to the Weibel mechanism [94] and is axial in contrast to the transverse bunching dominant in a CRM. Also, the SWCA interaction involves the coupling between a slow waveguide mode and a harmonic of the beam cyclotron mode. In a Cyclotron Auto-Resonance

Maser (CARM) (Fig. 2-5) the beam cyclotron mode and the waveguide mode interact very far away from the waveguide cut-off in contrast to a gyrotron oscillator or a gyro-TWT. Thus the CARM requires a highly relativistic beam for resonance with the waveguide mode in a region where the phase velocity of the waveguide mode is almost equal to that of light. Since the interaction happens in a region of near linear dispersion of the waveguide mode the synchronism between the beam and the waveguide mode is maintained over wide range of frequencies making the interaction very broadband. On the other hand the large value of the axial propagation constant, k_z makes the interaction very sensitive to velocity spread due to the $k_z v_z$ term in Eqn. (2.5). The CARM interaction has high efficiency because as the electrons lose energy during the interaction (γ and v_z decrease) the increase in $s\Omega/\gamma$ is compensated with the decrease in $k_z v_z$ which helps maintain synchronism, Eqn. (2.5), between the beam and the waveguide mode over a longer interaction length. This phenomenon is called auto-resonance. Auto-resonance is not observed in interactions closer to the waveguide cut-off where $k_z v_z$ is very small.

The dispersion plots shown in Fig. 2-3 applies to both CRM amplifiers (convective instability) and oscillators (absolute instability and backward propagating wave oscillation). The nature of the instability depends on the operating parameters such as the electron beam current, the magnetic field and the shape of the interaction structure. As a general rule, increasing the operating current leads to a transition from the convective instability to the absolute instability. The intersection of the beam mode dispersion relation with the waveguide modes at a negative value of the axial propagation constant can excite Backward Propagating Wave Oscillations (BPWO). These oscillations arise due to a feedback loop between the electron beam and a backward propagating circuit wave and is discussed in Sec. 2.6.

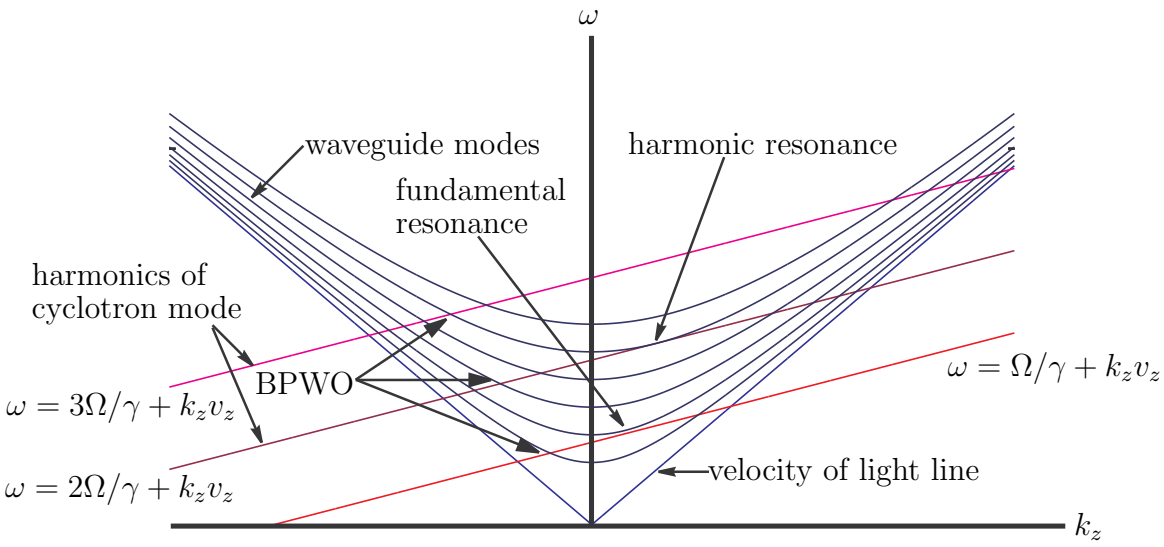

Figure 2-3: Dispersion diagram showing the region of interaction between the fast waveguide modes and the beam cyclotron modes on the beam. The intersection of the beam cyclotron modes with the waveguide modes at negative values of k_z causes the excitation of Backwad Propagating Wave Oscillations (BPWO).

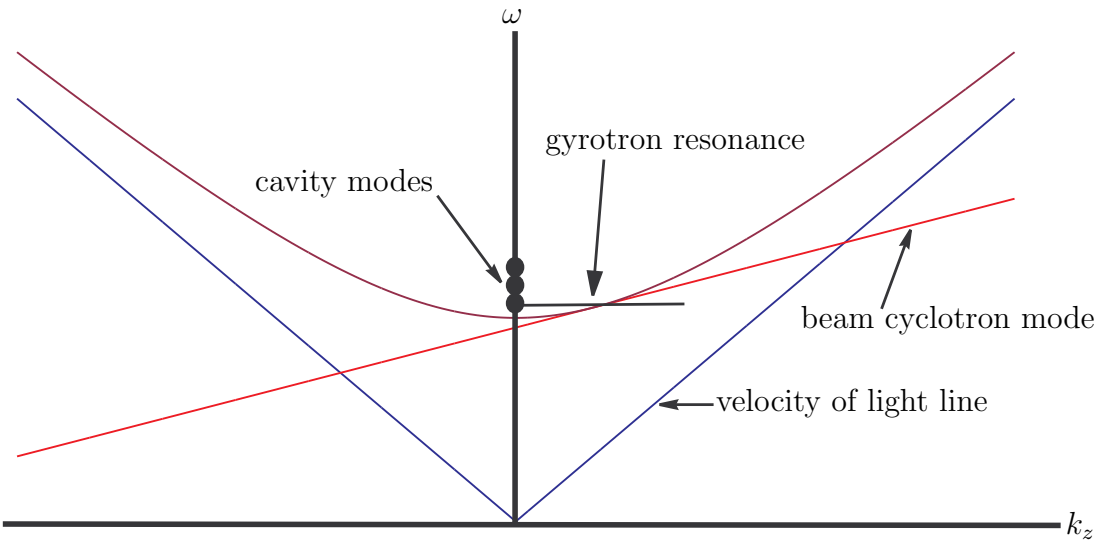

Figure 2-4: Dispersion diagram showing the region of interaction between a resonant cavity mode and a beam cyclotron mode in a gyrotron oscillator.

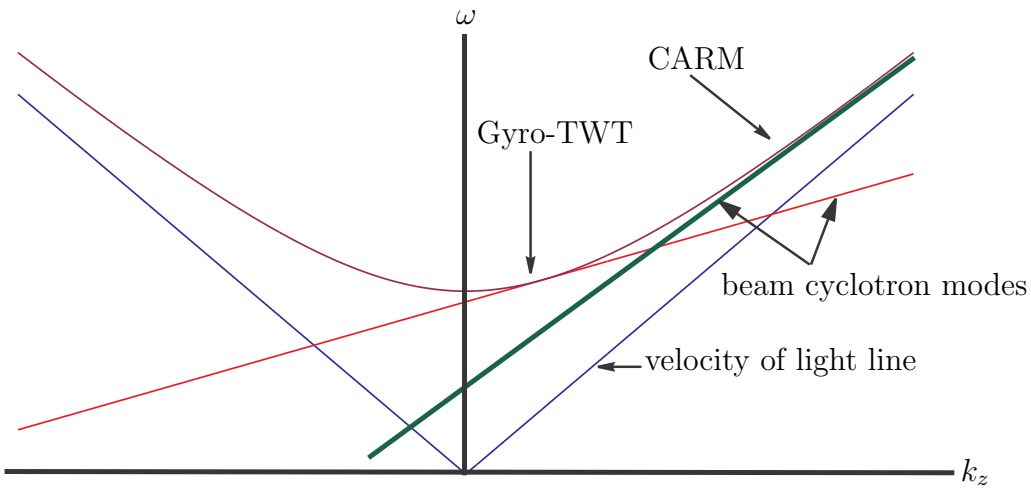

Figure 2-5: Dispersion diagram showing the interaction region between a fast waveguide mode and a beam cyclotron mode in a gyro-TWT and a CARM. The gyro-TWT interaction takes place near the waveguide cut-off while the CARM interaction takes place far away from the waveguide cut-off.

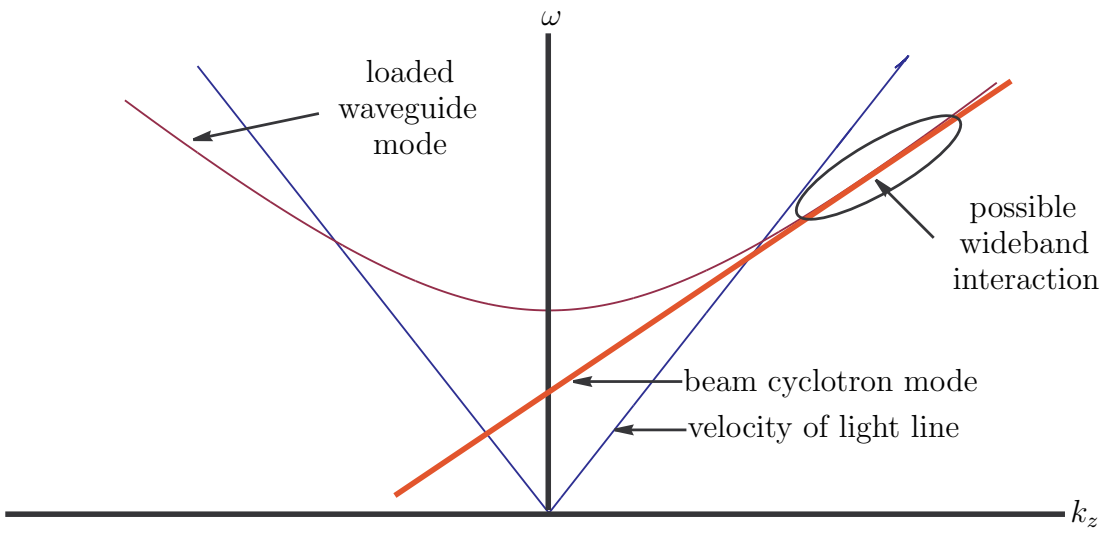

Figure 2-6: Dispersion diagram showing the interaction region between a slow waveguide mode and a beam cyclotron mode in a slow-wave cyclotron amplifier (SWCA).

2.3.1 Linear Dispersion Relation

System Configuration

We consider a CRM constituted by a hollow, mildly relativistic electron beam streaming through a cylindrical waveguide. A schematic of the system is shown in Fig. 2-1. A strong and finite static axial magnetic field serves the dual purpose of focussing the beam as well as inducing gyrations of finite Larmor radii to the electrons as the beam drifts in the tube. Such an electron beam is realized in practice by a MIG [135]. MIGs are operated in the temperature limited regime of electron emission in contrast to linear beam Pierce guns which operate in the space charge limited regime. Operation in the temperature limited regime minimizes the effect of DC space charge on the beam.

Derivation of the Dispersion Relation

The linear dispersion relation of a CRM can be derived from the kinetic approach by solving the relativistic Vlasov equation to obtain the perturbed electron distribution function in the presence of the electromagnetic wave. In this analysis we assume a tenuous electron beam which does not alter the transverse field profile of the waveguide mode. For a weak beam-wave coupling one expects the real part of the axial propagation constant of the beam-wave coupled system to be in the vicinity of the axial propagation constant of the beam absent interaction structure. Also, this analysis ignores the effect of space charge forces. A detailed derivation of the dispersion relation is based on the approach outlined in [118], [115] and has been presented by

the author in [134]. Following [115] the dispersion relation can be expressed as

$$\begin{aligned} D(\omega,k) &= k^2 - k_z^2 - k_t^2\left[1-(1+i)\left(1+\frac{m^2}{\nu_{mn}^2-m^2}\frac{\omega^2}{\omega_c^2}\right)\frac{\delta_{skin}}{r_w}\right] \\ &\quad + \frac{2\ e^2\ \mu_0}{m_{e0}\pi r_w^2\ K_{mn}}\int_0^{r_b} r_b\ dr_b \int_{p_t=0}^{\infty} p_t\ dp_t \int_{p_z=-\infty}^{\infty} dp_z\ \sigma_0\ h_b(r_b)\ g(p_t,p_z) \\ &\quad \times\left[\frac{(\omega^2-k_z^2c^2)\,p_t^2 H_{-s,m}}{\gamma^3 m_{e0}^2c^2\left(\omega-k_zv_z-s\frac{\Omega}{\gamma}\right)^2} - \frac{(\omega-k_zv_z)\,Q_{-s,m}}{\gamma\left(\omega-k_zv_z-s\frac{\Omega}{\gamma}\right)}\right] \\ &= 0. \end{aligned} \tag{2.6}$$

In the above equation δ_{skin} is the skin depth of the conducting waveguide wall, $\omega_c\,(=k_tc)$ is the cut-off frequency of the lossless waveguide. μ_0 is the permeability of free space, p_t and p_z are transverse and axial momenta of the electrons, respectively, σ_0 is the number of electrons per unit volume, $h_b(r_b)$ is the distribution of electrons in the radial direction and $g(p_t,p_z)$ represents the distribution of the electrons in the momentum space. The other quantities are defined as

$$K_{mn} = \left(1-\frac{m^2}{\nu_{mn}^2}\right)J_m^2(\nu_{mn}), \tag{2.7}$$

$$H_{-s,m} = J_{s-m}^2(k_tr_b)\,J_s'^2(k_tr_L), \tag{2.8}$$

$$Q_{-s,m} = 2J_{s-m}^2(k_tr_b)\left\{J_s'^2(k_tr_L) + (k_tr_L)\,J_s'(k_tr_L)\,J_s''(k_tr_L)\right\}$$

In the above equations $k_t\,(=\nu_{mn}/r_w)$ is the transverse propagation constant of the TE_{mn} mode under consideration, ν_{mn} is nth root of $J_m'(x)$, r_w is the radius of the waveguide wall, r_b is the mean beam radius, r_L is Larmor radius of the electrons and s is the beam cyclotron harmonic number. Eqn. (2.6) applies to CRM devices such as the gyrotron, the gyro-TWT and the CARM.

At this point the nature and form of the electron distribution function is yet to be specified. A choice remains for analyzing the beam-wave interaction for a variety of beams by merely choosing an appropriate form of the distribution function to obtain a specific dispersion relation from Eqn. (2.6). In the present work for simplicity, an

ideal beam with zero guiding center spread (infinitesimally thin beam) and no axial or transverse momentum spread (cold beam) is chosen. For a more exact treatment one may, choose to represent the momentum spread of the beam in the form of a Gaussian distribution. A spread in the axial momentum of the beam causes variation in the resonance condition Eqn. (2.5), thereby deteriorating the interaction.

For a gyro-TWT under the simplest case, the distribution function of the electron beam can be represented as

$$h_b\left(r_b\right) \;=\; A_b \frac{1}{r_b}\delta\left(r_b - r_{b0}\right), \tag{2.9}$$

$$g\left(p_t, p_z\right) \;=\; \frac{1}{2\pi p_t}\delta\left(p_t - p_{t0}\right)\delta\left(p_z - p_{z0}\right), \tag{2.10}$$

where A_b is the area of the beam cross-section, r_{b0} is the average beam radius (equal to r_b in our notation) and $p_{t0},\ p_{z0}$ are the mean transverse and longitudinal momenta, respectively. The $\delta\left(\right)$ functions are the Dirac delta functions. Identifying the beam current to be the number of electrons flowing per unit time through the waveguide cross-section, we may express the operating current, I_0 as

$$I_0 \;=\; \sigma_0\ A_b\ e\ v_z. \tag{2.11}$$

Substituting Eqns. (2.9 and 2.10) into Eqn. (2.6), and using Eqn. (2.11) to perform simple integrations over the momentum space one obtains

$$\begin{aligned} D\left(\omega, k_z\right) \;&=\; k^2 - k_z^2 - k_t^2\left[1 - (1+i)\left(1 + \frac{m^2}{\nu_{mn}^2 - m^2}\frac{\omega^2}{\omega_c^2}\right)\frac{\delta_{skin}}{r_w}\right] \\ &\quad + \frac{e\ \mu_0 c^2}{\gamma m_{e0}\pi\ r_w^2\ K_{mn}}\frac{I_0}{v_z} \\ &\quad \times\left[\frac{\left(\omega^2 - k_z^2 c^2\right)\beta_t^2 H_{-s,m}}{\left(\omega - k_z v_z - s\Omega/\gamma\right)^2} - \frac{\left(\omega - k_z v_z\right)Q_{-s,m}}{\left(\omega - k_z v_z - s\Omega/\gamma\right)}\right] \\ &=\; 0, \end{aligned} \tag{2.12}$$

where

$$\beta_t = \frac{p_t}{\gamma m_{e0} c} = \frac{v_t}{c}, \tag{2.13}$$

$$\beta_z = \frac{p_z}{\gamma m_{e0} c} = \frac{v_z}{c}. \tag{2.14}$$

Thus one finds in Eqn. (2.12) a dispersion relation for the beam-wave coupled system in a gyro-TWT. The complexity of the dispersion relation rules out a closed form analytical evaluation of $k = k(\omega_{\text{real}})$ except for the case of very weak-beam wave coupling. Under conditions of weak beam-wave coupling we can formulate a Pierce-type [93] gain equation for a gyro-TWT as in [129] for analyzing the gain-frequency response of the device.

The above dispersion relation can be numerically solved for complex solutions of k for real values of ω to obtain the growth rate of the CRM instability. One may employ the methodology developed in [32] to find the conditions for the excitation of absolute and convective instabilities.

2.4 Single Particle Theory for Gyrotron Amplifiers

In the kinetic theory developed in the previous section the electron beam was represented as a distribution function and its evolution in the presence of the electromagnetic wave and a static axial magnetic field was determined by solving the relativistic Vlasov equation. An alternate approach to studying the interaction mechanism is based on tracking the behavior of each electron separately as the beam drifts through the interaction region. The ensemble of the equations of all the representative electrons can be used to determine the net energy exchange in the beam-wave system. The benefits of this approach are numerous. It is applicable over a wider range of parameter space than a kinetic description of a cold plasma. The beam temperature effects such as momentum and energy spread can be included more easily in the anal-

ysis. Furthermore, this is a fully nonlinear description of the interaction process and models saturation effects. However, the space charge effects are ignored in this single particle theory.

A detailed derivation of the single particle theory is presented by the author elsewhere [134] following the approach developed by Yulpatov [106] and later generalized in [123] and [124]. The theory is valid for gyrotron traveling wave amplifiers operating at arbitrary cyclotron harmonics in a waveguide of arbitrary cross-section. The drift of the guiding centers of the electrons is also included for generality even though this effect is negligible in a gyro-TWT. Also included is the effect of inhomogeneity of the static magnetic field. It is well known that tapering of the external magnetic field to maintain synchronism with the slowing electrons enhances the interaction efficiency [125].

The whole interaction process can be represented by the following set of Eqns. (2.15–2.17) connecting the electron energy, the electron phase with respect to the electromagnetic wave and the field amplitude:

$$\frac{dw}{dz'} = -2\frac{(1-w)^{s/2}}{(1-bw)}\,\mathrm{Re}\left\{\mathcal{F}e^{-i\vartheta_s}\right\}, \tag{2.15}$$

$$\frac{d\vartheta_s}{dz'} = \frac{1}{(1-bw)}\left[\bar{\mu}w - \bar{\Delta} + s\,(1-w)^{\frac{s}{2}-1}\,\mathrm{Im}\left\{\mathcal{F}e^{-i\vartheta_s}\right\}\right], \tag{2.16}$$

$$\frac{d\mathcal{F}}{dz'} = -I_0^{'}\frac{1}{\pi}\int_0^{2\pi}\frac{(1-w)^{s/2}}{1-bw}e^{i\vartheta_s}d\vartheta_0, \tag{2.17}$$

where

$$\mathcal{F} = \frac{\mu_0 c}{\kappa}\frac{1-h\beta_{z0}}{\gamma_0\beta_{t0}\beta_{z0}}\frac{1}{2^s\,(s-1)!}\left(\frac{\kappa p_{t0}^{'}}{\mu}\right)^{s-1}A^{'}L_s\,(X,Y), \tag{2.18}$$

$$z^{'} = kz, \tag{2.19}$$

$$h = k_z/k, \tag{2.20}$$

$$\kappa = k_t/k, \tag{2.21}$$

$$p_{t0}^{'} = \frac{p_{t0}}{m_{e0}c}, \tag{2.22}$$

$$\mu = \frac{eB_0}{m_{e0}\omega}, \tag{2.23}$$

$$w = \frac{2\left(1 - h\beta_{z0}\right)}{\beta_{t0}^2}\frac{\gamma_0 - \gamma}{\gamma_0}, \tag{2.24}$$

$$b = \frac{h\beta_{t0}^2}{2\beta_{z0}\left(1 - h\beta_{z0}\right)}, \tag{2.25}$$

$$\bar{\mu} = \frac{\beta_{t0}^2}{2\beta_{z0}}\frac{1 - h^2}{1 - h\beta_{z0}}, \tag{2.26}$$

$$\bar{\Delta} = \frac{1}{\beta_{z0}}\left(1 - s\frac{\mu}{\gamma} - h\beta_{z0}\right), \tag{2.27}$$

$$\vartheta_s = s\theta - \left(\omega t - k_z z\right), \tag{2.28}$$

$$A^{'} = \frac{eA}{m_{e0}c\omega}, \tag{2.29}$$

where A is the amplitude of the RF fields which are expressed as

$$\vec{E} = \mathrm{Re}\left\{A\ \vec{E}_s\left(r_t\right)\ e^{i(\omega t - k_{z,c}z)}\right\}, \tag{2.30}$$

$$\vec{H} = \mathrm{Re}\left\{A\ \vec{H}_s\left(r_t\right)\ e^{i(\omega t - k_{z,c}z)}\right\}. \tag{2.31}$$

Functions $\vec{E}_s$ and $\vec{H}_s$ describe the transverse structure of the fields, r_t is the transverse coordinate and $k_{z,c}$ is the cold (beam absent) axial propagation constant of the waveguide.

The normalized current parameter, $I_0^{'}$ is defined as

$$I_0^{'} = \frac{e\left|I_0\right|}{N_s}\frac{2\mu_0^2}{k_t^2 m_{e0}\gamma_0}\frac{1 - h\beta_{z0}}{\beta_{z0}^2}\left(\frac{1}{2^s\left(s-1\right)!}\right)^2\left(\frac{\kappa p_{t0}^{'}}{\mu}\right)^{2(s-1)}\left|L_s\right|^2, \tag{2.32}$$

where I_0 is the DC beam current, $\beta_{z0}\left(=v_{z0}/c\right)$ and $\beta_{t0}\left(=v_{t0}/c\right)$ are the normalized axial and transverse velocities of the electron beam, μ_0 is the permeability of free space, γ_0 is the relativistic mass factor of the electrons, m_{e0} is the rest mass of the electrons, e is the charge of an electron, s is the cyclotron harmonic number and L_s is the Form Factor for the waveguide which depends on the transverse shape of the

waveguide and the operating mode and is defined as

$$L_s = \left(\frac{1}{k_t}\right)^s \left(\frac{\partial}{\partial X} + i\frac{\partial}{\partial Y}\right)^s \Psi\left(X, Y\right), \tag{2.33}$$

where X and Y are the transverse coordinates of electron guiding center. The Norm of the waveguide, N_s is defined as

$$N_s = \iint dS_\perp \left\{ \left[\vec{E}_s \times \vec{H}_s^*\right] - \left[\vec{H}_s \times \vec{E}_s^*\right] \right\} \hat{z}_0, \tag{2.34}$$

where $dS_\perp$ represents the unit area normal to the waveguide. The norm describes the power flowing through the waveguide cross-section for a wave of unit amplitude. Ψ is the eigenfunction for the Helmholtz equation $\Delta_t\Psi + k_t^2\Psi = 0$,and Δ_t is the Laplacian in the transverse direction. Ψ satisfies the following boundary conditions

$$\left.\frac{\partial\Psi}{\partial\hat{n}}\right|_{waveguide\ wall} = 0 \qquad \text{TE modes,} \tag{2.35}$$

$$\left.\Psi\right|_{waveguide\ wall} = 0 \qquad \text{TM modes,} \tag{2.36}$$

where $\hat{n}$ is a unit normal to the waveguide wall.

Eqns. (2.15–2.17) may be either solved numerically to fully describe the interaction including the nonlinear effects, or can be linearized to obtain a small signal dispersion relation.

2.4.1 Linear Growth Rate

The self-consistent equations Eqns. (2.15–2.17) can be linearized in the small signal limit, where the growing quantities are assumed to vary as $\sim e^{i\Gamma z'}$ to obtain the following small signal dispersion relation for real ω and complex k_z as

$$\Gamma^3 - \bar{\Delta}\Gamma^2 - I_0'\left(s - b\right)\Gamma + \left(\bar{\mu} - \bar{\Delta}b\right) I_0' = 0. \tag{2.37}$$

This equation was also obtained previously in [123] and for the case of fundamental operation ($s = 1$) was obtained in [42] and [115]. For large values of the parameter $\bar{\mu}$, Eqn. (2.37) can be reduced independent of the cyclotron harmonic number to a form similar to the well known dispersion equation of a TWT [93]

$$\delta^2 \left(\delta - \bar{\Delta}' \right) + 1 = 0, \tag{2.38}$$

where,

$$\delta = \frac{\Gamma}{\left(I_0' \bar{\mu} \right)^{1/3}}, \tag{2.39}$$

$$\bar{\Delta}' = \frac{\bar{\Delta}}{\left(I_0' \bar{\mu} \right)^{1/3}}. \tag{2.40}$$

At exact cyclotron resonance $\left(\bar{\Delta} = 0 \right)$ the normalized growth rate for the growing wave solution is given by

$$\mathrm{Im}\, \Gamma = -\frac{\sqrt{3}}{2} \left(I_0' \bar{\mu} \right)^{1/3}. \tag{2.41}$$

In Section 2.9.2 on page 63 we present numerical results to compare the linear growth rates from the kinetic and single particle theories for a cylindrical guide gyro-TWT.

2.4.2 Nonlinear Evolution

To study the full nonlinear behavior of the interaction we can numerically solve Eqns. (2.15–2.17) to compute the evolution of the electron energy, phase and the field amplitude along the interaction length. In the most simple case the losses in the system say, the wall losses due to the finite conductivity of the interaction structure, diffraction losses in an open waveguide like a confocal waveguide, which will be studied later, can be included as cold circuit loss after propagation of the solution through one step along the interaction length.

Later in this chapter in page 63 the numerically computed growth rates from the linear and nonlinear theories are compared to verify their agreement. The linear

growth rate obtained from the single particle theory is also compared with the linear growth rate obtained from an independent computer code based on the kinetic theory.

2.5 Norm and Form Factor

While formulating the single particle theory we defined the waveguide Norm in Eqn. (2.34) and the Form Factor in Eqn. (2.33) for an arbitrarily shaped interaction structure. For simple interaction structures like a cylindrical waveguide it is easy to derive analytical expressions for both the Norm and the Form Factor however, for an interaction structure having a complicated shape, e.g., a confocal waveguide it may not be possible to obtain closed form analytic solutions.

2.5.1 Cylindrical Waveguide

In case of a cylindrical waveguide, the fields can be expressed in terms of the scalar function

$$\Psi = C_{mn}\ J_m\left(k_t r\right) e^{im\phi}, \tag{2.42}$$

where the normalization factor C_{mn} is defined as

$$C_{mn} = \frac{1}{\sqrt{\pi\left(k_t^2 r_w^2 - m^2\right)} J_m\left(k_t r_w\right)}, \tag{2.43}$$

for the TE_{mn} mode with r_w as the waveguide radius and ϕ is the azimuthal angle. Substituting the above value of Ψ into the following field expressions

$$H_{sz} = \Psi \tag{2.44}$$

$$H_{sr} = i\frac{k_z}{k_t^2}\frac{\partial\Psi}{\partial r}, \tag{2.45}$$

$$H_{s\phi} = i\frac{k}{k_t^2}\frac{1}{r}\frac{\partial\Psi}{\partial\phi}, \tag{2.46}$$

$$E_{sz} = 0, \tag{2.47}$$

$$E_{sr} = i\mu_0 c\frac{k}{k_t^2}\frac{1}{r}\frac{\partial\Psi}{\partial\phi}, \tag{2.48}$$

$$E_{s\phi} = -i\mu_0 c\frac{k}{k_t^2}\frac{\partial\Psi}{\partial r}. \tag{2.49}$$

We can evaluate the following quantities as

$$L_s = C_{mn}J_{s-m}\left(k_t r_b\right), \tag{2.50}$$

$$N_s = \int\int dS_\perp\left(\vec{E}_s\times\vec{H}_s^* - \vec{H}_s\times\vec{E}_s^*\right) = 2\mu_0 c C_{mn}^2\frac{kk_z}{k_t^4}, \tag{2.51}$$

$$P = \frac{1}{2}\,\mathrm{Re}\left\{\int\int dS_\perp\left(\vec{E}_s\times\vec{H}_s^*\right)\right\} = 4N_s, \tag{2.52}$$

where r_b is the mean beam radius.

2.5.2 Confocal Waveguide

A confocal waveguide consists of two mirrors each having a radius of curvature, r_c separated by the same distance as shown in Fig. 3-11 on page 91. The HE_{06} mode

of the confocal waveguide has six nulls in the axial magnetic field amplitude perpendicular to the mirror and none along the mirror. The electric field variation in such a mode is shown in Fig. 3-12(d) on page 94. In the Fig. 3-12(d) we show the magnitude of the electric field because the location of the electron beam is determined by the location of the maxima of the electric field of the operating mode. A complete discussion of the confocal resonator is presented in Chapter 3.

From the field equations of the confocal waveguide in Sec. 3.3 it is not possible to obtain closed form expressions for the waveguide norm and form factor in this case. We evaluate all the derivatives occurring in those expressions analytically using Mathematica. The final integrations of these analytic expressions are however, carried out numerically by using the IMSL numerical routines (Compaq Visual Fortran 6.1 [139]) using multivariate quadrature algorithms.

2.6 Backward Propagating Wave Oscillations

As mentioned earlier in this chapter, the convective instability is not an exclusive entity on the beam-wave system. Various other instabilities thrive under different operating regimes of the device. The most dangerous of these parasitic effects for an amplifier are the absolute instability and the Backward Propagating Wave Oscillations (BPWO). From the small signal dispersion relation Eqn. (2.12) derived from the kinetic theory one may find conditions for the excitation of the absolute instability as described in detail in [118].

The BPWO instability results from the interaction of the gyrating electrons and an electromagnetic wave propagating in a direction opposite to the electron beam. This interaction is different from the Backward Wave Oscillation (BWO) in slow-wave devices where the phase and group velocities of the backward circuit wave are in opposite directions. In the case of the fast electromagnetic modes in a device like a gyro-TWT, which has a smooth walled interaction structure both the phase and group velocities of the electromagnetic wave are in the same direction [138].

The single particle theory is also valid for a gyro-BPWO operating far enough

from the waveguide cutoff to ensure that the interaction of the electrons with the non-synchronous waves can be neglected. The set of differential Eqns. (2.15–2.17) holds good for a gyro-BPWO however, the axial wavenumber k_z has to be replaced with $-k_z$ to describe the backward wave. The corresponding boundary conditions are

1. $u\left(z^{'}=0\right) = e^{i\vartheta_{0s}}$ where ϑ_{0s} is the initial phase uniformly distributed over $[0, 2\pi]$.

2. $F\left(z^{'}=L^{'}\right) = 0$ where $L^{'}(=Lk)$ is the normalized length of the tube. This condition assumes that the output end of the tube is perfectly matched for the wave in consideration.

We designate the two ends of the tube as the electron gun end and the collector end in the following explanation. The last boundary condition implies that no waves enter the tube from the collector end however, a counter propagating wave gets excited at the collector end and propagates towards electron gun end of the tube while gaining amplitude due to the BPWO interaction. At the electron gun end of the tube this wave can be extracted or reflected back from the cutoff narrowing of the tube. In the latter case the reflected wave now co-propagates with the electrons towards the collector end. This is a forward nonsynchronous wave which does not interact with the electrons and passes through an output window without reflections. One may obtain a small signal dispersion relation of the form Eqn. (2.37) from the non-linear equations with the above mentioned boundary conditions and inverting the sign of the axial propagation constant.

The small signal dispersion relation can be used to determine the start oscillation current for the BPWO for a given length of the tube. The length of each amplifying section of the tube should be chosen such that the operating current is below the BPWO start oscillation current. Obviously, this restricts the gain that one may achieve from each section of the tube, however, the overall gain of the tube can be increased by employing multiple amplifying sections separated by heavily lossy regions called severs. The severs cause the complete attenuation of the forward and backward

propagating waves leaving the current modulation in the beam unaffected. It may be shown that the hot loss (in the presence of the electron beam) for the forward wave is a mere 3.52 dB [136] while the loss for the backward wave which is not coupled to the beam is equal to the cold circuit loss. A novel technique for suppressing backward wave oscillations in a long interaction structure is to apply heavy loss throughout the circuit except in the final section where most of the gain takes place [76], [77]. This distributed loss structure, also known as a heavily loaded circuit does not rely on localized severs to suppress the backward wave and has demonstrated an impressive gain of 70 dB at 35 GHz [77].

2.7 Single Particle Theory for Gyrotron Oscillators

The nonlinear theory of gyrotron oscillators is well developed in the form of generalized pendulum equations [40], [102]– [105]. We summarize the results presented in [104] in this section. These results will be used for the design of gyrotron oscillators presented later in this work. The self-consistent equations of the electron energy and slowly varying phase for a weakly relativistic electron beam under the condition $s\beta_{t0}^2/2 \ll 1$ are as follows:

$$\frac{du}{d\zeta} = 2Ff(\zeta)(1-u)^{s/2}\sin\theta, \tag{2.53}$$

$$\frac{d\theta}{d\zeta} = \Delta - u - sFf(\zeta)(1-u)^{s/2-1}\cos\theta. \tag{2.54}$$

The normalized energy of the electrons defined as

$$u = \frac{2}{\beta_{t0}^2}\left(1 - \frac{\gamma}{\gamma_0}\right), \tag{2.55}$$

where the subscript 0 denotes initial value of the quantity under consideration, β_{t0} $(= v_{t0}/c)$ is the normalized transverse velocity of the electrons and γ is the relativistic

mass factor of the electrons. The slow-time scale phase variable is defined as

$$\theta = \omega t - s\phi, \tag{2.56}$$

where ϕ is the phase of the electron in its Larmor orbit. The normalized field amplitude of the cavity mode is defined as

$$F = \frac{E_0}{B_0}\beta_{t0}^{s-4}\left(\frac{s^{s-1}}{s!2^{s-1}}\right)J_{m\pm s}\left(k_t r_b\right), \tag{2.57}$$

where E_0 is the amplitude of the electric field, B_0 is the magnitude of the static axial magnetic field, s is the cyclotron harmonic number, k_t is the transverse propagation constant, r_b is average hollow beam radius, m is the radial index of the TE mode and $J(\ )$ is the Bessel function of the first kind. The plus and minus signs in the Bessel function subscript correspond to the two possible rotations of the RF field. $f(\zeta)$ is a function describing the longitudinal field profile of the resonator mode. Though typically, in gyrotrons $f(\zeta)$ is chosen to be a Gaussian function, which is a good description for a resonator open at both ends for diffractive coupling of power, other optimized field profiles can also be chosen to enhance the interaction efficiency. The detuning parameter Δ is defined as

$$\Delta = \frac{2}{\beta_{t0}^2}\left(1 - \frac{s\Omega}{\gamma\omega}\right). \tag{2.58}$$

The axial coordinate is normalized as

$$\zeta = \pi\frac{\beta_{t0}^2}{\beta_{z0}}\frac{z}{\lambda}, \tag{2.59}$$

where $\beta_{z0}\,(= v_{z0}/c)$ is the normalized axial velocity of the electrons and the normalized interaction length is

$$\mu = \pi\frac{\beta_{t0}^2}{\beta_{z0}}\frac{L}{\lambda}, \tag{2.60}$$

where L is the length of the resonator and λ is the wavelength of the operating mode. The initial conditions are $\theta = \theta_0\ \epsilon\ [0, 2\pi]$ and $u = 0$. The interaction efficiency is

given by

$$\eta = \frac{\gamma_0 - \gamma}{\gamma_0 - 1} = \frac{\beta_{t0}^2}{2\left(1 - 1/\gamma_0\right)}\eta_t, \tag{2.61}$$

where the transverse efficiency η_t, defined as the amount of transverse electron energy given up to the resonator field is

$$\eta_t = \left\langle u\left(\zeta_{out}\right)\right\rangle_{\theta_0}. \tag{2.62}$$

The brackets $\langle\rangle_{\theta_0}$ denote an average over initial phase and the subscript *out* denotes the end of the resonator. The field amplitude F is related to the beam current by an energy balance equation. The total resonator quality factor (Q), Q_T is given by

$$\frac{1}{Q_T} = \frac{1}{Q_{Ohm}} + \frac{1}{Q_{Diff}}, \tag{2.63}$$

where Q_{Ohm} and Q_{Diff} are the ohmic and diffraction quality factors. Q_T is related to the stored energy, U as $Q_T = \omega U/P$. The dissipated power, P which in this case is the energy extracted from the cavity by diffraction is

$$P = \eta I_0 V_0 = \frac{mc^2}{e}\frac{\gamma\beta_{t0}^2}{2}\eta_t I_0, \tag{2.64}$$

where I_0 is beam current in amperes and V_0 is the accelerating voltage. For a Gaussian field profile of the form

$$f\left(z\right) = e^{-\left(k_z z\right)^2} \text{ or } f\left(\zeta\right) = e^{-\left(2\varsigma/\mu\right)^2}, \tag{2.65}$$

where $k_z = 2/L$ defines the effective resonator length L, The energy balance equation can then be written as

$$F^2 = \eta_t I, \tag{2.66}$$

where I, the normalized current parameter is defined as

$$I = 0.238 \times 10^{-3}\left(\frac{Q_T I_0}{\gamma_0}\right)\beta_{t0}^{2(s-3)}\frac{\lambda}{L}\left(\frac{s^s}{2^s s!}\right)^2\frac{J_{m\pm s}^2\left(k_t r_b\right)}{\left(\nu_{mn}^2 - m^2\right)J_m^2\left(k_t r_b\right)}. \tag{2.67}$$

Using the above theory the transverse efficiency is reduced to a function of only three normalized variables namely, F, μ and Δ. The efficiency can be optimized with respect to the detuning parameter Δ; the optimum value of Δ is denoted by Δ_{opt}. This allows the optimized efficiency to be written as function of only two parameters $\eta_t = \eta_t(F, \mu)$. The contour plots of the optimized efficiency for various values of normalized current I and the normalized resonator length μ for up to the fifth cyclotron harmonic interaction are presented in [104]. These plots prove to be very useful for the initial design of a gyrotron oscillator because the relevant design constraints such as wall loading, beam voltage depression, and beam thickness effects can be expressed in terms of F and μ parameters.

From a linear theory of gyrotron oscillators [103], the starting current for oscillations in a gyrotron operating in the sth cyclotron harmonic is given in terms of the normalized current parameter I, by

$$I_{st}(\Delta, \mu) = \frac{4}{\pi \mu^2} \left(\frac{e^{2x^2}}{\mu x - s} \right), \tag{2.68}$$

where $x = \mu\ \Delta/4$. We see that the starting current is a function of the detuning parameter, Δ thus minimizing Eqn. (2.68) with respect to Δ yields, the expression for the minimum starting current which occurs at

$$x_{\min} = \frac{1}{2} \left[\frac{s}{\mu} + \left(\frac{s^2}{\mu^2} + 1 \right)^{1/2} \right]. \tag{2.69}$$

2.8 Computer Codes

Independent computer codes were developed as part of this work based on the gyrotron theories described in the earlier sections to help in the design of various experiments. A brief description of these codes is presented below.

2.8.1 Computer Code for the Linear Growth Rate in Gyrotron Amplifiers Based on the Kinetic Theory

The linear growth rates of the CRM instability can be computed using either the small signal dispersion relation from the kinetic theory, Eqn. (2.12) or the cubic dispersion relation, Eqn. (2.37) derived from the linearized single particle theory .

The beam-wave dispersion relation, Eqn. (2.12) derived using the kinetic theory can be solved to obtain the growth rate for the convective instability. This dispersion relation can also be used to study the onset of absolute instability in a CRM amplifier. The operating parameters namely, beam current and magnetic detuning are chosen to be below the threshold for absolute instability using the gyrotron oscillator code (to be described later) so that the growth rates computed by this code correspond to the convective instability.

This code assumes a cylindrical cross-section of the interaction structure namely, a cylindrical waveguide operating in a TE mode. The growth rates can be computed for a gyro-TWT or CARM amplifier employing either one or many beams. An example of a multibeam device is a double stream electron cyclotron maser. The code assumes an infinitesimally thin cold beam i.e., a beam with no momentum or energy spread. We solve the dispersion relation Eqn. (2.12), which is a cubic polynomial in (ω, k) for complex values of k for given real values of ω. The dispersion relation is represented as a polynomial with complex coefficients and the Jenkins-Traub three step algorithm is used to compute the roots. This routine is available in the IMSL Libraries of Compaq Visual Fortran 6.1 [139]. The convergence and stability of this routine are excellent for most parameters of interest in this study.

2.8.2 Computer Code for Gyrotron Amplifiers Based on the Single Particle Theory

This code is based on the single particle theory for gyrotron amplifiers. It is developed as part of a comprehensive design platform for gyrotron amplifiers at the MIT Plasma Science and Fusion Center.

Computation of Linear Growth Rate

The cubic dispersion relation, Eqn. (2.37) derived from the single particle theory was also solved using the Jenkins-Traub three step algorithm. The computed growth rates from the either equation can be used to determine the gain as a function of frequency for a range of operating parameters such as the voltage, current, velocity pitch factor, magnetic field etc. to enable a first cut parameter search.

Computation of Nonlinear Operation Characteristics

To solve the nonlinear system of equations we start with say, n_e macro electrons. Each macro electron represents a group of electrons starting with similar initial parameters. The accuracy of the simulation improves with the number of macroelectrons because the ensemble averages over the initial phases are calculated as discrete sums rather than continuous integrals. Typically, the results converge for $n_e > 64$. With n_e macro electrons we obtain a system of n_e equations for the energy, Eqn. (2.15); n_e equations for phase, Eqn. (2.16); and two equations for the real and imaginary parts of the field amplitude Eqn. (2.17) thus forming a system of $2n_e+2$ equations. All the electrons are assigned the initial transverse and longitudinal momenta based on the beam voltage, V_0 and the velocity pitch factor $\alpha\,(= p_t/p_z)$. For the case of zero velocity spread the phase (ϑ_s) of the electrons are uniformly distributed over the interval $[0, 2\pi]$.

For consideration of the velocity spread in a monoenergetic beam, which is typically Gaussian in the transverse momentum space with a finite beam temperature, we first create a Gaussian around the mean transverse momentum based on the value of the transverse momentum spread. For a monoenergetic beam, under adiabatic conditions, the longitudinal momentum spread is the square of the velocity pitch factor times the transverse momentum spread

$$\frac{(\Delta p_z)}{p_z} \approx \alpha^2 \frac{(\Delta p_t)}{p_t}. \tag{2.70}$$

For numerical computation the distribution of macro electrons is divided into n_v number of velocity classes. Typically, we choose $n_v = 7$ for $(\Delta p_z)/p_z < 0.1$. The

value of n_v should be increased for much larger spread values to effectively represent the electrons in the tail of the distribution. The number of macro electrons assigned to each of these velocity classes is determined by the weight of the Gaussian distribution and n_e, the total number of macro electrons. Each velocity class has the same initial transverse and longitudinal momenta and the initial phases of electrons within each velocity class are uniformly distributed over the interval $[0, 2\pi]$.

Independent computer codes have been developed for analyzing the interaction based on the kinetic theory and the single particle theory. A comprehensive package for designing the confocal interaction structure based on the single particle theory has been developed as part of this work. The code also supports the analysis of cylindrical waveguide interaction structures. This feature allows us to benchmark the results with those obtained from an independent code based on the kinetic theory described in Sec. 2.8.1.

Though presently not supported, the code has the capability to use a simulated distribution for the electron beam such as that output by EGUN [140]. This capability of the code allows it to model the interaction process better than the case in which a simple Gaussian spread in the longitudinal or transverse momentum is considered. The next version of the code will fully support this feature.

The results from this code have been benchmarked with an independent code based on the linear kinetic theory for the case of a cylindrical waveguide interaction structure. The simulation results from the codes described in Sec. 2.8.1 and Sec. 2.8.2 for the gain *vs* frequency plot for a cylindrical waveguide gyro-TWT have been compared in Fig. 2-7. We find an excellent agreement for the linear growth rates predicted by single particle code and the kinetic code. The numerical results from the kinetic code also agree with those presented in [118] for the TE_{01} mode cylindrical guide gyro-TWT.

The next step in the benchmarking process is to compare the growth rates predicted by solving the nonlinear equations of motion and that obtained from the linear dispersion relation in the small signal regime. The results of such a comparison for a confocal waveguide gyro-TWT are shown in Fig. 2-8. The difference in the output

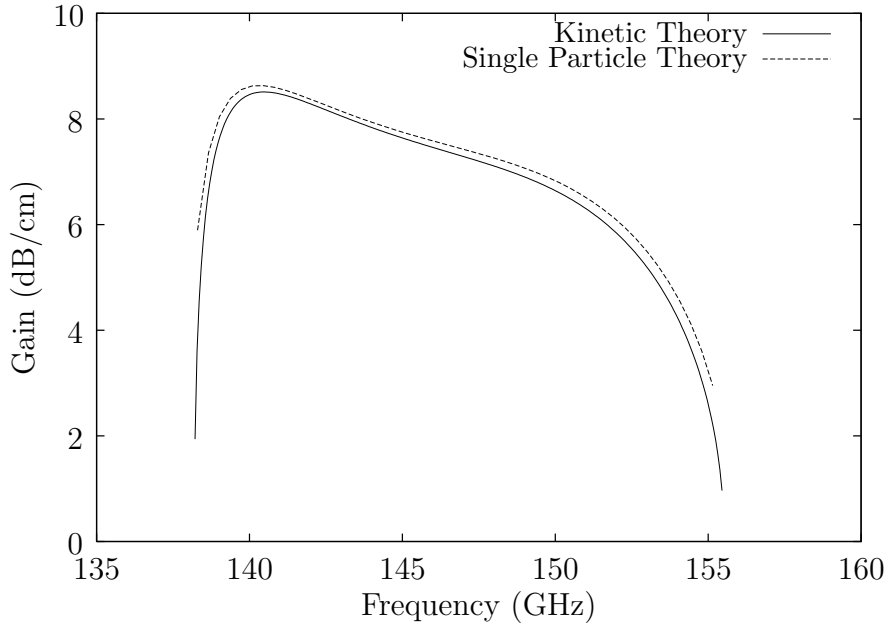

Figure 2-7: Comparison of the linear growth rates predicted by the kinetic theory and the single particle theory.V_0= 70 kV, I_0 = 5 A, α =1.2, r_b =1.24 mm, r_w = 2.96 mm, TE_{13} mode, $B_0 = B_g$, $(\Delta p_z)/p_z = 0\%$.

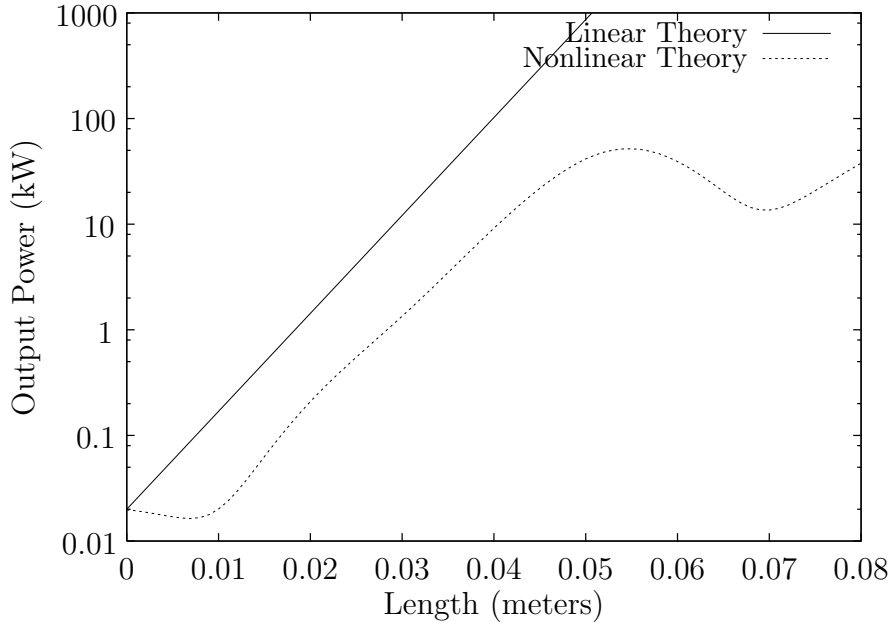

Figure 2-8: Comparison of the linear and nonlinear growth rates in a confocal wvaeguide gyro-TWT. V_0 = 65 kV, I_0 = 7 A, α = 1.2, r_b =1.81 mm, r_c = 6.79 mm, HE_{06} mode, $B_0 = 0.998\ B_g$, $\Delta p_z/p_z = 0\%$.

powers predicted by the linear and nonlinear codes is attributable to the launching loss, which is accounted for in the nonlinear theory. The launching loss occurs due to the distribution of the input power into three waves, namely, a forward growing wave, a forward decaying wave and a constant amplitude forward wave. At exact synchronism ($\Delta = 0$) the launching loss can be shown to be exactly 9.54 dB by following a Pierce type approach described in [129].

The phase bunching in a gyro-TWT is shown by the non-linear analysis which follows the electron trajectories along the interaction length. Using the results from the single particle code we plot the trajectories of various velocity classes of electrons for an assumed Gaussian-spread in the transverse momentum of the electron beam. The electrons in each velocity class are uniformly divided in the phase space $[0 - 2\pi]$. To avoid overlapping of the various electrons from different velocity classes, we have divided the phase space for each class from $2n\pi - 2(n+1)\pi$. The electron trajectories for typical operating parameters of a gyro-TWT are shown in Fig. 2-9 in page 66. With the description of the computer code based on the single particle theory we have outlined the design tool which will be used in the later chapters for the design and optimization of the gyro-TWT.

2.8.3 Computer Code for Gyrotron Oscillator Design

A computer code was developed to integrate the nonlinear pendulum equations for a gyrotron oscillator described in Sec. 2.7 to evaluate the interaction efficiency and to optimize the operating parameters. This code is very similar to the gyro-TWT amplifier code based on the nonlinear single particle theory described in the previous section. The only difference in the case of a gyrotron oscillator is the use of a stationary wave in a resonator instead of a traveling wave with a growing field amplitude as in the case of a gyro-TWT. Any kind of axial field profile, $f(\zeta)$ can be chosen based on the shape of the resonator. Several other gyrotron resonator design codes at the MIT-PSFC were used for studying the electromagnetic mode and computing the resonant frequency of the resonator.

2.9 Discussion

In this chapter some of the theoretical approaches to the CRM instability problem were outlined. The linear dispersion relation for the beam-wave interaction in a gyrotron amplifier obtained using the kinetic theory was described to evaluate the growth rate of the convective instability. A single particle theory to compute the evolution of the beam-wave system was presented. A linear dispersion relation derived from the nonlinear self-consistent equations of the beam-wave system was shown to be a cubic equation with one solution corresponding to a growing wave. The final set of nonlinear equations for the electron energy, phase and the amplitude of the electric field are presented for numerical computation to include the large signal and saturation effects. The equation for the starting current and the nonlinear theory for computing the efficiency in gyrotron oscillators was reviewed. Three computer codes written for the numerical implementation of the above theories were also described. These codes have served as the design tools for all the experiments described later in this work. The benchmarking of the codes against each other and also against results published elsewhere by other authors indicate good agreement.

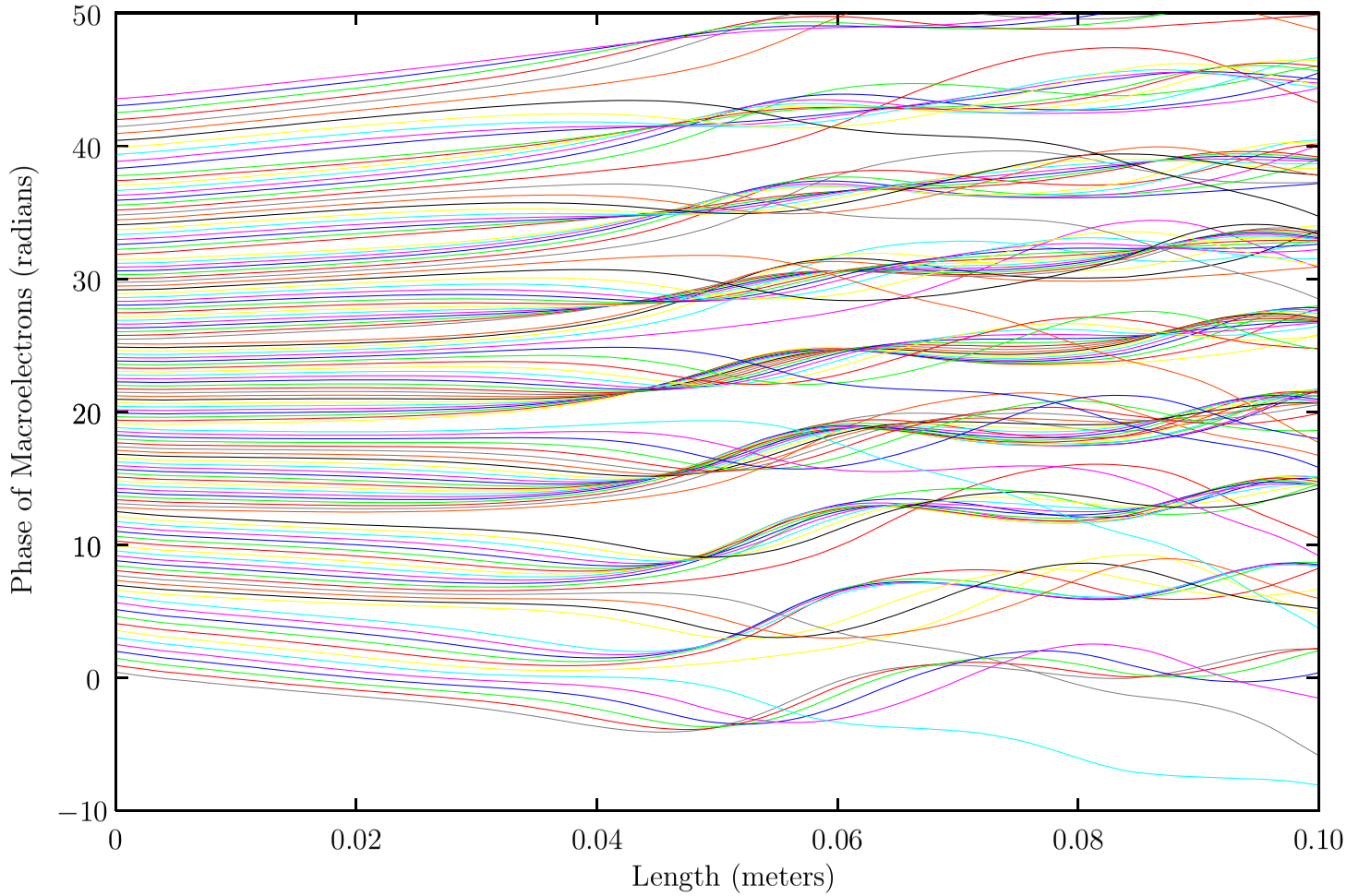

Figure 2-9: Bunching in CRM interaction as predicted by the particle tracking code. To avoid overlapping of the various electrons from different velocity classes, the phase space for each class is chosen from $2n\pi - 2(n+1)\pi$.

Chapter 3

Mode Selective Interaction Structures

Vacuum electron devices are important sources of high power microwave radiation for use in industrial heating, plasma heating in magnetic confinement fusion experiments, radar, communications, driving accelerators and many other applications [15]. Extension of the operating frequency of these sources to higher frequency is of great interest and would open up many new applications. One obstacle to the extension of the operating frequency is that high power, high frequency devices must operate in overmoded structures for several reasons. As the frequency increases to the millimeter-wave range, fundamental mode resonators have sub-millimeter dimensions so that accurate fabrication is difficult and expensive and most importantly the thermal loading on the walls of the interaction structure (resonator or a waveguide) per unit area becomes excessive. The state-of-the-art cooling technology is limited to about 1 or 2 kW/cm^2 for simple geometry structures such as the cylindrical resonators used in megawatt gyrotrons. Recent efforts to build sub-millimeter wave interaction structures for high power millimeter wave devices have proved to be very challenging and the experimental results far from successful . It is also very difficult to transmit an electron beam through such small structures without beam interception, the principal nemesis for the klystrino [142] a 94 GHz miniature conventional klystron built using microfabrication techniques. Though overmoded resonators al-

leviate these problems, their pitfall is mode competition – a limiting factor in the design and operation of millimeter-wave VEDs. Typically, mode competition causes several serious problems in a VED. The presence of parasitic modes directly reduces the efficiency of the main operating mode or prevents the access to the high efficiency operating regime of the design mode. Parasitic mode oscillations outside the desired frequency band renders a device unsuitable for radar applications because the power amplifier needs to be zero drive stable to permit the sensitive receiver to listen to the feeble echo from the target. The output section components in a high power microwave tube such as the internal mode converter and the window are designed for the operating mode and usually perform poorly for the parasitic modes resulting in trapped power in the tube. Even tens of kW's of trapped power in a megawatt power level gyrotron causes heating and outgassing which results in a severe deterioration of the vacuum inside the tube. The heating can also lead to catastrophic failure of the seals and brazes. This is a severe problem in megawatt gyrotrons for application in ECRH of fusion plasmas and has prompted the researchers at Germany [56] to install a 'relief' window in addition to the main output window.

While megawatt gyrotrons operate in highly overmoded resonators to keep the cavity thermal loading below 1 kW/cm^2, most recent successful gyrotron amplifiers have limited themselves to either the fundamental TE_{11} mode [77] or a very low order circuit mode such as the TE_{01} [19], [83] to mitigate the problem of mode competition and parasitic oscillations. The operating parameter space in an amplifier is more restricted than in oscillators due to the problem of the excitation of oscillations in addition to mode competition. It is now becoming increasingly evident that contemporary ideas of building very low order mode gyrotron amplifiers prevents the generation of more than a few tens of kW's at W-band (94 GHz) and the situation only gets worse at higher frequencies. The power capability of VED's scales with operating frequency as $f^{5/2}$, which severely limits the available power at millimeter wave frequencies. The most successful experiment to date has been the demonstration of 10 kW average power in the CPI/NRL gyroklystron [15] at W-band (94 GHz). Clearly, new ideas are needed to generate more than 100 kW average power in the

Ka band and W-band for future radar applications [144]–[146].

This work is devoted to the demonstration of novel concepts for building overmoded fast wave devices, however, the much larger segment of the VED market consisting of slow-wave tubes with fundamental mode interaction circuits can also directly benefit from the ideas demonstrated in this thesis. The slow-wave tubes boast of portability, lower cost and multioctave bandwidth as compared to fast-wave tubes but they are limited mainly to producing a few 100's of Watts of average power in the Ka-band (35 GHz). The only successful high power slow-wave tubes at W-band are the Millitron tubes [21] from CPI which come with a stiff price tag. These tubes in different configurations can produce up to 100 W of CW or 1 kW of peak power. The interaction circuit is either a double inline ladder structure (high power) or double-staggered ladder (20 % bandwidth and 100 W CW power) circuit with fabrication tolerances of 2 ten-thousandths of a mil (0.0002 inches) [21]! Recently, Thomson Tubes Electroniques has demonstrated a 94 GHz slow-wave TWT with an instantaneous bandwidth of 500 MHz, output power of 200 W and a maximum duty cycle of 10 % [22]. The state-of-the-art W-band extended interaction klystrons (EIK) [23] developed by CPI can produce slightly more than 1 kW of peak power over 5 GHz mechanically tunable bandwidth, however the duty factor of the EIKs is limited at the most to a fraction of 1 %.

The Holy Grail of building higher frequency VEDs is an interaction structure capable of stable single mode operation in a higher order mode. This will enable every class of microwave device to use an interaction structure with transverse dimensions much larger than the operating wavelength to meet the thermal load requirements and simplify fabrication. In this work, the idea of using overmoded yet mode-selective interaction structures has been the philosophy behind building the next generation VEDs capable of operating from 100 GHz to up to the Terahertz domain. While other contemporary researchers [141], [142] are exploring novel microfabrication techniques such as LIGA [143] for 94 GHz devices, the experience gained at MIT so far during the various experiments demonstrated as part of this work, does indicate that when it comes to higher power handling capability larger interaction structures seem to have

many advantages.

In this chapter we present the research on novel mode selective structures for applications in VEDs. Two different classes of structures relying on different electromagnetic properties for limiting the mode population and enhancing mode discrimination are described. Photonic Band Gap (PBG) structures described in Sec. 3.1 rely on the periodicity of the structure to provide frequency dependent losses while quasioptical open structures discussed in Sec 3.2 use diffraction from the open boundary of the structure for mode selectivity. The basic methodology for design of mode-selective interaction structures using either of these structures is also discussed.

3.1 Photonic Band Gap Structures

The use of one dimensional (1D) Bragg reflectors in both active [147] and passive microwave and optical devices is well known. A Bragg reflector is essentially a periodically modulated medium which shows a sharp contrast in the transmission coefficient with frequency and the angle of incidence. Photonic Band Gap (PBG) [148] structures are periodic two or three dimensional (2D or 3D) arrays of varying dielectric and/or metallic structures. In recent years, numerous advances have improved our understanding of the theory of PBG structures [149], [150]. This has led to new applications in passive devices for guiding and confinement of electromagnetic radiation. Their use in both microwave and optical devices has primarily been limited to passive devices such as waveguides and filters [151]–[153], though some applications in active devices have been reported [154]. The first VED using a PBG structure was experimentally demonstrated during the course of this work [155] and is discussed in Chapter 5. The results of investigation of the potential of PBG structures for accelerator cavities are also very promising [156]–[158].

3.1.1 Theory of Metallic PBG Structures

In the last decade there has been significant progress in the theory of both metallic and dielectric PBG structures [90], [149], [150]. In this section we briefly outline

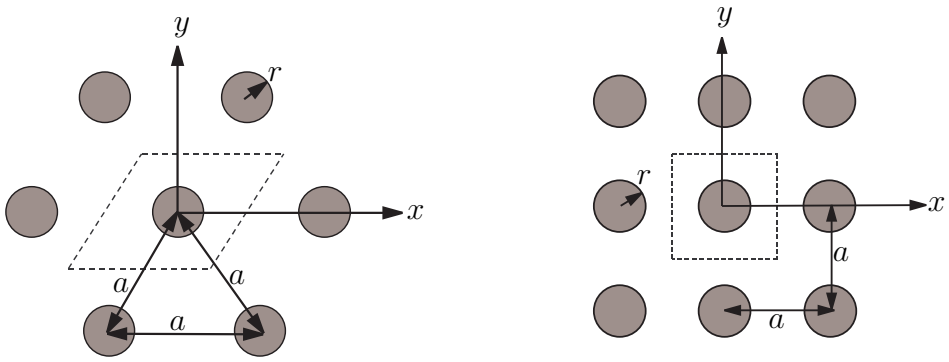

(a) Triangular lattice

(b) Square lattice.

Figure 3-1: Configuration of 2D metallic PBG structures of perfectly conducting cylinders in a triangular or square lattice. The dotted parallelogram and square show the boundary of a unit cell.

the technique for computing the electromagnetic wave propagation characteristics of metallic PBG structures which are of interest in VED's, particularly fast wave devices which operate in the TE modes. A very versatile simulation and modeling software (MIT Photonic Bands) developed at the MIT Physics Dept. [159] is very useful for designing two and three dimensional dielectric PBG structures. Since metallic structures were of initial interest for applications in VED's due to their mechanical strength and thermal capability, a different software was developed at the Waves and Beams Division of the MIT-Plasma Science and Fusion Center (PSFC) for computing the band gaps of 2D square and triangular lattices of cylindrical metal posts. The use of 3D structures in VEDs can be very interesting and is likely to be a focus area in future. The theory and implementation of the MIT software for computing the bulk properties of 2D metallic PBG structures is described in detail in [90] et al.

In this section we review the theory of computing the propagation characteristics of electromagnetic waves through a PBG structure from the work of Smirnova et al. [90]. A simple 2D array of metallic post in either a triangular or square lattice as shown in Fig. 3-1 constitutes a PBG structure. The system can be described by a periodic conductivity profile

$$\begin{aligned}
\sigma(\mathbf{x}) &= \sigma(\mathbf{x}_\perp) \\
&= \begin{cases} \infty, \left[x - \left(m + \frac{n}{2}\right) a\right]^2 + \left[y - \frac{\sqrt{3}}{2} na\right]^2 < r^2 \\ 0, \text{ otherwise} \end{cases} \quad \text{(tri. lattice)}, \qquad (3.1) \\
&= \begin{cases} \infty, (x - ma)^2 + (y - na)^2 < r^2 \\ 0, \text{ otherwise} \end{cases} \quad \text{(square lattice)}, \qquad (3.2)
\end{aligned}$$

where (x, y) are the transverse coordinates, $\mathbf{x}_\perp = x\hat{e}_x + y\hat{e}_y$, r is the radius of the metal cylinder, a is the lattice vector for each array, m and n are integers. We define a set of periodicity vectors $\mathbf{T}_{mn}$ for the transverse conductivity profile

$$\sigma(\mathbf{x}_\perp + \mathbf{T}_{mn}) = \sigma(\mathbf{x}_\perp), \qquad (3.3)$$

where

$$\begin{aligned}
\mathbf{T}_{mn} &= \left(m + \frac{n}{2}\right) a\hat{e}_x + \frac{\sqrt{3}}{2} na\hat{e}_y \text{ (triangular lattice)}, \qquad (3.4) \\
& \qquad (3.5) \\
&= ma\hat{e}_x + na\hat{e}_y \text{ (square lattice)}. \qquad (3.6)
\end{aligned}$$

From Maxwell's equations we can easily show that for 2D PBG structures the solution can be found separately for two independent classes of modes, namely, TE (electric field is transverse to the rod axis) and TM (magnetic field is transverse to the rod axis). All the field components in the TM (TE) modes can be expressed in terms of the axial component of the electric (magnetic) field, which is denoted by the function ψ. The absence of a third dimension in the problem allows us to express ψ as

$$\psi(\mathbf{x}, t) = \psi(\mathbf{x}_\perp, t)\, e^{i(k_z z - \omega t)}, \qquad (3.7)$$

where, k_z is the axial propagation constant and write the Helmholtz equation for the

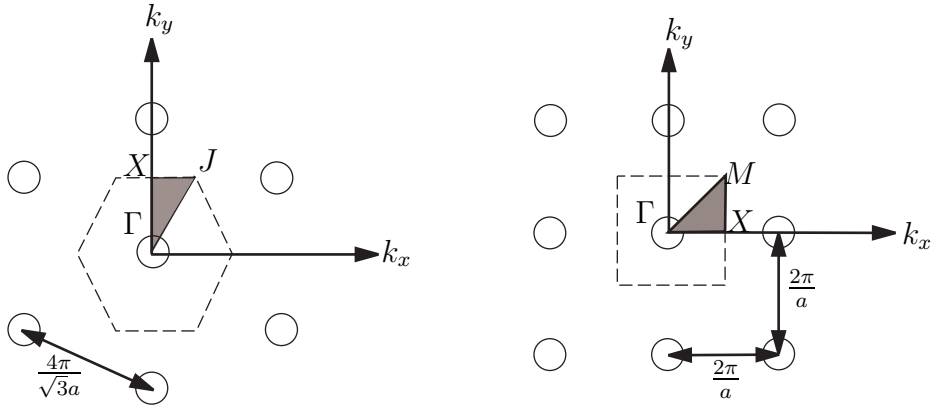

(a) Triangular lattice.

(b) Square lattice.

Figure 3-2: Reciprocal lattices and Brillouin zones for square and triangular lattice PBG structures. The irreducible Brillouin zones are shown shaded.

system as

$$\nabla_\perp^2 \psi(\mathbf{x}_\perp) = \left(k_z^2 - \frac{\omega^2}{c^2}\right) \psi(\mathbf{x}_\perp). \tag{3.8}$$

The relevant boundary conditions for the problem are

$$\psi|_S = 0 \qquad \text{(TM mode)}, \tag{3.9}$$

$$\left.\frac{\partial \psi}{\partial \mathbf{n}}\right|_S = 0 \qquad \text{(TE mode)}, \tag{3.10}$$

where, S denotes the surface of the rods and $\mathbf{n}$ is unit vector normal to the surface. The discrete translational symmetry of the conductivity profile permits us to express the fundamental solution of the Helmholtz equation in Bloch form so that

$$\psi(\mathbf{x}_\perp + \mathbf{T}) = \psi(\mathbf{x}_\perp) e^{i\mathbf{k}_\perp \cdot \mathbf{T}}, \tag{3.11}$$

where, $\psi(\mathbf{x}_\perp + \mathbf{T}) = \psi(\mathbf{x}_\perp)$, $\mathbf{k}_\perp = k_x \hat{e}_x + k_y \hat{e}_y$ is an arbitrary transverse wave vector and $\mathbf{T}$ is any vector of $\mathbf{T}_{mn}$.

The periodicity of the exponent in Eqn. (3.11) restricts the possible values of $\mathbf{k}_\perp$ to the irreducible Brillouin zones of the reciprocal lattices [149], which for the case of triangular and square lattices are shown in Fig. 3-2. The three special symmetry

points for the Γ , X , the J and M points are

$$\left.\begin{array}{ll} \Gamma: & \mathbf{k}_\perp = 0 \\ X: & \mathbf{k}_\perp = \frac{2\pi}{\sqrt{3}a}\hat{e}_y \\ J: & \mathbf{k}_\perp = \frac{2\pi}{3a}\left(\hat{e}_x + \sqrt{3}\hat{e}_y\right) \end{array}\right\} \text{(triangular lattice)} \tag{3.12}$$

$$\left.\begin{array}{ll} \Gamma: & \mathbf{k}_\perp = 0 \\ X: & \mathbf{k}_\perp = \frac{\pi}{a}\hat{e}_x \\ M: & \mathbf{k}_\perp = \frac{\pi}{a}\left(\hat{e}_x + \hat{e}_y\right) \end{array}\right\} \text{(square lattice).} \tag{3.13}$$

The technique for the computation of the eigenmodes of Eqn. (3.8) by a finite-difference method is described in detail in [90].

3.1.2 Calculation of Eigenmodes and Band Gaps

Using the PBGSS code [90] we can compute the propagation bands for waves incident at various angles on the PBG structure for the two different kinds of field polarizations namely, the TE and TM modes.

TM Modes

In Fig. 3-3 we show the first two propagation bands for the TM modes in triangular and square lattices. The absence of any k value for a particular frequency value on the ordinate represents a local band gap (or stop band). This gap is called a local gap because it is specific to the angle of incidence of the wave. If a local gap exists for all values of the incident angle of the wave then the structure is said to have a global band gap. For frequencies in the global band gap, which will be described later, the porous PBG structure acts like a perfect reflector. However, for regions outside the band gap the PBG structure reflects the electromagnetic wave depending on the angle of incidence and the frequency.

The interesting propagation characteristics of the lattice lie in the regions of a global band gap. In Fig. 3-4 the dispersion characteristics for the TM modes are shown as the $\mathbf{k}_\perp$ varies from the center of Brillouin zone (Γ point in Fig. 3-2) to

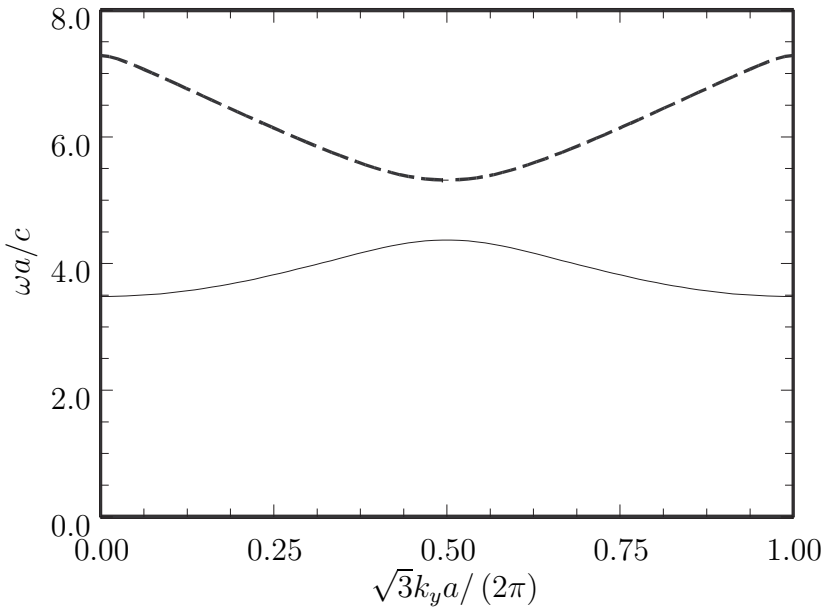

(a) The dispersion diagram for an electromagnetic wave propagating in the y direction with $k_x = k_z = 0$ in triangular lattice.

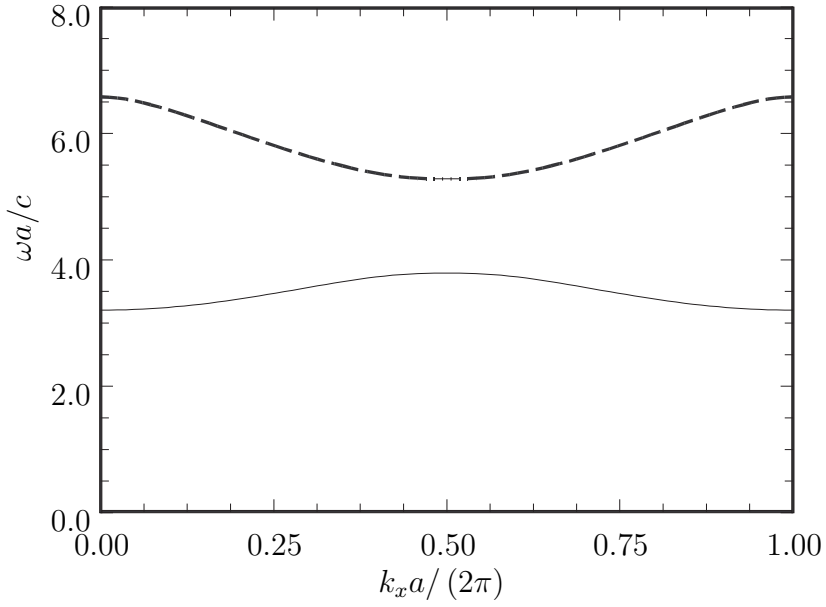

(b) Dispersion diagram for an electromagnetic wave propagating in the x direction with $k_y = k_z = 0$ in a square lattice.

Figure 3-3: First and second propagating TM modes in triangular and square lattice PBG structures [90] for $r/a = 0.2$. The solid and dashes curves represent the first and second propagating modes, respectively.

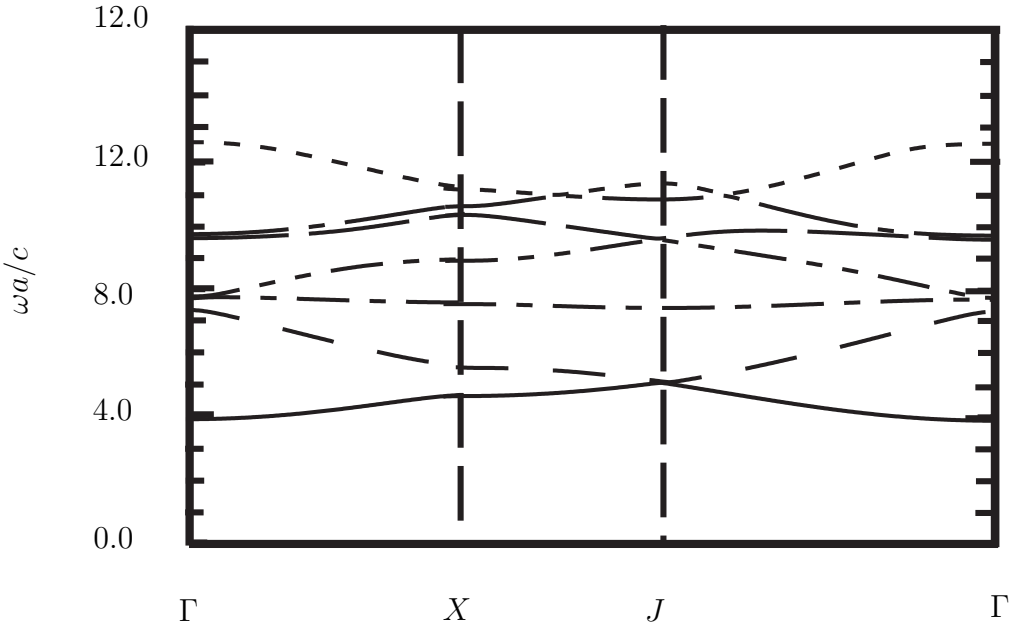

(a) Triangular lattice.

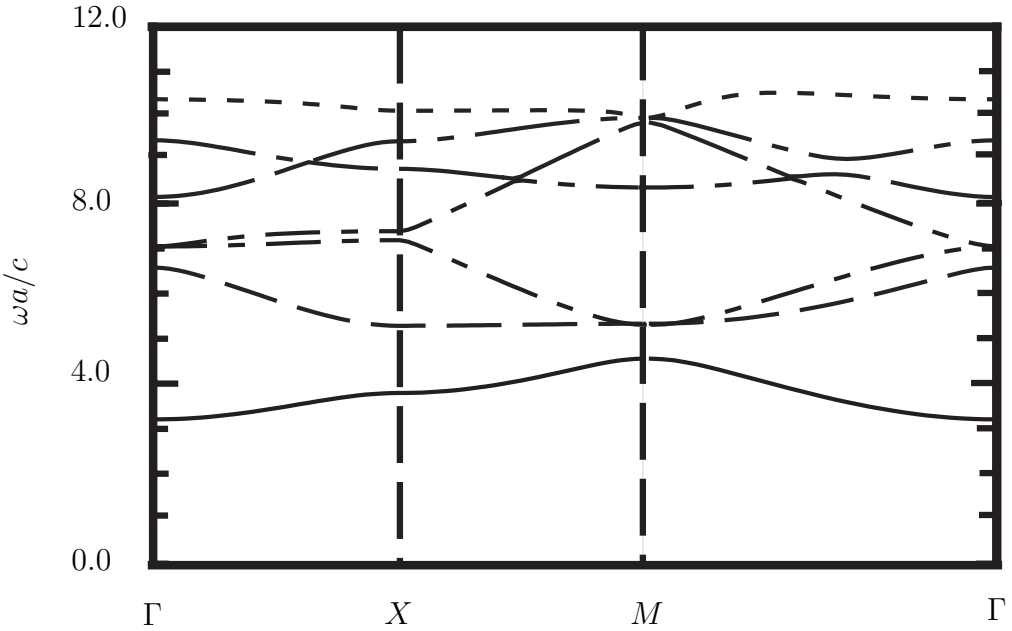

(b) Square lattice.

Figure 3-4: Plot of several lower TM eigenmodes of the triangular and square lattices for $r/a = 0.2$ [90]. Each different line represents a propagating mode.

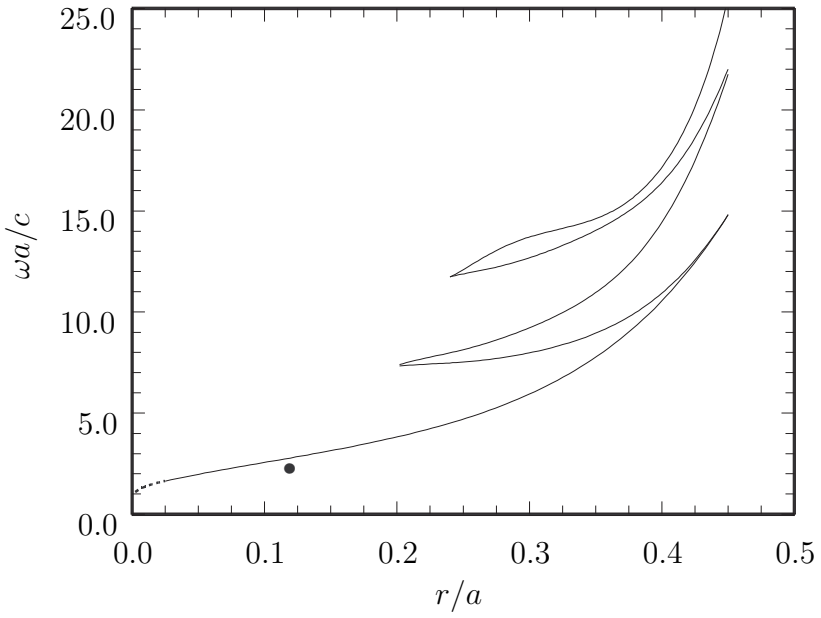

(a) Triangular lattice.

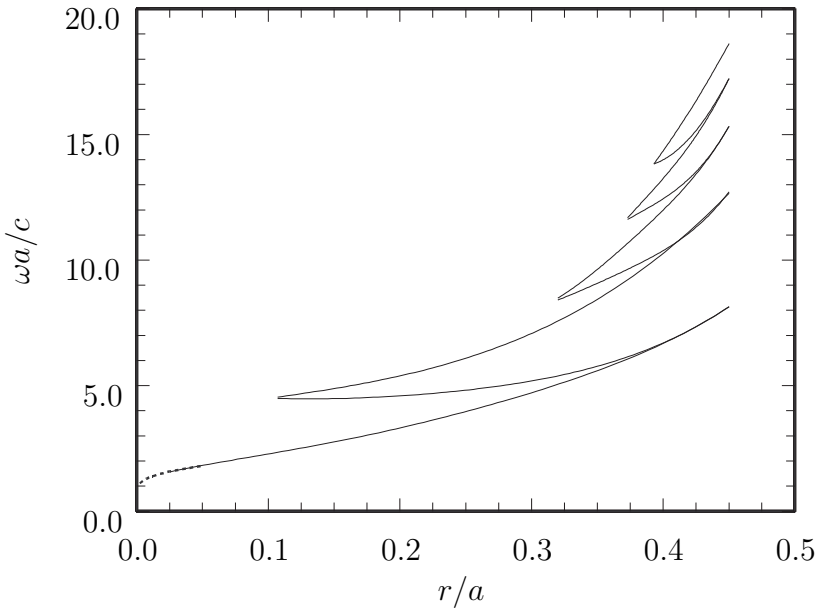

(b) Square lattice.

Figure 3-5: Global band gaps for TM modes in triangular and square lattice PBG structures [90]. The • represents the operating point of the 17 GHz TM_{010} -like MIT accelerator resonator [158].

the nearest edge of the Brillouin zone (X point) to the far edge of the Brillouin zone (M point for the square lattice and J point for the triangular lattice). The rod to lattice ratio of $r/a = 0.2$ was chosen for the above plots. It can be seen in Fig. 3-4 that for the square lattice a global band gap exists between the first and the second mode because for certain values of ω, there is no value of $\mathbf{k}_\perp$ that lies on the dispersion curves. On the other hand the first and second modes intersect in the case of a triangular lattice and there is no global band gap between them, however higher order band gaps are possible. In general for a metal lattice there is a cut-off frequency below which there is always a band gap independent of the rod to lattice (r/a) ratio.

A diagram showing the global band gaps as a function of the rod to lattice ratio would be very useful for understanding the PBG structure. Such plots for the TM modes in square and triangular lattices are shown in Fig. 3-5. It is evident that for TM modes the cut-off frequency (zero order band gap) exists even for very small rod to lattice ratio and goes logarithmically to zero as $r/a \to 0$. This can be simply explained by the large reflection of the electric field when it is polarized in the direction of the rods (TM modes). The dot in Fig. 3-5(a) represents the operating point of a 17 GHz TM_{01} cavity designed built and tested at MIT [158]. A brief discussion of this cavity is presented in Sec. 3.1.3.

TE Modes

In Fig. 3-6 we show the first two propagation bands for the TE modes in triangular and square lattices. Since the first mode goes to zero at the Γ point for both triangular and square lattices, in contrast to the TM modes there is no cut-off frequency (zero order band gap) for the TE modes, i.e., the lattice is always transparent at lower frequencies independent of the (r/a) ratio. In Fig. 3-7 the dispersion characteristics for the TE modes are shown as the $\mathbf{k}_\perp$ varies from the center of Brillouin zone (Γ point in Fig. 3-2) to the nearest edge of the Brillouin zone (X point) to the far edge of the Brillouin zone (M point for the square lattice and J point for the triangular lattice). The rod to lattice ratio $r/a = 0.2$ was chosen for the above plots. It can be

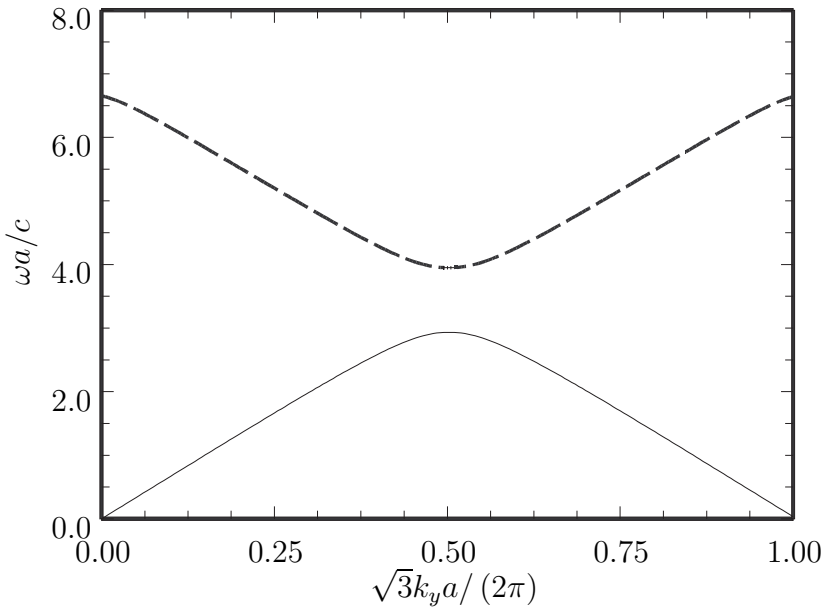

(a) The dispersion diagram for an electromagnetic wave propagating in the y direction with $k_x = k_z = 0$ in a triangular lattice.

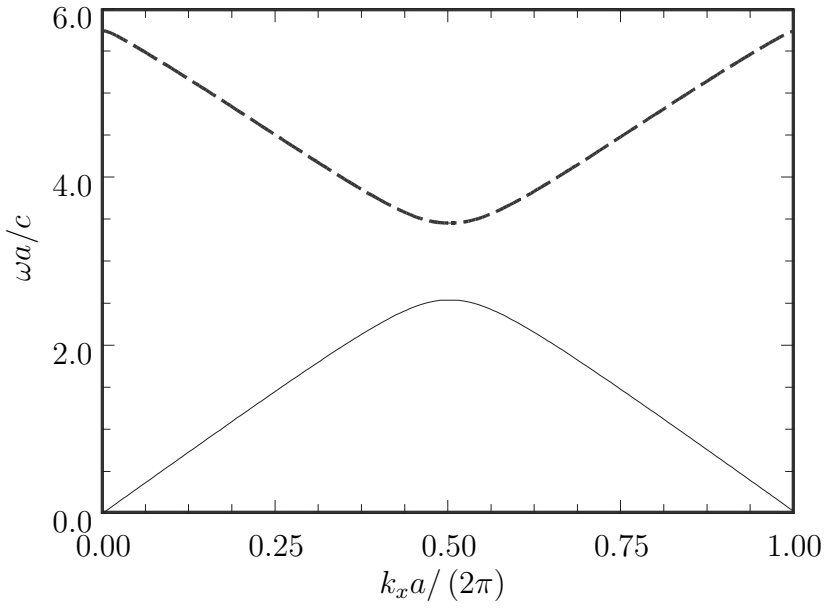

(b) The dispersion diagram for an electromagnetic wave propagating in the x direction with $k_y = k_z = 0$ in a square lattice.

Figure 3-6: First and second propagating TE modes in triangular and square lattice PBG structures [90] for $r/a = 0.2$. The solid and dashes curves represent the first and second propagating modes, respectively.

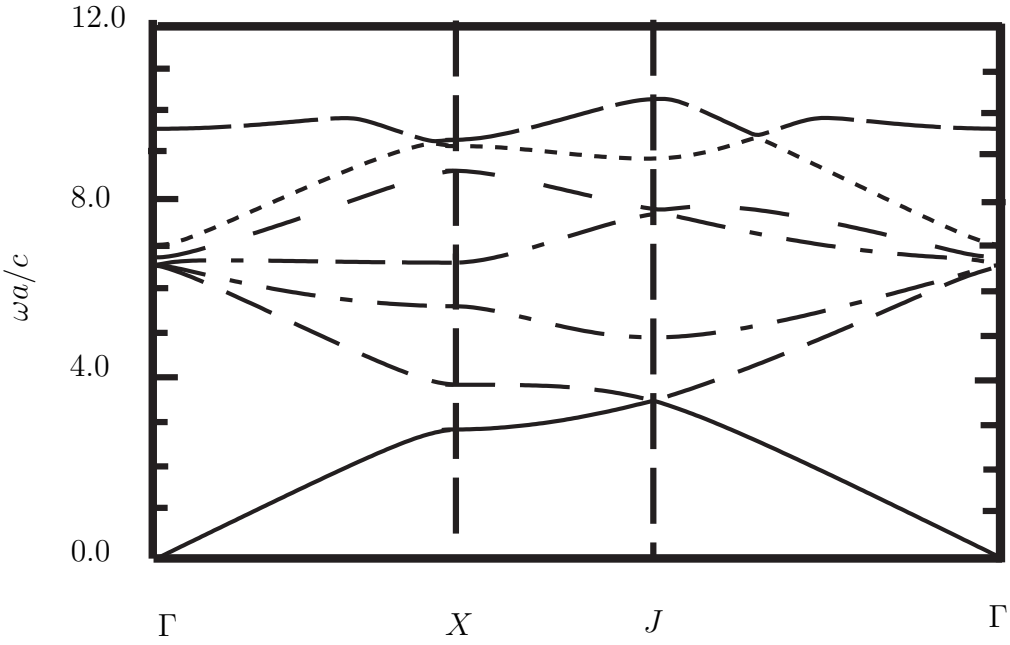

(a) Triangular lattice.

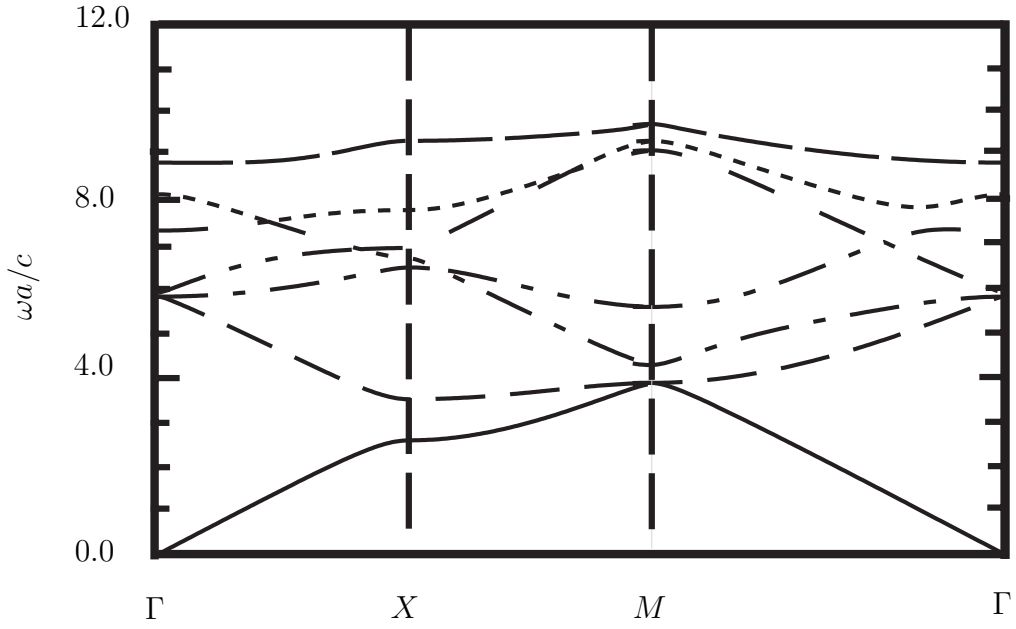

(b) Square lattice.

Figure 3-7: Plot of several lower TE eigenmodes of the triangular and square lattices for $r/a = 0.2$ [90]. Each different line represents a propagating mode.

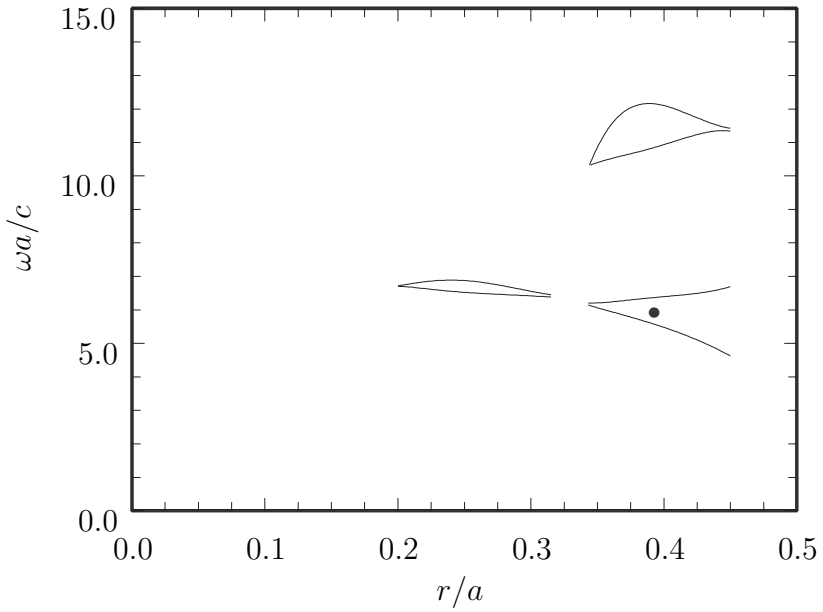

(a) Triangular lattice.

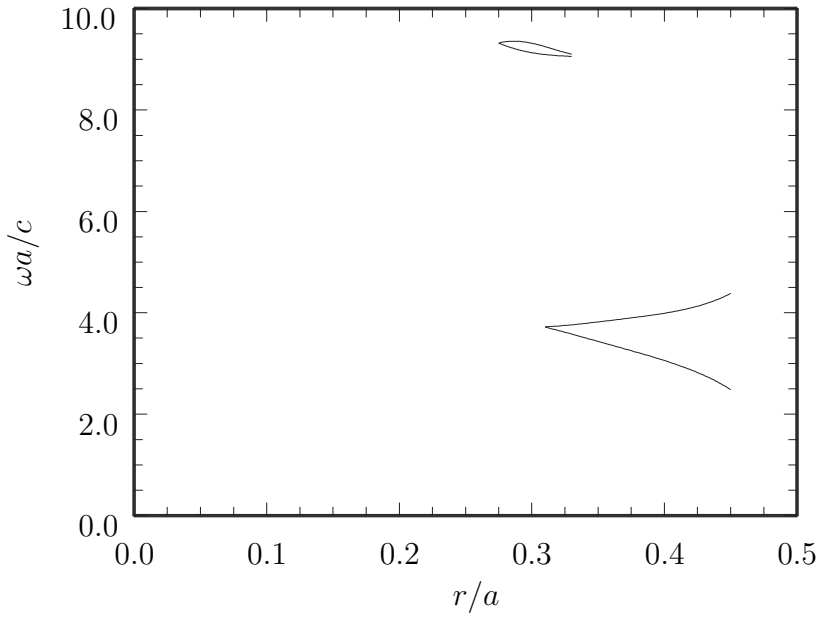

(b) Square lattice.

Figure 3-8: Global band gaps for TE modes in triangular and square lattice PBG structures [90]. The • represents the operating point of the 140 GHz TE_{041} -like MIT gyrotron resonator [155].

seen in Fig. 3-7 that for $r/a = 0.2$ there are no global band gaps for TE modes for either the square or the triangular lattice. This can be contrasted to the case of TM modes discussed earlier, where the first band gap occurs between the first and the second modes for $r/a > 0.1$ (Fig. 3-5(a)).

We also show the global band gaps for the TE modes in triangular and square lattices in Fig. 3-8. Three lowest global gaps for the TE modes are shown in Fig. 3-8(a). All the gaps tend to close with increasing r/a except the lowest one, which occurs for $r/a > 0.35$. A similar global band gap diagram for the square lattice is shown in Fig. 3-8(b). In this case the first global TE gap occurs for $r/a > 0.3$. The dot in Fig. 3-5(a) represents the operating point of the 140 GHz TE_{041} gyrotron resonator [155] designed built and tested as part of this work. The detailed design of the resonator will be presented in Chapter 4.

3.1.3 Design of PBG Resonators

In the previous section we discussed the bulk properties of PBG structures and the computation of the global TE and TM gaps in 2D metallic structures arranged in square or triangular lattices. The PBG structures act like an opaque wall for frequencies in the band gap while being partially transparent to other frequencies. This frequency dependent boundary condition can be utilized in creating a mode selective resonator, or a frequency selective waveguide. Normal resonators are made of either metal or dielectrics, whose role in discriminating frequencies is limited to either the varying skin depth or the relative permittivity and losses with frequency. The global band gaps in PBG structures provide a new and very powerful parameter for discriminating frequencies in the form of a frequency dependent reflection or transmission from the bulk structure.

If a defect is created in the lattice by the removal of one or more elements one may trap energy in the defect if the frequency is limited to within the global band gaps of the structure. The idea of defects in PBG structures is analogous to the creation of donor or acceptor levels in semiconductors. A mode trapped in the defect, henceforth referred to as a defect mode is confined completely by the otherwise transparent

lattice. The complete trapping of an electromagnetic wave such as light in a defect in a 3D PBG structure has interesting applications only limited by our own imagination.

The basic design methodology of PBG resonator can be summed in the following steps

1. Usually the mode and the frequency are determined by the nature of the application for which the resonator is intended. Depending on the amount of energy to be stored in the resonator one may choose either a metal or dielectric bulk PBG structure. The thermal considerations for active devices usually limit the tolerable ohmic losses in the bulk material of the PBG structure.

2. Depending on the bandwidth over which the resonator or the waveguide operation is desired, and the tolerable mode density far from the operating mode one may choose the kind of lattice. This is usually done by looking at the atlas of global band gaps (either TE or TM or both) for PBG structures made of different kinds of lattices. Such an atlas for TE and TM modes for 2D metallic PBG structures of triangular and square lattice is shown in Figs. 3-5 and 3-8. For example, if a higher order TM mode is to be localized in the defect without the presence of the lower order TM modes then a 2D metallic lattice cannot be chosen because there always exists a zero order band gap (cut-off) for TM modes in metallic lattices as shown in Fig. 3-5. Various kinds of dielectric PBG structures [149] may be used in this case.

3. Once the lattice vector, a is determined from the choice of the operating frequency and the shape of the lattice the width of the gap determines the r/a ratio and hence the value of the rod radius. For instance, one can tune the width of the band gap by changing the r/a ratio as can be seen from Figs. 3-8 and 3-5.

4. Based on the desired geometry of the defect mode (e.g. circular, or square etc.) and the operating frequency the transverse dimensions of the defect are determined.

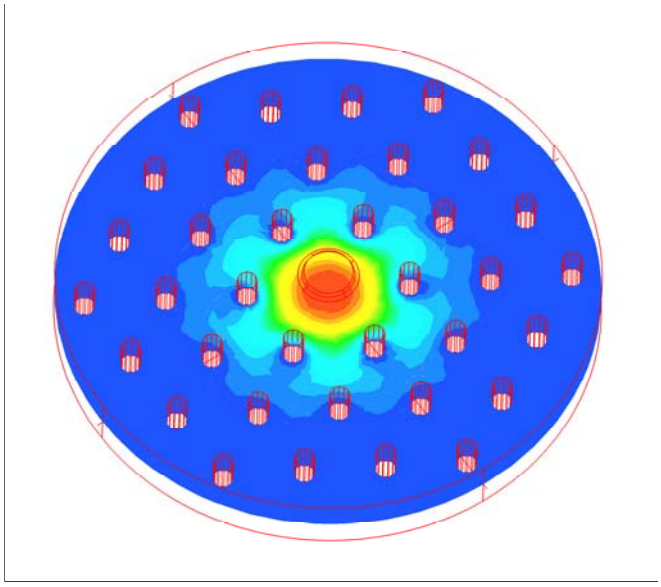

Figure 3-9: TM_{010} eigenmode at 17 GHz in a PBG resontator computed using HFSS. The magnitude of the electric field is plotted with the red color as the highest intensity and blue color as the lowest intensity. The metal rods are shown as hollow because the electric fields do not penetrate into them. An iris for the passage of the electron beam is also shown.

5. Often, while tuning the frequency of the resonant mode, the operating point on the global gap map might have to be altered.

6. Usually, a finite element based software such as HFSS [91] or SUPERFISH [161] is used to find the desired eigenmode as well as the neighboring modes in the circuit.

7. It is vital to thoroughly check the actual mode density in the PBG resonator by carefully scanning the frequency spectrum for confined modes using simulation codes such as HFSS. The absence of a TE or TM global gap does not guarantee the absence of confined modes. This is because a global gap ensures reflection for k vectors in all directions but for some modes with specific k vector direction even a local gap is sufficient to confine a particular mode.

Examples of PBG Resonators

17 GHz TM_{010} Mode PBG Resonator for Accelerator Applications This PBG resonator was built at MIT for demonstrating its potential for use in a linear accelerator structure [158]. Linear accelerator structures use a disc loaded waveguide or alternatively a stack of TM_{010} cavities coupled through a small iris which also serves as the beam tunnel [162]. The TM_{010} mode is the operating mode of each resonator and the longitudinal electric field of the mode accelerates the beam. However, other dipole modes such as the TM_{110} are also trapped in the resonator. The wakefields generated by a leading electron bunch couple to the parasitic modes in the resonator and tend to either decelerate or even impart a transverse kick to the trailing electron bunch. Hence, it is clearly desirable to have a resonator which confines the TM_{010} operating mode perfectly while suppressing the other parasitic modes to mitigate the problems of higher order modes and transverse wakefields. Shapiro et al. [158] designed built and tested a 17 GHz TM_{010} mode to demonstrate these features. The operating point of the resonator on the band gap map is shown as a • in Fig. 3-5(a). The resonator is made of a triangular lattice of metal rods of radius 0.79 mm and a lattice vector of 6.4 mm. A single rod is removed from the center to allow the confinement of a TM_{010} mode as shown in Fig. 3-9.

140 GHz TE_{041}like Mode PBG Resonator for a Gyrotron This PBG resonator was built for use in a gyrotron oscillator. To our knowledge this the first ever PBG resonator built for use in a VED. A detailed discussion on the design and this resonator is presented in Chapter 5. The resonator is made of a triangular lattice of copper rods of radius 1.59 mm and the lattice vector is 2.03 mm. Nineteen inner most rods were omitted to create a large defect to allow a TE_{041} mode to be resonant at 139.80 GHz in the resonator. The operating point of the resonator on the band gap map is shown as a • in Fig. 3-8(a) and the confined eigenmode is shown in Fig. 5-3 on page 114.

140 GHz TE_{041} Mode Cavity for Gyroklystrons In gyroklystrons, resonators with a low Q factor are desired to minimize the possibility of self excitation of gyrotron

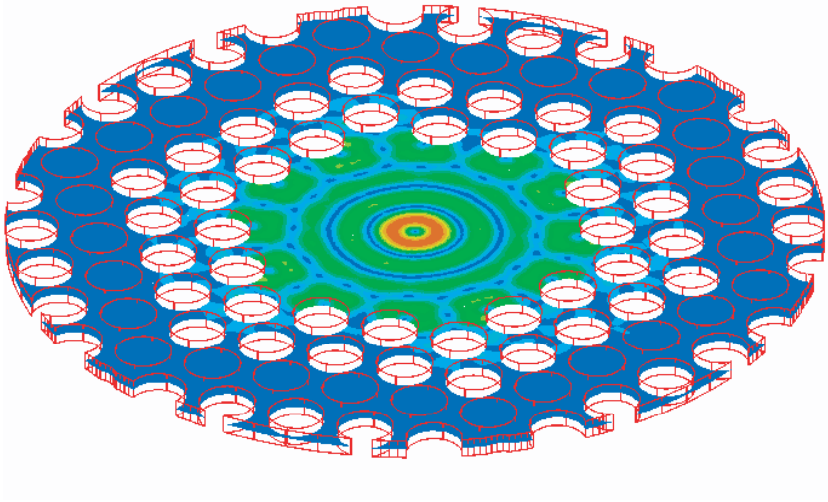

(a) Hybrid PBG resonator with the third row surrounding the defect made of dielectric rods while the other rods are metallic. The Q factor of the resonator is 854 and the resonant frequency is 139.33 GHz.

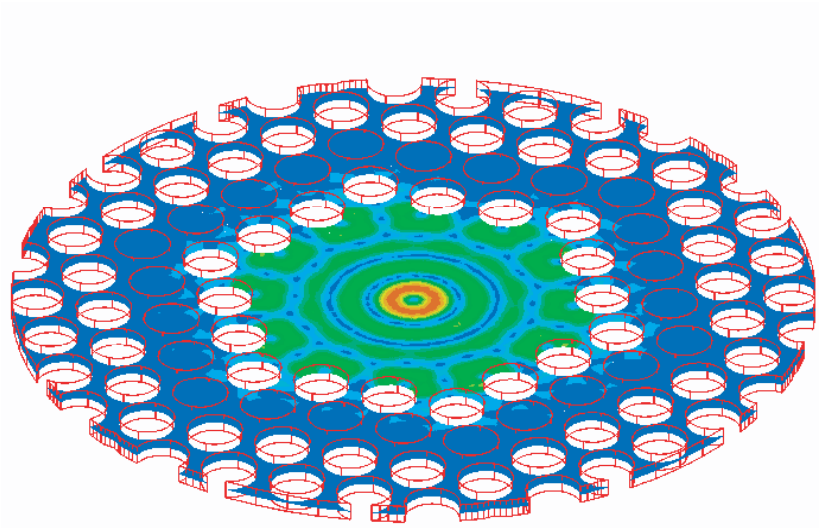

(b) Hybrid PBG resonator with the second row surrounding the defect made of dielectric rods while the other rods are metallic. The Q factor of the resonator is 176 and the resonant frequency is 139.50 GHz.

Figure 3-10: Hybrid PBG resonators with low Q factors for potential use in gyroklystron applications. The dielectric rods have $\epsilon_r = 12.27$ and $\tan(\delta) = 0.3$. The Q factor can be controlled by the location of the dielectric rods and their loss tangent.

oscillations. The theoretically predicted Q factor for an all metal PBG resonator as the one employed in the PBG gyrotron is 13,500 which is too high a value to prevent self excitation. One can control the Q of the PBG resonator by a sort of dielectric loading by replacing one or more of the metal rods with dielectric rods. The location of the rods and the loss tangent of the material used can be used to control the Q over a wide range. We show a simple example of how the all metal PBG gyrotron cavity with a Q of 13,500 can be modified by building a hybrid lattice of metal and dielectric element. The closer the lossy dielectric rods are to the defect the lower the Q factor of the mode. One of the advantages of this kind of dielectric loading compared to the conventional dielectric loading of fundamental or very low order cylindrical resonators commonly used in gyroklystrons is that the dielectric is farther from the center of the defect which would contain an electron beam in a VED. Typically, the presence of the electron beam leads to the charging of the dielectric which generate additional space charge forces and can lead to the disruption in electron beam propagation. In the dielectric loading scheme proposed for the PBG structures the dielectric is farther from the beam and most importantly is behind at least one row of metal rods shielding the dielectric from the electron beam. Such a scheme would minimize the problems with dielectric charging as well as reduce the thermal load on the dielectric rods. Besides, being an overmoded resonator the thermal load is definitely lower than that of a fundamental or lower order mode resonator. Another advantage of the PBG resonator in a gyroklystron is the ability to extract power from the transverse direction by removing one or more rods. The transverse extraction of power will prove to be useful say, for sub-millimeter wave gyroklystrons with long cavities which can have limited extraction efficiency due to a very high axial diffractive Q as explained later in Chapter 5.

3.2 Quasioptical Open Waveguide Structures

The key to mode selectivity in waveguides and resonators is the introduction of some parameter which discriminates frequencies, e.g. in the case of PBG structures it was

the frequency dependence of reflection from the waveguide walls. In this section we consider a class of structures in which the diffraction losses can be used to improve the mode selectivity. To use diffraction as a parameter we use open waveguide structures. Open waveguide structures have some part of the transverse boundary as an aperture for radiation. The size of the aperture, if very small can be treated as merely a perturbation to the existing mode of the original structure. For example, the use of longitudinal slots on a cylindrical or rectangular waveguide at specific positions to impart higher losses for the undesired modes is well known [163]. However, the most interesting properties of the waveguide come forth when the aperture is large enough to significantly alter the mode pattern of the original structure.

At the outset it is worthwhile to look at the advantages of quasioptical structures in confinement and propagation of electromagnetic waves. In the limit that the wavelength $\lambda \rightarrow 0$, the propagation of electromagnetic waves can be represented as a directed bundle of radiation and all the familiar techniques such as ray tracing can be used to study the propagation of electromagnetic waves. This is called the geometric optical limit and requires the dimensions of all the elements such as mirrors, lenses etc. to be much larger than the wavelength of the radiation under consideration.

In the other limit, if the wavelength is of the order of the structure dimensions then diffraction effects are dominant and the distribution of radiation from a source changes with the distance from the source. Familiar examples of this include the near field radiation of an antenna. The treatment of these problems usually leads to invoking the solution to Maxwell's equations in full rigor.

Quasioptics is the vast middle ground between geometric optics and diffraction dominated propagation. In this regime the dimensions of the system elements are larger than the wavelength, but the diffraction effects are still important. Quasioptical techniques of wave propagation are very important in the millimeter and sub-millimeter wave regime because the wavelength in this region of the spectrum is still not small enough for the system components to be large enough to use geometrical optics techniques, nor are the propagation losses in single mode waveguides small enough to use standard microwave techniques. Propagation in free space by

quasioptical techniques has a lot of advantages, including lower losses and simpler and elegant system design. The theoretical attenuation in a TE_{10} fundamental mode rectangular waveguide (WR-4) at 250 GHz is approximately 12 dB/m, whereas with a quasioptical transmission line with a series of Teflon lenses an attenuation of 1.5 dB/m has been demonstrated [164]. Another advantage of quasioptical systems is in spatial combining of power which is very useful for building a high power system with low power component modules.

3.2.1 Fundamentals of Gaussian Beam Propagation

In this section we review the fundamental concepts about Gaussian beam propagation which is the backbone of quasioptics. In the quasioptical limit the Helmholtz wave equation can be easily reduced to the paraxial wave equation, which in cylindrical coordinates can be expressed as [165]

$$\frac{\partial^2 u}{\partial r^2} + \frac{1}{r}\frac{\partial u}{\partial r} + \frac{1}{r}\frac{\partial^2 u}{\partial \varphi^2} + 2ik\frac{\partial u}{\partial z} = 0, \tag{3.14}$$

where, $u = u(r, \varphi, z)$ is a complex function that defines the non-plane wave part of the beam and is defined as

$$E(r, \psi, z) = u(r, \psi, z)\exp(ikz), \tag{3.15}$$

in which E is the electric field, z is the direction of propagation of the beam, and k is the free space propagation constant. For the case of axial symmetry, where u is independent of φ, one can write the solutions of Eqn. (3.14) in the form

$$u(r, z) = A(z)\exp\left[i\frac{kr^2}{2q(z)}\right], \tag{3.16}$$

where A and q are z dependent complex functions. Substituting Eqn. (3.16) into Eqn. (3.14) we obtain the following relationships

$$\frac{\partial q}{\partial z} = 1, \tag{3.17}$$

and

$$\frac{\partial A}{\partial z} = -\frac{A}{q}. \tag{3.18}$$

Without loss of generality we assume the initial position $z_0 = 0$, and using Eqn. (3.17) we define the complex beam parameter $q(z) = q(0) + z$. in the following form

$$\frac{1}{q} = \left(\frac{1}{q}\right)_r + i\left(\frac{1}{q}\right)_i. \tag{3.19}$$

Substituting the above equation into Eqn. (3.16) we can identify $\left(\frac{1}{q}\right)_r$ to be the radius of curvature, R of the beam. To cast Eqn. (3.16) into the form of a Gaussian distribution we take

$$\left(\frac{1}{q}\right)_i = \frac{2}{kw^2(z)} = \frac{\lambda}{\pi w^2}, \tag{3.20}$$

and thus define the beam radius w as the distance where the value of the field falls to $1/e$ of its value at the axis. With these definitions we can express the complex beam parameter as

$$\frac{1}{q} = \frac{1}{R} + i\frac{\lambda}{\pi w^2}, \tag{3.21}$$

where both R and w are functions of z. Defining the minimum beam radius to be the beam waist, w_0 which in our case occurs at $z_0 = 0$. The propagation of the quasioptical Gaussian beam can now be expressed in just the following couple of equations

$$R = z + \frac{1}{z}\left(\frac{\pi w_0^2}{\lambda}\right)^2, \tag{3.22}$$

$$w = w_0\sqrt{1 + \left(\frac{\lambda z}{\pi w_0^2}\right)^2}. \tag{3.23}$$

From the above equations we see that at the location of the beam waist the radius of curvature is infinite, which means that it is a plane wave front. Another very important parameter for a Gaussian beam is the confocal distance $\pi w_0^2/\lambda$, sometimes also called as the Raleigh range. The region $z \ll \pi w_0^2/\lambda$ is called the near field region and $z \gg \pi w_0^2/\lambda$ corresponds to the far field region of the Gaussian beam. In the near field region the beam radius is essentially unchanged from its value at

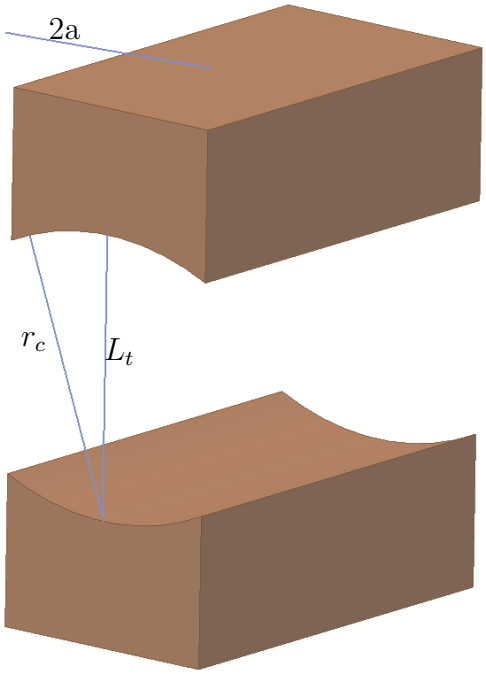

Figure 3-11: An isometric view of an open waveguide. If $L_t = r_c$ then the mirrors are confocal and the system is called a confocal waveguide. The aperture of the mirrors is $2a$.

the beam waist where as in the far field region w varies hyperbolically with z. Thus the confocal distance determines the transition point after which the beam radius diverges significantly.

3.2.2 Confocal Waveguide

In the previous section we saw that a Gaussian beam is a solution of the paraxial wave equation and it is fundamentally different from a plane wave as it has a finite transverse variation and from a geometric optics beam originating from a point source in that its origin (the beam waist) has a finite size. In the quasioptical limit diffraction has an important role however, the problem need not be defined entirely in terms of vector equations governing diffraction.

In this section we explore a quasioptical open wave guide, namely the confocal

guide. We consider a pair of identical mirrors as shown in Fig. 3-11 with a finite aperture, $2a$ and radius of curvature, r_c separated by a distance equal to the radii of curvature of the mirrors, hence the name confocal mirrors. It is evident that a Gaussian beam can propagate along the mirrors by bouncing between the two mirrors.

Eigenmodes of a Confocal Waveguide

In this section we derive some simple equations for the field pattern of the bouncing waves by using quasioptical techniques. We choose a more general problem where the mirrors have an identical radius of curvature r_c, and are separated by a distance of L_t (the subscript t stands for the transverse direction, which we have chosen to be the y direction). We consider the eigenmodes of the structure as a super-position of two Gaussian beams in which

$$\begin{pmatrix} E_x \\ H_z \end{pmatrix} \sim \exp\left[-iky - \frac{1}{2}\frac{x^2}{w^2(y)} - i\frac{1}{2}\frac{kx^2}{R(y)} + i\frac{1}{2}\arctan\frac{y}{kw_0^2}\right], \tag{3.24}$$

where w_0 is the Gaussian beam waist size at $y = 0$, $w(y)$ is the beam radius and $R(y)$ is the radius of curvature of the Gaussian beam. Using Eqns. (3.22 and 3.23) we obtain the following equations for a Gaussian beam propagating in the y direction

$$w(y) = w_0\left[1 + \left(\frac{y}{kw_0^2}\right)^2\right]^{1/2} \tag{3.25}$$

$$R(y) = y\left[1 + \left(\frac{kw_0^2}{y}\right)^2\right]. \tag{3.26}$$

On the surface of the top mirror ($y = L_t/2$), the radius of curvature of the beam must equal the curvature radius of the mirror and hence satisfies

$$r_c = \frac{L_t}{2}\left[1 + \left(\frac{kw_0^2}{L_t/2}\right)^2\right], \tag{3.27}$$

thus determining the beam waist size, w_0 as

$$w_0^2 = \frac{L_t}{2k}\sqrt{\frac{2r_c - L_t}{L_t}}. \tag{3.28}$$

The beam radius at the surface of the mirror is given by

$$w\left(\frac{L_t}{2}\right) = w_0\sqrt{1 + \left(\frac{L_t}{2kw_0^2}\right)^2} = \left(\frac{L_t}{2r_c - L_t}\right)^{1/4}\sqrt{\frac{r_c}{k}}. \tag{3.29}$$

The resonance condition for the mode needs the round trip phase shift to be equal to an integral number of wavelength. This condition can be expressed as

$$k_t L_t - \arctan\frac{L_t}{\sqrt{2r_c L_t - L_t^2}} = n\pi, \tag{3.30}$$

where n is an integer for the mode index representing the number of nulls of the axial magnetic field along L_t. Such modes are denoted as HE_{0n} modes. The subscript 0 indicates zero nulls of the magnetic field along the surface of the mirror (x direction).

In general, for a sufficiently large mirror aperture, modes with two or three nulls of the axial magnetic field in the x-direction may exist. Such modes with m nulls of the axial magnetic field in the x direction and n nulls in the y direction are designated as HE_{mn} modes. A few eigenmodes of the confocal waveguide computed by HFSS are shown in Fig. 3-12. In the Fig. 3-12 the magnitude of the electric field is plotted instead of the axial magnetic field because in our case the electron beam location in a VED is determined directly by the location of the maxima of the electric field. The real part of the transverse propagation constant for HE_{mn} modes for $(n > 4)$ can be expressed by the following asymptotic equation [87]

$$k_{tr} = \frac{\pi}{r_c}\left(n + \frac{1}{2}m + \frac{1}{4}\right). \tag{3.31}$$

Before discussing the diffraction losses in confocal mirrors it is expedient to define

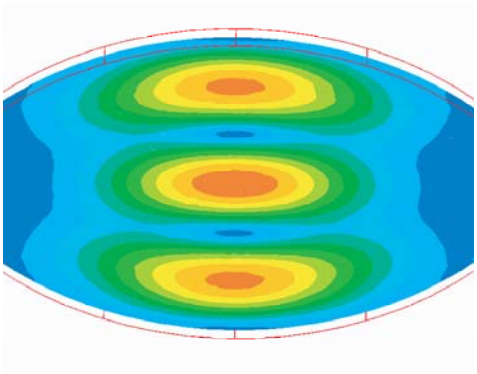

(a) HE_{03}

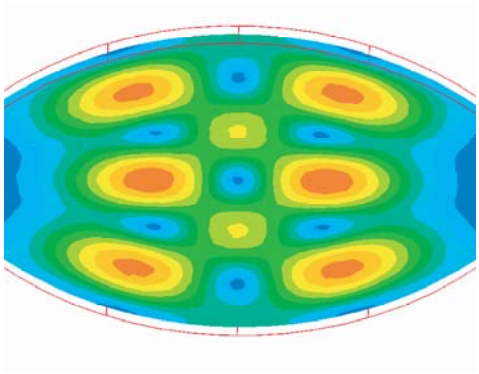

(b) HE_{13}

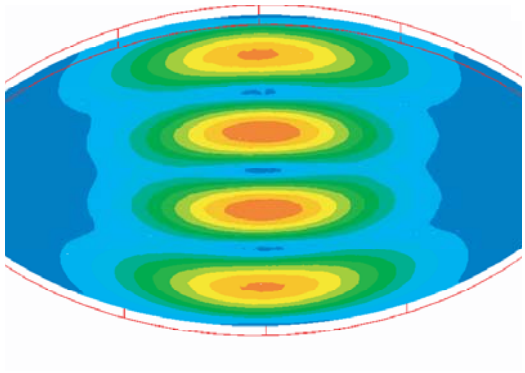

(c) HE_{04}

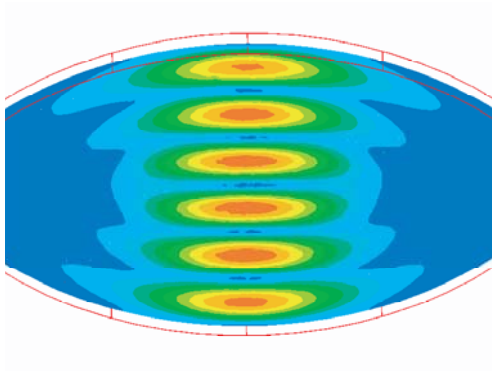

(d) HE_{06}

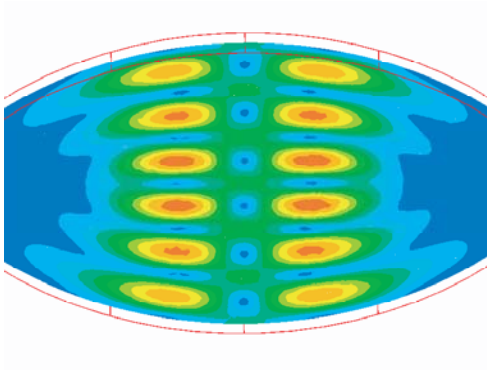

(e) HE_{16}

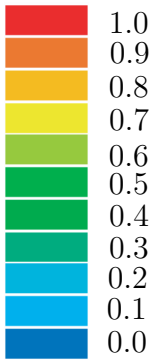

(f) Legend

Figure 3-12: Eigenmodes of a confocal waveguide computed using HFSS. The magnitude of the electric field is shown in the plots.

the Fresnel parameter which governs the degree of diffraction as

$$C_F = \frac{k_{tr} a^2}{r_c}.$$

The diffraction losses from the aperture in the confocal mirrors introduces an imaginary part k_{ti} to the transverse propagation constant, $k_t \left(= \sqrt{k_{tr}^2 + k_{ti}^2}\right)$. Boyd and Gordon [166] have studied the diffraction losses from a confocal resonator and have obtained the following expression for the imaginary part of the propagation constant

$$k_{ti} = \frac{1}{r_c} \ln \left[\sqrt{\frac{\pi}{2C_F}} \frac{1}{R_{0m}^{(1)}(C_F, 1)} \right] \tag{3.32}$$

where $R_{0m}^{(1)}(C, 1)$ is the radial wave function in prolate spheroidal coordinates. A table of the spheroidal wave functions can be found in [167]. The results calculated from the above formula are shown in Fig. 3-13 where quadratic fits to the results are also presented. The parameter Λ, is the transverse diffraction loss across the edge of the mirror and is defined as

$$\Lambda = 2k_{ti}L. \tag{3.33}$$

Another technique for the analysis of a confocal waveguide by spectral theory has been discussed by Shestapalov [168]. A comparison of the results from the spectral theory by Shestopalov [168] and the Boyd and Gordon approach [166] are presented in Table 3.1.

We see a good agreement between the results for the real part of the propagation constant, k_{tr} and the difference falls rapidly for $n > 4$ and is less than 0.2% for $n = 5$. However, the Boyd and Gordon [166] approach predicts lower diffraction losses than those presented by Shestopalov [168]. We also computed the diffraction losses for the HE_{06} mode using HFSS and the results were more closer to the results of Boyd and Gordon. The comparison of the results from Boyd and Gordon (Eqn. (3.32)) and Shestopalov [168] are shown in Table 3.1. Our studies based on HFSS simulation results indicate that the Boyd and Gordon formula is accurate and the Shestopalov theory is significantly less accurate.

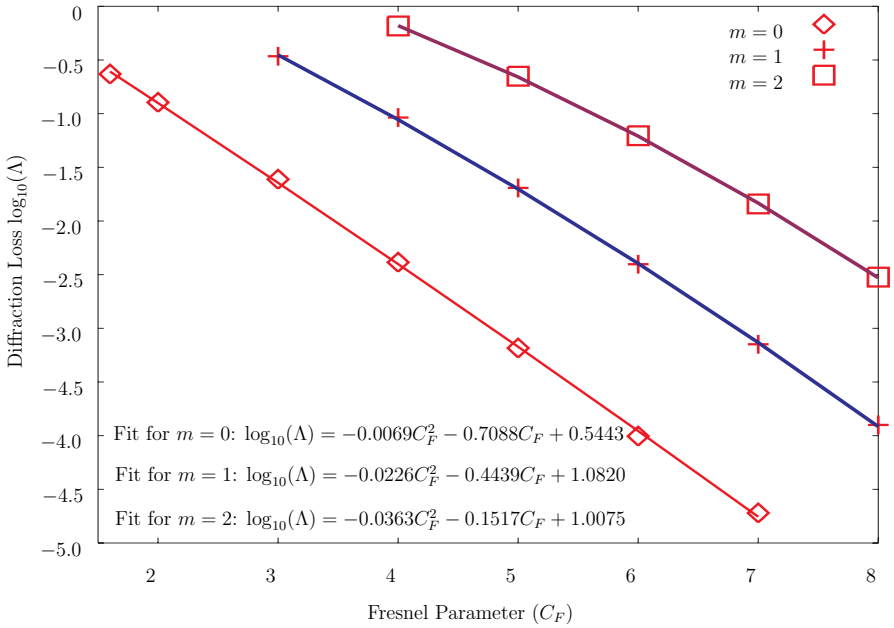

Figure 3-13: Variation of the diffraction losses in a confocal waveguide with the Fresnel parameter.

Mode	Shestopalov[168]	Boyd and Gordon[166]
HE_{02}	$6.9948 + i\ 3.7385 \cdot 10^{-2}$	$7.0686 + i\ 1.5864 \cdot 10^{-2}$
HE_{12}	$8.6431 + i\ 0.2339$	$8.6394 + i\ 2.5976$
HE_{03}	$10.142 + i\ 6.0803 \cdot 10^{-4}$	$10.2102 + i\ 1.8097 \cdot 10^{-3}$
HE_{13}	$11.757 + i\ 4.1188 \cdot 10^{-3}$	$11.7810 + i\ 1.6264 \cdot 10^{-2}$
HE_{04}	$13.294 + i\ 7.9296 \cdot 10^{-4}$	$13.3518 + i\ 1.9649 \cdot 10^{-4}$
HE_{14}	$16.894 + i\ 8.5723 \cdot 10^{-2}$	$14.9223 + i\ 2.2863 \cdot 10^{-3}$
HE_{05}	$16.450 + i\ 5.3688 \cdot 10^{-4}$	$16.4934 + i\ 2.1122 \cdot 10^{-5}$
HE_{15}		$18.064 + i\ 2.7322 \cdot 10^{-4}$
HE_{06}		$19.6350 + i\ 1.9973 \cdot 10^{-6}$
HE_{16}		$21.2058 + i\ 2.7790 \cdot 10^{-5}$

Table 3.1: Comparision of the normalized propagation constant, $r_c\,(k_{tr} + ik_{ti})$ for HE_{mn} modes predicted by Shestopalov [168] and Boyd & Gordon [166].

Field Expressions for a Confocal Waveguide

The scalar eigenfunction Ψ, from which the fields in the waveguide for HE_{0n} can be calculated using Eqns. (2.44 – 2.49) and can be expressed as

$$\Psi = \sqrt{\frac{w_0}{w\left(y\right)}} \exp\left[-\frac{x^2}{2w^2\left(y\right)} - i\frac{k_{tr}x^2}{2R\left(y\right)}\right] f\left(y\right), \tag{3.34}$$

where $w\left(y\right)$ and $R\left(y\right)$ are defined in Eqns. (3.25 – 3.26)and

$$f\left(y\right) = \sin\left(k_{tr}y - \frac{1}{2}\arctan\frac{2y}{r_c}\right), \qquad n = 3, 5, 7... \tag{3.35}$$

$$= \cos\left(k_{tr}y - \frac{1}{2}\arctan\frac{2y}{r_c}\right), \qquad n = 2, 4, 6... \tag{3.36}$$

3.2.3 Design of Mode Selective Confocal Structures

The key to the design of mode selective confocal structures lies in the effective use of diffraction losses to suppress the parasitic modes. In general from Fig. 3-13 it is evident that the modes with $m > 0$ have higher losses than the $m = 0$ modes due to the finite aperture of the mirrors. Typically, the operating mode is chosen based on the constraints on the size of the resonator, the radial location of the field maxima (for coupling to an electron beam) and the tolerable ohmic losses for the operating frequency and power level. The mirror aperture can thus be chosen to be a bare minimum to ensure the highest contrast in the diffraction loss of the operating mode with the neighboring lower order modes (with same m and lower n) and the modes with same n and higher m while limiting the diffraction losses in the operating mode to a manageable level. It is evident that higher order modes (larger n) have a narrower beam radius and hence lower diffraction losses than the operating mode. Typically, competition from higher frequency modes in a waveguide with a sparse mode population does not prove to be a serious problem. This is because of the wider mode separation, the interaction of the operating beam cyclotron harmonic mode with neighboring modes is ruled out and the interaction of any higher waveguide

mode with a higher beam cyclotron harmonic is usually much weaker.

3.3 Discussion

In this chapter we have discussed the theory of two kinds of novel mode selective interaction structures, namely, PBG structures and quasioptical open waveguides (specifically confocal waveguides). While the PBG structures rely on the presence of propagation band gaps in the bulk lattice for discriminating modes with different frequencies, the confocal waveguide relies on diffraction from the open edge of the waveguide to suppress unwanted modes. While PBG structures can confine a higher order mode within a specific band of frequencies (the band gap) while being heavily lossy for other frequencies which fall outside the band gap, the confocal waveguide favors higher order modes and frequencies because the higher order modes (larger n) have a smaller beam radius at the surface of the mirrors than the lower order modes and hence suffer lower diffraction losses. This makes the confocal waveguide suitable for high harmonic cyclotron masers which rely on the interaction of a higher order waveguide mode with a harmonic of the beam cyclotron mode. Such harmonic interaction needs strong suppression of the fundamental interaction with a lower order waveguide or resonator mode. The design of such a second harmonic gyrotron oscillator is described in Chapter 6.

While both kinds of structures provide electromagnetic mode selectivity, their application in VEDs requires consideration of other vital issues such as the symmetry of the fields, the suitability of the placement of an electron beam at the field maxima, thermal capability, ease of fabrication and so forth. The confocal waveguide is much easier to fabricate compared to its PBG counterpart. The simplicity in fabrication yields a big payoff for cooling the structure for high power operation. This is a particularly important requirement for high average power VEDs such as a W-band amplifier whose average power exceeds 10 kW. Another advantage of the confocal waveguide is its mechanical tunability by simply altering the separation of the mirrors, which alters the transverse propagation constant. This feature can be very useful in

building a tunable microwave source or amplifier. The use of quasioptical modes in a confocal waveguide makes it more suitable for the extraction of power from a confocal waveguide or a resonator by quasioptical techniques for the formation of a Gaussian beam for either free space propagation or coupling to the HE_{11} mode of a corrugated waveguide for ultra low loss transmission [169].

PBG structures have some different advantages and drawbacks compared to the confocal waveguide. The fields inside a PBG structure are symmetric (far from the walls in the center of the defect) thus the mode in a cylindrical PBG structure is very similar to that of a conventional cylindrical guide and would couple well to an hollow annular electron beam which is used in most gyrotrons. Since the confocal structures have an asymmetric field profile, the coupling is weaker, furthermore the weakness or the absence of any fields near the aperture reduces the efficiency of energy extraction from the electron beam. PBG structures are equally effective in the confinement of TM modes (electric field along the axis of the rods) as well the TE modes, a property that can be used to build higher order mode conventional slow wave devices such as TWTs which operate in TM modes. Confocal structures are not as effective for controlled diffraction of the TM modes. Another advantage of PBG structures is the possibility of power extraction from the transverse side of the resonator. This property would be a tremendous benefit in millimeter and sub-millimeter wave gyrotrons and has been discussed in Chapter 5.

We close this chapter with the following general comment about the application of PBG and quasioptical structures in VEDs. Quasioptical structures should be preferred for high power operation and frequencies up to 200 GHz in fast-wave devices. Confocal structures have unique advantages if mechanical tuning is a desired option. PBG structures would be more suitable from 30 GHz and above and at low average powers and moderate peak power. PBG structures can be used in both fast and slow wave devices.

Chapter 4

Experimental Setup and Diagnostics

In this chapter we describe the gyrotron test stand and the diagnostics that were used in all the experiments during the course of this work. A dedicated gyrotron test stand with a 6.5 T capable superconducting magnet was available for all the experiments described in this work. The main parts of the test stand and the diagnostic systems are discussed below.

4.1 High Voltage Modulator

The high voltage system used in the experiments is capable of up to 250 kV and 100 A operation in 3 μs pulses at up to 6 Hz repetition rate. The modulator consists of four main parts namely, a 0-30 kV, 0-300 mA constant current DC power supply, a pulse forming network (PFN), a thyratron switch and a step-up transformer. The constant current DC power supply charges up the capacitor banks in the PFN to a particular voltage and then the capacitors banks are discharged through the primary of the high voltage step-up transformer through a thyratron switch. The secondary of the high voltage transformer has a resistive load chain which is usually matched to the impedance of the gun (V_0/I_0). In the case of the present experiment a resistive load of 1225 Ω was connected to the secondary of the transformer. The high voltage

transformer is immersed in an oil bath which serves as an insulator. The cathode voltage is measured by a capacitive-resistive divider installed in the modulator oil tank. The latest calibration of the probe indicated a multiplication factor of 10.836 kV/V.

The body and the collector of the tube is grounded and the required negative potential, typically -60 to - 80 kV in this experiment is applied to the cathode from the secondary of the high voltage transformer. The electron gun used in the present experiments is a triode gun in which the cathode is maintained typically at -70 kV while the first anode is grounded and the second anode, also referred to as the mod anode is maintained at -60 to -55 kV. A higher difference between the cathode and the mod anode increases the velocity pitch factor of the beam by increasing the local transverse electric field at the cathode. Typically a set of resistive taps are provided on the resistive load at the secondary of the high voltage transformer to generate the mod anode voltage as a ratio of the cathode voltage. By changing the position of the taps one can control the mod anode voltage. This scheme is very simple and does not require a second power supply, transformer, PFN and a thyratron switch to generate the mod anode voltage, however it has several disadvantages. The control of the mod anode voltage is coarse due to the finite value of the resistive taps on the load on the transformer. Typically, for the settings in this experiment it is 10 steps of 0.5 % of the cathode voltage in each step. Secondly, the ratio of the cathode to the mod anode voltage is always fixed and this results in very high values of α at lower cathode voltages, which typically happens during the ramp up and ramp down of the voltage pulse. This local value of α is much higher than its quiescent value (used in the design of the interaction structure) at the flat top of the voltage and hence excites spurious oscillations at the start and end of the pulse. The power in the spurious modes show up as 'rabbit ears' sandwiching the design mode oscillation or amplified signal in the output signal. This effect is evident in the amplifier experiment and will be explained in detail in Chapter 7.

We tried to install a second smaller transformer in the same high voltage transformer tank with its own dedicated power supply and a thyratron switch to indepen-

dently control the mod anode voltage. Such a system would allow the fine tuning of the mod anode voltage and independent timing of the mod anode voltage pulse with respect to the cathode voltage pulse to prevent the high α regime during the start and end of the voltage pulse. Though the system worked in principle, there was a lot of interference between the cathode and the mod anode voltage pulses. This was due to the small size of the modulator tank which housed both the transformers close to each other. This system was abandoned and we returned to the old system with fixed taps for generating the mod anode voltage as a ratio of the cathode voltage. In future, it may be worthwhile to have a separate oil tank to house the mod anode step-up transformer to minimize the interference of the cathode and mod anode voltage pulses.

4.2 Superconducting Magnet

A 6.5 Tesla capable superconducting magnet was used in all the experiments conducted as part of this work. The operating magnetic field of about 5.4 T is typically necessary for gyrotron operation at 140 GHz. The magnet has two sets of coils that can be independently charged. The field homogeneity is better than 0.5 % over 5.0 cm and 1 % over 6.5 cm. The ratio of the magnetic field to the current in the coils when both coils are energized serially is 0.07614 Tesla/Ampere. The charging and discharging rate of the magnet is typically limited to below 0.065 Ampere/second.

4.3 Frequency System

A heterodyne receiver system is used as a frequency counter for the gyrotron experiments. A block diagram of the system is shown in Fig. 4-1. It consists of WR6 (110-170 GHz) double ended mixer (Hughes, Model No. 47448H-1002) to mix the incoming high frequency gyrotron signal with a harmonic of the tunable Local Oscillator (LO) signal. The LO in our set up is an 8-18 GHz YIG oscillator whose frequency can be counted with a precision of up to a few Hz using a microwave fre-

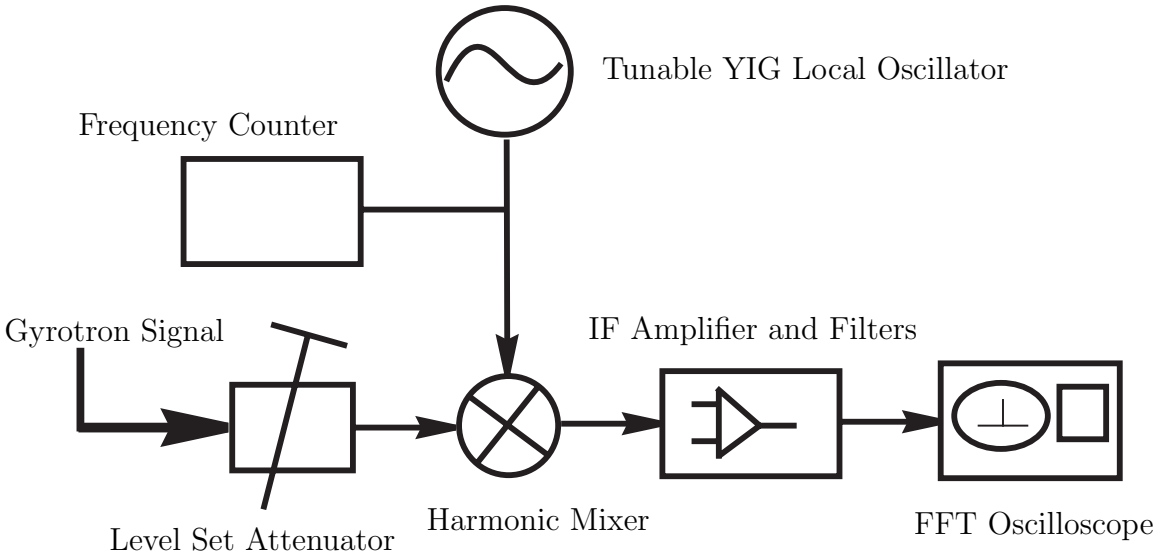

Figure 4-1: Block diagram of the frequency measurement system used in the experiments.

quency counter. The mixer output is filtered and amplified by a chain of filters and low noise solid-state amplifiers in the 0-500 MHz IF band. A Fast Fourier Transform (FFT) capable oscilloscope (Textronix DS400, 500 MHz bandwidth) is used to compute in real time the FFT of the IF signal. The local oscillator frequency is tuned such that one of its harmonic produces a baseband signal in the 0-500 MHz IF range. The peak in the IF signal is detected in real time by the FFT and the LO is tuned such that the peak lines up at 300 MHz. Such a case would correspond to

$$f_{gyro} = n f_{LO} \pm 0.3 \text{ GHz}, \tag{4.1}$$

where f_{gyro} is the unknown gyrotron frequency in GHz, f_{LO} is the known LO frequency in GHz and n is the unknown harmonic number. The ambiguity in the measurement of the gyrotron frequency due to n can be removed by choosing two LO frequencies such that

$$f_{gyro} = n f_{LO_{lower}} + 0.3 \text{ GHz}, \tag{4.2}$$

and

$$f_{gyro} = n f_{LO_{upper}} - 0.3 \text{ GHz}. \tag{4.3}$$

Now n can be uniquely determined by taking the difference of the above two equations to get

$$n = \frac{0.6}{f_{LO_{upper}} - f_{LO_{lower}}}. \tag{4.4}$$

Typically, in the present experiments $n = 10$ harmonic was used for measuring frequencies around 140 GHz. The use of higher harmonics enables the measurement of very high frequencies, however, the mixer signal amplitude falls rather dramatically for $n > 18$. Using this system frequencies up to 300 GHz have been measured in other experiments at MIT. This system can also be used for detecting very weak emission in parasitic modes which cannot be detected by a calorimeter or a video detector. The system is also very useful during measurement of the start oscillation current of various gyrotron modes.

4.4 Calorimeters

Dry calorimetry was employed during the course of the experiments described in this work to measure the output power. The biggest advantage of using dry calorimeters is their simplicity and quick response time. A number of such dry calorimeters which were originally meant for measuring the power of optical lasers were modified at MIT to suit the power measurement at millimeter wave frequencies. A detailed description of this technique is presented in [47]. In this section we outline the method used to modify one of the existing 10 cm diameter calorimeter by Kreischer et al. [47]. Also, the procedure and the results of the modification of another calorimeter during the course of this work will be described.

Power measurements are usually performed by keeping the calorimeter at least 5 cm from the window and inclining it an angle to prevent the reflected power from reentering the gyrotron experiment. A WR8 (90-140 GHz) or a WR6 (110-170 GHz) video detector diode is used to monitor the reflected signal to test the integrity of the

mode and its pulse shape is used to determine the peak power. The calorimeter was usually placed as far away from the window as possible to minimize the reflected power from directly entering the gyrotron while ensuring that all the power is collected by the calorimeter. In the course of experiments in this work the distance was never greater than 8-10 cm. Furthermore, a box made of Echosorb (microwave absorber from Emerson Cummings Inc.) was used to cover the calorimeter to prevent the air drafts from interfering with the readings. The Echosorb box also minimizes stray reflections from the gyrotron tube. The power recorded by the calorimeter is corrected for the finite amount of reflection from the surface of the calorimeter. The determination of the reflection coefficient is described below for two different calorimeters.

4.4.1 Analog, Scientech Inc., Calorimeter

A Scientech Inc., Model 36-0401 (Serial No. 477) calorimeter was modified by Kreischer et al. [47] at MIT for use in the 140 GHz gyrotron experiments. The original calorimeter consists of a 10 cm diameter aluminum plate painted with an absorbing layer of 3M Nextel paint calibrated at 1094 nm. The aluminum plate has several thermoelectric elements attached underneath the absorbing surface which determine the temperature rise. The power absorbed is determined from an analog meter connected to the thermocouple array. The original absorbing layer is quite reflective at 140 GHz and reflects power back into the gyrotron and alters the operation of the gyrotron. So the calorimeter was modified by Kreischer et al. [47] by applying a uniform layer of 3M Nextel paint approximately 0.3 mm thick. They measured an absorption of 85 % at 140 GHz by this method. It was pointed out that applying an additional 0.3 mm thick layer of 3M Nextel paint significantly improved the absorption at 140 GHz ($\lambda = 2.14$ mm). The application of too thick a layer of paint while increasing the absorption slows down the response time of the calorimeter. A variety of tests were done to calibrate the calorimeter and check the accuracy of the measurements. This included using the resistive heater at the backend of the calorimeter to check its calibration by applying a known amount of power on the plate. A second test was performed by using a calibrated 10 μ laser to measure the uniformity of absorption

across the surface of the calorimeter and it was determined that the uniformity of absorption was better than 1 %. A dispersive Fourier transform spectrometer was used to measure the dependence of the absorption on frequency and it was found that the reflectivity was less than 15 % in the 130–180 GHz range. The same measurement was also performed with a 10 mW IMPATT diode source available at MIT in the range of 135–143 GHz.

4.4.2 Digital, Scientech Inc., Calorimeter

A new calorimeter Scientech Inc., Model 36-0401 (Serial No. 5085) with an Interface Module 10748 (Serial No. 1037) and a digital indicator S310D (Serial No. 1412) was acquired during the course of this work and modified. Since Nextel 3M paint is no longer available, Krylon Ultra-Flat Black paint was used as a substitute and was found to be as good as the Nextel paint. About 15 coats were applied slowly to bring down the reflection coefficient to about 16 % at 139 GHz, without slowing the response of the calorimeter. The reflection from the calorimeter was measured by checking the strength of the signal reflected from the calorimeter against the reflection from a flat aluminum plate by using a WR8 video detector. The power reading from this calorimeter agreed very well with the analog calorimeter described in the previous section. The uniformity of absorption at 9 points on a 3×3 array on the absorbing face of the calorimeter was measured by directing the power ($\sim$ 100 W) from a 140 GHz Extended Interaction Klystron (EIK) by a small horn onto the specific regions. The uniformity of absorption was found to be better than 4 %. The change in reflection coefficient and absorption with frequency was not measured.

4.5 Beam Velocity Pitch Probe

In gyrotrons the transverse energy in the electron beam resides in the form of the gyrating of the electrons around the axial magnetic field. The beam also has longitudinal energy which allows it to drift through the interaction structure however, it is the transverse energy that is extracted in the CRM interaction. Hence, it is vital

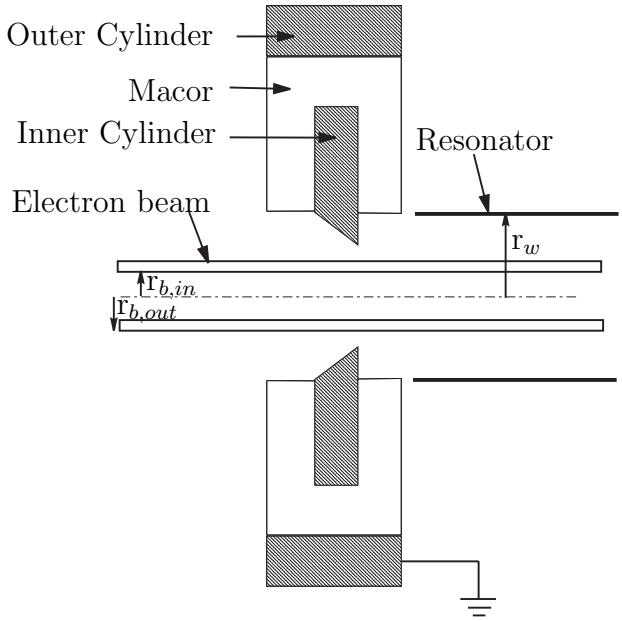

Figure 4-2: Longitudinal cross-section of the probe for measuring the beam velocity pitch factor, α.

to know the amount of transverse energy in the beam. The ratio of the transverse to longitudinal velocity is called the beam velocity pitch factor, $\alpha\,(= v_t/v_z)$. The total energy of the beam can be directly found by the applied accelerating voltage, V_0. Using a capacitive probe around the beam one can estimate the axial energy in the beam and as a result infer the transverse energy and estimate the pitch factor, α. This technique is described in [170]. A cross-section of the capacitive probe used in the present experiments is shown in Fig. 4-2. The inner and outer cylindrical electrodes are separated by a piece ring of Macor, a machinable ceramic. We briefly outline the theory of the probe for the case of the inner electrode being flat rather than tapered. The electrode is tapered in the experiment to prevent it from acting like a resonator which increases the susceptibility of the beam to parasitic oscillations. The probe is usually located just before the interaction structure to measure the α value. The principle of operation of the probe is rather straightforward. The drifting electron beam induces a potential on the inner electrode due to the radial electric field in the electron beam. For a beam with a constant axial charge density using Gauss's law

one can easily show the induced potential on the inner electrode (probe) to be

$$V_{probe} = \frac{e\lambda_e}{2\pi\varepsilon_0} \ln\left(\frac{r_b}{r_{probe}}\right) = \frac{e\lambda_e}{C_{probe}}, \tag{4.5}$$

where, λ_e is the electron density per unit length, r_b and r_{probe} are radii of the electron beam and the inner electrode respectively, and C_{probe} is defined to be the capacitance of the probe. Relating the beam current to the electron density per unit length and the average longitudinal beam velocity as

$$I_0 = e\lambda_e \langle v_z \rangle , \tag{4.6}$$

one may obtain the average longitudinal velocity $\langle v_z \rangle$ as

$$\langle v_z \rangle = \frac{I_0}{V_i C_{probe}}. \tag{4.7}$$

Once $\langle v_z \rangle$ is determined one may calculate the voltage depression in electron beam due to space charge as [171]

$$V_{dep} = \frac{1}{4\pi\varepsilon_0} \frac{I_0}{\langle v_z \rangle} \left[2\ln\left(\frac{r_w}{r_{b,out}}\right) + \left\{ 1 - \frac{2r_{b,in}^2}{\Delta r_b \left(r_{b,out} + r_{b,in}\right)} \right\} \ln\left(\frac{r_{b,out}}{r_{b,in}}\right) \right], \tag{4.8}$$

where $r_{b,in}$, $r_{b,out}$, $\Delta r_b \left(= r_{b,out} - r_{b,in}\right)$ are the inner, outer and the thickness of the electron beam, respectively, and r_w is the radius of the wall of the resonator. Now, the value of the beam velocity pitch factor can be calculated in the following steps

$$\gamma = 1 + \frac{e\left(V_0 - V_{dep}\right)}{m_{e0}c^2}, \tag{4.9}$$

$$v_t = c\sqrt{1 - \frac{1}{\gamma^2} - \left(\frac{v_z}{c}\right)^2}, \tag{4.10}$$

$$\alpha = \frac{v_t}{v_z}. \tag{4.11}$$

The geometry of the actual probe in the experiment is different from the one assumed in this simple analysis and hence even though it is possible to find an analytic expression for the value of C_{probe} it is usually easier and more accurate to measure its value in-situ. This is done by recording the voltage induced at the probe when almost all of the energy in the electron beam is in the longitudinal direction. Such a scenario is possible when the voltage on the second anode in the gun, also called the mod anode is very low (reduces transverse electric field at the cathode) and the magnetic field at the cathode is very high (reduces beam compression and hence α). One can record the voltage induced on the probe for a given beam current under conditions of $\alpha \approx 0$ and thus determine the constant C_{probe} and calibrate the probe.

This method of measurement of the beam velocity pitch factor, α is very reliable and yields results consistent with EGUN simulations. After extensive studies on the α probe in [170] it was pointed out that in addition to the calibration uncertainty, error in beam voltage and current measurements, the total error in the measurement of α is about 10% for $\alpha \geq 2$ and increases to about 20% for $\alpha = 1$.

Chapter 5

Photonic Band Gap Gyrotron Oscillator

In the previous chapter we discussed the challenges of building millimeter and submillimeter wave VEDs due to the rapid miniaturization of the circuit dimensions with the operating wavelength. Fundamental mode operation, where the transverse dimensions of the resonator are smaller than the wavelength is well suited below 30 GHz, however for higher frequency (>100 GHz) devices operation in fundamental mode is inevitably ruled out due to the following reasons. The ohmic losses due to the finite conductivity of the walls of the interaction structure become much more severe and issues such as surface roughness which could be ignored at microwave frequencies (< 30 GHz) need to be considered in the design. Furthermore, the small size of the interaction structure reduces its thermal capability and restricts the amount of electron beam current that can be safely transmitted through the circuit. All these factors dramatically reduce the power capability of these devices with increasing frequency in the millimeter wave regime and beyond.

Migration to a higher operating mode allows the dimensions of the circuit to be much larger than the operating wavelength but brings forth the problem of severe mode competition. The pitfalls of mode competition in gyrotrons are well catalogued [172]–[175] and prove to be a major hurdle for embracing higher order mode interaction structures in gyrotron amplifiers. In this chapter we report on the theory and

experiments on a promising novel approach to overcome the problem of mode competition in overmoded structures by the use of Photonic Band Gap (PBG) resonators. A PBG structure, is a periodic array of varying dielectric or metallic structures, was first described by Yablonovitch et al. [148]. A detailed discussion of PBG structures and the design methodology for overmoded yet mode-selective PBG resonators was presented in Chapter 3.

Gyrotron oscillators and amplifiers have made great progress in recent years [15]. Impressive results for gyrotron amplifiers have been obtained in the TE_{11} fundamental mode of circular waveguide [77], [83] at 35 GHz, where mode competition and conversion are absent. These excellent results cannot be extended to higher frequencies (>100 GHz) because the waveguide structure would be too small. Advanced research on a high power W-band gyroklystron amplifier has been successfully carried out in a slightly overmoded structure with the TE_{01} mode – the third TE mode of a cylindrical waveguide [19] at 94 GHz. The proof-of-principle PBG gyrotron oscillator experiment, the subject of this chapter differs from the gyroklystron results in that it uses a highly overmoded structure and demonstrates operation in a very high order mode (TE_{04} – the 30^{th} TE mode supported by a cylindrical waveguide) without mode competition. In gyrotron oscillators, successful operation can be achieved in overmoded cavities if careful techniques of resonator design are used together with placement of the electron beam at the optimum radius for the desired mode. However, at very high frequency, mode competition is still a major issue for gyrotron oscillators [172]–[175]. For devices in which mode competition is a limiting factor, the PBG cavity will be advantageous, especially at moderate power levels. The reduced mode competition observed in the present experiments and described below represents a clear and dramatic improvement over earlier results with a conventional cylindrical resonator. To our knowledge, the present results are the first use of a PBG cavity in an active high power microwave/millimeter wave device.

In this chapter we present the design of a 140 GHz proof-of-principle PBG gyrotron oscillator and the experimental results. After a brief outline of the operating principle of a gyrotron oscillator in Sec. 5.1, the detailed design of the resonator is presented

in Sec. 5.2 and is followed by the design of the gyrotron oscillator in Sec. 5.3. The details of the experimental setup and the diagnostics are presented in Sec. 5.4 which will be followed by conclusions and future prospects of PBG interaction structure based VEDs.

5.1 Operating Principle of a Gyrotron Oscillator

The electromagnetic radiation in a gyrotron is produced by the interaction of a mildly relativistic gyrating electron beam and TE wave close to cut-off in a cavity resonator. The oscillation frequency ω, of a TE_{mnq} mode of a cylindrical cavity of length L and radius r_0 is given by

$$\omega^2/c^2 = k^2 = k_\perp^2 + k_z^2, \tag{5.1}$$

where, $k_\perp$ $(= \nu_{mn}/r_0)$ and k_z $(= q\pi/L \ll k_\perp)$ are the transverse and longitudinal propagation constants of the TE_{mnq} wave, k is the free space propagation constant, c is the speed of light, ν_{mn} is the n^{th} root of $J_m^{'}(x) = 0$ and q is an integer. The resonance condition for the excitation of the cyclotron resonance maser (CRM) instability is satisfied when ω and k_z in Eqn. (5.1) satisfy the beam mode dispersion relation

$$\omega - k_z \beta_{z0} c \gtrsim s\Omega/\gamma, \tag{5.2}$$

where, Ω $(= eB_0/m_{e0})$ is the cyclotron frequency, $\gamma = \left(1 - \beta_{z0}^2 - \beta_{\perp 0}^2\right)^{-1/2}$ is the relativistic mass factor, $\beta_{\perp 0}$ and β_{z0} are respectively, the transverse and longitudinal velocities of the electrons normalized to the velocity of light, m_{e0} is the rest mass of an electron, e is the charge of an electron, s is the cyclotron harmonic number ($s = 1$ in this experiment) and B_0 is the magnitude of the static axial magnetic field. The beam parameters, the resonator dimensions and an optimum detuning of the magnetic field can be determined from the procedure outlined in [102]–[104] to optimize the interaction efficiency. The choice of the operating mode is dictated by the ohmic heat capacity of the resonator walls and the window for stable single-mode excitation at a high interaction efficiency. It is often noticed in gyrotrons that while optimizing

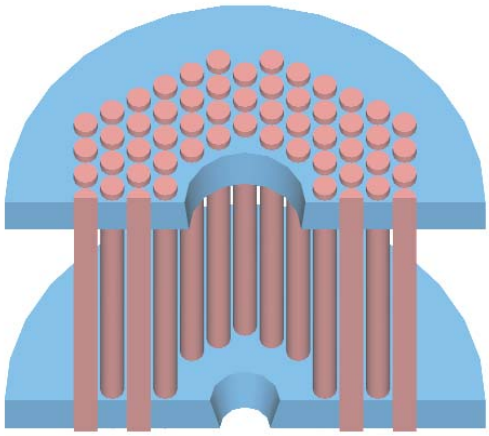

Figure 5-1: A section of the CAD drawing of the PBG resonator used in the gyrotron experiment. The small aperture on the lower end plate forms the input cutoff section and the bigger hole on the upper end plate is used to extract the radiation from the resonator.

the detuning of the magnetic field to increase the interaction efficiency of the design operating mode, the device slips into a different mode if the excitation conditions for the latter mode are satisfied. This mode hopping in a high mode density resonator can prevent the access to the high efficiency operating regime of the design mode, but with the use of a properly chosen start-up scenario, it can be avoided [173], [174].

In the present research, we have chosen to demonstrate the PBG gyrotron as a 140 GHz oscillator because of the availability of equipment in our laboratory. The present experiment is modeled on a previous device that was studied at MIT, a 140 GHz conventional cavity gyrotron oscillator operating in the TE_{031} mode [47].

5.2 Design of the PBG Resonator

The aim of the present experiments is to design build and test a PBG resonator for application in gyrotrons, which while operating in a higher order TE mode is still mode-selective or less susceptible to parasitic oscillations at the other competing modes. Traditional gyrotron cavities are cylindrical copper resonators with a downtaper to the cut-off radius at the entrance for mode confinement and an uptaper at the

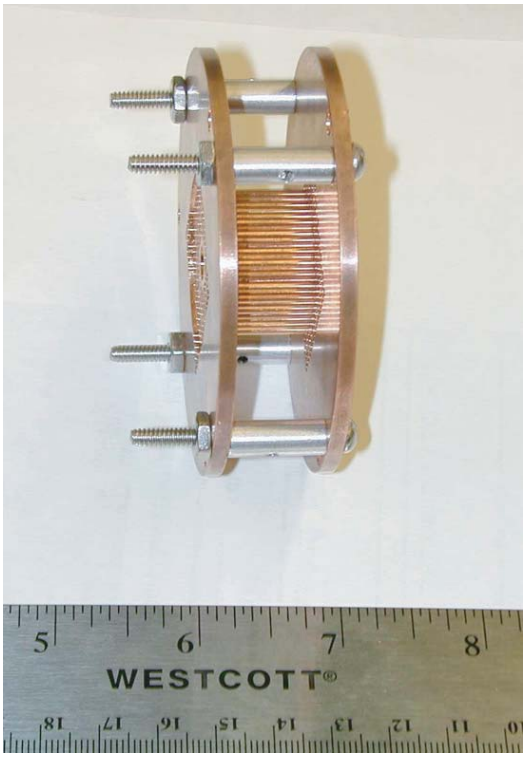

Figure 5-2: PBG resonator used in the gyrotron experiment. The small aperture on the left end plate forms the input cutoff section is barely visible in the picture.

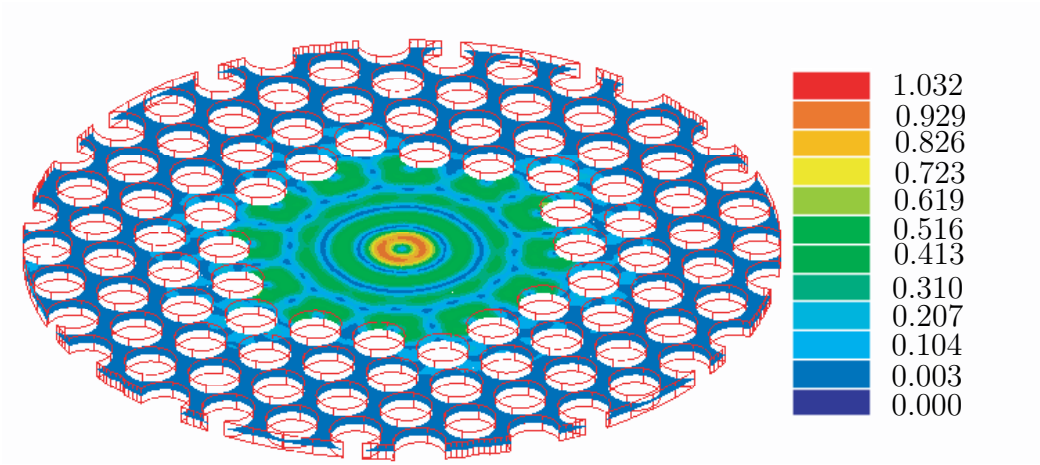

Figure 5-3: The TE_{040} eigenmode of the PBG resonator at 139.97 GHz. The magnitude of the electric field is shown and the simulations were performed on HFSS.

exit for output coupling [46]. A longitudinal section of the PBG resonator is shown in Fig. 5-1. In the present experiments the cylindrical outer copper wall is replaced with a PBG structure comprised of a triangular lattice of metal rods. These rods are placed parallel to one another and parallel to the axis of the gyrotron and magnetic field system. Two OFHC copper plates with an array of holes maintain the rods in position and form the end plates of a PBG gyrotron resonator as shown in Fig. 5-2. A number of rods are omitted from the center of the array to support a mode. The basic design methodology has already been described in detail in Section 3.1.3. A high order TE-like waveguide mode can exist in hole (defect) left by the vacant rods if its resonant frequency lies in the band gap or the stopband of the PBG structure. The band gap can be adjusted such that the resonant frequencies of all other neighboring modes lie in the passband of the lattice and hence can leak through the array that acts like a transparent wall at those frequencies. Radiation that passes through the array propagates out and is not reflected back into the lattice permitting a strong single mode operation in the design mode. 102 copper rods of radius $r = 0.794$ mm are held in a triangular array with the lattice vector $a = 2.03$ mm to form the PBG structure Fig. 5-1. Initial lattice dimensions were chosen using a quasistatic analytic theory (valid for $r/a \ll 1$) and simulations in SUPERFISH [161]; subsequently simulations using HFSS [91] (High Frequency Structure Simulator, Ansoft Corp.) helped refine these dimensions. The triangular lattice was chosen over the square lattice because the defect in a triangular lattice is more azimuthally symmetric than that in a square lattice. After the development of the PBGSS code [90], the operating point of the design corresponding to $a = 2.03$ mm, $r = 0.794$ mm, $r/a = 0.391$, and $\omega a/c = 5.952$ was indeed found to lie right in the first band gap of the TE modes in a triangular lattice. This point is shown as a $\bullet$ in Fig. 3-8(a). It is worth mentioning that the r/a ratio could have been further reduced to reduce the band gap around the operating mode, however, the availability of standard size copper rods at $r = 0.794$ mm was a strong reason for the design in a slightly wider band gap. A cross-section of the HFSS model of the PBG gyrotron cavity is shown in Fig. 5-3. In the figure, an empty circle designates the location of the rods since no electric field can exist at that location.

The array can hold 121 rods but the 19 innermost rods have been omitted to form the cavity resonator. The frequency of the confined eigenmode shown in the model Fig. 5-3 is 139.97 GHz in the TE_{040} mode. The two end plates were modeled as 'H Walls' in HFSS simulations which works well for TE modes and simulates the TE_{040} mode without a longitudinal variation in the amplitude of the electric field. This technique enables us to solve the 3D problem in HFSS within a reasonable time and limited memory resources of the computer by choosing a very short longitudinal length of the resonator which in this case was one quarter of the operating wavelength (2.14 mm) at 140 GHz. However, the gyrotron operates in a TE_{041} mode where the axial length of the resonator is about 8 operating wavelengths as described in the next section.

The reduction in mode density in the PBG resonator can be compared to an analogous cylindrical resonator by examining the density and the Quality factor of the modes in the neighborhood of the operating mode in both resonators. This is shown in Table 5.1 where we assume that there is no longitudinal variation in the mode (TE_{mn0}) mode because of the astronomical computation time and memory requirements to compute the longitudinal variation of the mode in such a large size overmoded resonator. This method used for convenience should not affect the results in case of a TE_{mn1} mode. In case of the cylindrical resonator the only loss is due to the finite conductivity of the wall, however in case of the PBG resonator the loss includes the ohmic effects over the surfaces of all the rods in the resonator and the final outer wall chosen as the boundary in HFSS. In the actual experiment as described later, there is no outer wall and hence the values of Q presented here are expected to be higher.

Cyl. Res. Mode	**Frequency (GHz)**	**Ohmic Q**	**PBG Res. Mode**	**Frequency (GHz)**	**Q**
$TE_{0,3,0}$	**106.488**	**15927**	**TE_{030}** like	110.158	**4063**
$TE_{5,2,0}$	**110.114**	**12537**			
$TE_{9,1,0}$	112.119	4805	The weakly confined modes		
$TE_{3,3,0}$	**118.760**	**15644**	with a poor azimuthal		
$TE_{1,4,0}$	**122.529**	**15090**	symmetry are unlikely		
$TE_{6,2,0}$	**122.832**	**12634**	to couple to the electron beam.		
$TE_{10,1,0}$	123.209	4767			
$TE_{4,3,0}$	**132.744**	**16014**	The Q factors of all the		
$TE_{11,1,0}$	134.258	4731	unconfined modes and		
$TE_{7,2,0}$	**135.362**	**12696**	bulk modes is less than 9000.		
$TE_{2,4,0}$	**137.857**	**17704**			
$TE_{0,4,0}$	**139.462**	**18227**	**$TE_{0,4,0}$**	**139.462**	**13537**
$TE_{12,1,0}$	140.039	3571			
$TE_{5,3,0}$	**146.407**	**16289**			
$TE_{8,2,0}$	147.751	12735			
$TE_{3,4,0}$	**152.673**	**18264**			

Table 5.1: Comparision of the mode density in the PBG gyrotron resonator to an analogous cylindrical resonator. The operating mode is a TE_{041} mode with a transverse field profile similar to the TE_{041} mode. The modes shown in bold have a stronger coupling coefficient to the electron beam and are more likely to be excited than the other modes.

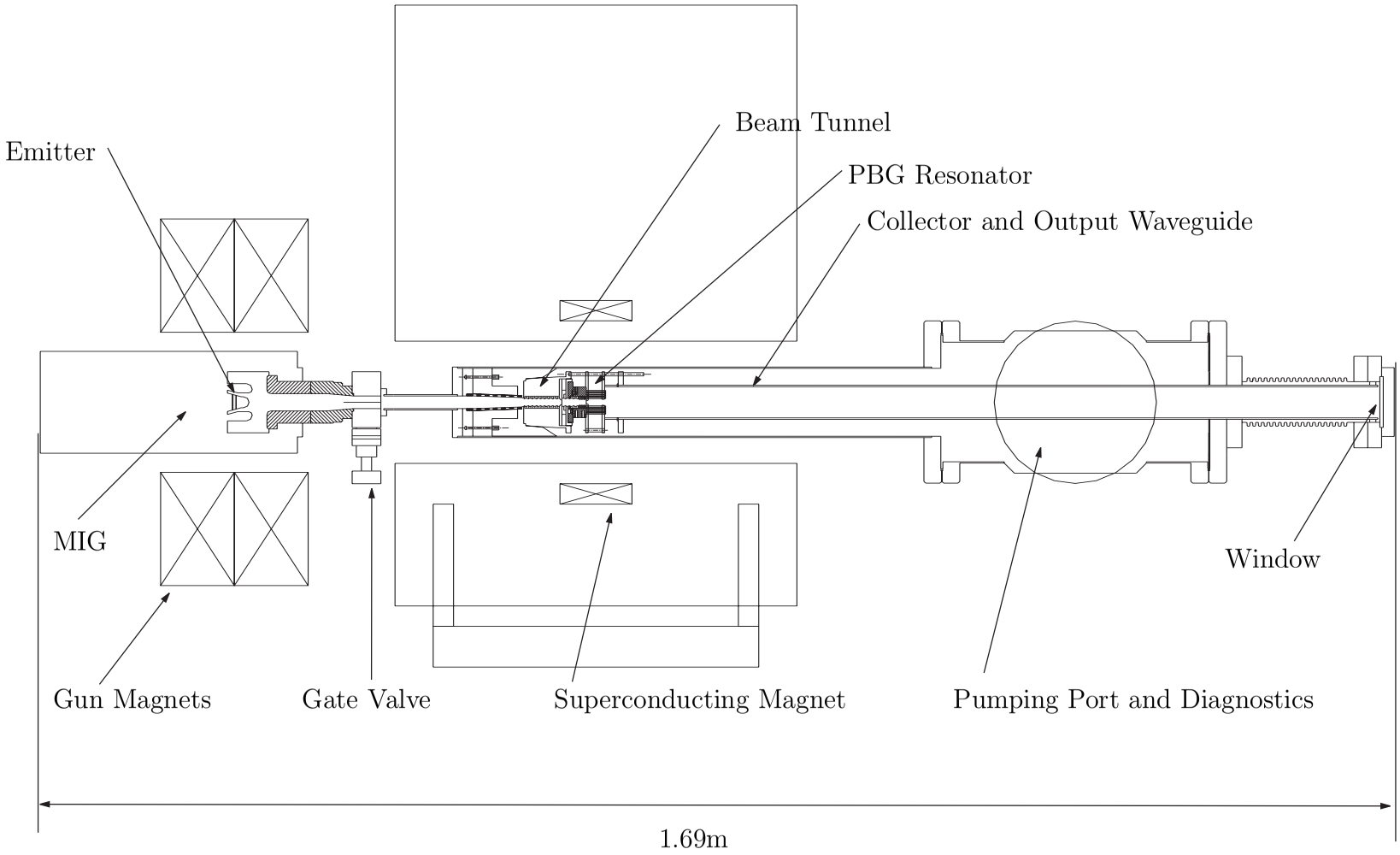

Figure 5-4: Setup of the PBG gyrotron experiment. The vacion pumps and other diagnostic features are not shown.

5.3 Design of the Gyrotron

The electron beam parameters for the experiment were chosen based on a readily available triode magnetron injection gun, VUW-8140 [181] at MIT. The nominal operating voltage is 68 kV at a current of 5 A, with a beam velocity pitch factor ($\alpha = \beta_{\perp 0}/\beta_{z0}$) equal to 1.2. The pitch factor α, can be varied from 0.5 to 1.9 by varying the modulating anode voltage or the magnetic field at the cathode. A moderate velocity pitch factor ($\alpha \sim 1.2$) was chosen to keep the velocity spread in the beam below 6 % and to prevent overbunching of the beam. The radius of the hollow electron beam is 1.82 mm which is the correct radius to excite the TE_{04} -like mode at its second radial maximum. The length of the cavity was chosen to be 8 wavelengths (2.14 mm) of the operating frequency (140 GHz) in order to optimize the efficiency.

A hollow annular electron beam from the VUW8140 MIG was guided through the PBG resonator immersed in a 5.4 Tesla magnetic field provided by a superconducting magnet. A schematic of the experimental setup is shown in Fig. 5-4 on page 118. The electron beam traversed the PBG cavity along its axis passing through the holes in the end plates. The spent electron beam emerging from the cavity after interaction was collected by a steel pipe which also served as a waveguide to transport the electromagnetic radiation from the cavity to the window of the gyrotron.

5.4 Experimental Results

In order to test the PBG gyrotron oscillator for mode selectivity, the device was operated at 68 kV, 5 A over the magnetic field range of 4.1 to 5.8 T to permit beam transmission without significant reflection or interception over the whole range. It is evident from Eqn. (5.2), that this range in magnetic field tuning corresponds to an equal range in the frequency space of about 30 %.

In Fig. 5-5 the experimentally measured start oscillation current of the design TE_{041} mode with varying magnetic field is compared with the theoretical results from a linear theory of a cylindrical resonator gyrotron [104]. This comparison is expected

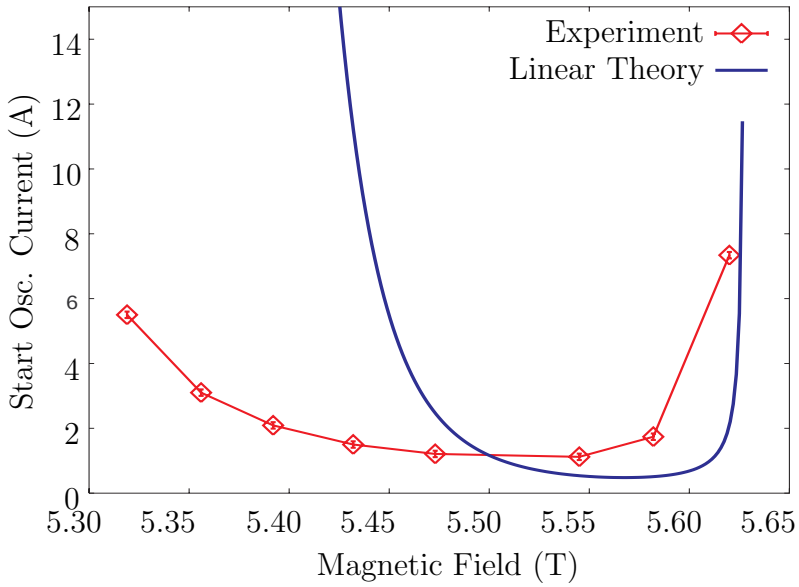

Figure 5-5: Experimentally measured start oscillation characteristics of the PBG gyrotron oscllliator compared to the results from a linear theory for an analogous cylindrical resonator. The oscillation frequency is 140.05 GHz in a TE_{041} mode with the beam parameters: 65 kV, $\alpha = 1.2$ and $Q_{total} = 8000$.

to work very well because at the design mode the PBG resonator should act about the same as a conventional cylindrical resonator. The experimentally measured start oscillation curve is wider than the theoretically predicted value and this can be explained as follows. In the theoretical model we assumed a Gaussian shaped axial field profile in the resonator. The Gaussian profile is a good approximation in traditional cylindrical gyrotron resonators with an output uptaper however, in our PBG resonator the ends of the resonator are abruptly terminated with copper endplates which may deviate the axial field profile from a Gaussian shape. The dependence of the shape of the start oscillation current with a sinusoidal and a Gaussian field profile has been studied in [103] for a cylindrical resonator gyrotron. The start oscillation curve when the axial field profile is assumed to have a sinusoidal shape is wider than the case when a Gaussian like field profile is assumed. Also, in the case of a sinusoidal field profile the start current curve is shifted slightly to the left than in the case of a Gaussian field profile. The experimental results from the PBG gyrotron indicate that the axial field profile in the resonator is different from the Gaussian field profile

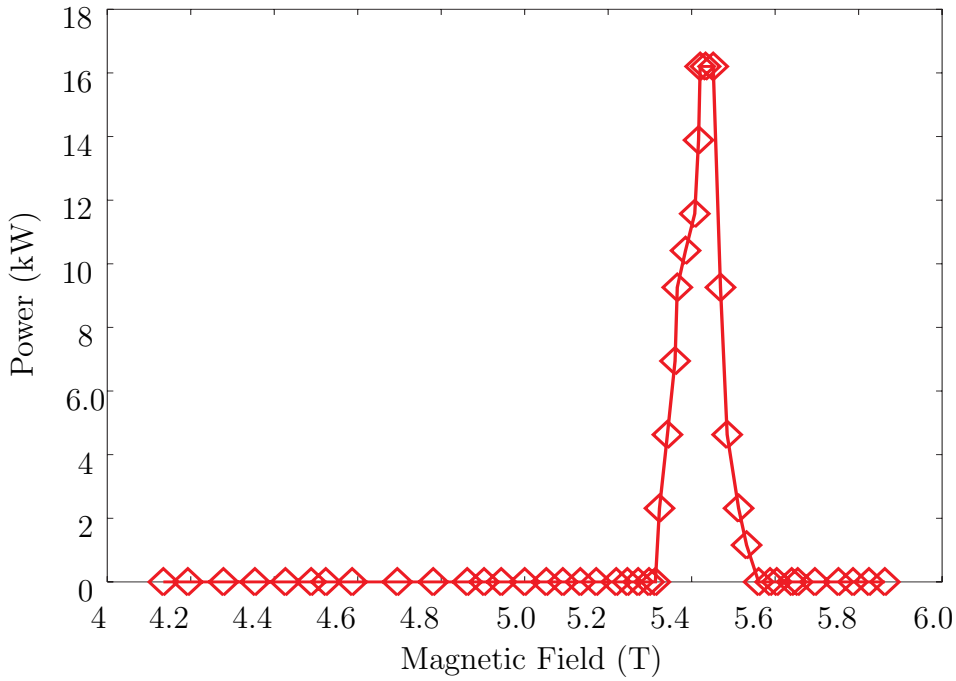

Figure 5-6: The variation of output power of the gyrotron with the main magnetic field. The radiation frequency is 140.05 GHz in a TE_{041}-like mode.

assumed in the linear theory based calculations. The difference in the value of the minimum start oscillation current can be explained by the uncertainty in the measurement of the velocity pitch factor, α. The start oscillation current increases with a decrease in α. The value of α was determined from theoretical simulations using the EGUN code [140]. The beam α can be measured by a capacitive probe but this was not installed in the present experiment. The details of the α probe are discussed in Sec. 4.5. Previous experience at MIT shows that the measured value of α is usually less than the theoretically predicted value from EGUN. This may also explain the widening of the start oscillation current graph.

The variation of output power with the magnetic field, the most vital indicator of the mode selectivity of the resonator, is shown in Fig. 5-6. The mode with an operating frequency of 140.05 GHz is the only strong mode emanating from the gyrotron. This result is direct confirmation of the mode selectivity of the PBG resonator. A conventional cylindrical resonator operating in the TE_{041} mode over the same range of magnetic field tuning of 30 % as in this experiment, would face strong competition

from at least 7 other modes. One of those competing modes, the TE_{241} mode, which is nearly degenerate with the TE_{041} mode and severely reduces its operating range and efficiency [175] is absent in the PBG structure. For the PBG resonator of length 10.54 mm used in this experiment the theoretical resonant frequency is 140.186 GHz. The experimentally measured frequency of 140.05 GHz differs from the theoretical design value by 0.1%, which is very good considering the tolerances in the rod radius and the machining tolerance of the lattice holes on the end plates. The maximum power recorded in the design mode for the operating voltage and current used for the magnetic field scan is about 16 kW. Operation at a different voltage and current produced up to 25 kW at an efficiency of 7 %.

The power in the operating mode was measured by the analog Scientech Inc. calorimeter described in Chapter 4. The frequency was measured by a heterodyne receiver system also described in Chapter 4 with a harmonic mixer and filters. At magnetic field values away from the high power operating mode, the gyrotron oscillator has very weak emission in other modes. The presence of the these modes was detected using either a WR-8 video diode detector or a heterodyne receiver system. The video diode could detect signals with power as low as 1 W, which is 44 dB down from the main signal. The calibrated diode measurements confirmed that the power in the points shown as 0 kW in Fig. 5-6 was everywhere less than 100 W, which is at least 22 dB below the main mode and represents an efficiency of less than 0.03%. These weak spurious modes may be generated in the output waveguide structure of the gyrotron. Detailed investigation of the nature of these modes was not conducted in the present experiment.

For convenience, in these first experiments, we have used a flat plate with a hole for output coupling as shown in Figs. 5-1 and 5-2. HFSS simulations predict an ohmic Q factor of about 13,500 and a diffractive Q factor of about 16,000 for this PBG cavity; these Q factors were not measured in cold test. The diffractive Q at the iris created by the output coupling hole and the finite width of the end plate was modeled in HFSS and another cold resonator analysis code to estimate the diffractive Q. The theoretical ohmic Q factor is comparable to that of an equivalent cylindrical

resonator. The value of the estimated diffraction and ohmic Q factors implies that more than half of the generated power is dissipated as ohmic heat on the walls of the resonator leading to a reduced efficiency of the device. In the future, we plan to test PBG cavities with optimized output coupling including transverse coupling to reduce the diffraction Q factor. The concept of transverse coupling was explained in Sec. 3.1.3. We have previously studied transverse coupling in a test structure at 17 GHz and obtained excellent results coupling into and out of a PBG structure [158]. For the operating parameters chosen in the experiment and the ratio of the diffractive Q to the ohmic Q, the experimentally observed efficiency agrees well with the predictions from a nonlinear theory [102]– [104].

5.5 Discussion

The successful demonstration of the first high power high frequency active millimeter wave device using a PBG interaction structure to suppress mode competition opens up a whole new world of possibilities in the design of VEDs. The basic philosophy of migration to an overmoded circuit without being severely constrained by mode competition is a very general principle and can be applied across the board for a wide variety of VEDs. The present experiment has already demonstrated the case of fast wave CRM devices such as the gyrotron however, many interesting applications in conventional slow-wave devices can benefit from this technique. The application of PBG structures to slow-wave devices will be elaborated later in Chapter 8.

The choice of metallic PBG structures was based on their ruggedness and good thermal properties compared to their dielectric counterparts. Furthermore, fast wave devices such as gyrotrons operate in TE modes which makes the metal PBG structures very suitable. It is evident in Fig. 3-8(a) that for TE modes there is no zero order band gap and hence if the operating mode is localized in the defect the modes with a lower frequency, which are usually the most dangerous are not confined due to transparency of the lattice at those frequencies. Indeed the higher order modes up to twice the frequency of the defect mode are also not confined. We see a second order band

gap for a triangular lattice PBG structure in Fig. 3-8(a), which may confine a mode that may interact with the next higher beam harmonic but usually higher harmonic interactions are much weaker than the lower order mode interactions. Other kinds of PBG structures with different lattice shapes such as a honeycomb lattice can also be used based on the kind of band structure desired to suppress unwanted modes.

PBG structures are expected to degrade gracefully compared to conventional single wall structures due to the distributed boundary. Also the lapse in symmetry of the defect due to the shape of the lattice adversely affects the symmetry of the weakly confined modes thus reducing their coupling coefficient to the cylindrical electron beam. The design mode which is usually a higher order mode has most of its fields farther away from the lattice than the weakly confined modes.

It is very clear that PBG structures give a powerful technique for electromagnetic control of mode-competition by improving the art of interaction structure design. This can be combined effectively with the well known electrodynamic techniques of mode-selection such as the proper beam radius, operating current, voltage and the magnetic field values.

Chapter 6

Confocal Gyrotron Oscillators

The merits of the use of mode selective open confocal resonators and waveguides was discussed in Chapter 3. Their potential for application as an overmoded interaction structure for a W-band (75-110 GHz) Gyrotron Traveling Wave Tube (gyro-TWT) amplifier has been the focus of this work. Prior to building a gyro-TWT the design and test of a gyrotron oscillator experiment, which is expected to be simpler was pursued as a proof-of-principle experiment to demonstrate the mode selective properties of the confocal resonator. This chapter describes two different experiments that were performed during the course of this work to test some basic properties of confocal resonator based gyrotrons.

The quasioptical confocal resonator experiments differ from other quasioptical gyrotron experiments described elsewhere [177]– [179] in that for the first time we use conventional TE modes in a cylindrical geometry with long mirrors whereas other earlier experiments used large spherical mirrors in the TEM modes, which resemble laser resonators. The benefit of using cylindrical geometry with long mirrors is that the structure can be used to support a convective instability necessary for the spatial growth of the signal as in a gyro-TWT amplifier. Furthermore, the present work is the first time that diffraction has been advocated as a tool for parasitic mode suppression for enabling the use of overmoded resonators and waveguides in VEDs at millimeter wave frequencies. In the gyrotron oscillator experiments described in this chapter and the gyrotron amplifier experiment to be described in the next chapter, the mirror

Figure 6-1: The confocal resonator used in the 140 GHz fundamental confocal gyrotron oscillator experiment.

aperture has been the most vital design parameter to control the mode population and improve the contrast in the diffraction losses between the design operating mode and other competing parasitic modes.

6.1 140 GHz Confocal Gyrotron Oscillator Experiment

A 140 GHz gyrotron oscillator using a confocal resonator was designed and tested at MIT by Hu et al. [88]. During the course of this work this gyrotron experiment was repeated to improve understanding of the confocal resonator prior design of the gyro-TWT amplifier, which is significantly more challenging than the oscillator experiment. The design and initial experiments of the confocal gyrotron oscillator experiment have been presented in detail in [88]. In the section we list the design parameters and describe the experiments performed during the course of this work.

Frequency	140 GHz
Operating Mode	HE_{061}
Beam Voltage (V_0)	68 kV
Beam Current (I_0)	6 A
Beam Pitch Factor (α)	1.2
Beam Radius(r_b)	1.82
Magnetic Field	5.28 T
Mirror Seperation (L_t)	6.7 mm
Mirror Aperture ($2a$)	6.2 mm
Resonator Length (L_z)	17 mm
Fresenel Parameter (C_F)	4.2
Transverse Diffraction Q (Q_t)	8000
Axial Diffraction Q (Q_z)	1600
Total Diffraction (Q_{tot})	1300

Table 6.1: Design parameters of the 140 GHz confocal gyrotron oscillator experiment.

6.1.1 Design

The confocal gyrotron oscillator was designed to operate in the HE_{061} mode (Fig. 3-12(d)) at 140 GHz of the confocal resonator to use the existing VUW-8140 MIG [181] at MIT. The MIG is designed for 70 kV, 5A operation at a velocity pitch factor (α) of up to 1.9. The perpendicular spread is about 6% at an α of 1.5. The nominal beam radius is 1.82 mm. The design parameters of the confocal gyrotron oscillator experiment are listed in Table 6.1.

The design exploits the mode selectivity of the confocal resonator to reduce the parasitic mode density around the operating HE_{061} mode, which would allow the access to the higher efficiency regime of the mode without the excitation of any parasitic mode. The HE_{061} mode is analogous to the TE_{031} mode of a cylindrical resonator. Such a TE_{031} mode gyrotron at 140 GHz was extensively studied by Kreischer et al. [47] at MIT and it was found that the TE_{231} ($\nu = 9.9695$) mode of the cylindrical resonator which is nearly degenerate with the TE_{031} ($\nu = 10.1735$) operating mode severely limits the operating parameter space of the TE_{031} mode and prevents the access to the high efficiency regime. If the Fresnel parameter, C_F is chosen to be small enough (= 4.2 in the present experiment) the nearest well confined mode is the HE_{051} mode at 114 GHz compared to the design mode, HE_{061} at 136 GHz.

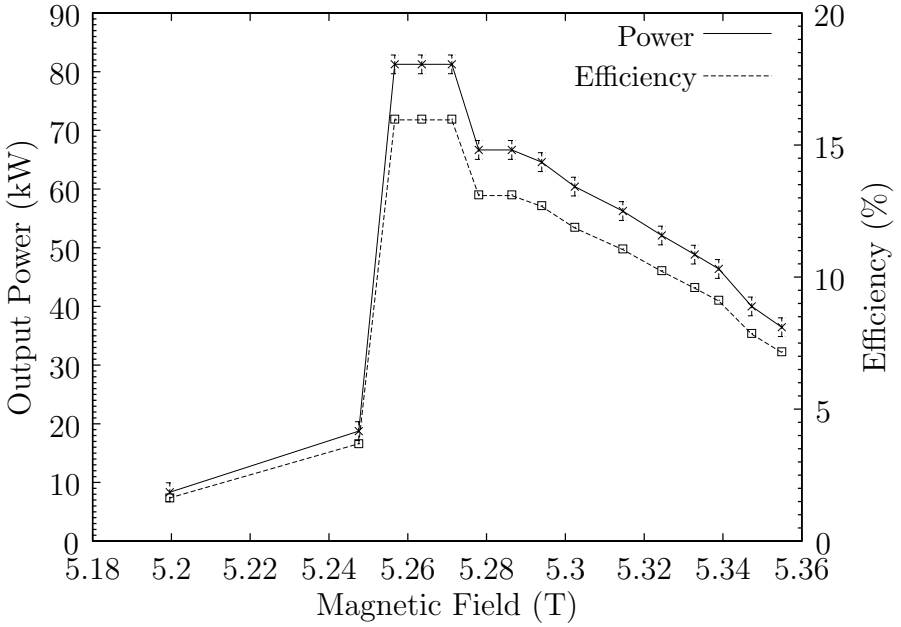

Figure 6-2: The variation of output power with magnetic field for HE_{06} mode at 136 GHz with V_0 = 74.76 kV, I_0 = 6.8 A and α=1.2.

The resonator used in the experiments is shown in Fig. 6-1.

6.1.2 Experimental Results

Initial investigation of this 140 GHz confocal gyrotron oscillator was performed by Hu et al. [88]. In this section we present the experimental results obtained during the course of this work. The experiment was rerun to gain valuable experience before the design and experiments on a 280 GHz second harmonic confocal gyrotron oscillator to be described in Sec. 5.2 and the confocal gyro-TWT to be described in Chapter 7.

The experimental investigation had two specific aims, firstly to try and produce higher power than obtained by Hu et al. [88] and also to check the possible excitation of the second harmonic resonance with the $HE_{0,12,1}$ mode. In Fig. 6-2 we show the variation of the output power with magnetic field for the operating HE_{061} mode at 136 GHz obtained during the course of this work. The frequency was lower than 140 GHz possibly due to the mirror separation being more than the design value by as little as 0.2 mm. We observe a wide range of magnetic field values where the HE_{061} design

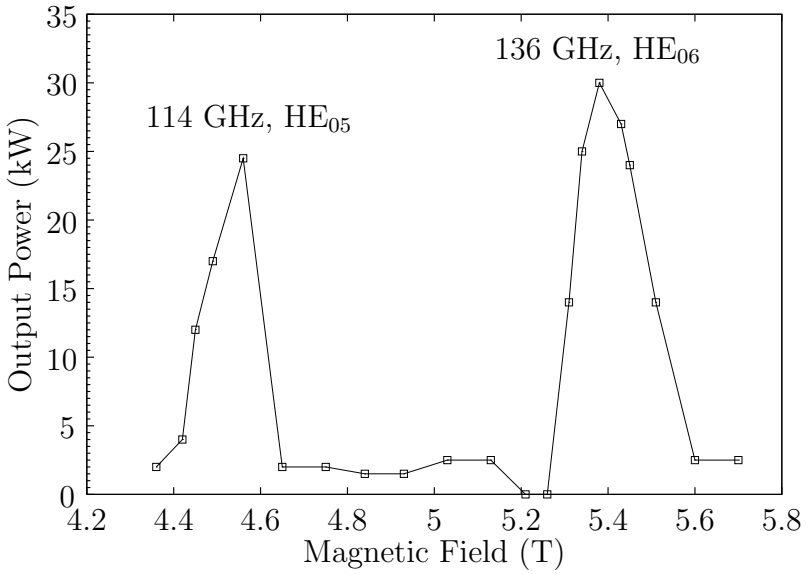

Figure 6-3: . The excitation regime of the HE_{05} and HE_{06} modes in the 140 GHz confocal gyrotron oscillator with varying magnetic field.

mode is excited without competition from the neighboring modes. The output power was measured using the analog, Scientech Inc. Calorimeter described in Section 7.4.1. A peak output power of 83 kW was obtained at 16 % efficiency. The mode selective properties of the gyrotron are demonstrated in Fig. 6-3 where we observe a wide range of magnetic field values where each mode is excited, which allows the access to the high efficiency operating point of the modes. The severe mode competition in an analogous TE_{031} mode, 140 GHz cylindrical resonator gyrotron studied in [47] is absent in the confocal gyrotron oscillator.

Another goal of the experiment was to study the possible excitation of the second harmonic resonance ($\omega \sim 2\Omega/\gamma$) by the interaction of the second beam cyclotron harmonic with the $HE_{0,12,1}$ mode of the resonator which has roughly twice the frequency of the HE_{061} mode. In a confocal resonator, as pointed out earlier in Sec. 3.2.2 the higher order modes have smaller beam radius at the mirror and hence are likely to be confined better than the lower order modes which suffer higher diffractive losses. In this experiment we could not observe the second harmonic due to the strong interaction at the fundamental in the HE_{061} mode. The second harmonic interaction is much

weaker and hence gets suppressed by the excitation of the fundamental mode resonance. To suppress the fundamental to allow the excitation of the second harmonic a new experiment was designed and is the subject of Sec. 5.2.

6.1.3 Conclusion

The successful operation of this gyrotron has been the first crucial step to the design of a second harmonic confocal gyrotron oscillator and a gyro-TWT amplifier experiment to be described later. A peak power of 83 kW was measured at an efficiency of 16 % during the course of this work. The operation of this experiment also provided valuable experience in running the other sub-systems which will be used in other experiments.

6.2 280 GHz Second Harmonic Confocal Gyrotron Oscillator

Second harmonic gyrotrons rely on the radiation at the second cyclotron harmonic of the electron beam ($\omega \sim 2\Omega/\gamma$) where, ω is the radiation frequency and Ω/γ is the relativistic cyclotron frequency and hence enjoy unique advantages over the fundamental resonance gyrotrons. The radiation at the second harmonic of the electron cyclotron frequency reduces the required static magnetic field to half the value required for fundamental interaction. Operation at higher cyclotron harmonics bring down the required strength of the magnetic field by the harmonic number. Since gyrotron require very high magnetic field ($\sim 28/\gamma$ GHz/Tesla), which is inevitably provided by superconducting magnets at millimeter wave frequencies, e.g. fundamental interaction at 140 GHz requires 5.4 T, any reduction in the strength of the magnetic field reduces the system cost. The higher harmonic interactions typically use higher order waveguide modes which allow larger transverse dimensions of the resonator. The use of second harmonic interaction in gyrotron amplifiers allows the use of higher beam current and hence the generation of higher output power [72].

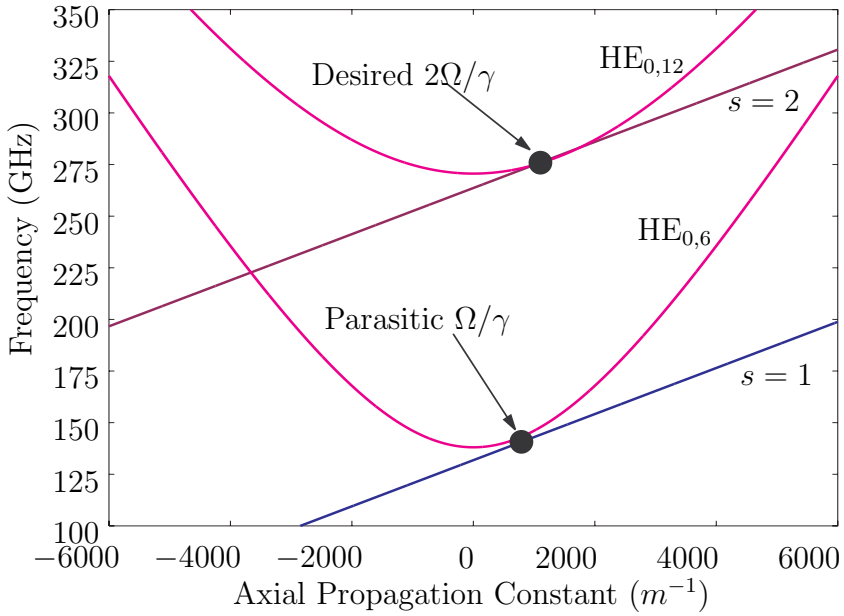

Figure 6-4: The dispersion diagram for a second harmonic gyrotron oscillator showing the potential for the excitation of a parasitic fundamental oscillation with a lower order mode.

All the mentioned advantages are accompanied by considerable design challenges to selectively excite the higher harmonic interaction while suppressing the lower order and most importantly the fundamental cyclotron interaction. The dispersion diagram for a second harmonic gyrotron oscillator is shown in Fig. 6-4 where the potential for the excitation of a fundamental beam cyclotron mode oscillation with a lower waveguide mode is also shown. The fundamental cyclotron interaction is much stronger than the higher harmonic interaction because in the former case the electron is synchronous with the electromagnetic wave over the entire Larmor orbit, whereas in the latter case it is synchronous only over a part of the Larmor orbit. Most of the excitation conditions for the fundamental and high harmonic interaction overlap and hence the fundamental mode interaction suppresses the second harmonic interaction unless special resonator design concepts which favor the harmonic interaction over the fundamental interaction, such as a slotted resonator are employed [58]. In addition to electromagnetic selection by proper resonator design, electrodynamic selection by the

Parameter	**Fundamental Design**		**2^{nd} Harmonic Design**	
Mode	$HE_{0,6,1}$	$HE_{0,12,1}$	$HE_{0,6,1}$	$HE_{0,12,1}$
Mirror Sep., $L_t = r_c$	6.70 mm		6.56 mm	
Axial Length, L_z	17.0 mm		13.92 mm	
Aperture, 2a	6.20 mm		4.10 mm	
Frequency (GHz)	140.20	274.40	143.25	280.19
Fresnel Parameter, C_F	4.2	8.23	1.92	3.76
Transverse Q, Q_t	7100	2.2×10^7	136	6300
Longitudinal Q, Q_z	1600	6100	2800	14500
Total Q, Q_{tot}	1300	6100	130	4400

Table 6.2: Resonator design parameters of the second harmonic confocal gyrotron experiment compared to the design of the fundamental confocal gyrotron oscillator experiment.

excitation of the higher harmonic interaction in the regime where the fundamental interaction is weaker is very important. Such techniques are well exemplified in [57] where the harmonic emission from a gyrotron design optimized for fundamental mode interaction at 140 GHz was studied.

6.2.1 Design

One of the many advantages of the confocal waveguide lies in its ability to confine the higher order higher frequency modes better than the lower order lower frequency modes. This feature can be explained in terms of the beam radius of the modes at the confocal mirrors. The higher order modes have a narrow beam waist and hence a narrower beam radius at the mirrors as compared to the lower order modes. Hence, if the mirror aperture is chosen to be small to provide a high contrast in the diffraction losses of the lower order mode to the higher order mode in consideration one may eliminate the excitation of the lower order mode by the electron beam.

A summary of the design parameters of the second harmonic gyrotron are presented in Table 6.2 where a comparison of the second harmonic design with the fundamental mode design discussed in the previous section is also presented.

In Table 6.2 we see that by reducing the aperture of the mirrors in the second harmonic resonator we can lower the transverse diffractive Q, Q_t of the $HE_{0,6,1}$ mode

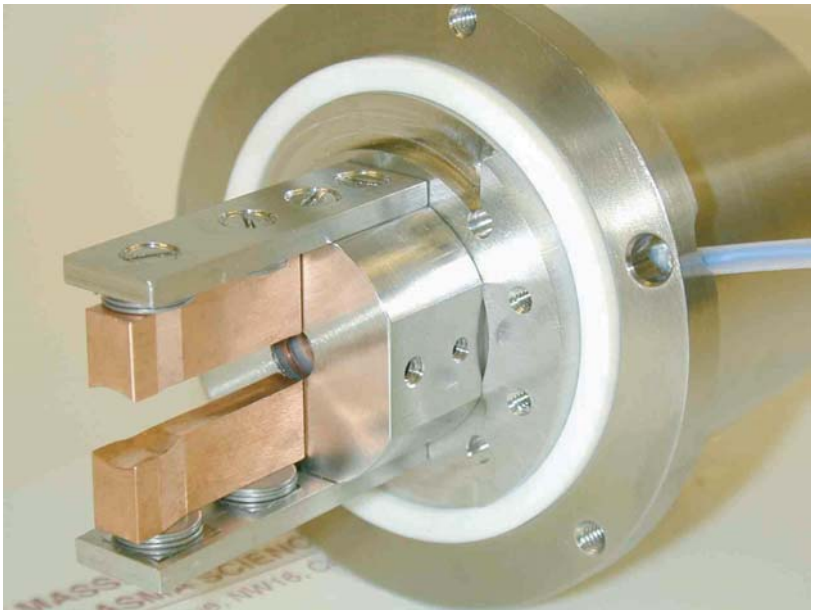

Figure 6-5: The confocal resonator used in the 280 GHz second harmonic gyrotron oscillator experiments. The resonator is shown mounted to the beam tunnel.

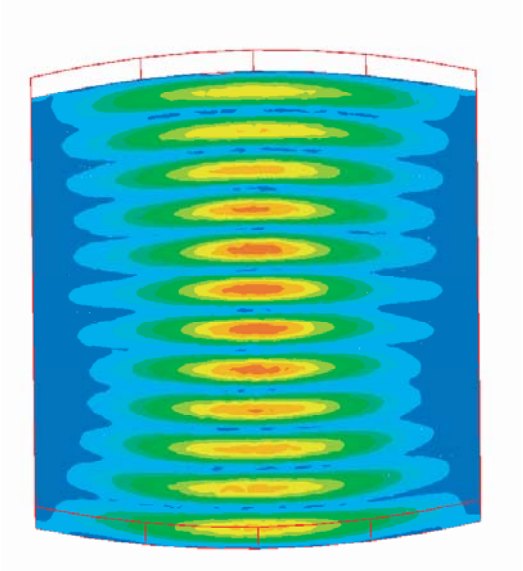

Figure 6-6: The $HE_{0,12}$ eigenmode resonant between the mirrors of the second harmonic gyrotron experiment. The mirrors are 4.1 mm wide and are separated by 6.56 mm.

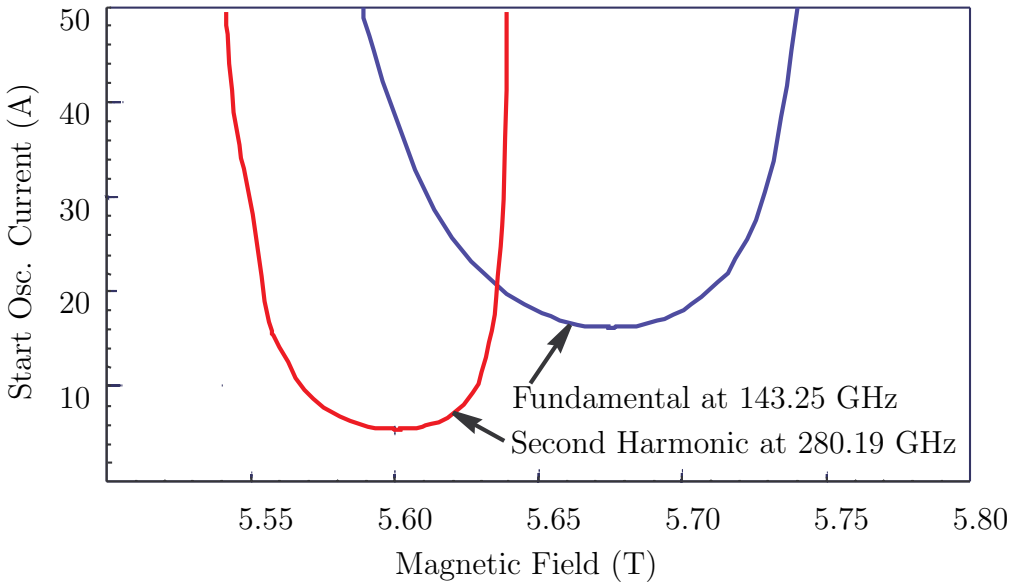

Figure 6-7: The starting conditions for the second harmonic and fundamental mode oscillations in the 280 GHz second harmonic confocal gyrotron oscillator design for $V_0 = 68$ kV and α=1.4.

which interacts with the fundamental beam cyclotron harmonic dramatically while keeping the corresponding value for the $HE_{0,12,1}$ operating mode about 46 time higher. This means that the diffraction losses in the transverse direction for the parasitic fundamental mode are very high compared to the second harmonic mode. This severe transverse diffraction loss for the fundamental mode reduces its overall Q factor and hence increases its start oscillation current. It is expected that the suppression of the fundamental mode by transverse diffraction losses would increase the regime of the stable excitation of the second harmonic interaction. The $HE_{0,12,1}$ eigenmode which is chosen as the operating mode is shown in Fig. 6-6 resonant in the mirror geometry chosen for this experiment. The actual resonator used in the experiment is shown in Fig. 6-5.

The choice of a relatively long resonator ($L_z = 13.92$ mm $= 12.75\lambda$ at 280 GHz) has resulted in a large axial diffractive Q for the second harmonic mode, which means that the efficiency of extraction of the power along the axis through diffractive coupling is

lower resulting in a significant trapping of the generated RF power in the resonator. This is a very common problem encountered millimeter in wave gyrotron designs, where a large value of the normalized resonator length μ, defined in Eqn. 2.60 for optimizing the electronic efficiency results in high value of the longitudinal diffraction Q, Q_z which leads to poor extraction from the cavity. A cold cavity computer code at MIT was used to predict the value of Q_z in this design but in general the axial diffraction Q factor for the TE_{0nq}modes in an open resonator can be expressed as [43], [180]

$$Q_z = \begin{cases} 8\pi \left(\frac{L_z}{\lambda}\right)^2, & \text{for } q = 1, \\ \frac{4\pi}{q} \left(\frac{L_z}{\lambda}\right)^2, & \text{for } q > 1. \end{cases} \tag{6.1}$$

In a gyrotron employing a PBG resonator, the ability to extract the power from the transverse direction by removal of one or more rods would prove to be very useful in situations where the very high value of the axial diffraction Q, chosen for higher efficiency prevents efficient extraction of power from the axial direction.

A plot of the start oscillation conditions for the second harmonic and the fundamental interaction is shown in Fig. 6-7. It is evident that due to the heavy transverse diffraction losses inflicted upon the $HE_{0,6,1}$ mode there is a wide window for the excitation of the $HE_{0,12,1}$ mode at the second beam cyclotron harmonic.

6.2.2 Experimental Results

The same setup used in the 140 GHz confocal gyrotron oscillator experiments described in Sec. 5.1 was used for the second harmonic experiment. The nominal electron beam parameters were as follows; V_0, 65–75 kV, I_0, 0–8 A and α <1.7. During the experiments very weak emission at the fundamental mode was observed and the measured power at the fundamental mode was less than 1 kW at a beam current over 9 A and an estimated beam velocity pitch factor of $\alpha = 1.5$. No second harmonic emission was observed during the experiments and one or more of the following reasons were perhaps responsible for the excitation of the second harmonic. The electron beam quality from this electron gun is poor at $\alpha > 1.4$, which causes a longitudinal

velocity spread of about 16 %. The second harmonic interaction is very sensitive to velocity spread and hence may require a beam with a lower velocity spread at $\alpha = 1.5$. Furthermore, the electron gun is optimized for operation at 5-6 A and at higher current (> 8A) the beam quality degrades quite rapidly [47]. The theoretical estimate of the start oscillation current for the fundamental and second harmonic shown in Fig. 6-7 assumed a zero velocity spread, and so a large velocity spread may have increased the starting current of the second harmonic to a value higher than 10 A which is the limit on the current available from the present electron gun.

6.2.3 Conclusion

Though second harmonic emission could not observed in the 280 GHz second harmonic confocal gyrotron oscillator it has validated the most important design criteria, namely, the suppression of the fundamental mode by transverse diffraction losses by the choice of narrow aperture of the mirrors. Since the confocal gyro-TWT amplifier experiment needed to be tested at a higher priority further research on the second harmonic experiment was not possible. To indeed observe the second harmonic a better electron gun with a lower velocity spread might be necessary.

6.3 Discussion

The gyrotron oscillator experiments described in this chapter have provided valuable experience in understanding and demonstrating the properties of confocal resonators and their applications in gyrotrons. The fundamental gyrotron oscillator experiment at 140 GHz produced 83 kW of power at 16 % efficiency and demonstrated excellent mode selectivity over a wide range of magnetic field values. Though second harmonic emission was never observed in the second harmonic experiment it did verify the design technique of suppressing the fundamental mode interaction by reducing the mirror aperture to increase the diffraction losses of the HE_{06} mode interacting with the fundamental beam cyclotron harmonic. An electron beam with a lower velocity spread is necessary for the successful excitation of the second harmonic.

We close this chapter with a discussion on the potential of confocal resonators in gyrotrons. The advantages of using open confocal resonators are many. The good mode selectivity of the resonator allows the stable operation in a higher order mode resulting in larger transverse dimensions of the resonator with a concomitant better thermal capacity. The use of two separate mirrors instead of a cylindrical pipe used in conventional gyrotron resonators provides a unique ability for mechanical tuning of the frequency. Such a capability is very useful in a variety of applications such as in low power drivers and other sources used for collective Thomson spectroscopy of fusion plasmas [182]–[184]. The use of a Gaussian-like eigenmode in the resonator may simplify the internal mode converter used to convert the higher order resonator mode to a TEM_{00} free space Gaussian beam for transmission via a low loss corrugated waveguide [169]. Since the eigenmode is already in a Gaussian shape in the x direction the launcher used to radiate the mode into the mirrors of the internal mode converter is expected to be simpler.

One of the disadvantages of the confocal resonator is that due to the azimuthal asymmetry of the fields a part of the electron beam does not couple to the RF fields and hence has a lower efficiency than a cylindrical waveguide. However, the use of a sectored electron beam which is present only where the RF fields reside can be used to increase the efficiency of the device. Such an electron beam may not be hard to form because it only needs a cathode with a sectored emitter.

The potential of application of the open confocal resonator in millimeter and sub-millimeter wave gyrotrons does seem to be very promising. The successful gyrotron amplifier results obtained with a confocal waveguide interaction structure described in Chapter 7 make it a very strong competitor for use in a high average power ($>$ 20 kW) gyrotron amplifier in the W-band (75-110 GHz) and beyond. The confocal gyrotron has the added advantage of tunability by varying the mirror separation. The advantages of using a confocal resonator in second harmonic gyrotron oscillators is very promising and may be a good alternative for experiments such as the second harmonic gyrotron oscillator at 460 GHz for applications in DNP experiments [89] in NMR spectroscopy.

Chapter 7

Confocal Gyrotron Amplifier

High power gyrotron amplifiers can extend modern communication and radar systems into the W-band and beyond where the unavailability of high power amplifiers has stymied system development. Conventional slow-wave TWTs are not a viable option above the Ka-band (26.5–40 GHz) and hence there is a strong need for high power high gain amplifiers for harnessing the millimeter wave spectrum. Gyrotron amplifiers can operate effectively in the W-band and beyond while generating two orders of magnitude or higher output power than conventional TWTs.

The advantages of millimeter wave communication systems are numerous. Some of the unique advantages include the availability of low attenuation bands also called windows at 35 GHz and 94 GHz which can be used very effectively for long distance communications. The small wavelength of the millimeter waves reduces the antenna size and improves the directivity when compared to traditional microwave systems. W-band communication systems can provide the much needed relief from congestion in the conventional microwave frequencies. The advantages of a W-band (75-110 GHz) radar are many and significant when compared to the conventional microwave radar. At millimeter wave frequencies due to the smaller wavelength and higher directivity, higher energy density and angular resolution can be achieved with a smaller antenna aperture and lower power when compared to a conventional microwave radar. Furthermore, the availability of wider bandwidth (effective bandwidth is a fixed percentage of operating frequency) at millimeter wavelengths results in an

increased Doppler shift for a given spread of radial velocities [144]. Due to these advantages the W-band radar is uniquely qualified for tracking low earth orbit satellites and space debris – applications that are becoming increasingly important for both military and space science applications.

In this chapter we describe the theory, design and experiments on a novel high power (100 kW peak power) Gyrotron Traveling Wave Tube (gyro-TWT) amplifier potentially capable of operating at high average power ($>$ 10 kW) in the W-band and beyond. A gyro-TWT is chosen over the other gyrotron amplifiers namely, the gyroklystron and the gyrotwystron because it employs a traveling wave nonresonant interaction structure and hence has wider bandwidth than the resonant structures used in the gyroklystron and the gyrotwystron.

There has been increased interest in the development of gyro-TWTs since the early eighties as listed in Table 1.1 on page 32 however most of the experiments have been limited to the Ka band. The primary reason for the lack of development of high average power capable amplifiers in the W-band is the rapid miniaturization of the transverse dimensions of the interaction structure if fundamental mode operation is chosen. Fundamental mode operation is very advantageous because of wider bandwidth and the absence of mode competition however, its pitfall is sub-wavelength scale structure dimensions which dramatically increase the fabrication complexity and limit the amount of power that can be safely generated in the device. Migration to a higher order operating mode allows the interaction structure dimensions to be larger than the operating wavelength but brings forth the problem of mode competition. Mode competition severely limits the amount of power that can be generated in the higher order operating mode and thus the overall system performance.

This thesis has been devoted to the demonstration of novel ideas which would allow stable single mode operation in highly overmoded interaction structures. The PBG resonator gyrotron and the confocal gyrotron oscillators with an open quasioptical resonator described in Chapters 5 and 6 respectively, have demonstrated the effectiveness of using novel interaction structures for mode selective operation in higher order modes. The gyro-TWT amplifier described in this chapter uses a quasioptical

open confocal waveguide instead of a resonator as in the confocal gyrotron experiment to demonstrate stable single mode operation in a higher order mode. The large transverse dimensions of the circuit ($\sim$ 3 wavelengths) compared to sub-wavelength scale fundamental mode structure makes the structure potentially capable of up to 100 kW CW operation at 94 GHz.

The experiments during the course of this work were done at 140 GHz due to a readily available electron gun and an Extended Interaction Klystron (EIK) driver at 140 GHz. The results achieved during the course of this work can be directly scaled down to 94 GHz without any degradation in performance. An initial design study of a 94 GHz confocal gyro-TWT is presented in Chapter 8. This chapter is organized as follows. We describe the design of the experiment in Sec 7.1, the experimental setup in Sec. 7.2 and the experimental results in Sec. 7.3. Finally a discussion on the results and the future prospects of this novel gyro-TWT are presented in Sec. 7.4.

7.1 Design

In this section we describe the design of the interaction structure and the gyro-TWT experimental setup. Some of the equipment used in the experiment such as the electron gun and the superconducting magnet are from prior gyrotron experiments at MIT.

7.1.1 Target Specifications of the Gyro-TWT Amplifier

The gyro-TWT is intended for use in W-band operating at 94 GHz. However, in the present research we have chosen to work at a much higher frequency of 140 GHz due to a readily available electron and a EIK driver. The target specifications for the gyro-TWT are listed in Tab. 7.1

Frequency	140 GHz
Output Power	100 kW
Saturated Gain	$\sim$ 38 dB
Saturated Bandwidth	$\sim$ 4 %
Efficiency	$\sim$ 30 %
Beam Voltage	65 – 75 kV
Beam Current	5 – 10 A
Velocity Pitch Factor	0.5 – 1.2
Long. Momentum Spread	$<$ 10 %
Beam Radius	$\sim$ 1.8 mm
Magnetic Field	$<$ 5.3 T
Cyclotron Harmonic	Fundamental
Operating Mode	HE_{06} Confocal

Table 7.1: Specifications of the proposed 140 GHz gyro-TWT experiment at MIT.

7.1.2 Electron Gun

The electron gun used in the experiment is an old gun from prior 140 GHz gyrotron experiments at MIT [47], [57]. The VUW-8140 [181] electron gun is a Magnetron Injection Gun (MIG) built by Varian Associates (now CPI Inc.), CA. The gun has three electrodes; the cathode operated at about -68 kV, the main anode operated at the ground potential, and the second anode (mod anode) operated usually between -42 kV and -58 kV. The electron beam parameters of this gun were optimized for a 140 GHz, TE_{031} mode gyrotron oscillator at 100 kW power level. A table of the optimum operating parameters for the electron gun are listed in Tab. 7.2.

The electron beam radius was designed to interact with the second radial maximum of the TE_{031} mode at 140 GHz. In addition to the above electron gun which is a nonlaminar gun, a laminar gun (VUW-8140A) was also available. The laminar gun has 4.0 A/cm^2 cathode current density which is twice that of the nonlaminar gun. The electron orbits do not intersect in the laminar gun and hence it is expected to perform better at higher beam current. To achieve laminar flow with nonintersecting electron orbits the cathode slant angle in the laminar gun is 25° compared to the 15° in the nonlaminar gun.

During the earlier gyrotron oscillator experiments [47] it was found that higher efficiency was obtained with the nonlaminar gun than the laminar gun and was ex-

Beam Voltage	65 kV
Mod Anode Voltage	19.6 kV
Beam Current	5.0 A (7.5 A max.)
Cathode Current Density	2.0 A/cm^2
Cathode Angle	15°
Anode Angle	15°
Velocity Pitch Factor	1.49
Perp. Velocity Spread	2.68 %
Beam Radius	1.81 mm
Beam Thickness	0.46 mm
Magnetic Compression	25.5
Magnetic Field	5.64 T

Table 7.2: Optimum parameters of the VUW-8140 MIG used in the 140 GHz gyro-TWT experiments.

plained by the possibility of achieving a higher velocity pitch factor with a low velocity spread in the case of the nonlaminar gun. Hence, in the gyro-TWT experiments the nonlaminar gun was used and the laminar gun was retained as a backup.

Extensive simulations were performed during the course of this work to find the optimum operating parameters of the nonlaminar gun using EGUN [140]. The evolution of the trajectory of the electrons computed by EGUN is shown in Figs. 7-1 – 7-3.

In the experiment the velocity pitch factor of the beam could be controlled by changing the voltage on the mod anode and the local magnetic field at the cathode by a conventional copper solenoid. An increase in the voltage difference between the cathode and the mod anode increases the velocity pitch factor. The beam radius was controlled by changing the local magnetic field at the cathode by the use of a conventional copper solenoid. The solenoid could be operated in a configuration in which its magnetic field added to the residual field from the main superconducting solenoid (lower compression) or subtracted the residual field of superconducting solenoid (higher compression). The magnetic compression is defined as the ratio of the peak axial magnetic field at the interaction region in the center of the superconducting solenoid to the local axial magnetic field at the cathode. Under adiabatic conditions the beam radius scales as the square root of the magnetic compression. In

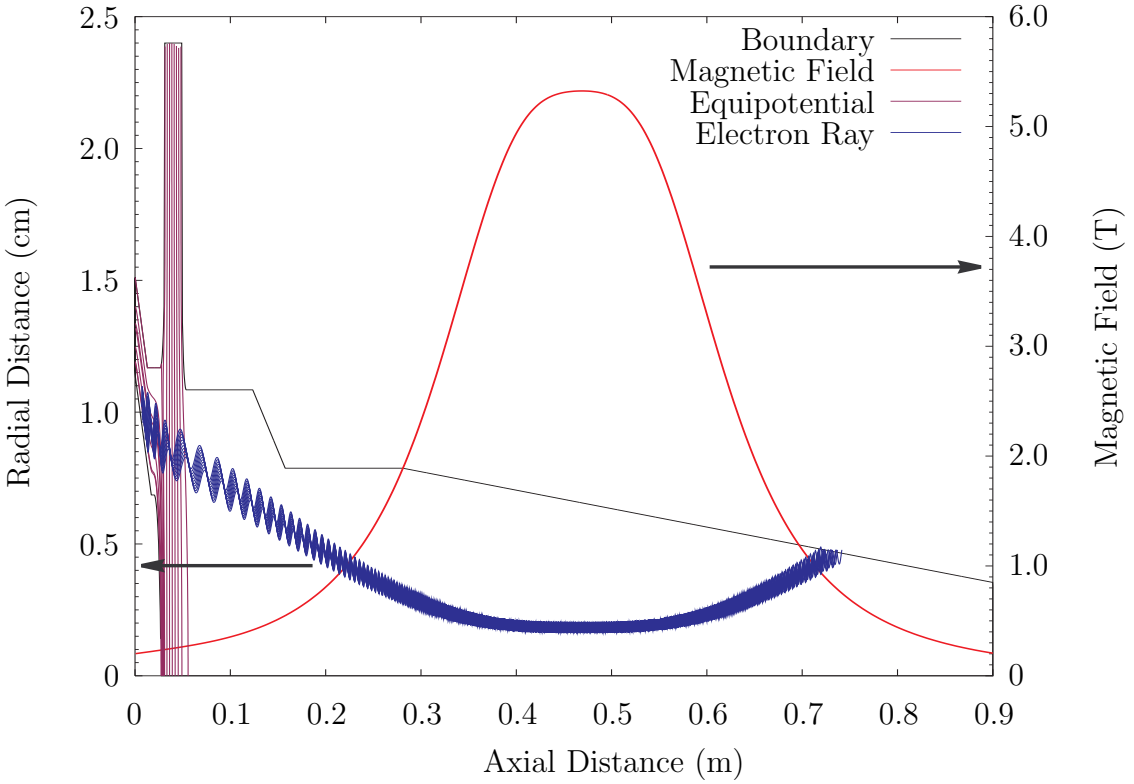

Figure 7-1: The evolution of the electron trajectories in the VUW-8140 MIG. The equipotential lines and the axial magnetic field are also shown.

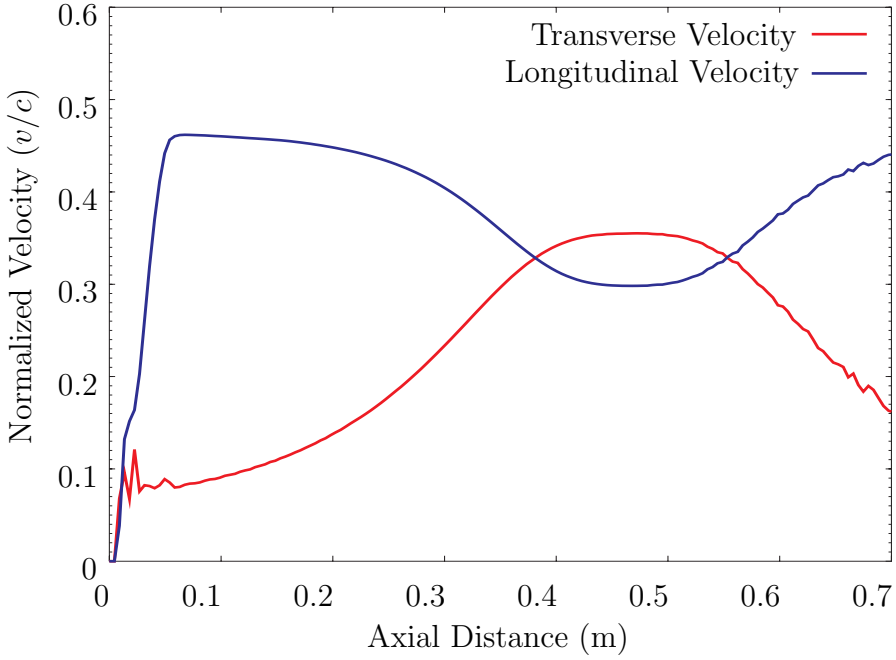

Figure 7-2: The evolution of the transverse and axial velocities of the electrons in the VUW-8140 MIG.

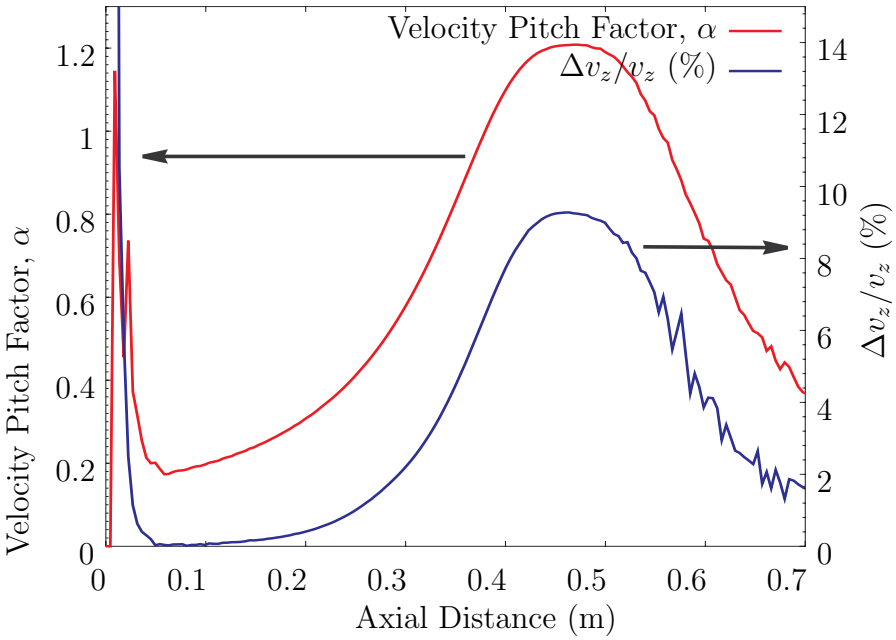

Figure 7-3: The evolution of the velocity pitch and the longitudinal momentum spread in the VUW-8140 MIG.

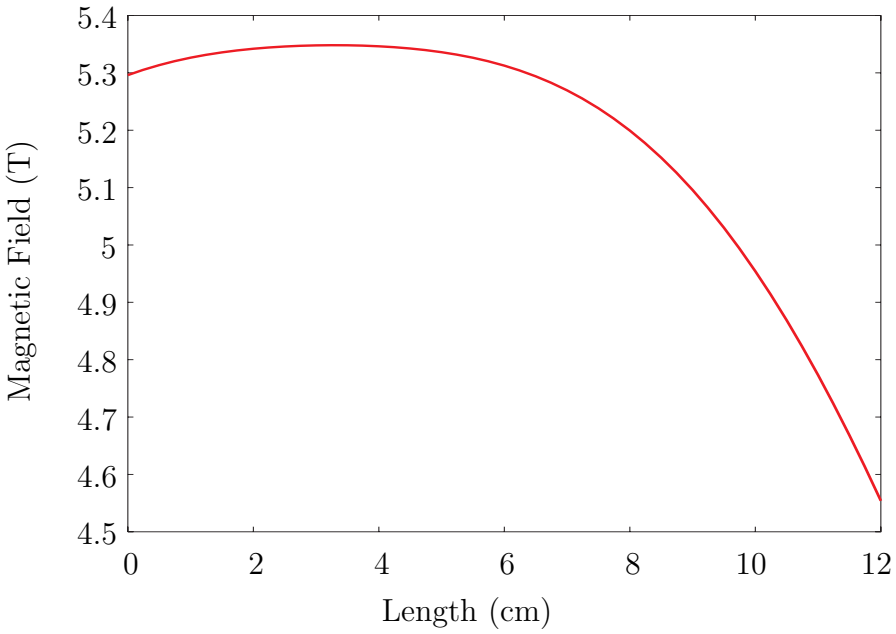

Figure 7-4: Actual magnetic field profile of the superconducting magnet. The field homogeneity is 0.5 % over 5.0 cm and 1 % over 6.5 cm.

the adiabatic domain an increase in compression while reducing the beam radius also increases the velocity pitch factor [135].

7.1.3 Superconducting Magnet

A superconducting magnet capable of operating at up to 6.5 T was used in the amplifier experiment. This magnet was successfully used in prior gyrotron oscillator experiments at MIT. The magnet was typically operated at 5.4 T during the gyrotron amplifier experiments. Since the magnet was designed for gyrotron oscillator experiments it has a short flat field region because gyrotron resonators are typically 5 to 10 operating wavelengths (λ =2.14 mm at 140 GHz) long. At the center of the solenoid the field homogeneity was 0.5 % over 5.0 cm and 1.0 % over 6.5 cm. The short flat field region proved to be the major constraint in achieving the 100 kW output power and 38 dB gain as aimed in the design of the gyro-TWT. Some operating details of the magnet are discussed in Sec. 4.2. During the design of the amplifier we assumed

a sufficiently long flat field to predict the optimum performance of the amplifier. The actual field profile of the magnet is shown in Fig. 7-4.

7.1.4 Interaction Structure

The gyro-TWT employs an overmoded quasioptical open confocal waveguide as the interaction structure. The choice of a higher order operating mode in a highly overmoded circuit allows the transverse dimensions of the interaction structure to be a few times the operating wavelength thus providing significantly higher thermal capability than fundamental mode gyro-TWTs with sub-wavelength scale interaction structures. The electromagnetic properties of the quasioptical open confocal waveguide have already been discussed in Sec. 3.2.

The operating mode was chosen using the following criteria. Firstly, the existing electron gun beam radius has to lie on one of the local maxima of the azimuthal electric field. Secondly, for 100 kW average power propagating along the structure the ohmic losses in the walls of the interaction structure had to be below 1-2 kW/cm^2, the limit for conventional cooling technology. These constraints led to the choice of the HE_{06} operating mode which is shown in Fig. 3-12(d). Higher order operating modes can also be chosen to satisfy the above criteria, however, the gain is lower at higher order modes.

The operating frequency and the operating mode directly lead to the transverse dimensions of the interaction structure from Eqn. 3.31. Typically, the center frequency of a gyro-TWT is designed to be 3-4% above the cut-off frequency of the operating mode. This region of the dispersion curve is ideally located to yield a high gain at moderate bandwidths. The linear gain of the tube rapidly decreases with increasing values of the axial propagation constant.

The next important parameter in the design is the choice of the mirror aperture designated by $2a$. The dimensions of the mirror aperture are determined such that while minimizing the diffraction losses for the operating mode the losses are large enough to sufficiently suppress the lower order HE_{05} mode which can interact with the s = 1 beam cyclotron mode and produce Backward Propagating Wave Oscillations

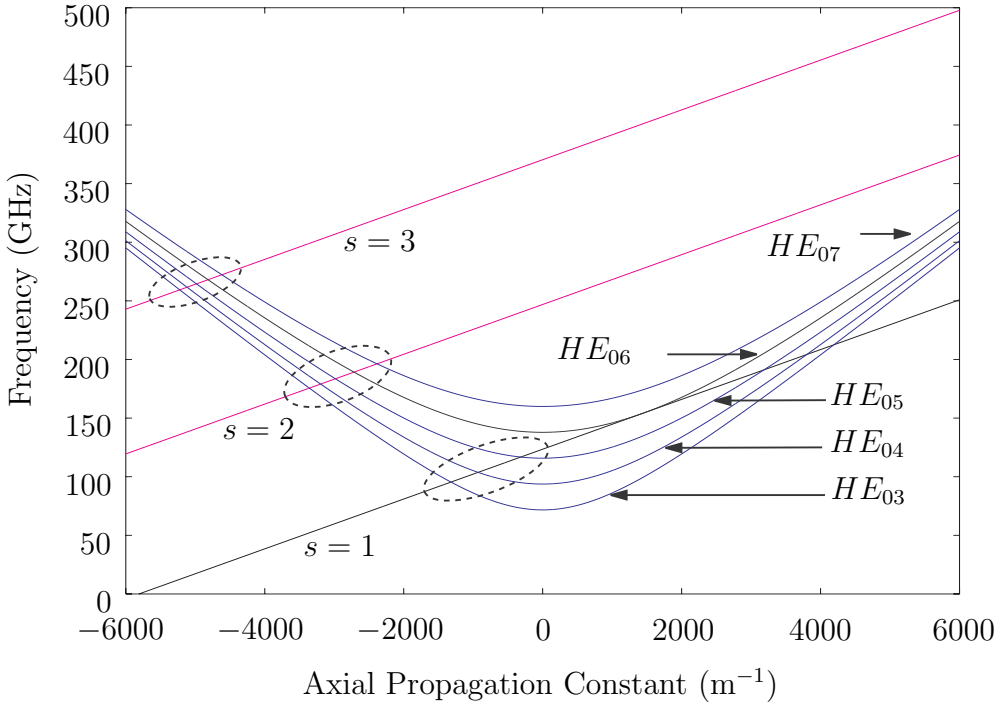

Figure 7-5: Mode spectrum of the confocal gyro-TWT interaction structure. The potential BPWO excitation points are shown as dotted ellipses.

(BPWO). The diffraction losses for a particular mode with the mirror aperture can be determined from Eqn. 3.32. In the present design a mirror aperture of 5.7 mm corresponding to a Fresnel Parameter of $C_F = 3.46$ for the operating HE_{06} mode and 2.91 for the parasitic HE_{05} mode was chosen. It must be remembered that lower values of the Fresnel parameter imply higher losses (Fig. 3-13).

The mode spectrum of the confocal waveguide around the operating mode is shown in Fig. 7-5. The grazing intersection between the s = 1 beam cyclotron mode and the HE_{06} mode is the operating point of the amplifier. The overall length of the interaction structure is determined from the saturation characteristics of the amplifier. However, a threshold for the length of each section is imposed by the excitation of the BPWO mode at the operating current. A plot of the threshold length for BPWO oscillations with operating current is shown in Fig. 7-6. The threshold length was calculated for the case of zero velocity spread using the linear theory described in Sec. 2.6.

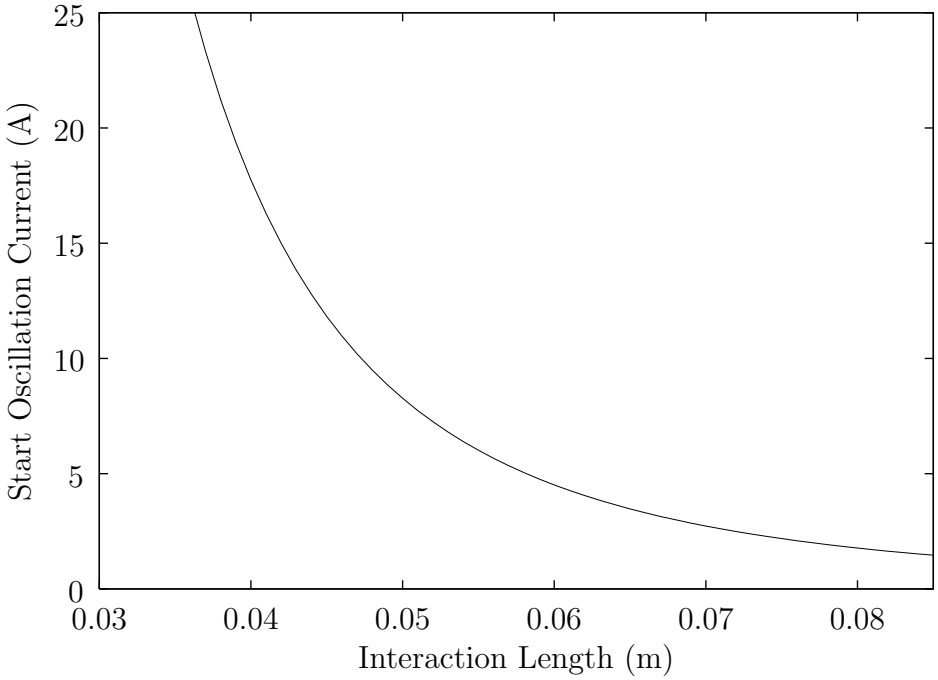

Figure 7-6: The thresold current for the excitation of HE_{05} BPWO at 121 GHz. The operating parameters are listed in Tabs. 7.3 and 7.4 with $\Delta v_z/v_z = 0$ %.

In our computations we assumed an ideal beam with zero velocity spread and zero reflections from the output end of the tube. A finite value of velocity spread increases the threshold for BPWO where as the finite reflectivity from the output end decreases the threshold. The electron beam used in the present experiments is likely to have 7-10 % longitudinal spread at a pitch factor of $\alpha = 1.2$. A more accurate nonlinear study of the BPWO interaction is possible by using a modified form of the single particle gyrotron amplifier code described in 2.8.2. but this was not done during the course of this work because the computations from the linear theory are sufficient to determine the threshold length for BPWO at a particular operating current. The intersections of the s = 2 beam cyclotron harmonic with higher order waveguide modes also can cause harmonic BPWO interactions but these interactions are weaker than the fundamental mode BPWO interactions with the lower order parasitic modes. From Fig. 7-6 it is evident that each section of the interaction structure should be less than 5.5 cm in length corresponding to a desired operating current of 7 A. To

obtain the desired overall gain we choose two interaction sections separated by a sever section. The optimum length of each of these sections is decided from the results of the nonlinear simulation runs. The electron beam should be mildly bunched before entering the sever section to avoid a sharp discontinuity in the system due to the sudden attenuation of the RF signal in the sever. Nonlinear simulations indicate that a lower momentum spread in the beam allows a stronger prebunching before the sever section without deteriorating the output power or bandwidth. This study indicates that good quality electron beams with a low velocity spread are necessary for multi-section interaction structures.

The present design is constrained by the existing electron gun and the superconducting magnet. The electron gun yields the best beam quality at a radius of 1.82 mm and operating voltage in the range of 65-75 kV at current up to 7 A. The short flat field region of the superconducting magnet is a serious constraint on the overall length of the interaction structure. During the design we assumed a sufficiently long flat field region to optimize the design. However, an operating point close to the cut-off was chosen to obtain a high gain per unit length to obtain the desired overall gain of 38 dB. These constraints considerably complicate the design because a high gain per unit length means shorter interaction sections to prevent the backward wave oscillations. The nonlinear simulations indicate that the presence of a sever enhances the deterioration of the interaction for a beam with high a velocity spread. Since the electron gun chosen for this experiment is likely to have no less than 8 % longitudinal velocity spread at the operating parameters the nonlinear simulations indicate that the present experiment cannot afford more than one sever section.

Based on the above considerations the final dimensions of the interaction structure were determined and they are listed in Tab. 7.3. The second gain section was chosen to be 7 cm instead of the 5.5 cm limit suggested by BPWO simulations because we assumed an electron beam with zero velocity spread resulting in a tighter constraint and to maximize the length of the interaction structure to compensate for the short flat field region.

The nonlinear single particle code described in Sec. 2.8.2 was used to determine

Mirror Sep.= Curv. Rad.	6.79 mm
Mirror Aperture	5.7 mm
Fresnel Parameter (HE_{06})	3.46
Fresnel Parameter (HE_{05})	2.91
Length of First Section	2.5 cm
Length of Sever Section	2.5 cm
Length of Second Section	7.0 cm

Table 7.3: Dimensions of the confocal waveguide interaction structure used in the gyro-TWT experiments.

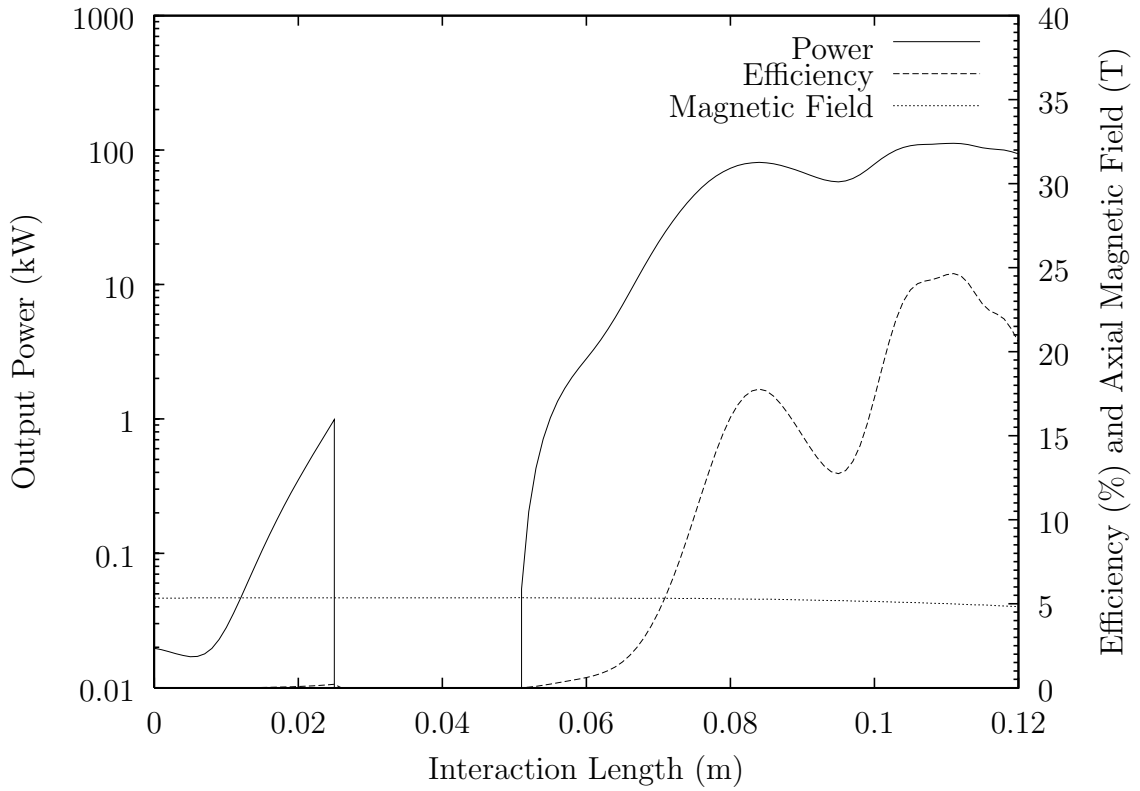

Figure 7-7: Spatial power profile at 140 GHz in the gyro-TWT interaction structure. The operating parameters are listed in Tabs. 7.3 and 7.4.

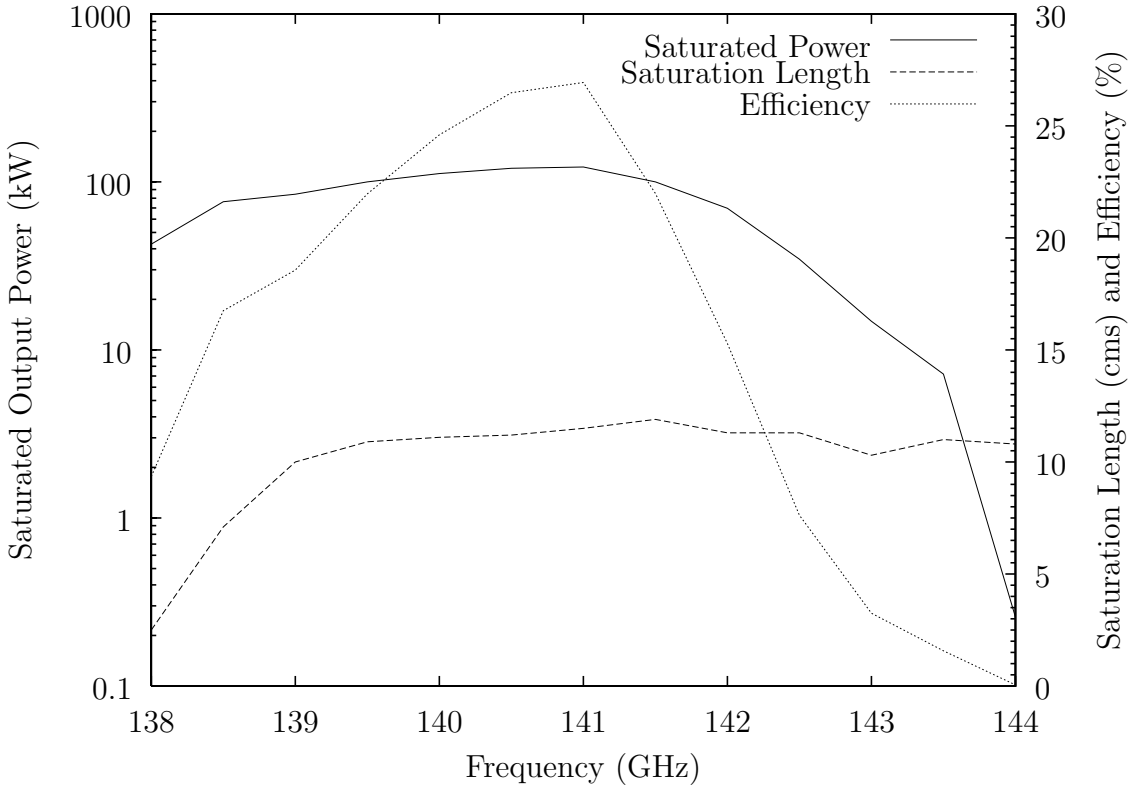

Figure 7-8: Design saturated bandwidth characteristics of the gyro-TWT. The operating parameters are listed in Tabs. 7.3 and 7.4.

Frequency	141 GHz
Peak Output Power	122 kW
Saturated Gain	38 dB
Saturated Bandwidth	2.9 %
Peak Efficiency	27.5 %
Beam Voltage	65 kV
Beam Current	7 A
Velocity Pitch Factor	1.2
Long. Momentum Spread	8 %
Beam Radius	1.82 mm
Magnetic Field	5.31 T

Table 7.4: Optimized design performance of the 140 GHz confocal gyro-TWT experiment.

the power bandwidth characteristics of the gyro-TWT. The spatial power profile at 140 GHz is shown in Fig. 7-7. The saturated output power and the saturation length predicted by the nonlinear code is shown in Fig. 7-8. Table 7.4 lists the optimized performance parameters of the gyro-TWT design. The design achieves a peak output power of 122 kW at 141 GHz with 27.5 % efficiency and a saturated gain of 38 dB. The modest 3 % saturated bandwidth of the device can be improved by using a tapered interaction section or other broadbanding schemes after observing the performance of this *proof-of-principle* experiment.

The effect of the short flat field region of the superconducting magnet on the actual spatial evolution of the amplified signal is shown in Fig. 7-9. Since the actual flat field region in the superconducting magnet is shorter than that assumed in the optimized design presented earlier in this section we expect the experimentally measured gain and output power to be lower than the design values.

7.1.5 Input Coupler

Operation in a higher order mode usually complicates the design of the input coupler to achieve a high coupling efficiency. Typically, for higher order axisymmetric modes such as the TE_{01} a wrap around coupler is used to excite the TE_{01} mode from a fundamental waveguide through a TE_{411} coaxial resonator as described in [83]. The wrap around converter is quite complicated to build at 94 GHz due to the miniature

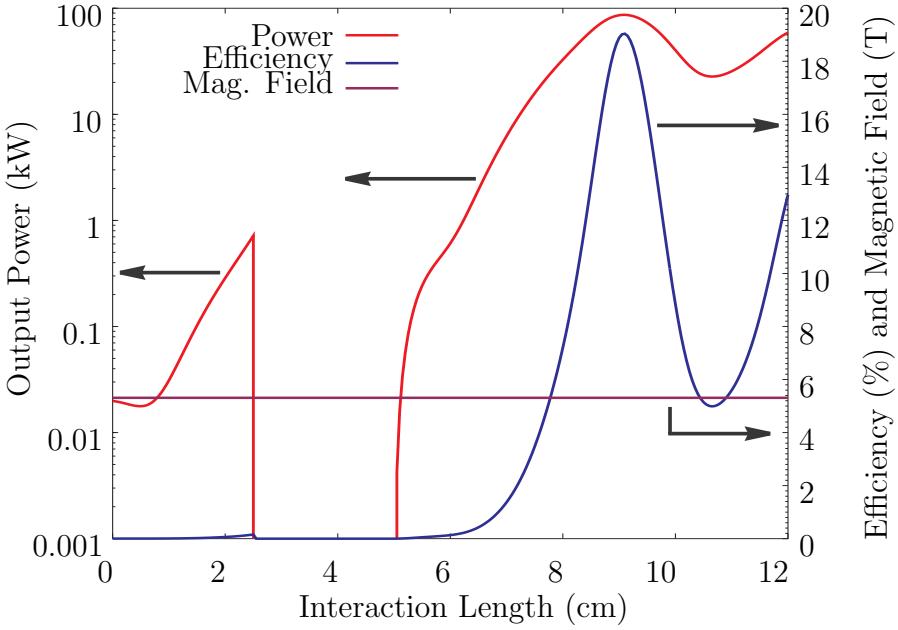

(a) Power evolution in an optimum flat field profile.

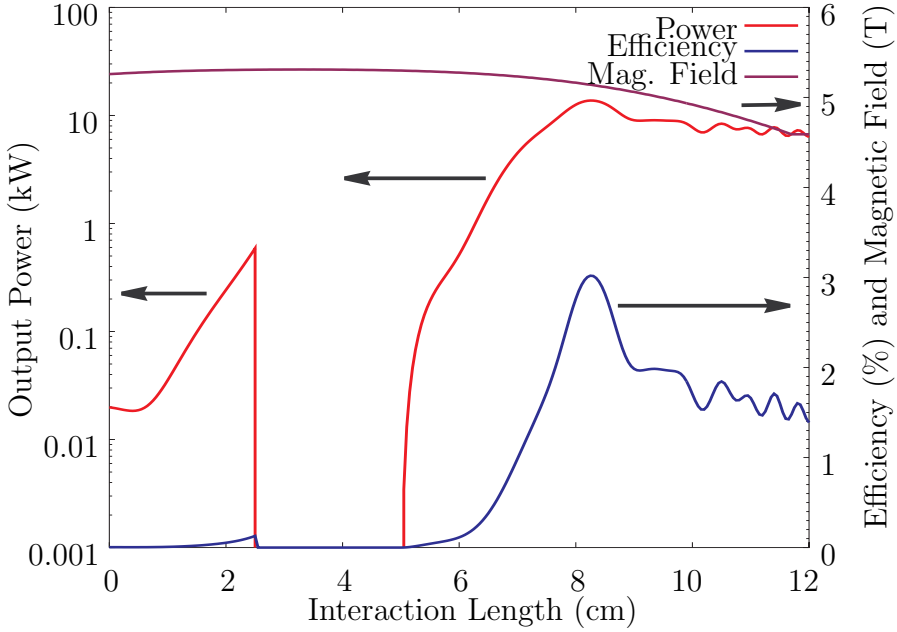

(b) Power evolution in the actual field profile of the superconducting magnet.

Figure 7-9: Evolution of spatial power profile at 140 GHz in the gyro-TWT interaction structure for different magnetic field profile. The operating parameters are listed in Tabs. 7.3 and 7.4.

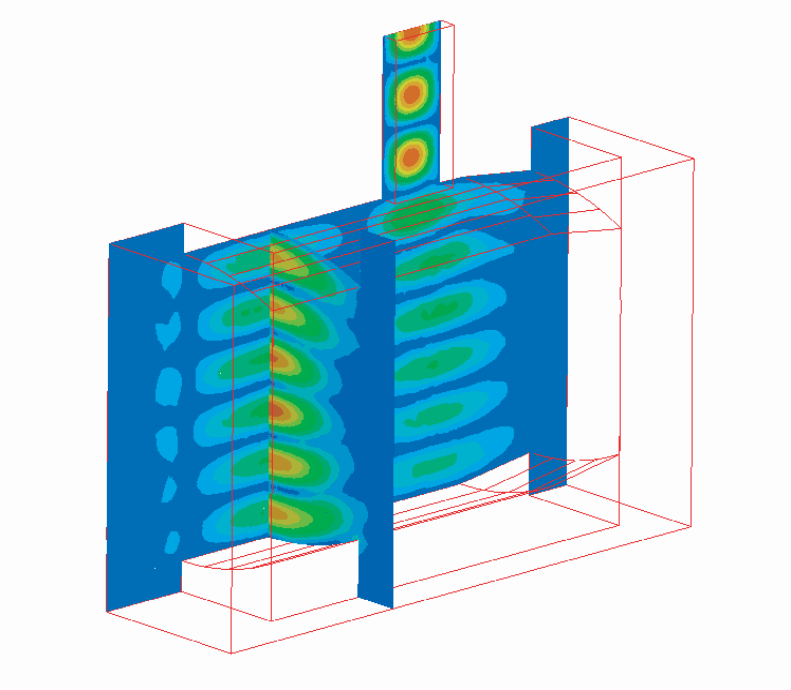

Figure 7-10: An HFSS simulation showing the excitation of the HE_{06} operating mode in the confocal waveguide by the input coupler.

dimensions of the interaction structure. The mode selectivity of the confocal waveguide allows us to attempt direct aperture coupling for the excitation of the mode. We use a standard WR8 (90-140 GHz) fundamental waveguide aperture to directly couple from the WR8 rectangular waveguide to the confocal waveguide to excite the HE_{06} operating mode. An HFSS simulation of the excitation of the HE_{06} operating mode from the TE_{10} mode in a fundamental waveguide is shown in Fig. 7-10. The corresponding reflection coefficient at the input port of the coupler is shown in Fig. 7-11. Due to the diffraction losses in the structure a low value of S_{11} does not guarantee a better coupling to the operating mode. The real figure of merit for the coupler is the coupling efficiency which is defined as the ratio in percentage of the amount of power coupled to the desired mode to the total power incident at the input port of the coupler. For the input coupler used in this design the coupling efficiency is 53 % at 141 GHz and on the band edges falls to 37 % at 139 GHz and 29 % at 142 GHz. These calculations were performed using the simulation results from HFSS

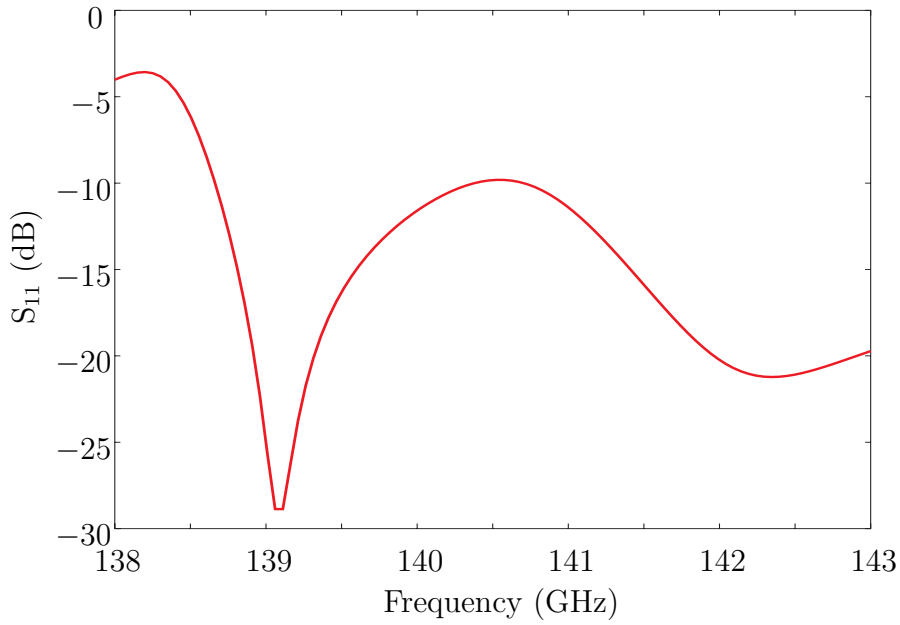

Figure 7-11: The reflectivity of the input coupler of the gyro-TWT computed using HFSS. The mirror separation is 6.78 mm and the input waveguide is a WR8 standard rectangular waveguide.

by computing the ratio of the Poynting power at a cross-section of the input coupler to the Poynting power incident at the input port. Based on the power coupled to the operating mode we find that the coupler works fairly well from 139-141.5 GHz. This simple design can be optimized with a proper choice of coupling aperture or using multiple coupling holes for a broadband response. These optimizations would be necessary for a real broadband (4-8 GHz bandwidth) device. We also found that a wide mirror aperture may be necessary near the coupling aperture to maximize the power coupling to the desired mode.

7.1.6 Sever

A sever is a highly lossy section separating two adjacent gain sections each of whose length is less than the threshold length for BPWO oscillations. The use of sever sections allows the overall gain to be higher than the limit imposed due to the excitation of the BPWO. The sever works by providing infinite attenuation to the electromag-

netic waves propagating through it. The backward wave starts growing from the collector end of the tube towards the gun end and the presence of a lossy section completely attenuates the BPWO by decreasing its round trip gain by the amount of loss in the sever. However, for the forward traveling wave the heavy loss in the sever does not dramatically affect the gain because the bunching in the electron beam is preserved during the transit of the electron beam through the sever. Upon entry into a gain section the electron beam rapidly induces RF fields in that section as can be seen in Fig. 7-7. Just like in a TWT where an infinite loss in the sever region translates to an infinite loss for the backward wave and a mere 3.52 dB loss for the forward growing wave [136] one can show a similar phenomenon in a gyro-TWT.

Traditionally, severs are built as a heavy lossy dielectric loading in the region of the interaction structure where the sever is desired. Such an approach has several limitations in the W-band. Due to the very small transverse dimensions of the circuit the lossy dielectric is very close to the electron beam, which brings forth problems of effective thermal dissipation, beam interception and the charging of the dielectric due to the electron beam. For a 100 kW CW device with one sever at least 1–2 kW of RF power is expected to be dumped into the sever necessitating a very good thermal conduction path.

In our experiments we introduce a novel concept for building a high average power sever by using quasioptical techniques. The open aperture from the confocal waveguide allows effective extraction of RF power from the interaction structure by reducing the mirror aperture. The sever is formed by a gradual reduction in the mirror aperture and then a gradual increase to match the mirror aperture in the second section. This extracted power can be absorbed by a lossy dielectric over a wide area. This would allow the easy cooling of the dielectric and because the dielectric is far away from the electron beam the problems of dielectric charging and beam interception are also mitigated. A CAD drawing of the quasioptical diffraction sever is shown in Fig. 7-12.

In the experiments during the course of the work we have chosen not to use an absorbing dielectric but rely on the absorption of the diffracted power in the large

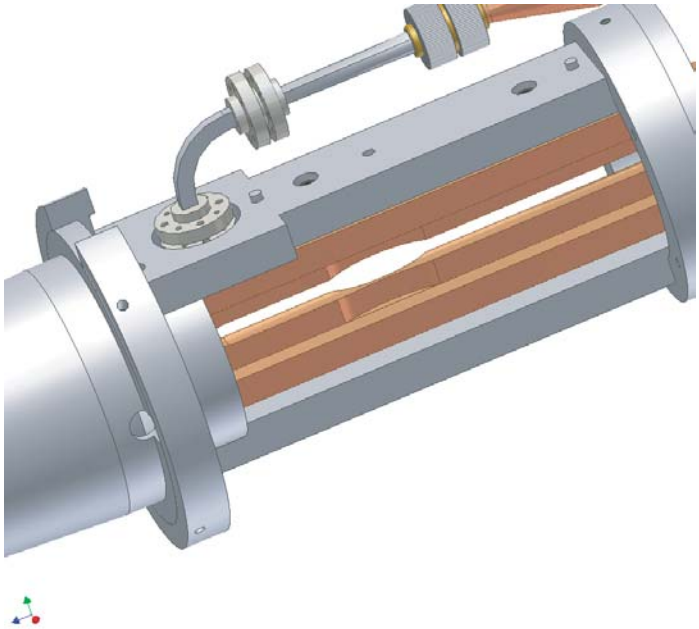

Figure 7-12: CAD drawing of the gyro-TWT interaction structure showing a high average power capable quasioptical sever. The outer absorbing dielectric shell not shown in this figure is necessary for high average power operation. The sever is the region with a reduced mirror aperture.

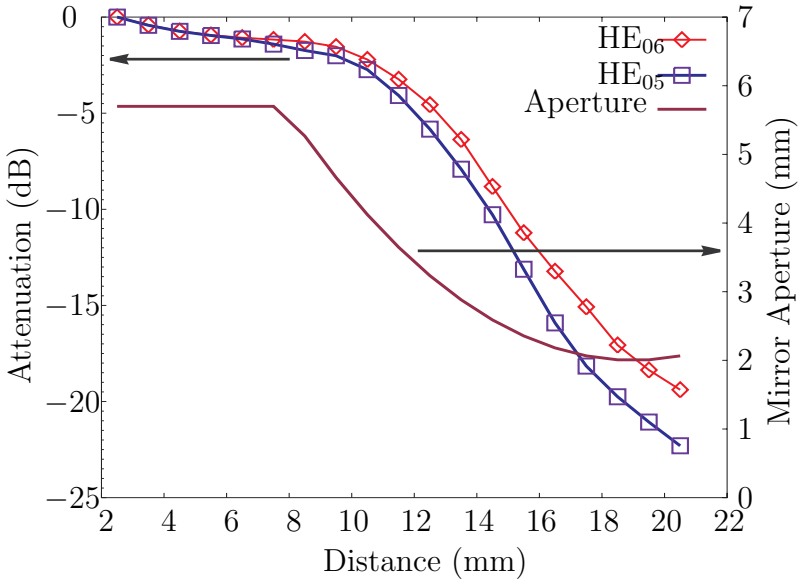

Figure 7-13: HFSS simlation results showing the diffractive losses in the sever for the HE_{05} and HE_{06} modes with the profile of the mirror aperture.

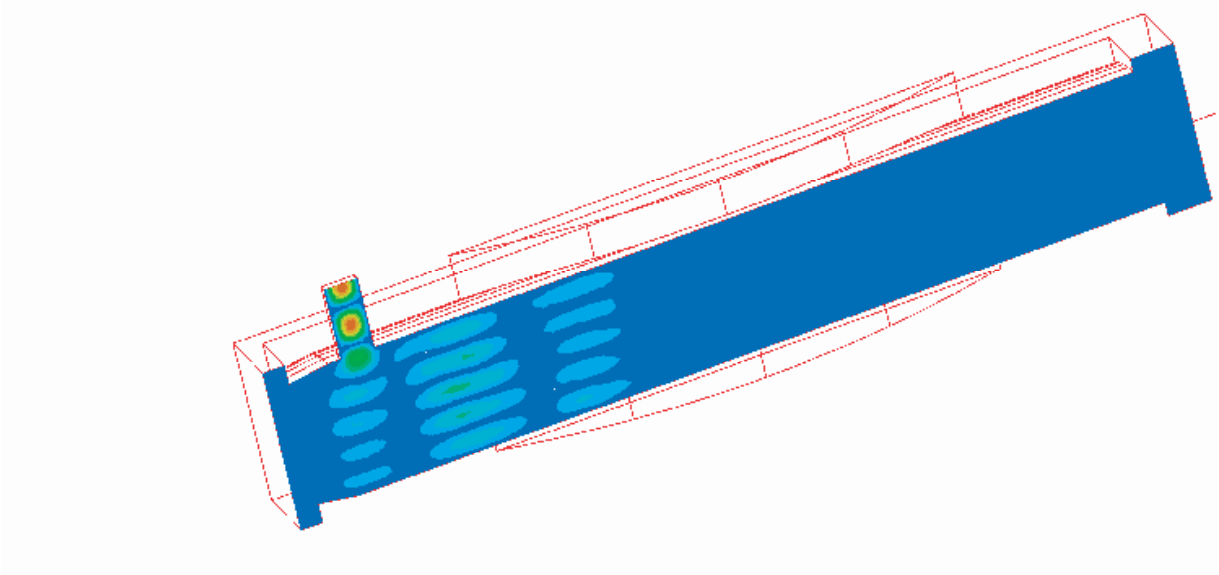

(a) HE_{05} mode attenuation in the sever.

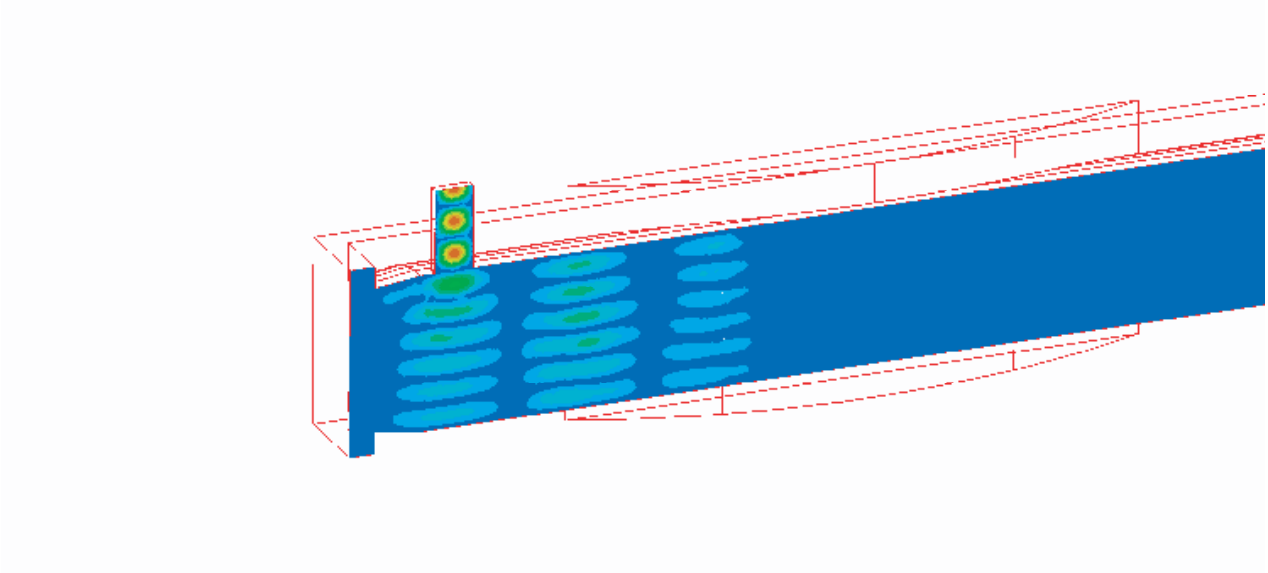

(b) HE_{06} mode attenuation in the sever.

Figure 7-14: HFSS simulations showing the attenuation of the HE_{05} and the HE_{06} modes in the sever. The model is split into one half to take advantage of the symmetry of the structure to reduce computation time in HFSS.

vacuum jacket used in the experiment. Since we have a pulsed experiment (3 μs, 6 Hz repetition rate) the average power absorbed in the walls of the vacuum jacket should pose no problems.

HFSS simulations were performed to evaluate the performance of the sever. The mirror aperture profile and the computed diffraction loss in one half section of the sever computed using HFSS is shown in Fig. 7-13. The HFSS model for the sever (Fig. 7-14) uses a short input section for the excitation of the HE_{05} and the HE_{06} modes followed by the actual size sever and then an output section. The input section is derived directly from the HFSS model for the input coupler. The diffraction loss for both the operating HE_{06} mode and the parasitic HE_{05} mode along the length of the sever is shown in Fig. 7-13 where we see that the total loss over the whole sever section is about 44 dB for the HE_{05} mode which is sufficient for absorbing the backward wave completely. In these HFSS simulations we have not used a lossy dielectric and have simply let the diffracted power exit the structure through a radiation boundary in the HFSS simulations. The attenuation of the HE_{06} and HE_{05} fields in the sever is shown in Fig. 7-14.

A variety of lossy dielectrics with good thermal conductivity can be chosen for the absorbing shell in the actual sever. Ceradyne Inc., CA has wide range lossy dielectrics which can be chosen for use in this high average power sever [185]. Other high thermal conductivity lossy dielectrics have been reported in [186]. Research on ultra high absorption beam dumps for detecting small signals from Thomson scattering experiments provides some ideas for an effective design of the dielectric surface for the absorption of the microwaves with low reflection. It was reported in [187] that high density (3.1 g/cm^3) Silicon Carbide (SiC) has a reflectivity of -26 dB for a pyramidal structure with apex angle of 45 degree at 60 GHz. The studies also indicated that the SiC sample showed no outgassing problem up to 500 degrees Celsius. The surface of the dielectric may be designed to be a moth eye surface [188], [189] to reduce the surface reflection. Detailed investigation of the lossy dielectric shell has to be done to actually build a high average power gyro-TWT for a real application.

7.1.7 Output Coupler

A gyro-TWT for application in a radar or a communication system needs the output radiation in a free space Gaussian Mode (TEM_{00}) at the window for effective coupling to the HE_{11} mode of a corrugated guide [169] for ultra low loss transmission to the antenna. The efficient transformation of the operating mode from the interaction structure to a TEM_{00} Gaussian beam at the window is a complex problem. A lot of research has been done on the conversion of the higher order whispering gallery modes (TE_{mnp}, m $\gg$ n) into a Gaussian beam at the window and this technique is routinely used in megawatt power level gyrotrons for fusion applications [190], [191]. Techniques for conversion of the TE_{0n} axisymmetric modes into a Gaussian beam have also been investigated [192]. A review of mode converters for high power gyrotrons is presented in Chapter 7 of [46].

Transformation of the HE_{06} operating mode of confocal waveguide to a Gaussian beam should in principle be easier than transforming a TE_{0n} mode into a Gaussian beam because in the case of the confocal guide the HE_{06} mode already has a Gaussian shape in the x direction. A simple technique like a dimpled wall launcher or a space periodic quasioptical converter can be directly implemented on the confocal waveguide to focus the Brillouin flow of rays into a tight bunch for eventual extraction from an aperture on the waveguide. In this proof-of-principle gyro-TWT experiment we have not investigated a detailed design of the mode converter. However, in this section we present two simple techniques based on geometric optics for the transformation of the HE_{06} confocal waveguide mode into a standard circular or rectangular waveguide mode for eventual conversion into a Gaussian beam using standard techniques.

In the experiments done during the course of this work we have used simple adiabatic uptapers to collect the radiation from the confocal waveguide into a 2.85 cm (1.12 inch) diameter cylindrical waveguide which also serves as a collector of the spent electron beam. Two adiabatic uptapers were designed assuming a TE_{03} mode was incident at the input of the first uptaper at 140 GHz. The details of the uptapers are provided in Table 7.5. The initial radius of Taper #1 was chosen to match the

Parameter	Taper #1	Taper #2
Initial Radius (mm)	3.52	6.29
Final Radius (mm)	6.29	14.22
Length (mm)	50.80	101.60
TE_{03} mode purity (%)	99.10	91.55

Table 7.5: Dimensions of the output uptapers used in the gyro-TWT experiments.

transverse propagation constant of the HE_{06} confocal waveguide mode to the TE_{03} cylindrical waveguide mode.

Simple techniques of quasioptically transforming the HE_{06} operating mode to standard cylindrical or rectangular waveguide modes can also be used in the output coupler. In the geometric optics representation the confocal waveguide can be regarded as a continuum of lenses of focal length, $F_{confocal} = r_c$, where r_c is the radius of curvature (equal to the separation of the mirrors) and a cylindrical waveguide can be assigned a corresponding focal length of $F_{cyl} = r_c$, where r_c is the radius of the waveguide. An intermediate lens can be designed with a radius of curvature equal to $2r_c/3$ as a transformer from the confocal waveguide to the cylindrical waveguide. The length of the lens is chosen to be twice the Brillouin length in the confocal waveguide. A HFSS simulation of such a quasioptical transformer for converting the HE_{06} confocal waveguide mode to the TE_{03} mode in an oversized cylindrical waveguide is shown in Fig. 7-15(a). The TE_{03} mode can be converted into a Gaussian beam using well known mode converting techniques. A transformer can also be designed to convert the HE_{06} mode of the confocal waveguide to the TE_{60} mode of an oversized rectangular waveguide as shown in Fig. 7-15(b).

In future experiments a more complete investigation of the internal mode converter has to be carried out as part of the output coupler design for the efficient extraction of the output power from the confocal waveguide to form a TEM_{00} Gaussian beam at the window.

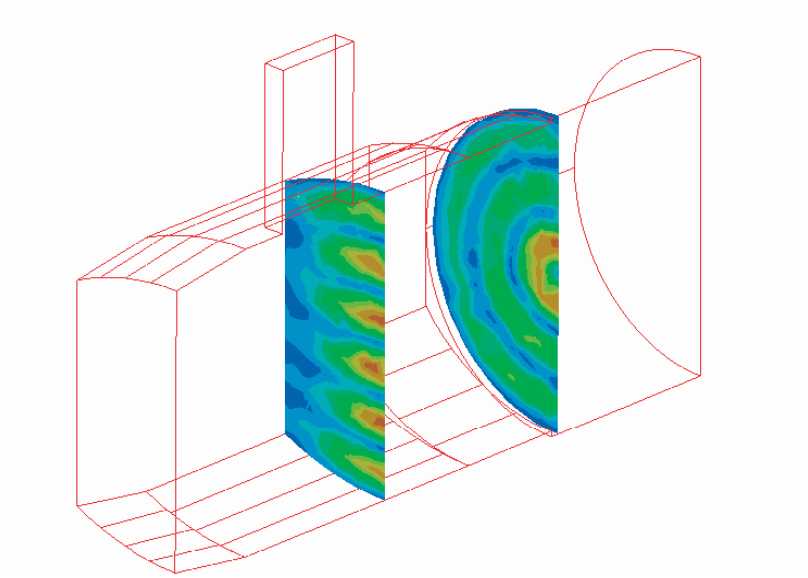

(a) Converter for the HE_{06} mode of the confocal waveguide to the TE_{03} mode of an oversized cylindrical waveguide.

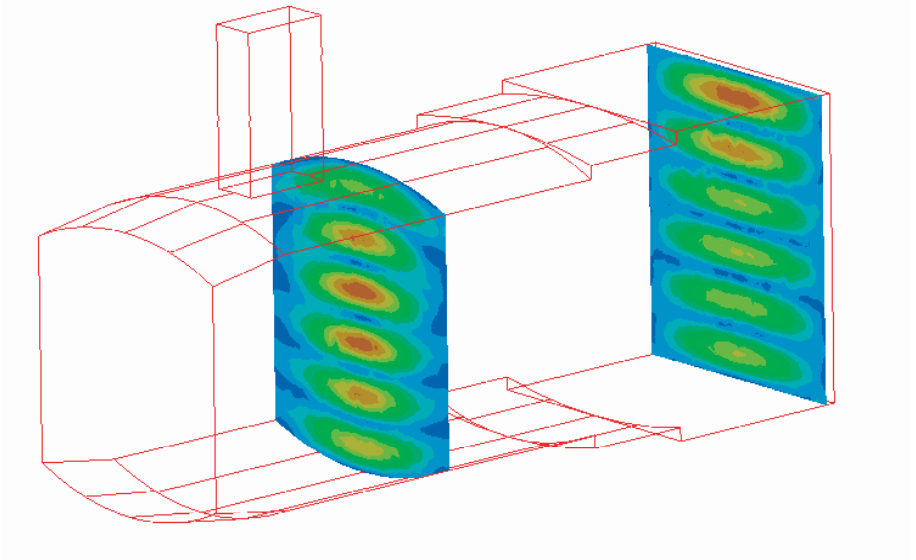

(b) Converter for the HE_{06} mode of the confocal waveguide to the TE_{60} mode of an oversized rectangular waveguide.

Figure 7-15: HFSS simulations of quasioptical transformers for converting the HE_{06} mode of the confocal waveguide to cylindrical and rectangular waveguide modes.

7.1.8 Windows

For high average power operation the choice of a low loss window with a very high thermal conductivity is essential. Typically, megawatt level gyrotrons for fusion applications use a CVD diamond window [193], [194] because conventional Boron Nitride windows cannot meet the average power requirements. CVD diamond windows with up to 10 cm aperture are available these days. A loss tangent of 1.3 $\times 10^{-4}$ at 170 GHz and a thermal conductivity of 1800 W/mK were experimentally confirmed in high power 170 GHz gyrotron experiments reported in [194]. The low loss tangent, high thermal conductivity and mechanical strength of diamond give it unique advantages with the only disadvantage being the high price ($\sim$ USD 100,000). For a CW gyro-TWT operating at 100 kW level in the W-band a CVD diamond window is a good choice.

For a wideband gyro-TWT, say from 92-100 GHz single disc windows cannot provide the necessary bandwidth. A moth eye window [189] or a Brewster angle window [196] are candidates for a wideband window. A moth eye window was tried at a 140 GHz gyrotron oscillator experiment at MIT. The disadvantages of the moth eye window stem from its larger thickness due to the corrugations on its surface. Besides, a material like diamond cannot be machined to form the moth eye surface.

The Brewster angle window is being used in wideband step-tunable gyrotrons [196]. The operating principle is based on the zero reflection for a parallel polarization from a surface for waves incident at the Brewster angle. Furthermore, the power absorbed in a Brewster angle window is lower than that of a multi band-pass window of equal thickness [195]. This makes the Brewster angle diamond window a very good candidate for a wideband high average power gyro-TWT.

In the experiments described in this work we have used single disc fused quartz (Corning 7940) windows at both the input and output ports. The pulsed operation of the tube allows the safe use of fused quartz window without any cooling. Some parameters of the window are listed in Table 7.6.

Material	Corning 7940
Rel. Perm. (ε_r)	1.956
Reflection Coeff.	0.105
Thickness (mm)	3.28 (=3 λ)
Output Window Dia.(mm)	61.21
Input Window Dia. (mm)	38.10
Transm. at (138,140,142 GHz)	0.95,1.00,0.97

Table 7.6: Parameters of the input and output windows used in the gyro-TWT experiment.

7.1.9 Input Transmission Line

A low loss input transmission line relaxes the driver power level as well as the gain requirement of the gyro-TWT to achieve saturated operation. The development of a low loss transmission line can directly benefit from the research and development on ultra low loss transmission lines for transmitting the power from a high power gyrotron to a tokamak for Electron Cyclotron Resonance Heating (ECRH). TE_{on} modes have diminishing wall losses at higher frequencies however, they are unpolarized and produce undesirable conical radiation pattern with zero energy content on the axis. For efficient ECRH an axisymmetric, narrow, pencil-like microwave beam with a well defined polarization is desirable. The HE_{11} mode (hybrid of TE_{11} and TM_{11}) of a corrugated waveguide is the best choice for the above requirements. Furthermore, the transmission loss for the HE_{11} mode is 65 % of that of the TE_{01} mode and for a given loss the bends in a HE_{11} mode can be made much smaller than that of the TE_{01}. The advantages of using HE_{11} mode over the TE_{01} mode are explained in [197].

A low loss input transmission line for the gyro-TWT can be implemented using an HE_{11} corrugated transmission line using contemporary technology. However, the corrugated transmission line is very expensive and hence for the present experiments we have built two oversized transmission lines using standard waveguides and transitions.

The first transmission line is a combination of a standard X-band (8-12.4 GHz) and Ka-band (26.5-40 GHz) waveguide with an E and H plane bend in fundamental mode WR8 rectangular waveguide. The line comprises of the following parts listed sequentially: WR8 to WR28 standard transition, WR28 to WR92 standard transition,

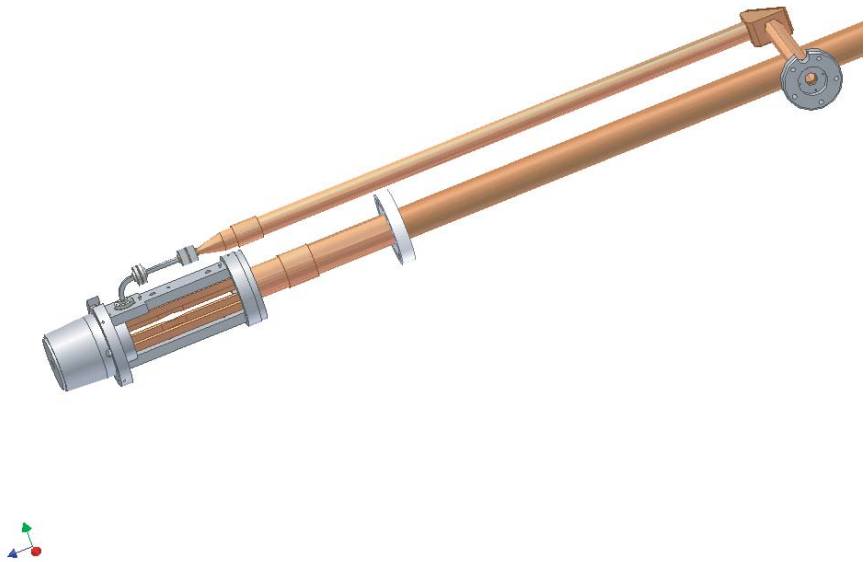

Figure 7-16: CAD drawing of the assembly of the beam tunnel, interaction structure, collector and input transmission line of the confocal gyro-TWT experiments. A part of the beam tunnel is inside the conical piece behind the interaction structure. The outer vacuum jacket with vacion pumps and other diagnostics attached to it and the electron gun are not shown.

WR92 waveguide (2.0 m long), WR92 to WR28 standard transition, input window between WR28 waveguide, WR28 waveguide, WR28 to WR8 standard transition, WR8 90° E-plane bend, WR8 to WR28 standard transition, WR28 waveguide (45 cm long), WR28 to WR8 standard transition and WR8 90° H-plane bend. The line is about 3 m long from the driver (WR8 waveguide) to the input to the confocal waveguide (WR8 waveguide) and includes the input window described in Sec. 7.1.8. The average measured loss for this line over 138-142 GHz was 5.0 ± 1.5 dB. Due to the large number of transitions the line had trapped higher order modes which manifested as sharp resonances over the desired operating band.

The second transmission line uses an oversized 12.57 mm diameter cylindrical waveguide operating in the TE_{11} mode. The 90° bend in the line is directly imple-

mented as a miter bend in the oversized cylindrical waveguide. This line comprises of the following parts listed sequentially: WR8 rectangular to 1.88 mm diameter cylindrical standard transition, 1.88 to 12.57 mm diameter adiabatic uptaper for TE_{11} mode, 12.57 mm diameter cylindrical waveguide (2.0 m long), input window with 12.57 mm diameter, 12.57 mm diameter cylindrical waveguide (11.53 cm long), 90° TE_{11} miter bend in 12.57 mm diameter cylindrical waveguide, 12.57 mm diameter cylindrical waveguide (45 cm), 12.57 to 1.88 mm diameter adiabatic downtaper for TE_{11} mode and 1.88 mm diameter cylindrical waveguide to WR8 rectangular waveguide standard transition. This line is also about 3 m long from the driver (WR8 waveguide) to the input to the confocal waveguide (WR8 waveguide) and includes the input window described in Sec. 7.1.8. The part of this transmission line inside the tube is also shown in Fig. 7-16. The mirror on the miter bend was sliced on both ends to open up the line for efficient pumping inside the vacuum jacket. The base vacuum in the tube was significantly better with this line than the completely closed rectangular waveguide. The measured transmission loss for this line was 3.6 dB ± 0.5 dB over 138-142 GHz. As expected this line had less severe resonances due to trapped modes.

For a gyro-TWT intended for use in a high average power application such as a W-band radar a corrugated transmission line for both the input and output is the most desirable solution. The output Gaussian beam from the window can couple to the HE_{11} mode of the corrugated line with almost 99.0 % efficiency.

7.2 Experimental Setup

The experimental setup is shown in Fig. 7-17. The electron gun is behind the superconducting magnet and its high voltage leads are visible. The VUW-8140 MIG used in the gyro-TWT and gyrotron oscillator experiments is shown in Fig. 7-18. An Extended Interaction Klystron (EIK) driver capable of producing up to 200 W peak power in the 139-142 GHz range was used to drive the gyro-TWT. The driver can be operated at up to 2 μs pulses at a total duty cycle of less than 0.5 %. The driver is

Figure 7-17: The confocal gyro-TWT experiment with Mr. Ivan Mastovsky. The high voltage leads for the electron gun and the high voltage modulator are visible behind the superconducting magnet. The EIK driver (not visible in this picture) is located behind the grey cabinets.

mechanically tunable with stepper motor and a bellows attachment to the EIK. The driver and some diagnostics attached to it to observe the BPWO are shown in Fig. 7-19. The high voltage modulator used in the experiments is described in Sec. 4.1. The frequency is measured by a heterodyne receiver system described in Sec. 4.3. The output power was measured by one of the two dry calorimeters described in Sec. 4.4.

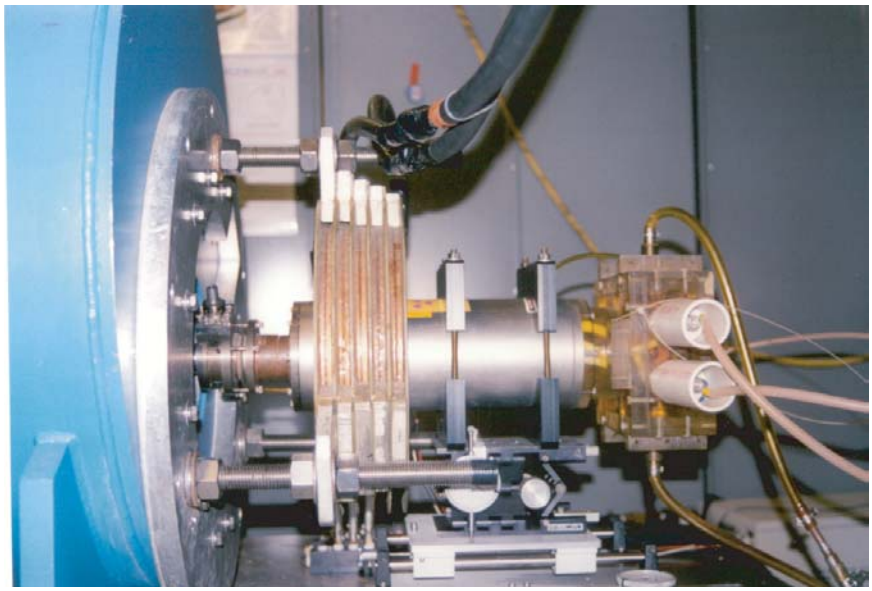

Figure 7-18: The VUW-8140 MIG used in the gyro-TWT and gyrotron oscillator experiments. A copper gun solenoid centered on the cathode and the gate valve used to isolate the gun are also shown.

Figure 7-19: The 140 GHz, 200 W EIK driver used in the confocal gyro-TWT experiments. The power supply for the EIK is also shown. A wavemeter and a diode to measure the power and frequency of the BWO is also visible.

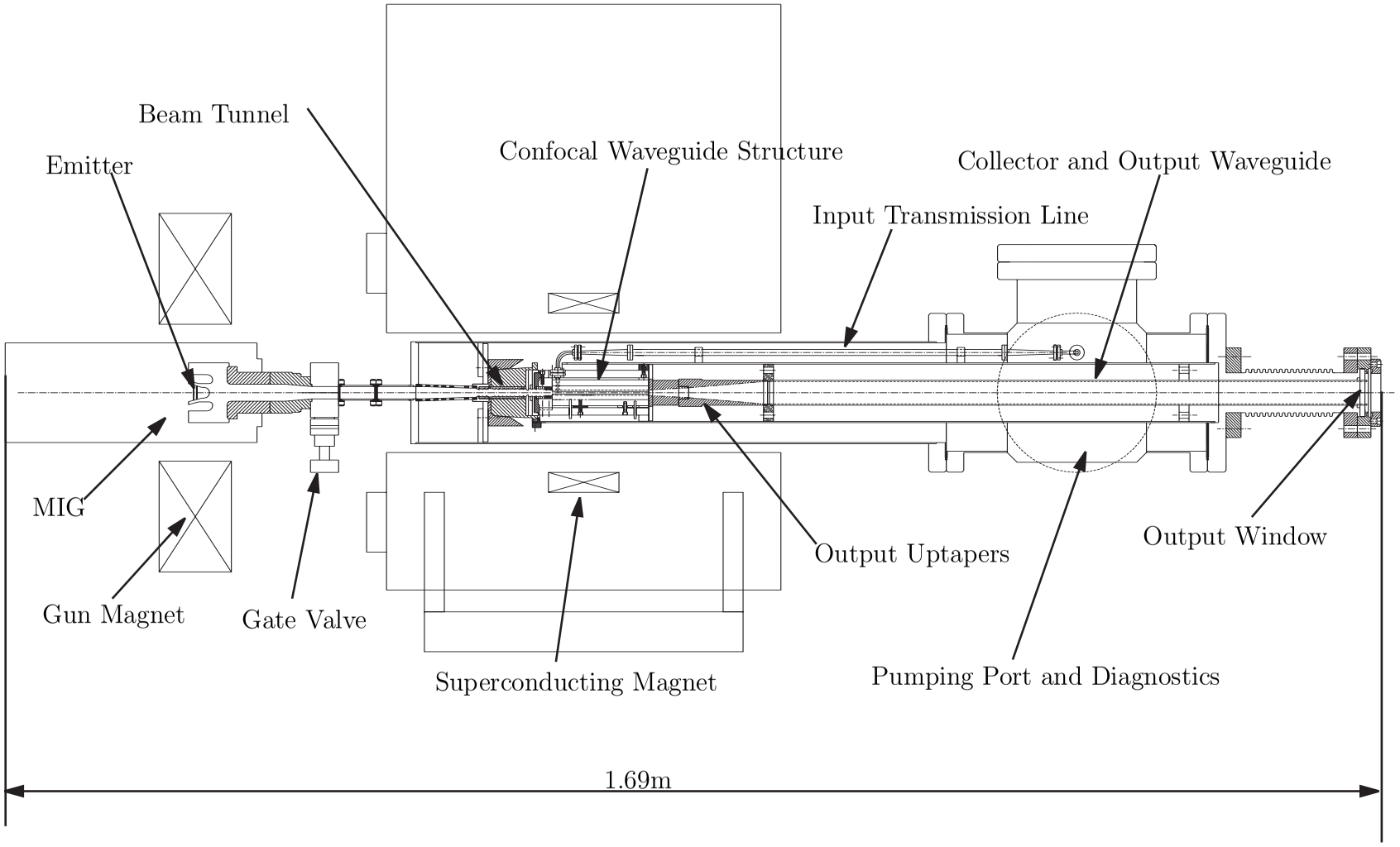

Figure 7-20: CAD drawing of the confocal gyro-TWT experiment. The Vacion pumps and other diagnostic features are not shown.

7.3 Experimental Results

The gyro-TWT was operated over a wide range of parameters to find the optimum operating point and observe the deterioration in its performance with the detuning of various operating parameters. Oscilloscope traces from a typical shot are shown in Figs. 7-21 and 7-22. The shape of the body current can be explained by the charging and discharging of the capacitance associated with the tube body during a voltage pulse. The signal from the beam velocity pitch (alpha) probe is also shown in Fig. 7-21(b). The voltage induced on the probe is proportional to the beam current and the axial velocity of the electron beam and can be used to compute the velocity pitch ratio (α) using the method described in Sec. 4.5. During the shot shown in Figs. 7-21 and 7-22, $\alpha \approx 0.7$ in the flat top region of the voltage pulse. Typically, during the rise and fall time of the voltage pulse the local values of α can be quite higher than the value of α at the flat top of the voltage and thus sparking either BPWO or gyrotron oscillations in the shape of rabbit ears sandwiching the amplified signal as shown in Fig. 7-23(b). Since any beam instability in the beam tunnel couples to the Alpha probe signal it provides a way to monitor any beam instabilities in the beam tunnel. Gyrotron oscillations at 137.46 GHz were observed during the ramp down of the voltage pulse. This is a cut-off oscillation of the HE_{06} mode. The 130.74 GHz oscillation frequency could not be identified as any confocal waveguide mode oscillation and hence was being generated either in the beam tunnel or in the output uptapers. If the velocity pitch factor is increased above $\alpha > 1.5$ we see strong oscillations inside the beam tunnel as evidenced in the unstable signal from the Alpha probe shown in Fig. 7-23(b). The output RF signal shows a sharp increase in power due to a transition from the amplifying to the self oscillatory regime.

In the present experiments we did not use a lossy dielectric shell to absorb the power radiated by the sever into the vacuum jacket. Some of the radiated power after multiple reflections can couple back into the circuit thus lowering the threshold of the operating current for generating BPWO. However, the demonstration of up to 29 dB linear gain is a strong indication that the quasioptical sever is working well. To our

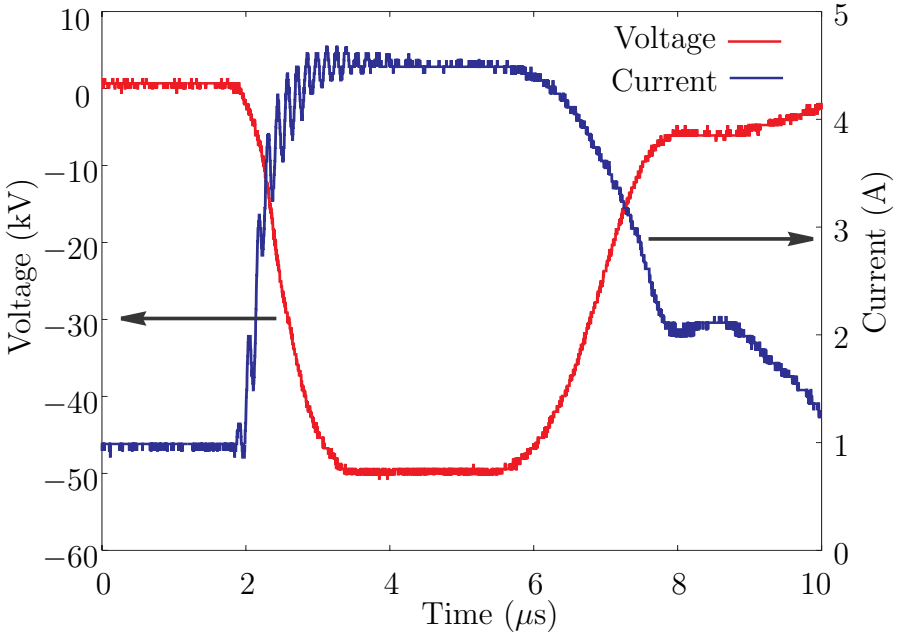

(a) The beam voltage and current.

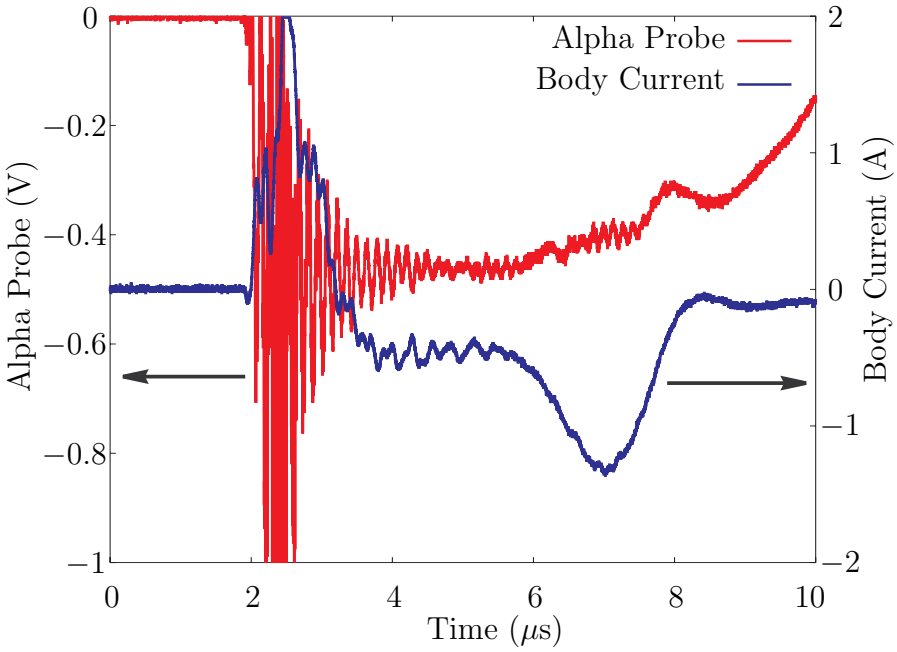

(b) The signal on the Alpha probe and the body current.

Figure 7-21: Oscilloscope traces of the electron beam signals during a typical shot in the gyro-TWT operation.

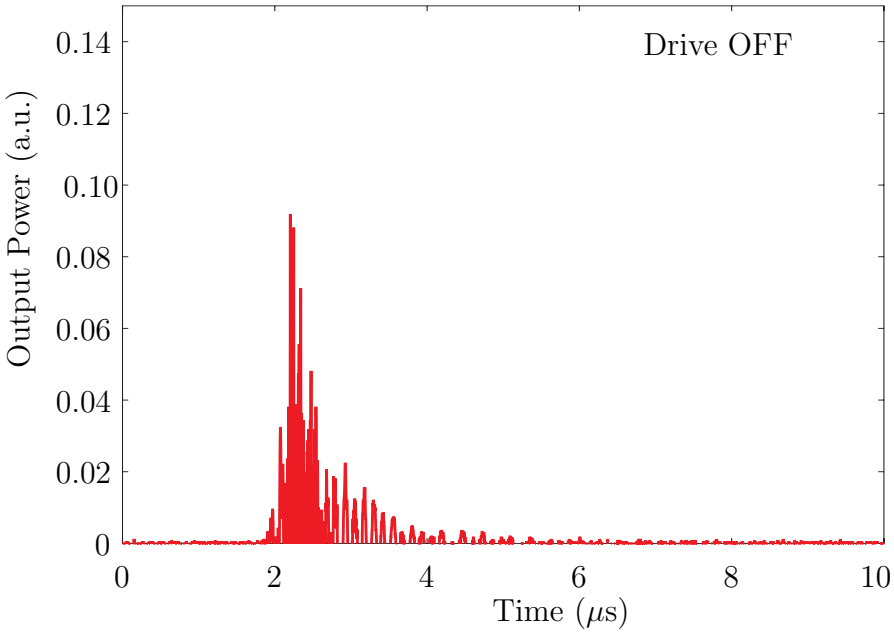

(a) The detector signal monitoring the output power with the drive turned OFF.

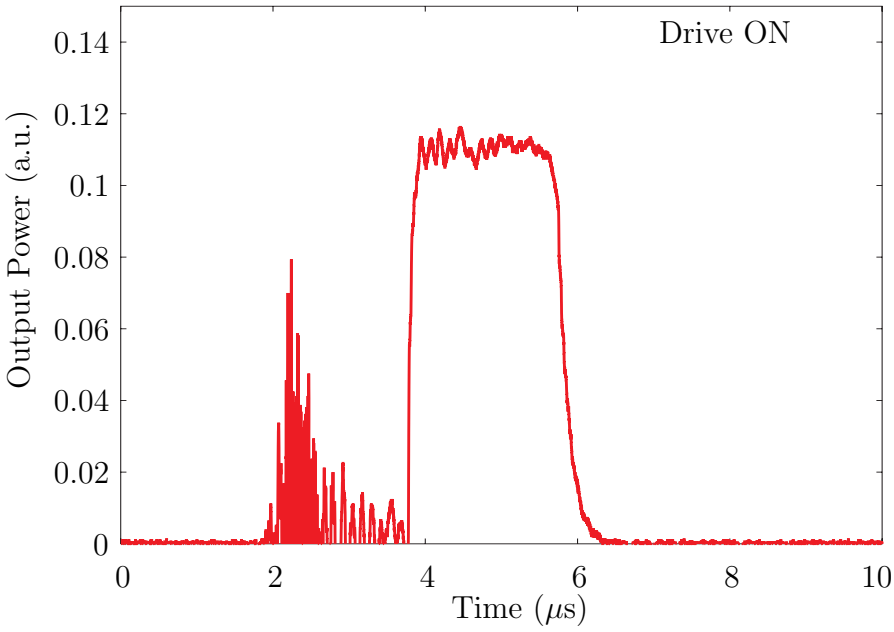

(b) The detector signal monitoring the output power with the drive turned ON.

Figure 7-22: Typical oscilloscope traces from the detector monitoring the output RF power when the drive is tuned ON and OFF. The large amplitude noise begining at 2 μs and gradually decaying is actually the electrical noise from the switching of the voltage pulse.

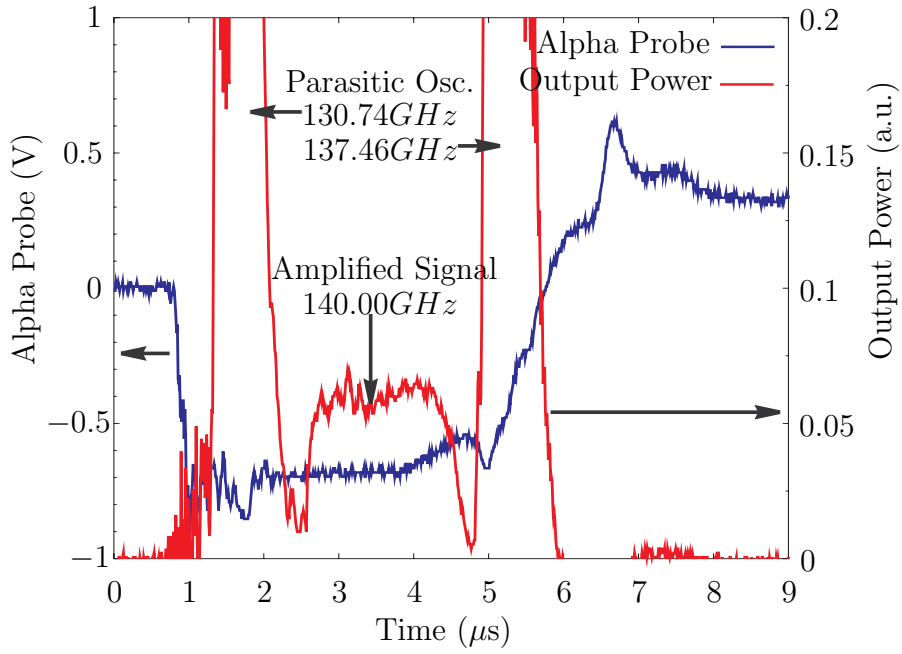

(a) The onset of cut-off gyrotron oscillations at due to a high value of α. during the voltage ramp up and ramp down.

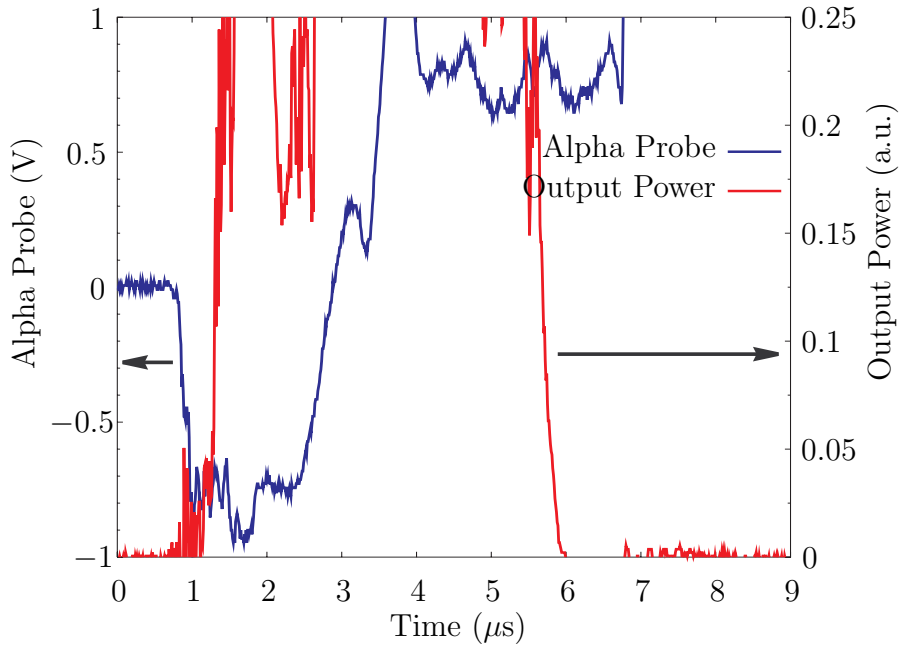

(b) For high values of α the beam instability in the beam tunnel couples to the Alpha probe signal driving it unstable.

Figure 7-23: Typical oscilloscope traces of the electron beam signals during a typical shot with a high value of α in the gyro-TWT operation.

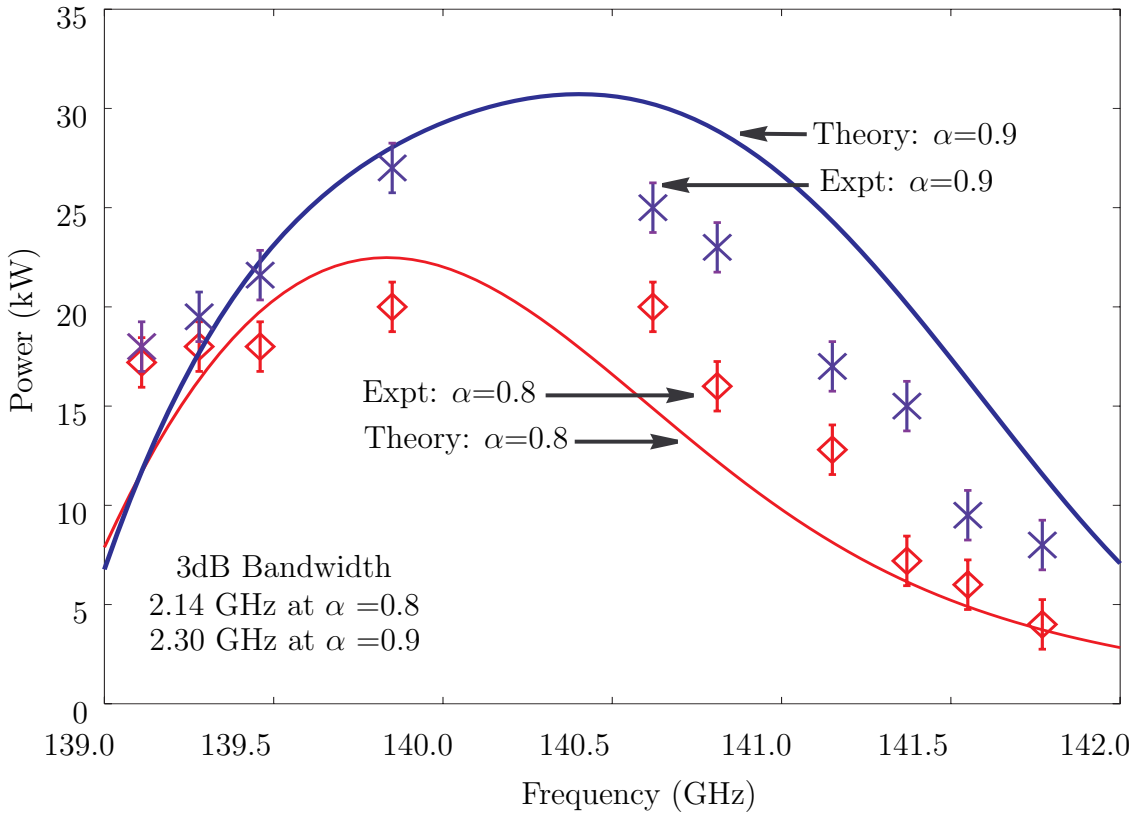

Figure 7-24: Comparison of the experimentally measured bandwidth with theoretical predictions fo $V_0 = 50$ kV, $I_0 = 3.9$ A and $\Delta v_z/v_z =$ 3 % was assumed for $\alpha = 0.8$ and 5 % for $\alpha = 0.9$.

knowledge, this is the first time that such a diffraction sever has been implemented in a high power VED.

The zero drive stability of the amplifier is shown in Fig. 7-22. These particular traces were for a velocity pitch factor of $\alpha \approx 0.7$.

Typical frequency bandwidth characteristics of the amplifier are shown in Fig. 7-24. The amplifier could not be run in a zero drive stable condition for $\alpha > 1.0$ and the optimum performance was observed around $\alpha = 0.9$. A 3 dB bandwidth of 2.30 GHz was measured at $\alpha = 0.9$ and 2.14 GHz at $\alpha = 0.8$. The experimentally measured output power is in fairly good agreement with the results from the single particle nonlinear code described in Sec. 2.8.2. Theoretical results indicate a higher bandwidth for $\alpha = 1.0$ however, in the experiment a peak power of only 7 kW and

a 3 dB bandwidth of 1.97 GHz was measured for $\alpha = 1.0$. A longitudinal velocity spread of 3 % and 5.0 % was used in the theoretical calculations for $\alpha = 0.8$ and 0.9, respectively. These values were obtained from EGUN simulations. The actual velocity spread in the experiment is expected to be higher than the EGUN predictions which do not include the effect of surface roughness of the emitter, temperature nonuniformity on the surface of the emitter, work function spread of the emitter and magnetic field inhomogeneity, and local electric field inhomogeneity. The biggest contribution to the velocity spread comes from the surface roughness of the emitter [198]. The lack of increase in power and bandwidth at $\alpha \geq 1.0$ can be due to the following reasons. The quality of the electron beam, especially the velocity spread increases rapidly for $\alpha \geq 1.0$ causing a sharp drop in the gain and output power at higher frequencies. It is well known that a higher velocity spread is more detrimental to higher frequencies which have a larger Doppler upshift ($k_z v_z$). HFSS simulations indicate that the present design of the input coupler works well in the range of 139-141.5 GHz and its coupling efficiency deteriorates rapidly above 141 GHz. The nearly identical bandwidth obtained for $\alpha = 0.9$ and $\alpha = 0.8$ may be explained in terms of the overall system bandwidth being limited by the bandwidth of the input coupler. The peak efficiency in this set of runs is 11.6 %. Also, there was evidence of beam tunnel oscillations at $\alpha \geq 1.0$.

The amplifier could not be driven to saturation due to a lower value of gain obtained experimentally. The peak experimental gain in the runs shown in Fig. 7-24 was 26 dB. Peak power of up to 20 kW was measured at a gain of 29 dB with 2 GHz bandwidth at a voltage of 70 kV and a beam current of 4.0 A. The gain was limited in the experiment primarily due to the short flat field region of the superconducting solenoid. The 0.5 % magnetic field homogeneity at the center of the superconducting solenoid is limited to 5.0 cm which prevents achieving the optimum high gain and saturation in the amplifier. For a crossing intersection between the beam mode dispersion line and the waveguide mode dispersion a peak power of up to 30 kW was measured over a narrow bandwidth of 0.3 GHz.

For simplicity the present experiments did not use an internal mode converter

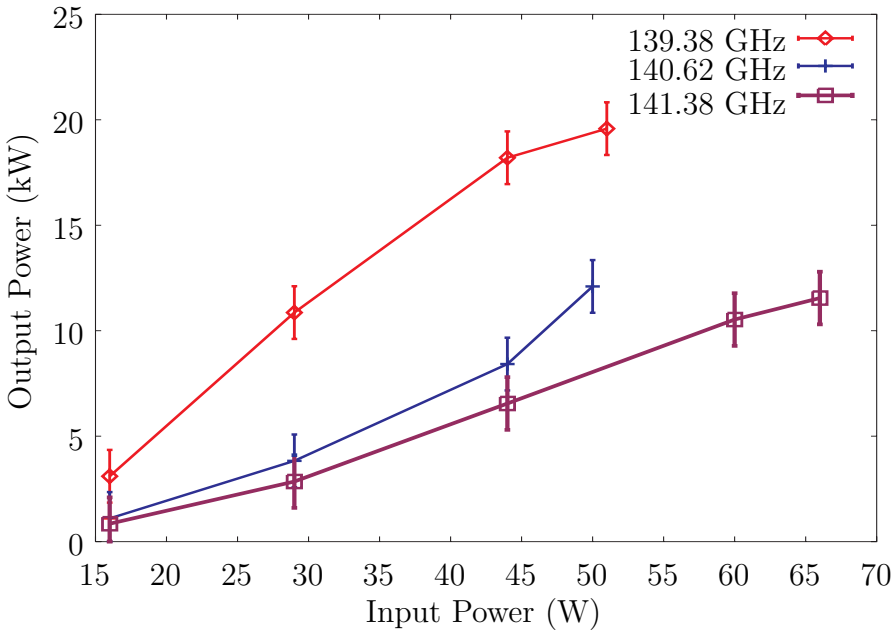

Figure 7-25: Linearity characteristics of the confocal gyro-TWT. The operating parameters are $V_0 = 70$ kV and $I_0 = 4.0$ A.

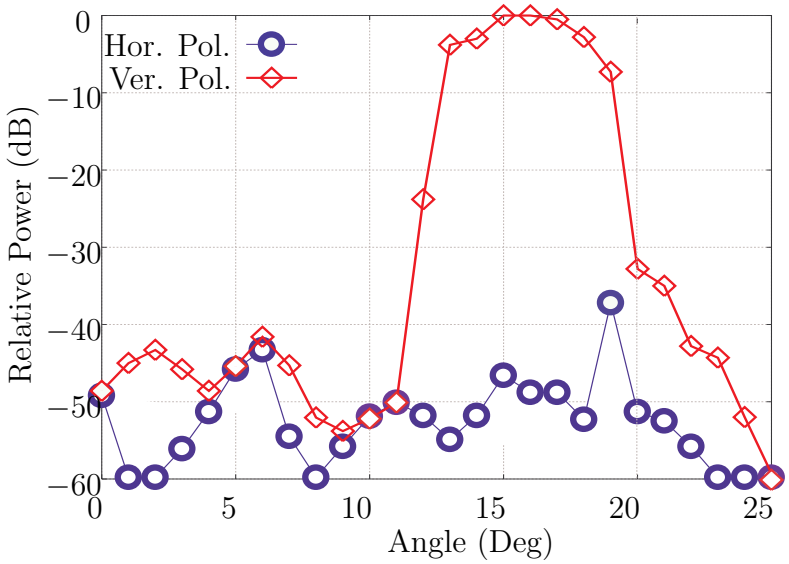

Figure 7-26: Experimentally measured far field pattern of the amplified signal. The receiving horn is located on the axis of the collector and the data are taken along the azimuth in the horizontal plane.

as part of the output coupler as explained in Sec. 7.1.7. Two simple adiabatic uptapers designed assuming a TE_{03} incident mode (the TE_{03} mode in a cylindrical waveguide corresponds to the HE_{06} mode of the confocal waveguide) were used in the experiments. A measurement of the far field radiation pattern yielded a startling purity in the polarization and directivity of the radiation emerging from the window. A plot of the far field radiation pattern from the gyro-TWT at 140.58 GHz is shown in Fig. 7-26. The polarization of the radiation emanating from the window is primarily vertical with a very low content of the horizontal polarization. The main lobe of the radiation emerges at an angle of 15°. The theoretical far field radiation pattern for a mode from an open cylindrical waveguide [199] is

$$P = P_0 \left[\frac{(k_z + k\cos\theta)\, J_m^{'}(kr_w \sin\theta)}{1 - (k\sin\theta/k_t)^2} \right], \tag{7.1}$$

where P_0 is a normalization constant, $k,\ k_z,\ k_t$ are the free space, axial and transverse propagation constants, respectively, r_w is the waveguide radius, $k_t = \nu_{mn}/r_w$ and ν_{mn} is the n^{th} root of $J_m^{'}(x)$. From the above equation it is evident that in the case of no mode conversion, the main lobe of the radiation pattern occurs at $\theta \simeq \sin^{-1}(k_t/k)$ or $\theta \simeq \sin^{-1}(R_o/r_w)$ where R_o is the radius of exit of interaction structure assuming it is a cylindrical pipe. In our case the value of R_o was chosen so that at the transition between the confocal waveguide and the first cylindrical uptaper the transverse propagation constant in both sections is matched. In our case r_w is the collector radius which also serves as the output waveguide. Using $R_o = 3.52$ mm and r_w =14.22 mm we find that for the case of a pure TE_{03} mode the main lobe should be directed at 14.3° which is very close to the 15° measured in the experiment. For a pure TE_{03} mode two lower lobes power (≈ -8 dB from the main lobe) are also present which were not measured in the experiment. This suggests that the emanating mode is probably a combination of TE_{03} ($\nu_{mn} = 10.1735$) and TE_{23} ($\nu_{mn} = 9.9695$) modes in a particular phase relationship which leads to the suppression of the two inner sidelobes. Since this is not the desired configuration of the output coupler further analysis was not performed to estimate the mode purity and the phase relationship

between the constituents of the mode mixture.

7.4 Discussion

The successful operation of this experiment has demonstrated several novel concepts for a high average power W-band amplifier. This is the first gyro-TWT experiment with a highly overmoded, mode selective, quasioptical confocal waveguide interaction structure. Furthermore, this is the first high power gyro-TWT experiment at 140 GHz which is a much higher frequency than the 94 GHz necessary for a W-band radar. While other contemporary gyro-TWT experiments [79], [83], [85] use either the fundamental waveguide mode, the TE_{01} mode or a lower order hybrid mode at the Ka-band (35 GHz) to avoid the problems associated with mode competition, our gyro-TWT experiment uses a highly overmoded quasioptical open interaction structure for allowing larger circuit dimensions for high average power operation. Mode competition is suppressed in this highly overmoded interaction structure by the effective use of diffraction from the open sidewalls of the interaction structure. The mirror separation is 6.79 mm in the present 140 GHz experiments using an HE_{06} mode and a scale down of this design to 94 GHz will ensure even a larger size of the interaction structure or allow the possibility of operation in the next lower order mode, the HE_{05} to improve the gain per unit length. The highly overmoded interaction structure can be easily scaled for higher frequency operation. For example, a 100 W, 460 GHz gyrotron oscillator being developed at MIT [89] for use in DNP/NMR experiments could be built as a confocal gyrotron amplifier at the same frequency with added advantages of phase control and easy switching of the high power 460 GHz signal by merely switching the low power driver.

The other novel feature demonstrated in these gyro-TWT experiments is the use of a high average power capable diffraction sever described in Sec. 7.1.6. The highly overmoded quasioptical circuit allows the easy extraction of power from the interaction structure to suppress the Backward Propagating Wave Oscillation (BPWO). The successful operation of the diffraction sever qualifies another new concept in

overmoded quasioptical circuit elements.

The average ohmic heating density (W/m^2) is the most important criteria for the choice of an interaction structure in a high average power device. For the HE_{06} mode at 140 GHz used in this experiments, for 100 kW average power operation, the average ohmic heat density is 0.65 kW/cm^2 for ideal copper at room temperature ($\sigma = 5.7 \times 10^7\ \Omega^{-1}\ m^{-1}$). If the conductivity of annealed Oxygen Free High Conductivity (OFHC) copper at 250° C is assumed with $\sigma = 3 \times 10^7\ \Omega^{-1}\ m^{-1}$ the average ohmic heating density is 0.9 kW/cm^2. The average ohmic heat density scales as $\sigma^{-0.5}\omega^{2.5}$ [45]. For a 94 GHz gyro-TWT designed with the same HE_{06} operating mode average ohmic heat density is 0.24 kW/cm^2 for ideal copper at room temperature and 0.33 kW/cm^2 for annealed OFHC copper at 250° C. These average ohmic heat density numbers are well below the 1-2 kW/cm^2 limit for contemporary cooling technology.

This confocal gyro-TWT is the only high power gyro-TWT experiment demonstrating the performance needed for a high average power wideband amplifier needed for a state-of-the-art 94 GHz radar. In these initial experiments we have not focussed on building a wideband device, however the 2.3 GHz (1.6 %) unsaturated bandwidth achieved so far is very promising. The theoretical estimate for the saturated bandwidth is 4.0 GHz (2.8%) at 140 GHz but could not be measured in the experiments because saturation could not be achieved due to a lower than expected gain. The gain was limited by the short flat field region of the superconducting magnet. Well known design techniques of simultaneously tapering the magnetic field and the interaction structure to improve the bandwidth [66], [74] can be easily incorporated in the confocal waveguide.

The present experiments have demonstrated an unsaturated efficiency of 11.6 % which implies that the saturated efficiency will be higher. The theoretical design efficiency for the present device with a high quality electron beam and a sufficiently long flat field of the superconducting magnet is 28 %. This can be further increased by using a depressed collector or a sectored electron beam with electrons only in the region of the confocal waveguide fields.

The performance of this confocal gyro-TWT was limited by the electron beam

quality and the short flat field region of the superconducting solenoid used in the experiments. The electron gun and the superconducting magnet were used from prior gyrotron oscillator experiments and hence were not optimized for the gyro-TWT experiment, however they proved to be very useful in the quick demonstration of the proof-of-principle of using highly overmoded yet mode selective interaction structures for high average power ($>$ 10 kW) gyro-TWTs in the W-band and beyond.

The confocal gyro-TWT has many advantages but it also has a few disadvantages compared to the standard cylindrical waveguide interaction structure. The open side walls of the interaction structure imply the absence of a ground plane close to electron beam in those regions which increases the voltage depression in the electron beam which may result in an increased velocity spread in the electron beam. The loss in symmetry of the mode due to open side walls reduces the coupling of the electron beam to the mode and thus lowers the efficiency of the device. A sectored electron beam with electrons only in the region of the confocal waveguide fields can be used to improve the efficiency. While operation at a higher order mode lowers the average ohmic heat density it also lowers the gain per unit length of the interaction structure. This in turn would imply a longer interaction structure which is not very desirable due to the problems associated with transporting and maintaining a high quality of the electron beam over large distances. The interaction length in our scheme (12 cm = 56 λ at 140 GHz) is about twice that reported in [83] (27 cm = 32 λ at 35 GHz) for the heavily loaded interaction circuit. Migration to the HE_{05} mode can increase the gain which will help reduce the length of the interaction structure. The heavily loaded interaction structure being pursed at NTHU [76], [77] and NRL [83] can suppress the BPWO and the absolute instabilities very effectively because most of the absolute instabilities have a predominantly backward power flow [76] and hence a heavily loaded section located upstream preferentially attenuates the parasitic oscillatory modes. In the confocal waveguide by a proper choice of the waveguide aperture the contrast in the diffraction losses of the operating mode and the lower order parasitic modes can be dramatically increased to stabilize BPWO. However, such stabilization of the absolute instability in the form of gyrotron oscillations at

the cut-off the operating mode can not be done very effectively.

The heavily loaded scheme also called the distributed loss scheme in contrast to the localized loss (sever section as in our experiments) can be easily implemented in a confocal waveguide by profiling the aperture of the mirrors. This scheme would allow stable operation at a very high gain in an overmoded circuit. This confocal gyro-TWT experiment has advanced the state-of-the-art in W-band high average power capable amplifiers. This is a welcome development for many novel radar and communication applications in the W-band.

Chapter 8

Discussion and Conclusions

The successful demonstration of two gyrotron oscillators and a gyro-TWT amplifier experiment during the course of this work has firmly established a novel approach to building high frequency (> 100 GHz) millimeter wave sources and amplifiers by the approach of using highly overmoded yet mode selective interaction structures. Two different classes of novel mode selective interaction structures namely, Photonic Band Gap (PBG) structures and quasioptical open confocal structures were investigated and were used in high power gyrotron experiments to demonstrate their advantages. The work involved the first demonstration of a high power Vacuum Electron Device (VED) with a PBG interaction structure and the first quasioptical gyrotron amplifier. Linear and nonlinear theory of gyrotron amplifiers was also developed based on prior theoretical work by others and the theory was modified to suit the novel kind of interaction structures used in our experiments. Independent computer codes were developed for the design and optimization of the gyrotron experiments. Good agreement was obtained between the theoretical design and the experimental results

8.1 PBG Structure Based Experiments

During the course of this work the first Vacuum Electron Device (VED) with a PBG structure was demonstrated. A highly overmoded PBG resonator operating in the TE_{041} mode was used as a cavity resonator in a 140 GHz gyrotron. The gyrotron

showed no excitation of spurious modes over 30 % tuning of the magnetic field which corresponds to an equal tuning of the cyclotron frequency thus confirming the mode selectivity of the PBG resonator. A peak power of 25 kW was generated at 140 GHz without any mode competition. The absence of other competing modes in the vicinity of the operating mode allows access to the high efficiency regime of the operating mode. The biggest advantage of using a PBG resonator is that it allows the operation in a very higher order mode allowing the transverse dimensions of the interaction structure to be many times the operating wavelength. This is very crucial for building millimeter and sub-millimeter wave microwave sources where the diminishing wavelength dramatically complicates the fabrication process and reduces the thermal capability of the interaction structure which prevents high power operation.

In the PBG gyrotron experiments we chose an all metal PBG structure for its mechanical strength and high thermal conductivity. However, in the case of VED's using TM modes (such as conventional TWTs and klystrons), a simple metal PBG structure may not prove to be the panacea for suppressing mode competition. In the case of TM modes the presence of a zero order band gap as seen in Fig. 3-5, ensures the confinement of lower order modes. This prevents the use of a higher order mode like that in the case of the gyrotron experiment, without risking excitation of lower order parasitic modes. However, the presence of passbands above the zero order band gap present the opportunity to suppress competition from the nearest neighboring TM_{110} ($\nu_{11} = 3.8317$) mode while operating in the TM_{010} ($\nu_{11} = 2.4048$) mode. This is attractive for a conventional klystron at 35 GHz. Such design techniques can also be used to suppress the wakefields in TM_{010} mode accelerator cavities [158]. It must be mentioned that some slow wave devices use TE mode interaction structures such as the TE_{10} mode folded waveguide TWT [200] and hence may directly use metallic PBG structures in the form of a PBG waveguide.

Dielectric PBG structures have been widely studied and their applications in passive waveguide bends [151] and optical fibers [152] are well known. The TM mode global band gaps for dielectric structures [149] provide more design space for mode control. Dielectric structures can be a choice for either low or high Q resonators.

The use of lossy dielectrics in part of or the entire array can bring down the Q of the desired modes to make them stable to self excitation in the presence of an electron beam. This is a very important consideration for gyroklystrons as explained in Section 3.1.3. The use of low loss dielectrics at very high frequencies (up to THz) where, metals are quite lossy can make the design of very high Q resonators feasible. Numerous applications for such resonators come to mind – interaction structures for future Terahertz VED sources, dielectric waveguides and so forth. Microscale dielectric PBG structures can be grown using the well developed techniques of fabricating semiconductor devices in microelectronics.

8.2 Quasioptical Structure Based Experiments

The other class of mode selective structures investigated during this work are quasioptical open waveguides and resonators. Quasioptical structures are oversized and are favorable for high power operation. The use of open boundaries allows the use of diffraction as a powerful tool to suppress the parasitic modes. A high contrast in the diffraction losses between the operating mode and the lower order parasitic modes by a proper choice of the mirror aperture has demonstrated stable single mode operation over a wide range of operating parameters in a confocal gyrotron oscillator experiment.

During the course of this work Ansoft HFSS was successfully used to model the various quasioptical open components in the experiments. Significant insight was gained in modeling of the open boundaries in the quasioptical structures using HFSS. The good agreement in between the theoretical results from the confocal gyro-TWT and the experiments validates the design techniques used during the course of this work.

8.2.1 Confocal Gyrotron Oscillator

An overmoded confocal gyrotron oscillator was successfully operated without any mode competition over a wide range of parameters. The absence of competing modes

in the vicinity of the main operating mode (HE_{061}) is a big advantage when compared to the conventional cylindrical resonator operating in an analogous TE_{031} mode where the excitation of the nearly degenerate TE_{231} mode prevents access to the high efficiency operating regime of the TE_{031} mode. A peak power of 83 kW was produced at an efficiency of 16 %. An enhancement in efficiency by the use of a depressed collector and a sectored electron beam is possible.

8.2.2 Second Harmonic Confocal Gyrotron Oscillator

A second harmonic confocal gyrotron oscillator experiment was designed, built and tested. The better confinement of the higher order modes in a confocal waveguide can be used for selective interaction of higher beam cyclotron harmonics with a higher order waveguide mode while suppressing the stronger fundamental mode interaction. This principle was used in the design of the second harmonic confocal gyrotron oscillator at 280 GHz. A relatively poor beam quality was the most likely reason for the failure to generate the second harmonic in the experiment however, the stabilization of the fundamental mode interaction verified the basic principle of the design. With a higher quality electron beam ($\sim$ 3% transverse spread) the second harmonic generation should be possible.

8.2.3 Confocal Gyrotron Traveling Wave Amplifier

The successful demonstration of stable high power operation of the overmoded confocal gyro-TWT experiment during the course of this work has led to the advancement of the state-of-the-art in high average power capable amplifiers in the W-band. A peak power of up to 30 kW was generated at 140 GHz and an unsaturated bandwidth of 2.30 GHz was measured when the peak power at the center of the band was 27 kW peak power. A peak efficiency of 11.6 % was measured in the experiments. Since the output power of the tube could not be saturated due a lower gain in the experiment as a result of the short flat field region of the superconducting magnet, a higher saturated bandwidth and efficiency is expected in an optimized design using

Anode Voltage	65 kV
Mod Anode Voltage	17 kV
Beam Current	6.0 A
Velocity Ratio	1.5
Transverse Velocity Spread	1.6 %
Max. Beam Radius	1.23 mm
Beam Guiding Center	0.80 mm
Circuit Magnetic Field	3.6 T
Magnetic Compression	25
Cathode Current Density	6.76 A/cm^2

Table 8.1: Optimum parameters of a 94 GHz MIG available from CPI Inc., CA [201].

a superconducting magnet with a sufficiently long flat field region. A higher quality electron gun than the one used in these initial experiments can further improve the performance of the gyro-TWT. To estimate the performance of a similar gyro-TWT in the W-band (94 GHz) which would be useful for a W-band radar we performed an initial design study in Sec. 8.3.

8.3 W-Band Confocal Gyro-TWT: An Initial Design Study

In this section we present a preliminary design for a W-band confocal gyro-TWT at 94 GHz. This design will allow us to estimate the performance of a 94 GHz version of the present 140 GHz experiment which would be of great interest for a W-band radar transmitter.

We based our design on an existing high quality triode MIG available from CPI Inc., CA. This gun [201] was developed for the W-band gyroklystron and gyrotwystron experiments performed at NRL and CPI. The quoted parameters for the electron gun are shown in Table 8.1.

We chose the HE_{04} mode Fig. 3-12(c) of the confocal waveguide so that the beam radius of the CPI gun falls on a maximum of the electric field. In this initial design study we assumed a tapered interaction structure to improve the bandwidth of the device. The strongest backward wave interaction will be between the HE_{03}

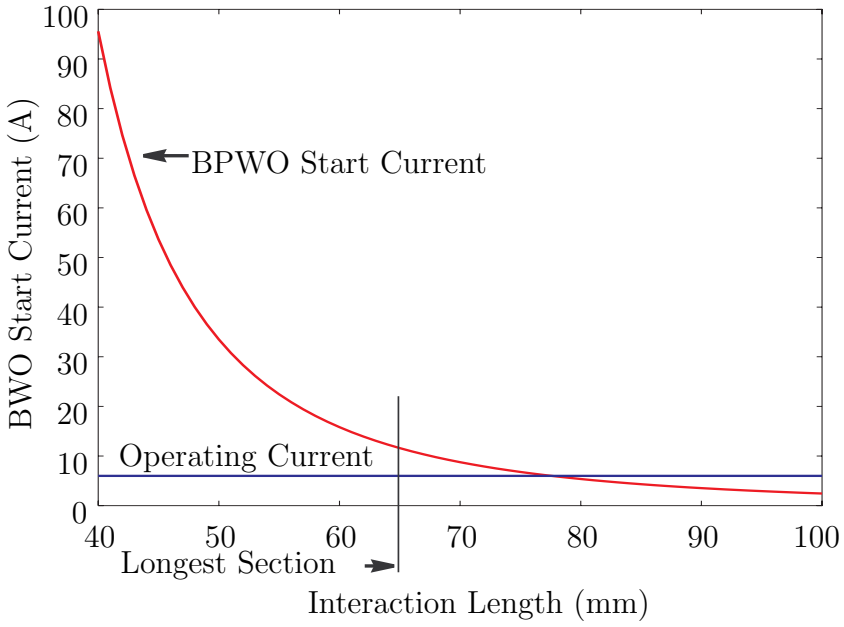

Figure 8-1: Variation of the threshold current for the excitation of BWO in the W-band gyro-TWT. The operating parameters are listed in Tabs. 8.2 and 8.3.

mode and the s = 1 fundamental beam cyclotron mode. The variation in the start oscillation current for BPWO in the HE_{03} mode with the length of the interaction structure is shown in Fig. 8-1. The BPWO threshold current was calculated for the case of zero beam velocity spread and assuming a uniform interaction structure with dimensions equal to that at the start of the profiled interaction structure listed in Tab. 8.2. It is evident that the length of each gain section has to be below the threshold length of 77 mm for the 65 kV and 6 A. The length of each gain section, the sever and the overall profile of the interaction structure were optimized to get the highest constant drive saturated bandwidth. The magnetic field is simultaneously tapered with the dimensions of the interaction structure to maintain a near grazing intersection (B_0=0.985 B_g) of the beam mode and the waveguide mode at every point along the interaction structure. This linear tapering of the magnetic field profile can be reasonably generated with a superconducting solenoid with three or more coils. In Fig. 8-2 we show the spatial evolution of the amplified signal at 92.25 GHz.

Although no significant gain is observed in the first section there is very good

Parameter	First Section	Sever	Second Section
Mirror Seperation (r_c) at the start	7.00 mm	7.00 mm	7.00 mm
Mirror Seperation (r_c) at the end	6.48 mm	7.00 mm	7.10 mm
Mirror Aperture ($2a$) at the start	7.00 mm	7.00 mm	7.00 mm
Mirror Aperture ($2a$) at the end	7.00 mm	7.00 mm	7.00 mm
Length	65 mm	15 mm	50 mm

Table 8.2: Dimensions of the confocal interaction structure for the 94 GHz gyro-TWT.

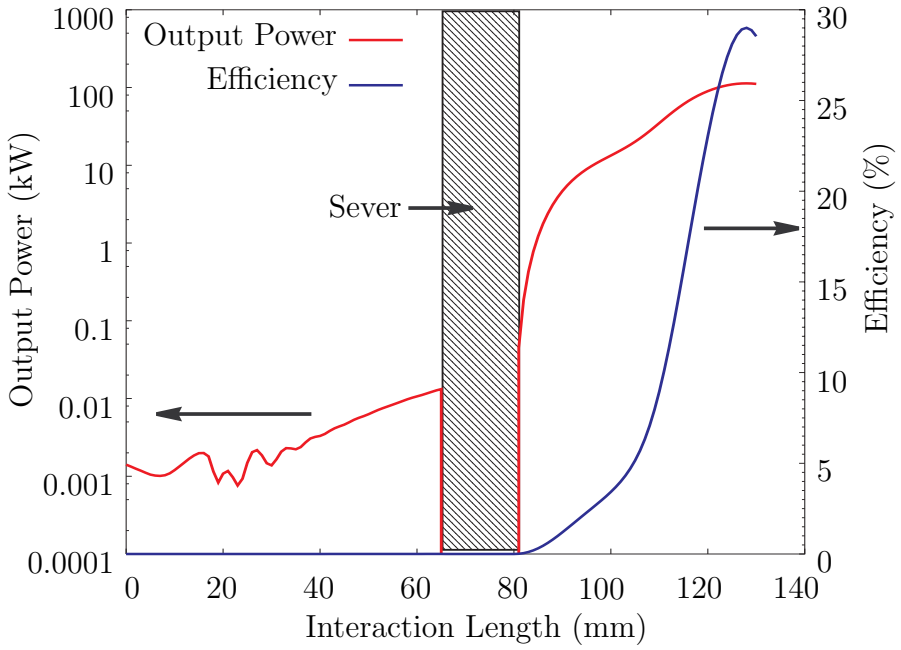

Figure 8-2: Constant drive saturated bandwidth characteristics of the W-band gyro-TWT.

bunching of the electron beam which results in a rapid power buildup in the second section. The distributed nature of the interaction structure due to the tapering allows the optimum interaction of each frequency with the electron beam at different points along the length of the interaction structure. If good bunching is achieved in the first section even a mildly tapered second gain section as listed in Tab. 8.2 is sufficient to achieve a wide band amplification.

The sever section between the two gain sections can be a quasioptical diffraction sever as used in the 140 GHz gyro-TWT experiments described in Chapter 7.

The constant drive saturated bandwidth characteristics of the W-band gyro-TWT

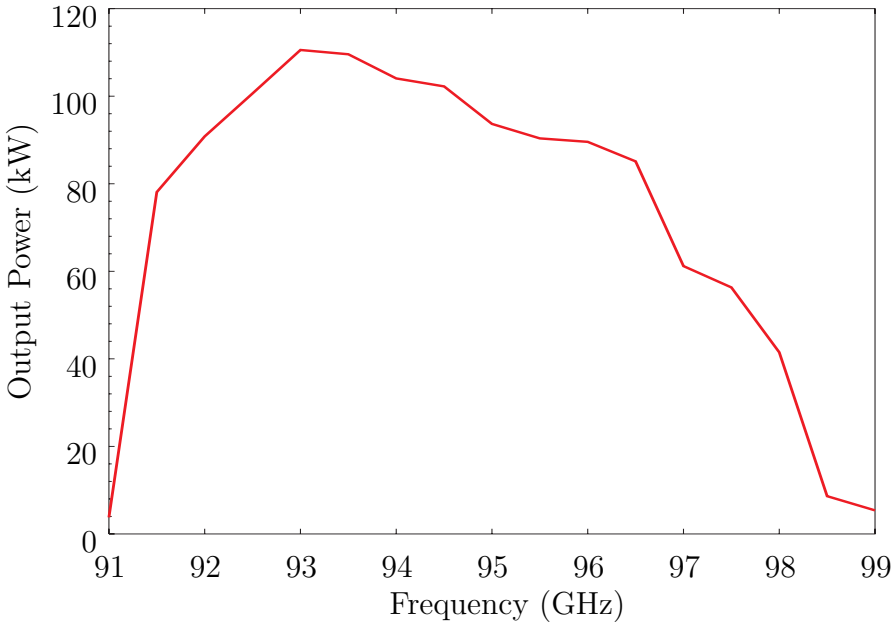

Figure 8-3: Constant drive saturated bandwidth characteristics of the W-band gyro-TWT.

are shown in Fig. 8-3. This simulation was performed for a drive power equal to 2.0 W. The saturated bandwidth is 6.25 GHz (6.7%) centered around 94 GHz. The peak saturated gain at the center of the band is 47.5 dB and the peak efficiency is 29 %. The optimum operating parameters for the W-band gyro-TWT are summarized in Tab. 8.3.

We have not investigated the design of the input and output coupler and the internal mode converter in this design study. The input coupler can be similar to the one used in the present 140 GHz gyro-TWT with multiple apertures for a broadband coupling. Concepts discussed in Sec. 7.7 can be used to build an output coupler and an internal mode converter.

A peak efficiency of 29 % was also computed for this initial design. An increase in efficiency by 10-15 % to yield a total efficiency of 39-45 % using a single stage depressed collector is very much in the realm of possibility. Furthermore, a sectored electron beam with electrons only in the region of the confocal waveguide fields can be used to achieve an even higher efficiency.

Frequency	94 GHz
Peak Output Power	112 kW
Peak Saturated Gain	47.5 dB
Saturated Bandwidth	6.25 GHz (6.7%)
Peak Efficiency	29 %
Beam Voltage	65 kV
Beam Current	6 A
Velocity Pitch Factor	1.0
Long. Momentum Spread	3 %
Beam Radius	0.8 mm
Operating Mode	HE_{04} confocal
Avg. Ohmic Heat Den.	0.52 kW/cm^2 ($\sigma = 3 \times 10^7 \Omega^{-1} m^{-1}$) for 100 kW average power operation

Table 8.3: Operating parameters for the W-band gyro-TWT obtained from the initial design study.

The results from this quick initial design study of a W-band gyro-TWT are very promising. A more careful design of the interaction structure after a detailed investigation can further improve the performance of the device. The interaction structure can also be tailored to have a distributed loss (heavily loaded) to further improve the gain so that ultimately a solid-state driver with 25 mW of power can be used to directly drive the gyro-TWT into saturation. A peak gain of 47.5 dB was computed for this initial design which needs an input power of 2 W for saturation. The use of a 25 mW solid-state driver would require an additional 19 dB gain which would mean that the overall system gain has to about 66 dB. A gain of 70 dB has already been demonstrated in the distributed loss interaction structure at NTHU [77] which indicates that achieving 66 dB gain in the W-band confocal waveguide should be possible. The distributed loss can be easily incorporated by profiling the aperture of the mirrors and using quasioptical techniques to extract the power from the circuit in a manner suitable for high average power operation.

These results are a representative first calculation, the design should be optimized with more detailed calculations.

8.4 Future Work

PBG resonators appear to be very useful in gyrotron oscillators at moderate average power levels. However, at high average power the rods of the PBG structure may not be able to dissipate ohmic losses as effectively as the smooth walls of conventional cylindrical cavities. This can be mitigated by using thicker rods and by cooling the rods with water flowing through channels in the center of each rod. The PBG structures would be able to handle high peak power levels, and would be particularly well suited to high peak power, moderate average power level amplifiers. They are also very attractive for use as the buncher cavities in gyroklystron and gyrotwystron amplifiers at any power level. A gyro-TWT with a PBG interaction structure will not be susceptible to BPWO because the BPWO frequencies will lie in the passband of the lattice thus allowing the complete stabilization of the BPWO modes. This will allow the use of a long interaction structure without the need for severs for achieving high gain. At very high frequencies, where moderate power levels are of interest, the PBG structures also appear to be very attractive. A potential application would be a high power ($>$ 10 kW) conventional millimeter-wave klystron or coupled cavity traveling wave tube operating in a higher order mode with a PBG resonator. Another interesting device is a 100 W CW conventional TWT with an overmoded PBG interaction structure with 5 GHz bandwidth at the W-band (94 GHz). Such a device will be capable of higher output power than the Millitron tubes [21] because of its simple and rugged interaction structure. The simplicity of the structure will improve the fabrication yield and hence lower the manufacturing cost. Such a development would be very useful as a preamplifier in a W-band radar transmitter and can relieve the gain requirement of the main power amplifier and as a result obtain a wide bandwidth.

Higher frequency sub-millimeter wave sources with moderate power, e.g., 100 W CW power at 500 GHz for DNP experiments can be built with either PBG or quasioptical interaction structures. The absence of mode competition allows the structure dimensions to be much larger than a conventional cylindrical waveguide interaction

structure.

Bibliography

[1] H. Sobol and K. Tomiyasu, Milestones of Microwaves, *IEEE Trans. Microwave Theory and Tech.*, vol. 50, no. 3, pp. 594-611, March 2002.

[2] R. F. Varian and S. F. Varian, A High Frequency Oscillator and Amplifier, *J. Appl. Phys.*, vol. 10, pp. 321-327, 1937.

[3] R. Kompfner, *The Invention of the Traveling-Wave Tube*, San Franscisco Press, San Franscisco, 1964.

[4] R. Kompfner, The Invention of the Traveling-Wave Tubes, *IEEE Trans. Electron Dev.*, vol. 23, pp. 730-738, 1976.

[5] See papers in the Proc. IAEA Tech. Comm. Meeting on ECRH Phys. and Tech. for Fusion Deices, Special Issue of Fusion Engg. and Design., vol. 53, pp. 1-594, 2001.

[6] V. Erckmann, G. Dammertz, D. Dorst, L. Empacher, et. al, ECRH and ECCD with High Power Gyrotrons at the Stellarators W7-AS and W7-X, *IEEE Trans. Plasma Sci.*, vol. 27, no. 2, pp. 538-546, 1999.

[7] M. Thumm, State-of-the-Art of High Power Gyro-Devices and Free Electron Masers Update 2001, Wissenchaftliche Berichte, FZKA 6708, Forschungszentrum Karlsruhe, Germany, February 2002.

[8] R. H. Abrams, B. Levush, A. A. Mondelli, and R. K. Parker, Vacuum Electronics for the 21st Century, *IEEE Microwave Mag.*, vol. 2, no. 3, pp. 61-72, September 2001.

[9] R. S. Symons, Modern Microwave Power Sources, *IEEE AESS Sys. Magazine*, pp. 19-26, January 2002.

[10] R. J. Trew, Wide Bandgap Seminconductor Transistors for Microwave Power Amplifiers, *IEEE-Microwave-Magazine*, vol. 1, no.1, pp. 46-54, March 2000.

[11] R. M. Phillips, D. W. Sprehn, High-Power Klystrons for the Next Linear Collider, Proc. IEEE., vol. 87, no. 5, pp. 738-751, 1999.

[12] V. L. Granatstein and W. Lawson, Gyro-Amplifiers as Candidate RF Drivers for TeV Linear Colliders, *IEEE Trans. Plasma Sci.*, vol. 24, no. 3, pp. 648-665, June 1996.

[13] M. Blank, P. Borchard, S. Cauffman, K. Felch et al., Design of a 50 MW 30 GHz Gyroklystron Amplifier for Accelerator Applications, Proc. 3rd Int. Vacuum Electron. Conf., Monterey, CA, pp. 85-86, April, 2002.

[14] J. Neilson, R. L. Ives, M. Read, M. Mizuhara, et al., Development Status of a 10 mW, 91 GHz, Gyroklystron, Proc. of the 27 Int. Conf. on IRMM Waves, San Diego, CA, pp. 237-238, 2002.

[15] K. Felch, B. G. Danly, H. R. Jory, K. E. Kreishcher, W. Lawson, B. Levush, and R. J. Temkin, Characteristics and Applications of Fast-Wave Gyrodevices, *Proc. of the IEEE*, vol. 87, no. 5, pp. 752-781, 1999.

[16] K. Sakamoto, M. Tsuneoka, A. Kasugai, T. Imai et al., Major Improvements of Gyrotron Efficiency With Beam Energy Recovery, Phys. Rev. Lett., vol. 73, no. 26, pp. 3532-3535, 1994.

[17] K. Kreischer, C. Farrar, R. Griffin, R. Temkin, and J. Vieregg, The Development of a 250 GHz CW Gyrotron for EPR and NMR Spectroscopy, *Proc. of the 24th Int. Conf. on IRMM Waves*, Monterey, CA, Paper TU-A3, September 1999.

[18] T. Idehara, I. Ogawa, S. Mitsudo, M. Pereyaslavets, N. Nishida, and K. Yoshida, Development of Frequency Tunable, Medium Power Gyrotron (Gyrotron FU

Series) as Submillimeter Wave Radiation Sources, *IEEE Trans. Plasma Sci.*, vol. 27, no. 2, pp. 340-354, April 1999.

[19] M. Blank, B. G. Danly, B. Levush, P. E. Latham, and D. E. Pershing, Experimental Demonstration of a W-Band Gyroklystron Amplifier, *Phys. Rev. Lett.,* vol. 79, no. 22, pp. 4485-4488, December 1997.

[20] B. G. Danly, M. Blank, J. P. Calame, B. Levush et. al., Development and Testing of a High-Average Power, 94 GHz Gyroklystron, *IEEE Trans. Plasma Sci.*, vol. 28, no. 3, pp. 706-711, June 2000.

[21] B. G. James, Coupled-Cavity TWT Designed for Future Mm-Wave Systems, *MSN Microwave Sys. News and Comm.Tech.*, vol.16, no.10, p.105-111, September 1986.

[22] W. Gerum, G. Lippert, P. Malzahn, and K. Schneider, 94-GHz TWT for Military Radar Applications, *IEEE Trans. Elec. Dev.*, vol. 48, no. 1, pp. 72-73, January 2001.

[23] A. Roitman, P. Horoyski, M. Hyttinen, and B. Steer, Wide Bandwidth, High Average Power EIKs Drive New Radar Concepts, *Proc. Int. Vac. Electron. Conf.*, Monterey, CA, Paper 3.5, May 2000.

[24] M. A. Boyd, R. A. Dehn, J. S. Hickey, and T. G. Mihran, The Multiple-Beam Klystron, *IRE Trans. Electron Dev.*, vol. 9, no. 3, pp. 247-252, 1962.

[25] E. A. Gelvich, L. M. Borisov, Y. V. Zhary, A. D. Zakurdayev, A. S. Pobedonostsev, V. I. Poognin, The New Generation of High-Power Multiple-Beam Klystrons, *IEEE Trans. Microwave Theory and Tech.*, vol. 41, no. 1, pp. 15-19, Jan. 1993.

[26] Y. Besov, Multiple Beam Klystrons, *AIP-Conference-Proceedings,* no.474, pp. 91-106, 1999.

[27] C. Bearzatto, A. Beunas, G. Faillon, Long Pulse and Large Bandwidth Multi-beam Klystron, *AIP-Conference-Proceedings,* no.474, pp. 107-116, 1999.

[28] D. Yaogen, P. Jun, Z. Yunshu, Shi Shaoming, Theoretical and Experimental Research on Multi-Beam Klystron, *AIP-Conference-Proceedings,* no.474, pp. 126-135, 1999.

[29] G. Link, L. Feher, M. Thumm, H. Ritzhaupt-Kleissl, R. Bohome, and A. Weisenburger, Sintering of Advanced Ceramics Using a 30GHz, 10kW, CW Industrial Gyrotron, *IEEE Trans. Plasma Sci.*, vol. 27, no. 2, pp. 547-554, 1999.

[30] L. R. Becerra, G. J. Gerfen, R. J. Temkin, D. J. Single, and R. J. Griffin, Dynamic Nuclear Polarization with a Cyclotron Resonance Maser at 5T, *Phys. Rev. Lett.*, vol. 71, pp. 3561-3564, 1993.

[31] R. J. Briggs, *Electron Stream Interaction with Plasmas*, MIT Press, Cambridge, MA 1964.

[32] A. Bers, *Handbook of Plasma Physics*, vol. 1, Editors M. N. Rosenbluth and R. Z. Sagdeev, North-Holland Publishing Company, New York, 1983.

[33] T. G. Verhoven et. al., First Mm-Wave Generation in the FOM Free Electron Maser, *IEEE Trans. Plasma Sci.*, vol. 27, no. 4, pp. 1084-1091, 1999.

[34] G. R. Neil, C. L. Bohn, S. V. Benson, G. Biallas, D. Douglas et al., Sustained Kilowatt Lasing in a Free-Electron Laser with Same-Cell Energy Recovery, *Phys. Rev. Lett.*, vol. 84, 662-665, January 2000.

[35] G. R. Neil, Trends and Opportunities in Light Source Development, *Nucl. Instr. and Methods in Phys. Res.– A*, vol.483, no.1-2, pp.14-20, May 2002.

[36] R. Q. Twiss, Radiation transfer and the possibility of negative absorption in radio astronomy, *Australian J. Phys*, vol. 11, p. 564, 1958.

[37] J. Schneider, Stimulated emission of radiation by relativistic electron in a magnetic field , *Phys. Rev. Lett.*, vol. 2, p. 504-505, 1959.

[38] A. V. Gaponov, Addendum, *Izv. VUZ Radiofizika*, vol. 2, p. 837, 1959 an addendum to A. V. Gaponov, Interaction between electron fluxes and electromagnetic waves in waveguides, *Izv. VUZ Radiofizika*, vol. 2, p. 450, 1959.

[39] J. L. Hirshfield, I. B. Bernstein, and J. M Wachtel, Cyclotron resonance interaction of microwaves with energetic electrons, *IEEE J. of Quant. Electron.*, vol. 1, no. 6, pp. 237-245, 1965.

[40] V. A. Flyagin, A. V. Gaponov, M. I. Petelin, and V. K. Yulpatov, The Gyrotron, *IEEE Trans. Microwave Theory Tech.*, vol. 25, pp. 514-521, 1977.

[41] R. E. Collin, Foundations for Microwave Engineering, Second Edition, IEEE Press, Piscataway, NJ 1990.

[42] V.L. Bratman, N.S. Ginzburg, G.S. Nusinovich, M.I. Petelin and P.S. Strelkov, Relativistic Gyrotrons and Cyclotron Autoresonance Masers, *Int. J. Electron.*, vol 51, no. 4, pp. 541-567, 1981.

[43] A. V. Gaponov, V. A. Flyagin, A. L. Gol'denberg, G. S. Nusinovich, Sh. E. Tsimring, V. G. Usov, and S. N. Vlasov, Powerful Millimetre-Wave Gyrotrons," *Int. J. Electron.*, vol. 51, no.4, pp.277-302, 1981.

[44] V. L. Granastein, B. Levush, B. G. Danly, and R. K. Parker, A Quarter Century of Gyrotron Research and Development, *IEEE Trans. Plasma Sci.*, vol. 25, pp. 1322-1335, 1997.

[45] K. E. Kreischer, B. G. Danly, J. B. Schutkeker, and R. J. Temkin, The Design of Megawatt Gyrotrons, *IEEE Trans. Plasma Sci.*, vol. 13, no. 6, December 1985.

[46] C.J. Edgcombe, Gyrotron Oscillators – Their Principles and Practice, Taylor and Francis, London,1993.

[47] K.E. Kreischer, J.B. Schutkeker, B.G. Danly, W.J. Mulligan, and R.J. Temkin, High Efficiency Operation of a 140 GHz Pulsed Gyrotron, *Int. J. of Electron.*, vol. 57, no. 6, pp. 835-850, 1984.

[48] K. E. Kreischer, T. L. Grimm, W. C. Guss, A. W. Mobius, and R. J. Temkin, Experimental Study of a High-Frequency Megawatt Gyrotron Oscillator, *Phys. Fluids - B*, vol. 2, no. 3, pp. 640-646, March 1990.

[49] T. L. Grimm, K. E. Kreischer, and R. J. Temkin, Experimental Study of a Megawatt 200-300 GHz Gyrotron Oscillator, *Phys. of Fluids B*, vol. 5, no. 11, p. 4135-4143, 1993.

[50] K. Felch, M. Blank, P. Borchard, T. S. Chu, et al., Long-Pulse and CW Tests of a 110-GHz Gyrotron with an Internal, Quasi-Optical Converter, *IEEE Trans. Plasma Sci.*, vol. 24, no. 3, pp. 558-569, June 1996.

[51] K. E. Kreischer, T. Kimura, B. G. Danly, and R. J. Temkin, High Power Operation of a 170 GHz Megawatt Gyrotron, *Phys. Plasmas,* vol. 4, no. 5, pp. 1907-1914, 1997.

[52] C. T. Iatrou, O. Braz, G. Dammertz, S. Kern, M. Kuntze, B. Piosczyk, and M. Thumm, Design and Experimental Operation of a 165 GHz, 1.5 MW, Coaxial-Cavity Gyrotron with Axial RF output, *IEEE Trans. Plasma Sci.*, vol. 25, no. 3, pp. 470-479, 1997.

[53] B. Piosczyk, O. Braz, G. Dammertz, C. T. Iatrou, S. Illy, M. Kuntze, G. Michel, A. Mobius, M. Thumm, V. A. Flyagin, V. I. Khishnyak, A. B. Pavelyev, and V. E. Zapevalov, Coaxial Cavity Gyrotron with Dual RF Beam Output, *IEEE Trans. Plasma. Sci.,* vol. 26, no. 3, pp. 393-401, 1998.

[54] B. Piosczyk, O. Braz, G. Dammertz, C. T. Iatrou, S. Illy, M. Kuntze, G. Michel, and M. Thumm, 165 GHz, 1.5 MW-Coaxial Cavity Gyrotron with Depressed Collector, *IEEE Trans. on Plasma Sci.*, vol. 27, no. 2, pp. 484-489, 1999.

[55] R. Advani, J. P. Hogge, K. E. Kreischer, M. Pedrozzi, M. E. Read, J. R. Sirigiri, and R. J. Temkin, Experimental Investigation of a 140-GHz Coaxial Gyrotron Oscillator, *IEEE Trans. on Plasma Sci.*, vol. 29, no. 6, pp. 943-950, 2001.

[56] G. Dammertz, S. Alberti, A. Arnold, E. Borie, et. al., Progress of the 1 MW, 140 GHz, CW Gyrotron for W7-X, *Proc. of the 27th Int. Conf. on IRMM Waves*, San Diego, CA, pp. 3-4, September 2002.

[57] J. Byerly, B. G. Danly, K. E. Kreischer, R. J. Temkin, W. J. Mulligan and P. Woskoboinikow, Harmonic emission from high-power-high-frequency gyrotrons, *Int. J. Electron.*, vol. 57, no. 6, pp 1033-1047, 1984.

[58] S. Spira-Hakkarainen, K. Kreischer, and R. J. Temkin, Slotted-Resonator Gyrotron Experiments, *IEEE Trans. Electron Dev.*, vol. 38, no. 6, pp. 1544-1552, June 1991.

[59] B. G. Danly, J. Cheung, V. Gregers-Hansen, G. Linde, and M. Ngo, WARLOC: A High-Power Millimeter-Wave Radar, Proc. of the 27th Int. Conf. on IRMM Waves, San Diego, CA, pp. 233-234, 2002.

[60] I. I. Antakov, E. V. Zasypkin, and E. V. Sokolov, Design and Performance of 94 GHz, high power, multicavity, gyroklystron amplifier, *Proc. 18^{th} Int. Conf. on IRMM Waves*, pp. 466-467, September 1993.

[61] M. Blank, B. G. Danly, B. Levush, D. E. Pershing, Experimental investigation of W-band (93GHz) gyroklystron amplifiers, *IEEE Trans. Plasma Sci.*, vol. 26, no. 3, pp. 409-415, 1998.

[62] M. Blank, B. G. Danly, and B. Levush, Experimental Demonstration of W-Band Gyroklystron Amplifiers with Improved Gain and Efficiency, *IEEE Trans. Plasma Sci.*, vol. 28, no. 3, pp. 609-612, August 2001.

[63] M. Blank, B. G. Danly, B. Levush, Circuit design of a wideband W-band gyroklystron amplifier for radar applications, *IEEE Trans. Plasma Sci.*, vol. 26, no. 3, pp. 426-432, 1998.

[64] M. Blank, B. G. Danly, B. Levush, Experimental Demonstration of a W-band (94GHz) gyrotwystron amplifier, *IEEE Trans. Plasma Sci.*, vol. 27, no. 2, pp. 405-411, 1999.

[65] G. S. Nusinovich, T. M. Antonsen. Jr., H. Guo, and V. Granatstein, Theory of clustered-cavity gyroklystron, *Phys. of Plasmas*, pp. 4032-4039, September 2002.

[66] L. R. Barnett, Y. Y. Lau, K. R. Chu, and V. L. Granatstein, An Experimental Wideband Gyrotron Traveling-Wave Amplifier, *IEEE Trans. Electron Dev.*, vol. 28, pp. 872-875, 1981.

[67] P. E. Ferguson, G. Valier, and R. S. Symons, Gyrotron-TWT Operating Characteristics, *IEEE Trans. Microwave Theory Tech.*, vol. 29, pp. 794-799, 1981.

[68] R. S. Symons, H. R. Jory, S. J. Hegji, and P. E. Ferguson, An Experimental Gyro-TWT, *IEEE Trans. Microwave Theory Tech.*, vol. 29, pp. 794-799, 1981.

[69] L. R. Barnett, L. H. Chang, H. Y. Chen, K. R. Chu, Y. K. Lau, and C. C. Tu, Absolute Instability Competititon and Suppression in a Millimeter-Wave Gyrotron Traveling-Wave Tube, *Phys. Rev. Lett.*, vol. 63, pp. 1062-1065, 1989.

[70] K. R. Chu, L. R. Barnett, W. K. Lau, L. H. Lang, and H. Y. Chen, A Wide-Band Millimeter-Wave Gyrotron Traveling-Wave Amplifier Experiment, *IEEE Trans. Electron Dev.*, vol. 37, pp. 1557-1560, 1990.

[71] K. C. Leou, D. B. McDermott, A. H. Balkcum, and N. C. Luhmann, Jr., Stable High Power TE_{01} Gyro-TWT Amplifiers, *IEEE Trans. Plasma Sci.*, vol. 22, pp. 585-592, 1994.

[72] Q. S. Wang, D. B. McDermott, and N. C. Luhmann, Jr., Demonstration of Marginal Stability Theory by a 200-kW Second Harmonic Gyro-TWT Amplifier, *Phys. Rev. Lett.*, vol. 75, pp. 4322-4325, 1995.

[73] D. B. McDermott, A. J. Balkcum and N. C. Luhmann, Jr., 35-GHz 25-kW CW Low-Voltage Third-Harmonic Gyrotron, *IEEE Trans. Plasma Sci.*, vol. 24, no. 3, pp. 613-619, June 1996.

[74] G. S. Park, J. J. Choi, S. Y. Park, C. M. Armstrong, A. K. Ganguly, R. H. Kyser, and R. K. Parker, Gain Broadening of Two-Stage Tapered Gyrotron Traveling Wave Tube Amplifier, *Phys. Rev. Lett.*, vol. 74, pp. 2399-2402, 1995.

[75] G. S. Park, S. Y. Park, R. H. Kyser, C. M. Armstrong, A. K. Ganguly, and R. K. Parker, Broadband Operation of a Ka-band Tapered Gyro-Traveling Wave Amplifier, *IEEE Trans. Plasma Sci.*, vol. 22, no. 5, pp. 536-543, 1994.

[76] K. R. Chu, L. R. Barnett, H. Y. Chen, S. H. Chen, Ch. Wang, Y. S. Yeh, Y. C. Tsai, T. T. Yang, and T. Y. Dawn, Stabilizing of Absolute Instabilities in Gyrotron Traveling-Wave Amplifier, *Phys. Rev. Lett.*, vol. 74, pp. 1103-1106, 1995.

[77] K. R. Chu, H. Y. Chen, C. L. Hung, T. H. Chang, L. R. Barnett, S. H. Chen, and T. T. Yang, Ultra High Gain Gyrotron Traveling Wave Amplifier, *Phys. Rev. Lett.*, vol. 81, pp. 4760-4763, 1998.

[78] K. R. Chu, H.Y. Chen, C. L. Jung, T. H. Chang, L. R. Barnett, S. H. Chen, T. T. Yang, and D. J. Dialetis, Theory and Experiment of a Ultrahigh-Gain GyrotronTraveling Wave Amplifier, *IEEE Trans. Plasma Sci.*, vol. 27, no. 2, pp. 391-404, 1999.

[79] G. G. Denisov, V. L. Bratman, A. W. Cross, W. He, A. D. R. Phelps, K. Ronald, S. V. Samsonov, and C. G. Whyte, Gyrotron Traveling Wave Amplifier With a Helical Interaction Waveguide, *Phys. Rev. Lett.*, vol. 81, no. 25, pp.5680-5683, 1998.

[80] G. G. Denisov, V. L. Bratman, A. D. R. Phelps, and S. V. Samsonov, Gyro-TWT With a Helical Operating Waveguide: New Possibilities to Enhance Effi-

ciency and Frequency Bandwidth, *IEEE Trans. Plasma Sci.*, vol. 26, no. 3, pp. 508-518, 1998.

[81] V. L. Bratman, A. W. Cross, G. G. Denisov, W. He, A. D. R. Phelps, K. Ronal, S. V. Samsonov, C. G. Whyte, and A. R. Young, High-Gain Wide-Band Gyrotron Traveling Wave Amplifier with a Helically Corrugated Waveguide, *Phys. Rev. Lett.,* vol. 84, no. 12, pp. 2746-2749, March 2000.

[82] S. J. Cooke and G. G. Denisov, Linear Theory of a Wide-Band Gyro-TWT Amplifier Using Spiral Waveguide, *IEEE Trans. Plasma Sci.*, vol. 26, no. 3, pp. 519-530, 1998.

[83] M. Garven, J. P. Calame, B. G. Danly, K. T. Nguyen, B. Levush, F. N. Wood, and D. E. Pershing, A Gyrotron Traveling Wave Tube Amplifier Experiment with a Ceramic Loaded Interaction Region, *IEEE Trans. Plasma Sci.*, June 2002 (to be published).

[84] J. P. Calame, M. Garven, B. G. Danly, B. Levush, and K. T. Nguyen, Gyrotron-Traveling Wave-Tube Circuits Based on Lossy Ceramics, IEEE Trans. Elec. Dev. vo. 49, no. 8, pp. 1469-1477, August 2002.

[85] G. G. Denisov, V. L. Bratman, V. N. Manuilov, G. I. Kalynova, et al., New Test Results on Broad-Band Gyro-TWT and Gyro-BWO with Hellically Grooved Operating Waveguides, Proc. 27th IEEE Int. Conf. on IRMM Waves, San Diego, pp. 197-198, Sept. 2002.

[86] W. L. Menninger, B. G. Danly and R. J. Temkin, Multimegawatt Relativistic Harmonic Gyrotron Traveling-Wave Tube Amplifier Experiments, *IEEE Trans. on Plasma Sci.*, vo. 24, no. 3, pp. 687-699, 1996.

[87] L. A. Weinstein, Open Resonators and Open Waveguides, Golem Press, Boulder, CO, 1969.

[88] W. Hu, M. A. Shapiro, K. E. Kreischer, and R. J. Temkin, 140 GHz Gyrotron Experiments Based on a Confocal Cavity, *IEEE Trans. Plasma Sci.*, vol. 26, no. 3, pp. 366-374, 1998.

[89] M. Hornstein, V. S. Bajaj, R. G. Griffin, K. E. Kreischer, I. Mastovsky, M. A. Shapiro, and R. J. Temkin, Design of a 460 GHz Second Harmonic Gyrotron Oscillator for use in Dynamic Nuclear Polarization, *Proc. Int. Conf. on IRMM Waves*, San Diego, pp. 193-194, September 2002.

[90] E. I. Smirnova, C. Chen, M. A. Shapiro, J. R. Sirigiri, and R. J. Temkin, Simulation of Photonic Band Gaps in Metal Rod Lattices for Microwave Applications, *J. App. Phys.*, vol. 91, no. 3, pp. 960-968, 2002.

[91] High Frequency Structure Simulator – Version 6.0.12, Ansoft Corporation, Pittsburg, PA, 1999.

[92] A. H. W. Beck, Space-Charge Waves, and Slow Electromagnetic Waves, Pergamon Press, New York, 1958.

[93] J. R. Pierce, *Traveling -Wave Tubes*, D. Van Nostrand, New York, 1965.

[94] E. S. Weibel, Spontaneously Growing Transverse Waves in a Plasma Due to an Anisotropic Velocity Distribution, *Phys. Rev. Lett.*, vol. 2. pp. 83-85, 1959.

[95] P. Sprangle and W. M. Manheimer, Coherent Nonlinear Theory of a Cyclotron Instability, *Phys. Fluids*, vol. 18, pp. 224-230, 1975.

[96] P. Sprangle and A. T. Drobot, The Linear and Self-Consistent Non-Linear Theory of the Electron Cyclotron Maser Instability, *IEEE Trans. Microwave Theory Tech.*, vol. 25, pp. 528-544, 1977.

[97] V. L. Granatstein and I. Alexeff, *High-Power Microwave Sources*, Artech House, Boston, 1987.

[98] K. R. Chu and J. L. Hirshfield, Comparative Study of the Axial and Azimuthal Bunching Mechanisms in Electromagnetic Cyclotron Instabilities, *Phys. Fluids*, vol. 21, pp. 461-466, 1978.

[99] S. Ono, K. Yamanouchi, Y. Shibata, Y. Koike, *Proc. 4th Int. Conf. on Microwave Tubes*, pp. 355,363, 1962.

[100] G. Dohler, Peniotron Interactions in Gyrotrons. I. Qualitative Analysis, *Int. J. Electron.*, vol.56, no.5, pp.617-627, 1984.

[101] G. Dohler, Peniotron Interactions in Gyrotrons. II. Qualitative Analysis, *Int. J. Electron.*, vol.56, no.5, pp.629-640, 1984.

[102] G.S. Nusinovich and R.E. Erm, Elektron. Tekh., Ser. 1, Elektron. SVCh, 55, 1972.

[103] K. E. Kreischer and R. J. Temkin, Linear Theory of an Electron Cyclotron Resonance Maser Operating at the Fundamental, *Int. J. of IRMM Waves*, vol. 1, no. 2, pp. 195-223, 1980.

[104] B. G. Danly and R. J. Temkin, Generalized Nonlinear Harmonic Gyrotron Theory, *Phys. Fluids*, vol. 29, no. 2, pp. 561-567, February 1986.

[105] O. Dumbrajs and J. P. T. Koponen, Generalized gyrotron theory with inclusion of electron velocity and energy spreads, *Phys. of Plasmas*, vol. 6, no. 6, pp. 2618-2621, 1999.

[106] V. K. Yulpatov, Nonlinear theory of the interaction between a periodic electron beam and an electromagnetic wave, Radiophysics and Quantum Electronics, vol. 10, pp. 471-476., 1967.

[107] J. L. Seftor, V. L. Granatstein, K. R. Chu, P. Sprangle, and M. E. Read, The Electron Cyclotron Maser as a High Power Traveling-Wave Amplifier of Millimeter Waves, *IEEE J. Quantum Electron.*, vol. 15, pp. 848-853, 1979.

[108] K. R. Chu, A. T. Drobot, H. H. Szu, and P. Sprangle, Theory and Simulation of the Gyrotron Traveling Wave Amplifier Operating at Cyclotron Harmonics, *IEEE Trans. Microwave Theory Tech.*, vol 28, pp. 313-317, 1980.

[109] J. Y. Choe and S. Ahn, General Mode Analysis of a Gyrotron Disperion Equation, IEEE Trans. Electron Dev., vo. 28, no. 1, pp. 94-102, January 1981.

[110] Y. Y. Lau, K. R. Chu, L. R. Barnett, and V. L. Granatstein, Gyrotron Traveling Wave Amplifier: I. Analysis of Oscillations, *Int. J. IRMM Waves*, vol. 2, pp. 373-393, 1981.

[111] Y. Y. Lau, K. R. Chu, L. R. Barnett, and V. L. Granatstein, Effects of Velocity Spread and Wall Resistivity on the Gain and Bandwidth of the Gyrotron Traveling-Wave Amplifier, *Int. J. IRMM Waves*, vol. 2, pp. 395-413, 1981.

[112] A. K. Ganguly and S. Ahn, Self-Consistent Large Signal Theory of the Gyrotron Traveling Wave Amplifier, *Int. J. Electron.*, vol. 53, pp. 641-658, 1982.

[113] A. K. Ganguly and S. Ahn, Large-Signal Theory of a Two-Stage Wide Band Gyro-TWT, *IEEE Trans. Electron Dev.*, vol. 31, pp. 474-480, 1984.

[114] Q. F. Li, S. Y. Park, and J. L. Hishfield, Theory of Gyrotron Traveling-Wave Amplifiers, *IEEE Trans. Microwave Theory and Tech.*, vo. 34, no. 10, pp. 1044–1058, October 1986.

[115] A. W. Fliflet, Linear and Nonlinear Theory of the Doppler-Shifted Cyclotron Resonance Maser Based on TE and TM Waveguide Modes, *Int. J. Electron.*, vol. 61, pp. 1049-1080, 1986.

[116] A. T. Lin, K. R. Chu, and A. Abromborsky, Stability and Tunability of a CARM Amplifier, *IEEE Trans. Electron Dev.*, vol. 34, pp. 2621-2624, 1987.

[117] K. D. Pendergast, B. G. Danly, R. J. Temkin, and J. S. Wurtele, Self-Consistent Simulation of Cyclotron Autoresonance Maser Amplifiers, *IEEE Trans. Plasma Sci.*, vol. 16, pp. 122-128, 1988.

[118] K. R. Chu and A. T. Lin, Gain and Bandwidth of the Gyro-TWT and CARM Amplifier, *IEEE Trans. Plasma Sci.*, vol. 16, pp. 90-104, 1988.

[119] J. A. Davies, Conditions for Absolute Instability in the Cyclotron Resonance Maser, *Phys. Fluids B*, vol. 1, pp. 663-669, 1989.

[120] A. T. Lin, C. C. Lin, and K. R. Chu, Stability of a High Order Mode CARM Amplifier, *IEEE Trans. Electron Dev.*, vo. 36, pp. 785-788, 1989.

[121] A. T. Lin and C. C. Lin, Stabilization of the Absolute Instability in Cyclotron Resonance Maser Amplifiers by a Drive Wave, *Phys. Fluids B*, vol. 1, pp. 2286-2288, 1989.

[122] K. R. Chu, L. R. Barnett. W. K. Lau, L. H. Chang, A. T. Lin, and C. C. Lin, Nonlinear Dynamics of the Gyrotron Traveling-Wave Amplifier, *Phys. Fluids, vol. B3*, pp. 2403-2408, 1991.

[123] G. S. Nusinovich and H. Li, Theory of gyro-travelling-wave tubes at cyclotron harmonics, Int. J. Electron., vo. 72, nos. 5 and 6, pp. 895-907, 1992.

[124] G. S. Nusinovich and H. Li, Large-Signal Theory of Gyro-Traveling Wave Tubes at Cyclotron Harmonics, *IEEE Trans. Plasma Sci.*, vol. 20, no. 3, pp. 170-175, 1992.

[125] G. S. Nusinovich, Cyclotron Resonance Masers With Inhomogeneous External Magnetic Fields, *Phys. Fluids - B*, vol. 4, pp. 1989-1997, 1992.

[126] A. T. Lin, K. R. Chu, C. C. Lin, C. S. Kou, D. B. McDermott, and N. C. Luhmann, Jr., Marginal Stability Design Criterion for Gyro-TWT's and Comparison of Fundamental with Second Harmonic Operation, *Int. J. Electron.,* vol. 72, pp. 873-885, 1992.

[127] C. S. Kou, Q. S. Wang, D. B. McDermott, A. T. Lin, K. R. Chu, and N. C. Luhmann, Jr., High-Power Harmonic Gyro-TWT's I: Linear Theory and Oscillation Study, *IEEE Trans. Plasma Sci.*, vol. 20, pp. 155-162, 1992.

[128] C. S. Kou, Q. S. Wang, D. B. McDermott, A. T. Lin, K. R. Chu, and N. C. Luhmann, Jr., High-Power Harmonic Gyro-TWT's II: Nonlinear Theory and Design, *IEEE Trans. Plasma Sci.*, vol. 20, pp. 155-162, 1992.

[129] S. J. Rao, P. K. Jain, and B. N. Basu, Amplification in gyro-travelling-wave tubes – dispersion relation and gain-bandwidth characterisitics, IETE Tech. Review (India), vol. 13, no. 3, pp. 141-150, 1996.

[130] C. S. Kou and F. Tseng, Linear Theory of Gyrotron Traveling Wave Tubes with Nonuniform and Lossy Interaction Structures, *Phys. Plas.*, vol. 5, no. 6, pp. 2454-2461, June 1998.

[131] G. S. Nusinovich, M. Walter, and J. Zhao, Excitation of Backward Waves in Forward Wave Amplifiers, *Phys. Rev. E*, vol. 58, no. 5, pp. 6594-6605, November 1998.

[132] G. S. Nusinovich, W. Chen, and V. L. Granatstein, Analytic Theory of Frequency-Mulitplying Gyro-Traveling-Wave-Tubes, *Phys. Plas.*, vol. 8, no. 2, pp. 631-637, February 2001.

[133] G. S. Nusinovich, O. V. Sinitsyn, and A. Kesar, Linear Theory of Gyro-Traveling-Wave-Tubes with Distributed Losses, *Phys. Plas.*, vol. 8, no. 7, pp. 3427-3433, July 2001.

[134] J. R. Sirigiri, Theory and Design Study of a Novel Quasi-Optical Gyrotron Traveling Wave Amplifier, S.M. Thesis submitted to the Dept. of Electr. Engg. and Comp. Sci., Massachusetts Institute of Technology, October 1999.

[135] J. M Baird and W. Lawson, Magnetron injection gun design for gyrotron applications, *Int. J. of Electron.*, vol. 61, pp. 953-967, 1986.

[136] B. N. Basu, *Electromagnetic Theory and Applications in Beam-Wave Electronics*, World Scientific, Singapore, 1996.

[137] K. R. Chu, A. K. Ganguly, V. L. Granatstein, J. L. Hirshfield, S. Y. Park, and J. M Baird, Theory of a Slow Wave Cyclotron Amplifier, *Int. J. Electron.*, vol. 51, pp. 493-502, 1981.

[138] G. S. Nusinovich and O. Dumbrajs, Theory of gyro-backward wave oscillators with tapered magnetic field and waveguide cross section, IEEE Trans. Plasma Sci., vol. 24, no. 3, pp. 620-629, 1996.

[139] User's Manual for Compaq Visual Fortran Version 6.1, Compaq Corporation, Houston, TX, 1999.

[140] W. B. Hermannsfeldt, *Electron Trajectory Program*, Technical Report SLAC-226, UC-28, Stanford Linear Accelerator Center, 1979.

[141] G. Scheitrum, G. Caryotakis, B. Arfin, A. Haase, et. al., *Proc. Int. Vac. Electron. Conf.*, Monterey, CA, Paper 1.5, May 2000.

[142] G. Scheitrum, A. Burke, G. Caryotakis, A. Haase, D. Martin and B. Arfin, Initial RF Testing of 95 GHz Klystrino, *Proc. Third Int. Vac. Electron. Conf.*, Monterey, CA, pp. 324-325 April 2002.

[143] J. Hruby, Overview of LIGA Microfabrication, High Energy Density and High Power RF, Ed. B. E. Carlsten, AIP Conf. Proc. 625, 2001.

[144] A. A. Tolkachev, B. A. Levitan, G. K. Solovjev, V. V. Neytsel and V. E. Farber, A Megawatt Power Millimeter-Wave Phased-Array Radar, IEEE AES Sys. Magazine, vol. 15, no. 7, pp. 25-31, July 2000.

[145] M. D. Abouzahra, and R. K. Avent, The 100 kW Millimeter-Wave Radar at the Kwajalein Atoll, *IEEE Ant. Prop. Magazine,* vol. 36, no. 2, pp. 7-19, 1994.

[146] M. T. Ngo, B. G. Danly, R. Myers, D. E. Pershing, V. Gregers-Hansen, and G. Linde, High-Power Millimeter-Wave Transmitter for the NRL WARLOC Radar, *Proc. of the Third Int. Conf. Vacuum Electron.*, Monterey, CA, pp. 363-364, April 2002.

[147] V. L. Bratman, G. G. Denisov, N. S. GInzburg, and M. I. Petelin, FEL's With Bragg Reflection Resonators: Cyclotron Autoresonance Masers Versus Ubitrons, IEEE J. Quant. Electron., vo. 19, n0. 3, pp. 282-296, March 1983.

[148] E. Yablonovitch, T. J. Gmitter, K. M. Leung, Photonic Band Structure: The Face-Centered-Cubic Case Employing Nonspherical Atoms, *Phys. Rev. Lett.,* vol. 67, no. 17, pp. 2295-2298, 1991.

[149] J. D. Joannopoulous, R. D. Meade, and J. N. Winn, Photonic Crystals: Molding the Flow of Light, Princeton University Press, Princeton, NJ, 1995.

[150] S. G. Johnson, and J. D. Joannopoulous, Photonic Crystals: The Road from Theory to Practice, Kluwer Academic Publishers, Boston, MA, 2002.

[151] A. Mekis, J. C. Chen, I. Kurland, S. Fan, P. R. Villeneuve, and J. D. Joannopoulos, High Transmission Through Sharp Bends in Photonic Crystal Waveguides *Phys. Rev. Lett.,* vol. 77, no. 18, pp. 3787-3790, 1996.

[152] J. Broeng, D. Mogilevstev, S. E. Barkou, and A. Bjarklev, Photonic Crystal Fibers: A New Class of Optical Waveguides, *Optical Fiber Technology*, vol. 5, pp. 305-330, 1999.

[153] E. Chow, S. Y. Lin, S. G. Johnson, P. R. Villeneuve, et. al., Three-Dimensional Control of Light in a Two-Dimensional Photonic Crystal Slab, *Nature*, vol. 407, pp. 983-986, 2000.

[154] V. Radisic, Y. Qian, and T. Itoh, Novel 2-D Photonic Bandgap Structure for Microstrip Lines , *IEEE Microwave Guided Wave Lett.*, vol. 8, no. 2, pp. 69-71, 1998.

[155] J. R. Sirigiri, K. E. Kreischer, J. Machuzak, I. Mastovsky, M. A. Shapiro and R. J. Temkin, Photonic-Band-Gap Resonator Gyrotron, *Phys. Rev. Lett.*, vol. 86, no. 24, pp. 5628-5631, June 2001.

[156] D. R. Smith, S. Schultz, N. Kroll, M. Sigalas, K. M. Ho, and C. M. Soukoulis , Experimental and Theoretical Results for a Two-Dimensional Metal Photonic Band-Gap Cavity, *App. Phys. Lett.*, vol. 75, no. 5, pp. 645-647,1994.

[157] N. Kroll, D. R. Smith, and S. Schultz, Advanced Acclerator Concepts, Ed. J. S. Wurtele, AIP Conf. Proc., No. 279, pp. 197-, AIP, New York, 1993.

[158] M. A. Shapiro, W. J. Brown, I. Mastovsky, J. R. Sirigiri and R. J. Temkin, 17 GHz Photonic Band Gap Cavity With Improved Input Coupling, *Phys. Rev. Spl. Topics – Acc. and Beams*, vol. 4, pp. 042001, 2001.

[159] S. G. Johnson, and J. D. Joannopoulous, The MIT Photonic-Bands Package Home Page, http://ab-initio.mit.edu/mpb/.

[160] N. A. Nicorovici, R. C. McPhedran and L. C. Botten, Photonic Band Gaps for Arrays of Perfectly Conducting Cylinders, Phys. Rev. E., vol. 52, no. 1, pp. 1135-1145, 1995.

[161] J.H. Billen and L.M. Young, POISSON/ SUPERFISH on PC compatibles, Proceedings of the 1993 Particle Accelerator Conference (Cat. No.93CH3279-7), IEEE, vol. 2, pp. 790-, New York,1993.

[162] H. Weideman, Particle Accelerator Physics - I: Basic Principles and Linear Beam Dynamics, Springer-Verlag, New York, 1999.

[163] K. T. Nguyen, J. P. Calame, D. E. Pershing, B. G. Danly, M. Garven, B. Levush, and T. M. Antonsen, Design of Ka-Band Gyro-TWT for Radar Applications, *IEEE Trans. Electron Dev.*, vol. 48, no. 1, pp. 108-115, January 2001.

[164] W. B. Lynch, K. A. Earle, and J. H. Freed, 1-mm Wave ESR Spectrometer, Rev. Sci. Instrum., vol. 59, pp. 1345-1351, August 1988.

[165] P. Goldsmith, Quasioptical Systems: Gaussion Beam Quasioptical Propagation and Applications, IEEE Press, Piscataway, NJ, 1998.

[166] G. D. Boyd and J. P. Gordon, Confocal Multimode Resonator for Millimeter Through Optical Wavelength Masers, *Bell Sys. Tech. Journal*, vol. XL, no. 2, pp. 489-508, 1961.

[167] J. A. Stratton, P. M. Morse, L. J. Chu, J. D. C. Little and F. J. Corbator, Spheroidal Wave Functions, Including Tables of Separation Constants and Coefficients, Technology Press of MIT and Wiley, New York, 1956.

[168] V. P. Shestopalov, and Y. V. Shestopalov, Spectral Theory and Excitation of Open Structures, IEEE, London, 1996.

[169] J. L. Doane, Propagation and Mode Coupling in Corrugated and Smooth-Wall Circular Waveguides, Infrared and Millimeter Waves, Ed. K. J. Button, vol. 13, Chap. 5, 1985.

[170] W. C. Guss, T. L. Grimm, K. E. Kreischer, J. T. Polevoy, and R. J. Temkin, Velocity Ratio Measurements of a Gyrotron Electron Beam, *J. Appl. Phys.*, vol. 69, no. 7, pp. 3789-3795, April 1991.

[171] A. K. Ganguly, and K. R. Chu, Limiting Current in Gyrotrons, *Int. J. IRMM Waves*, vol. 5, no. 1, pp. 103-121, 1984.

[172] D. R. Whaley, M. Q. Tran, T. M. Tran, T. M. Antonsen, Jr., Mode Competition and Startup in Cylindrical Cavity Gyrotrons Using High-Order Operating Modes, IEEE Trans. Plasma Sci., vol. 22, no. 5, pp. 850-860, 1994.

[173] G.P. Saraph, T.M. Antonsen, B. Levush, and G.I. Lin, Regions of Stability of High-Power Gyrotron Oscillators, *IEEE Trans. Plasma Sci.*,vol. 20, no. 3, 115-125, 1992.

[174] G.P. Saraph, T.M. Antonsen, G.S. Nusinovich, and B. Levush, Nonlinear Theory of Stable, Efficient Operation of a Gyrotron at Cyclotron Harmonics, *Phys. Fluids B-Plasma Phys.*,vol.5, no.12, p.4473-85, 1993.

[175] Y. Carmel, K.R. Chu, D. Dialetis, A. Fliflet, M.E. Read, K.J. Kim, B. Arfin, and V.L. Granatstein, Mode Competition, Suppression, and Efficiency Enhancement in Overmoded Gyrotron Oscillators, *Int. J. IRMM. Waves*, vol. 3, no. 5, pp. 645-665, 1982.

[176] P. H. Seigel, Terahertz Technology, *IEEE Trans. Microwave Theory Tech.*, vol. 50, no. 3, pp. 910-928, March 2002.

[177] T. A. Hargreaves, K. J. Kim, J. M. McAdoo, S. Y. Park, R. D. Seley, and M. E. Read, Experimental Study of a Single-Mode Quasi-Optical Gyrotron, *Int. J. Electron.*, vol. 57, pp. 977-84, 1984.

[178] M. E. Read, M. Q. Tran, J. McAdoo, and M. Barsanti, Experimental Study of a 115 GHz Quasi-Optical Gyrotron With a Large Cavity, *Int. J. Electron.*, vol. 65 pp. 309-325, 1988.

[179] M. Q. Tran, T. M. Tran, Quasioptical Gyrotron Development at the Centre de Recherches en Physique des Plasmas, in Gyrotron Oscillator: Their Principles and Practice, Ed. C. J. Edgcombe, Taylor and Francis, London, 1993.

[180] S. N. Vlasov, G. M. Zhislin, I. M. Orlova, M. I. Petelin, and G. G. Rogacheva, Irregular Waveguides and Open Resonators, *Radiophys. Quantum Electron.*, vol. 12, pp. 972-978, 1969.

[181] Operator's manual for the VUW-8140A gyrotron gun, Varian Associates, Palo Alto, CA, July 1982.

[182] P. Woskoboinikow, Development of Gyrotrons for Plasma Diagnostics, *Rev. Sci. Instrum.*, vol. 57, no. 8, pp. 2113-2118, August 1986.

[183] J. S. Machuzak, D. Y. Rhee, P. P. Woskow et al., Development of High-Power Millimeter and Submillimeter Wavelength Collective Thomson Scattering Diagnostics for Energetic Ion Measurements in Tokamaks, *Rev. Sci. Instrum.*, vol. 61, no. 11, pp. 3544-3547, November 1990.

[184] F. Orsitto and G. Giruzzi, Review of Possibilities for a Collective Thomson Scattering System on ITER, *Rev. Sci. Instrum.*, vol. 68, no. 1, pp. 686-688, January 1997.

[185] B. Mikijelj and D. K. Abe, AlN-Based Lossy Ceramics for High Power Applications, *Third IEEE Int. Vac. Electron. Conf.*, Monterey, CA, pp. 32-33, April 2002.

[186] E. Savrun, V. Nguyen, and D. K. Abe, High Thermal Conductivity Aluminium Nitride Ceramics for High Power Microwave Tubes, *Third IEEE Int. Vac. Electron. Conf.*, Monterey, CA, pp. 34-35, April 2002.

[187] H. Park, N. Bretz, R. Cutler, R. Ellis, J. S. Machuzak, P. P. Woskov, T. Biglow, Materials and Design Criteria for Ultra High Transmission and Absorption of High Power Microwaves, Presented at the U.S.-Japan Workshop on Millimeter and Submillimeter Wave Plasma Diagnostics, UCLA, Los Angeles, Dec. 1992.

[188] S. J. Wilson and M. C. Hutley, The Optical Properties of 'Moth Eye' Antireflection Surfaces, *Optica Acta*, vol. 29, no. 7, pp. 993-1009, 1982.

[189] J. Y. L. Ma and L. C. Robinson, Night Moth Eye Window for the Millimeter and Sub-Millimeter Wave Region, *Optica Acta*, vol. 30, no. 12, pp. 1685-1695, 1983.

[190] S. N. Vlasov, L. I. Zagryadskaya, and M. I. Petelin, Transformation of a Whispering Gallery Mode, Propagating in a Circular Waveguide, into a Beam of Waves, *Radio Engg. and Electronic Phys.*, vol. 12, no. 10, pp. 14-17, 1975.

[191] G. G. Denisov, A. N. Kuftin, V. I. Malygin, N. P. Venediktov, D. V. Vinogradov, and V. E. Zapelov, 110 GHz Gyrotron With Built-In High Efficiency Converter, *Int. J. Electron.*, vol. 72, no. 5, pp. 1079-1091, 1992.

[192] M. Thumm, High Power Mode Conversion for Linearly Polarized HE_{11} Hybrid Mode Output, *Int. J. Electron.*, vol. 61, no. 6, pp. 1135-1153, 1986.

[193] R. Heidinger, Dielectric Property Measurements on CVD diamond Grades for Advanced Gyrotron Windows, *Conf. Digest of Int. Conf. on IRMM Waves*, pp. 277-278, 1994.

[194] K. Sakamoto, A. Kasugai, M. Tsuneoka, K. Takahashi, and T. Imai, High Power 170 GHz Gyrotron With Synthetic Diamond Window, *Rev. Sci. Instr.*, vol. 70, no. 1, pp. 208-212, 1999.

[195] O. Braz, G. Dammertz, M. Kuntze, and M. Thumm, D-Band Frequency Step-Tuning of a 1 MW Gyrotron Using a Brewster Output Window, *Int. J. of IRMM Waves*, vol. 18, no. 8, pp. 1465-1477, August 1997.

[196] M. Thumm, A. Arnold, E. Borie, O. Braz, et al., Frequency Step-Tunable (114-170 GHz) Megawatt Gyrotrons for Plasma Physics Applications, *Fusion Engg. and Des.*, vol. 53, pp. 407-421, 2001.

[197] J. L. Doane, Mode Converters for Generating the HE 11 (Gaussian-Like) Mode From TE 01 in a Circular Waveguide, *Int. J. Electron.*, vol. 53, no. 6, pp. 573-585, 1982.

[198] T. Kimura, Experimental Study of a 1 MW, 170 GHz Gyrotron Oscillator, Ph.D. Thesis submitted to the Dept. of Physics, Massachusetts Institute of Technology, Cambridge, MA, September 1997.

[199] L. J. Chu, Calculation of the Radiation Properties of Hollow Pipes and Horns, *J. App. Phys.*, vol. 11, pp. 603-610, 1940.

[200] J. F. Gittins, Power Travelling-Wave Tubes, American Elsevier, New York, 1965.

[201] K. T. Nguyen, B. G. Danly, B. Levush, M. Blank et al., Electron Gun and Collector Design for 94-GHz Gyro-Amplifers, *IEEE Trans. Plasma Sci.*, vol. 26, no. 3, pp. 799-813, June 1998.